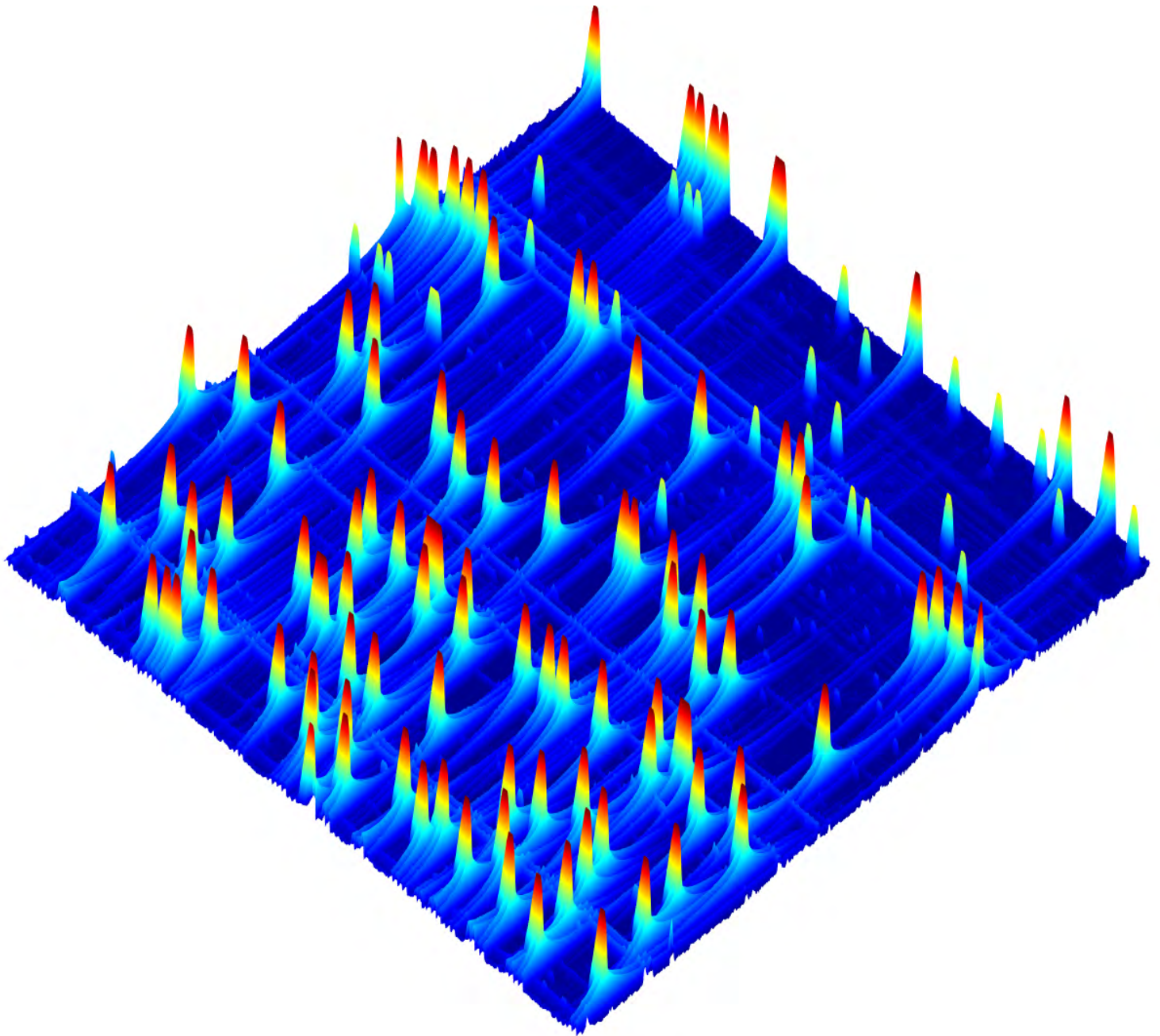


Hermes José Loschi



**Modulation Algorithms of Power Electronic
Converters for Shaping of Conducted Interference**

Institute of Automatics, Electronics and Electrical Engineering
Automatics, Electronics and Electrical Engineering
University of Zielona Gora

Modulation Algorithms of Power Electronic Converters for Shaping of Conducted Interference

Hermes José Loschi
August 2022

This dissertation has been approved by:

Prof. dr. Robert Smolenski
Institute of Automatics, Electronics and Electrical Engineering
University of Zielona Gora



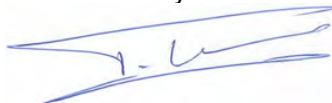
Signed by /
Podpisano przez:

Robert Smoleński

Date / Data:
2022-08-19
14:10

Supervisor's signature and date.


Prof. dr. ir. Frank B. J. Leferink
Department of Electrical Engineering, Mathematics and Computer Science
University of Twente



19 August 2022

Supervisor's signature and date.

Prof. dr. Dave W. P. Thomas
Department of Electrical and Electronic Engineering
University of Nottingham



Supervisor's signature and date.

18/8/2022

Summary

Electromagnetic compatibility has been consolidated as a necessary and inherent process in designing electrical and electronic devices that, due to smart cities, become part of an interconnected systems-of-systems infrastructure. DC micro-grids, DC nano-grids, solar photovoltaic, and thermal energy systems are examples of grids infrastructure that led to a significant increase in the number of power electronic converters connected to the electricity grid. Hence, leading to an increase in the electromagnetic interference in smart grids.

Remarkably, over the last few decades, the electromagnetic interference within 9 to 150 kHz was especially accentuated since the switching frequency of power electronic converters is still limited to several kHz. Thus, bringing up the debate on regulation. From the point of view of the electromagnetic interference noise shape, two cases represent the extremes of possibilities among the various possible converter control algorithms: the deterministic and pseudo-random modulation. Over the last decades, pseudo-random modulation has been considered a complementary methodology to achieve electromagnetic compatibility, jointly with the electromagnetic interference filters and improvements on the printed circuit board layouts.

However, the research carried out and presented in this thesis aims to understand if it is possible to develop new, dedicated converter control algorithms that allow shaping the spectrum of disturbances to meet standardization or technical requirements. Although it seems trivial, the electromagnetic interference measured level depends on the setting of the EMC-test bench system, and the impact of pseudo-random modulation on measured conducted electromagnetic interference is still unclear for the low frequency range.

For instance, evaluating any electromagnetic interference noise spreading approach is not apparent once it depends on several pseudo-random modulation parameters, dwell time and resolution bandwidth. The conventional super-heterodyne frequency band stepping EMI test receiver defines the dwell time and the resolution bandwidth. For this reason, historically, pseudo-random modulations have been questioned and accused of being a fraudulent way of passing regulations. Nonetheless, research has been presented over the last decades to support the electromagnetic interference noise spreading approach in practical situations, e.g., with power

line communication systems.

The research carried out and presented in this thesis, as well as providing an innovative insight into the behaviour of rectangular pulse trains and the conducted electromagnetic interference measurements standards, show that it is possible to develop new, dedicated converter control algorithms that allow shaping the spectrum of disturbances to meet standardization or technical requirements. Furthermore, once it has been found that the conventional EMC test based on frequency scanning might not be sufficient to evaluate randomly modulated DC/DC converter appropriately. A methodology is proposed to control the switching rate of change of DC/DC converters using pseudo-random modulation, which can achieve a suitable EMI measurement, regardless if long dwell times are considered.

The developed modulation algorithms using the National Instruments PXI platform as a fast prototyping platform were defined as an EMC-friendly pulse-width modulation technique. The control of the pulse-width modulation generation scheme shapes the electromagnetic interference noise from the critical fault areas of the information and communications technology devices. Thus, increasing the effectiveness of an electromagnetic interference filter already implemented, thereby strengthening EMC compliance for DC systems in smart grids.

Therefore, the objectives of this thesis are related to the identification and realization of whether it is possible to develop new, dedicated converter control algorithms that allow shaping the spectrum of disturbances to meet standardization or technical requirements, based on:

- Usage of National Instruments PXI with Field-Programmable Gate Array based control hardware with a fixed point processor as a cyber-physical fast prototyping platform enabling electromagnetic compatibility investigations of pseudo-random modulated converters;
- EMC-friendly PWM technique: the control of the pulse width modulation generation scheme, shaping the electromagnetic interference noise from the critical fault areas of the information and communications technology equipment (increasing the effectiveness of an already implemented EMI filter);
- Description of a concept of the control algorithm for power electronic converters, enabling electromagnetic interference shaping, providing 30% reduction of Frame Error Rate in Power Line Communication;
- Case study showing possibility of development of new, dedicated converter control algorithms that allow shaping of the spectrum of disturbances to meet standardization or technical requirements as well as presentation of the system for flexible implementation and validation of developed concepts.

Contents

Summary	iii
List of acronyms	ix
1 Introduction	1
1.1 Motivation	4
1.2 Research objectives	6
1.3 Outline of the thesis	8
2 Controlling the Switching Rate of Change	11
2.1 Randomization of Rectangular Pulse Trains	11
2.2 Summary	16
3 Measurement Standards for EMI Shaping	19
3.1 Discrete-Fourier Transform	19
3.1.1 Spectrum of the Hanning Window	21
3.1.2 Windowing a Sinewave	23
3.2 Short-Time Fourier Transform	24
3.3 Measurement Standards	25
3.4 Standardized settings for EMI measurements	30
3.5 Summary	31
4 Cyber-Physical System for Evaluation of PWM Techniques	35
4.1 Cyber-Physical System	36
4.1.1 Intel Core i7 embedded controller - NI PXIe-8135	37
4.1.2 LabVIEW projects	39
4.1.3 FPGA R-Series Multifunction RIO - PXI-7854R	40
4.1.4 PWM Modulator Algorithm	43
4.1.5 Random Number Generator	44
4.2 Several FPGA-based RanM approaches	45
4.2.1 Single Randomization	46
4.2.2 RanM with RSCTL—Additional Randomization	50

4.2.3	RanM2—Split Distribution of Variable	51
4.2.4	RanM2 with RSCTL	52
4.2.5	FPGA PXI-7854R Implementation	53
4.2.6	RanM3—Controlling the Switching Rate of Change	54
4.2.7	Shaping the RanM3	56
4.3	Summary	58
5	The Validation of PWM Algorithms	61
5.1	EMC-Test Bench System	62
5.2	Conducted Emission Behaviour	66
5.3	The Measurements of Conducted Emissions for DC-DC Converter	69
5.3.1	The Deterministic and Pseudo-random Modulation	71
5.3.2	The Pseudo-random Modulation 3	79
5.3.3	Shaping the Pseudo-random Modulation 3	82
5.3.4	Aggregated Conducted EMI with Deterministic and Pseudo-random Modulation	85
5.4	EMI Noise Shaping with Power Line Communication System	93
5.4.1	Experimental Setup Description	93
5.4.2	Data analysis	96
5.5	Summary	101
6	Conclusions and Directions for Further Research	105
6.1	Conclusions	105
6.1.1	Chapter 2	106
6.1.2	Chapter 3	107
6.1.3	Chapter 4	108
6.1.4	Chapter 5	109
6.2	Directions for Further Research	111
7	Acknowledgments	113
8	Biography and List of my Publications	117
8.1	Biography	117
8.2	List of My Publications	118
8.3	Articles in Process of Publication	125
	References	127
	Appendices	

A	Rectangular Pulse Trains	143
A.1	Fourier Transform Approach	145
A.2	Even and Odd Harmonics	147
A.3	Aggregation of Rectangular Pulse Trains	153
A.4	The Lebesgue Integral	155
B	MATLAB scripts	159
B.1	MATLAB script used in the appendices A.2 and A.3	159
B.2	Complementary MATLAB script used in appendices A.2 and A.3	161
B.3	MATLAB script used in the section 2.1 and subsection 4.2.1	169
B.4	MATLAB script used in the section 3.1	171
B.5	MATLAB script and function used in the section 3.3	173
B.6	MATLAB script used in the subsection 4.2.7	176
C	Differences in the Control Hardware Features	179
C.1	Experimental Setup Description	179
C.2	Results and Discussions	180

List of acronyms

ADCs	Analog/Digital Converters
AV	Average Detector
CE	Conducted Emission
CISPR	Comité International Especial des Perturbações Radioélectriques
CM	Common-Mode
CPS	Cyber-Physical System
CPU	Central Processing Unit
D	Duty Cycle
DACs	Digital/Analog Converters
DDR	Double Data Rate
DetM	Deterministic Modulation
DFT	Discrete Fourier Transform
DM	Differential-Mode
DMI	Direct Media Interface
DSP	Digital Signal Processors
EM	Electromagnetic Environment
EMC	Electromagnetic Compatibility
EMI	Electromagnetic Interference
ENBW	Equivalent Noise Bandwidth
EPP/ECP	Enhanced Parallel Port/Enhanced Capability Port

EUT	Equipment Under Test
FER	Frame Error Rate
FFT	Fast Fourier Transform
FPGA	Field-Programmable Gate Array
GPIO	General Purpose Interface Bus
GPU	Graphics Processing Unit
GRP	Ground Reference Plane
HLS	High-Level Graphical Synthesis
ICT	Information and Communications Technology
IDE	Integrated Development Environment
IEC	International Electrotechnical Commission
IEEE	Institute of Electrical and Electronics Engineers
IF	Intermediate Frequency
IFBW	Intermediate Frequency Bandwidth
IGBT	Insulated Gate Bipolar Transistors
I/O	Input/Output
IPEM	Integration of Power Electronic Modules
LCG	Linear Congruential Generator
LISN	Line Impedance Stabilization Network
LPF	Low Pass Filter
LPC	Low Pin Count
LUT	Look up Table
MAC	Media Access Controller
MOSFET	Metal Oxide Semiconductor Field-Effect Transistors
NCQ	Native Command Queuing

NI	National Instruments
OFDM	Orthogonal Frequency Division Multiplexing
PCB	Printed Circuit Board
PCI	Peripheral Component Interconnect
PCIE	PCI-Express
PDF	Probability Density Functions
PE	Protective Earth
PHY	Physical Layer
PLC	Power Line Communication
PLL	Phase-Locked Loop
PQ	Power Quality
PRF	Pulse Repetition Frequency
PWM	Pulse Width Modulation
QP	Quasi-Peak Detector
RanM	Pseudo-Random Modulation
RBW	Resolution Bandwidth
RCFMFD	Random Carrier Frequency Modulation Fixed Duty
RCFMVD	Random Carrier Frequency Modulation Variable Duty
RPPM	Random Pulse Position Modulation
RPWM	Random Pulse Width Modulation
RSN	Random Stream of Numbers
SATA	Serial Advanced Technology Attachment
SCTL	Single-Cycle Timed Loops
SDRAM	Synchronous Dynamic Random-Access Memory
SMB	Server Message Block

SO-DIMM Small Outline Dual In-line Memory Module

SPI Serial Peripheral Interface

TRLs Technology Readiness Levels

STFT Short-Time Fourier Transform

TTL Transistor-Transistor Logic

USB Universal Serial Bus

VI Virtual Instruments

Introduction

The Electromagnetic Interference (EMI)¹ has always been an issue in electrical and electronic devices [2]. Based on today's electronics, EMI-related problems have been receiving considerable attention [3]. Several standards have been developed aiming to impose (guarantee) Electromagnetic Compatibility (EMC), within several technological fields [4]–[7]. Nevertheless, the low frequency emission² has been carefully discussed, fundamentally for power electronic converters application into smart grids [9]–[11]. The growing demand for power electronic systems and infrastructures, such as Integration of Power Electronic Modules (IPEM), often end up restricted by the rapid increase of EMI problems that occur through the interaction of power electronic systems with Information and Communications Technology (ICT) equipments. This interconnected systems-of-systems infrastructure creates a complex Electromagnetic Environment (EM) in which EMC has to be achieved [3].

The EMC can be broadly linked with [1]: I) the ability to fit the power spectrum of any interfering signal radiated/conducted to a circuit/system; II) the ability of a circuit/system to withstand incoming radiated/conducted EMI below a prescribed mark at a given level. In other words, as defined by [1]: "any electronic equipment must not generate EMI above a tolerable level, and must be not susceptible to EMI if below a tolerable level." Thus, bringing definitions I and II to the range of low frequency emission, the concerns focus on conducted EMI predominantly generated by power electronic converters.

Classic approaches for mitigation the conducted EMI generated by power electronic converters aims at reducing the coupling between the source and the victim with filtering [12]–[15]. The EMI filter is applied at the propagation path of the EMI

¹The electromagnetic interference usually refer to any unintentional power transfer between a source (circuit/system) and a victim (circuit/system), either being radiated (i.e., propagated through space) or conducted (i.e., propagated through a grounding, power or signal conductor) [1].

²The term "low frequency emission" is used within Institute of Electrical and Electronics Engineers (IEEE) EMC society to refer to frequencies below 150 kHz. Within International Electrotechnical Commission (IEC) the term "low frequency" refers to frequencies below 9 kHz [8].

currents [16]–[18]. Furthermore, more specific solutions can be used, e.g., Printed Circuit Board (PCB) layout strategies have been proposed to EMI mitigation [19], [20], in cases where the source and the victim circuits belong to the same integrated circuit [21]. Additionally, the vast majority of power electronic converters operate with switching technologies [22]. The development and implementation of switching control strategies³ that are committed to EMI requirements has been treated by many authors over the last decades as an EMI mitigation technique [24].

Pointedly, the EMC in power electronic converters must be addressed from several perspectives. Nevertheless, the research carried out and presented in this thesis is strictly related to the switching control strategies. Further information can be found at motivation (section 1.1) and research objectives (section 1.2). There are many assumptions for the switching control strategies development [25]. However, from the point of view of the EMI noise shape, two cases represent the extremes of possibilities, i.e., Deterministic Modulation (DetM) and Pseudo-Random Modulation (RanM)⁴. Being the RanM treated by many authors as a way of EMI mitigation [24].

The RanM can be applied to any circuit showing a non-negligible switching activity. Even the RanM find applications also in medium- and high-power converters [26]–[29]. The research presented in this thesis concentrate on low-power converters, such as DC/DC switching mode power converters⁵, due to their ubiquitous adoption and operation in the low frequency range [1]. The adoption of a RanM technique aims to change the EMI noise shape, spreading the spectrum components peak levels [1]. The main idea underlying this technique is the randomization of the switching actions. Carefully, the RanM technique can be considered as complementary methodology concerning the classic ones mentioned above, such as the adoption of EMI filter and improvements on the PCB layouts.

In recent years, RanM techniques have been used in many applications, for example, as suggested by [1] for microprocessor clock generators [30], and electronic ballasts [31]. The applications of RanM techniques in DC/DC converters is also a widely studied topic [32]–[38], and also, in this case, several commercial products are already available [39]–[42].

Figure 1.1 illustrates the EMI noise shape by adopting DetM or RanM, considering the application of DC/DC converters in smart grids and the use of the DC-link by

³Switching control techniques address EMI mitigation on power electronic converters [23].

⁴In the research presented in this thesis, we chose to use the terminology pseudo-random modulation instead of the dithering or spread spectrum. Once, from the author's point of view, the terminology pseudo-random modulation faithfully defines the process studied. It is a process that considers a signal generated by hardware-based a finite random stream of numbers.

⁵Switched-mode converters are DC/DC converters that supply DC loads with a regulated output voltage, and protection against overcurrents and short circuits.

miscellaneous systems associated with smart grids applications.

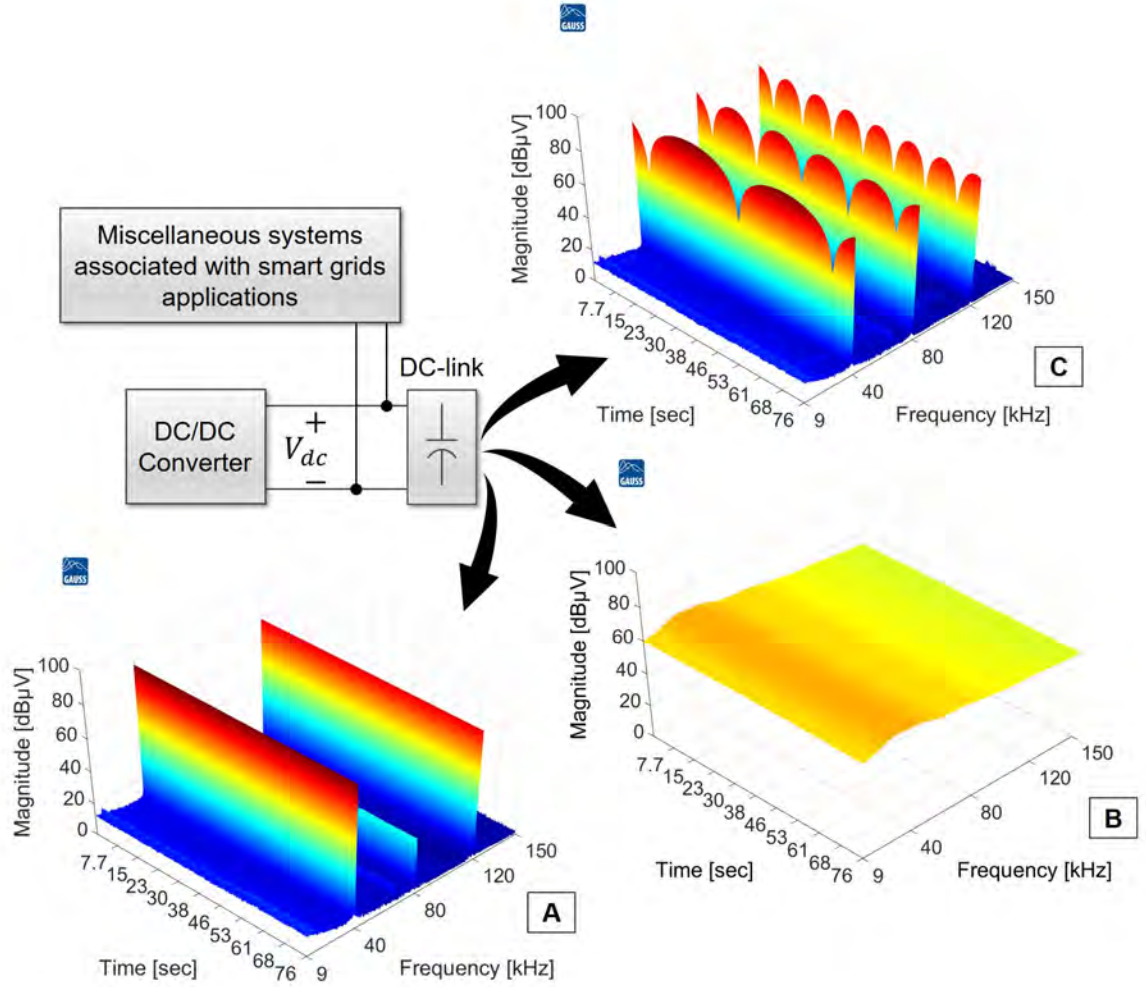


Figure 1.1: The extremes of possibilities for the EMI noise shape by adopting DetM or RanM. (A) A single DC/DC converter with DetM, (B) a single DC/DC converter or cases with multiple DC/DC converters, considering RanM; and (C) the case of multiple DC/DC converters with DetM.

The EMI noise shape illustrated in Figure 1.1-A is the distribution of the spectrum components for a single DC/DC converter with DetM [43]. In the case of Figure 1.1-B, it is the EMI noise shape often obtained in measurements of a single DC/DC converter or cases with multiple DC/DC converters, considering RanM [44]. Finally, in the case of Figure 1.1-C, it is the EMI noise shape often obtained in measurements of multiple DC/DC converters with DetM [45].

Thus, based on the context of Figure 1.1, the objectives of this thesis are related to the identification and realization of whether it is possible to develop new, dedicated converter control algorithms that allow shaping the spectrum of disturbances to meet standardization or technical requirements. Although it seems trivial, EMI

measured level depends on the setting of the EMC-test bench system [46], and the tradeoffs of random modulated DC/DC converters and conducted EMI measurements are still unclear for low frequency range. For example, given the difficulty to define a general behavioral model of EMI victim circuits in the presence of conducted EMI [1], [47], [48]. Evaluating any EMI noise spreading approach is not apparent, once it depends on several RanM parameters, and also on the dwell time⁶ and the Resolution Bandwidth (RBW), both defined by the conventional super-heterodyne frequency band stepping EMI test receivers. For this reason, historically, RanM techniques have been questioned and accused of being a fraudulent way for passing international regulations [1]. Nonetheless, several papers have been presented to support the EMI noise spreading approach in practical situations, including television signals decoding [49], FM radio systems [50], wideband digital communications systems [51], and especially considering the low frequency range, the Power Line Communication (PLC) system [52]–[55].

The research carried out and presented in this thesis shows that the correct understanding of the EMI noise spreading, due to the use of RanM, depends on:

- How RanM parameters have to be set? This question guided us to understand how to develop new, dedicated converter control algorithms that allow shaping the spectrum of disturbances to meet standardization or technical requirements;
- Which measurement settings allow good adherence between conducted EMI and the RanM effects on the EMI noise shape? This question guided us to understand the tradeoffs of random modulated DC/DC converters and conducted EMI measurements at low frequency range.

Further informations about the motivation (section 1.1), research objectives (section 1.2) and outline of the thesis (section 1.3) are presented below.

1.1 Motivation

The central motivation of the research carried out and presented in this thesis is based on the emission and immunity aspect (limit lines) of the EMI level assessment process. Figure 1.2 illustrates the conducted emissions limits from the Comité International Especial des Perturbações Radioélectriques (CISPR) 11. The CISPR 11 is the international standard for EMI from industrial, scientific and medical equipment. The official title of the standard is: Industrial, Scientific, and Medical Equipment

⁶Both commercial and military EMC testing standards require specific amounts of measurement time, in order to ensure that impulsive signals are appropriately characterized.

- Radio-Frequency Disturbance Characteristics - Limits and Methods of Measurements.”

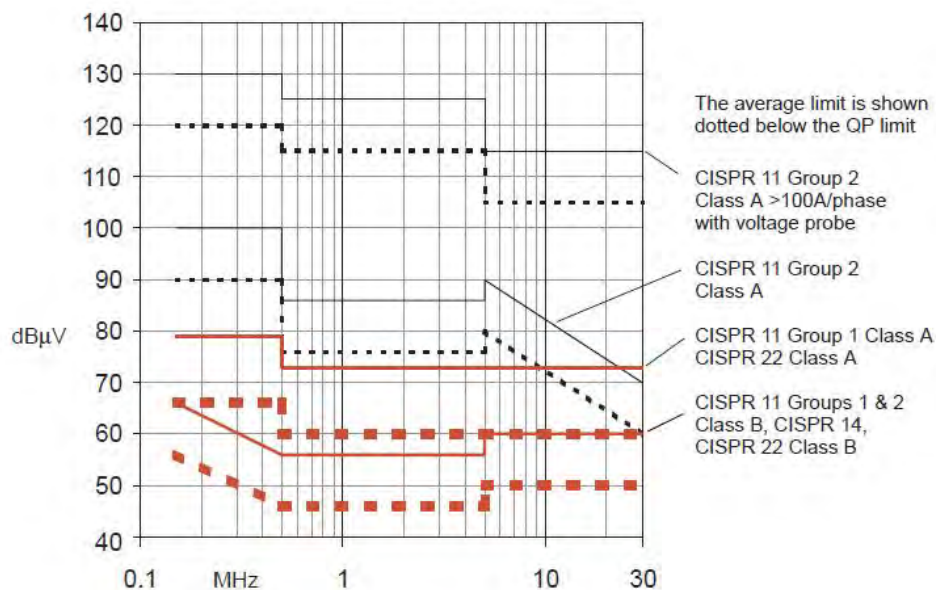


Figure 1.2: The conducted emissions limits from the CISPR 11.

Figure 1.2 shows that the standard considers different limits levels for different frequencies in the spectrum. Thus, a technique that can be used to deal with this situation is adopting switching control strategies that aim to shape the EMI noise. On the other hand, historically the quality of supply (voltage), i.e. Power Quality (PQ), and the emission (of current) caused by electrical and electronic equipment has been defined and agreed in standards. However, even considering recent progress, such as the last amendment included in the IEC 61000-2-2 in 2018 [56]. The dynamics of interoperation required by smart grids make EMC a challenge [57]–[59]. Once smart grids permeate different environments, e.g., industrial, residential, where each environment has its own recommendations on EMC assurance [60].

Furthermore, we cannot fail to consider a recurring scenario, where electrical engineers assume the only victims on a power system are other electrical equipments. On the other hand, communications engineers assume the only significant frequencies on a power system are the fundamental frequencies (50 or 60 Hz) [60]. This non-convergence scenario between the conducted EMI acceptable limits and the different requirements to the EMC assurance mainly affects the smart grids related communication processes [61].

Thus, EMC issues due to the EMI generated by DC/DC converters operating in the low frequency range (from 9 kHz to 150 kHz) become a real predicament in smart grids. Since situations may arise where best engineering practices, whether from the point of view of power electronic converters [53], [57], [62]–[65] or telecom-

munications devices [52], [61], [66]–[69], may not be electromagnetically compatible.

The mentioned non-convergence scenario for the low frequency range can also introduce problems into the conducted EMI measurement. For instance, the operating frequency of a Line Impedance Stabilization Network (LISN) typically specified in EMC standards does not fully cover the 2–150 kHz range [70]. This shows that even considering equipment traditionally used. There is still a debate about the “good practices” for conducted EMI measurements in the low frequency range.

On assuming that the noise shape of conducted emissions depends on the EMI source, as well as complex phenomena accompanying the EMI currents. The random modulated DC/DC converters makes conducted EMI measurement even more challenging. For instance, fast switching edges (by using DetM) lead to harmonics even up to frequencies in the range of 100 MHz, which can then couple to other sensitive parts of the power electronic system [60]. This is why beyond the adoption of EMI filters, the utilization of RanM techniques is suitable in some cases. However, the conducted EMI measurement settings to evaluate random modulated DC/DC converters are still unclear for the low frequency range, e.g., what would be the appropriate parameters for RanM to provide the shaping of conducted interference? This question is in line with what has been presented in this chapter 1, and defines the research objectives presented in the following section 1.2.

1.2 Research objectives

Considering the scenario defined in the introduction and section 1.1 of this chapter 1, it can be attested that the dynamic development of power electronic systems, utilizing DC/DC converters as interfaces, forces the cooperation of specialists representing various fields to assure EMC of so-called smart grids.

This cooperation could be considerably impeded by means of a different development environments used by power system, power electronic, control and EMC engineers. Therefore, in the research carried out and presented in this thesis, the Cyber-Physical System (CPS) based on National Instruments (NI)-PXI platform is presented as a fast prototyping platform. This CPS might be flexibly used by engineers representing various fields to develop compatible electromagnetic solutions for the interaction of power electronic systems with ICT equipments.

In order to standardize the EMC requirements, the IEC has published the international standard IEC 62920:2017 Photovoltaic power generating systems - EMC requirements and test methods for power conversion equipment [71]. This standard includes requirements on the emission of radio frequency disturbances (CISPR 11), low frequency emission (IEC 61000-3-2), and immunity to electromagnetic disturbances (IEC 61000-4-X). However, the EMC requirements standardized by IEC

62920: 2017 do not necessarily apply to DC/DC converters used in smart grids, especially in stand-alone photovoltaic systems [72].

In smart grids, most of the power electronic converters used are DC/DC converters [73]. These DC/DC converters rely on the use of switching devices, such as Metal Oxide Semiconductor Field-Effect Transistors (MOSFET) and Insulated Gate Bipolar Transistors (IGBT). Hence, control devices are used to modulate and control the DC/DC converters. The CPS with Field-Programmable Gate Array (FPGA)-based control hardware are innovative solutions for DC/DC converters [64]. However, despite offering high flexibility and customization of Pulse Width Modulation (PWM) techniques, when the FPGA considers floating-point processors [65], the CPS with FPGA-based control hardware does not prevent DC/DC converters from inducing conducted EMI due to the switching actions [63].

There are new modulations schemes for inverters allowing variable switching frequencies between 4 kHz to 10 kHz to decrease the EMI impact [74]. As for DC/DC converters, it is challenging to define the frequency range to be randomized. Once the vast majority of DC/DC converters work between 10 kHz to 100 kHz for efficiency purposes given by the passive components used [75].

Although the implementation of PWM control techniques has been the subject of research over the past decades [24]. Only through the hardware implementation of the PWM control algorithms is it possible to scale the necessary coding effort. Especially because specific features of the control hardware can change PWM control algorithm' coding philosophy, such as fixed-point operations, matching the range of fixed-point numbers, lack of options for building PWM hardware circuits, and limitations in arithmetic operations [65].

Taking into account the presented research problems, the thesis can be formulated, which reads: **it is possible to develop new, dedicated converter control algorithms that allow shaping the spectrum of disturbances to meet standardization or technical requirements.**

Therefore, in the research carried out and presented in this thesis, the proposed PWM algorithms for DetM and RanM have a neutral effect on the DC/DC converter energy processes. However, assuming RanM, a variation of the fundamental switching frequency of the DC/DC converter is expected. Nevertheless, maintaining the average switching frequency, there are no changes in the DC/DC converter's efficiency, and the losses in the system are approximately the same compared with DetM [76]. Throughout the development of the proposed PWM algorithms for DetM and RanM, the number of switches were monitored and constantly observed to ensure that both PWM algorithms for DetM and RanM provide on average the same number of switches. Additionally, by controlling the PWM generation scheme, one is able to shape the EMI noise from the critical areas of failure of the ICT equipment.

Furthermore, the definition of measurement settings to allow good adherence between conducted EMI and the RanM effects on the EMI noise shape is the subject of the investigation. The research carried out and presented in this thesis shows that the conventional methods used by the EMC test standard based on frequency scanning might not be sufficient to appropriately evaluate random modulated DC/DC converter. Therefore, a methodology is proposed to control the switching rate of change of DC/DC converters using RanM, which can be used to achieve a suitable EMI measurement.

The objectives of this thesis are related to the identification and realization of whether it is possible to develop new, dedicated converter control algorithms that allow shaping the spectrum of disturbances to meet standardization or technical requirements, based on:

- Usage of National Instruments PXI with FPGA based control hardware with a fixed point processor as a cyber-physical fast prototyping platform enabling EMC investigations of RanM converters;
- EMC-friendly PWM technique: the control of the PWM generation scheme, shaping the EMI noise from the critical fault areas of the ICT equipment (increasing the effectiveness of an already implemented EMI filter).
- Description of a concept of the control algorithm for power electronic converters, enabling EMI shaping, providing 30% reduction of Frame Error Rate (FER) in PLC.
- Case study showing possibility of development of new, dedicated converter control algorithms that allow shaping of the spectrum of disturbances to meet standardization or technical requirements as well as presentation of the system for flexible implementation and validation of developed concepts.

1.3 Outline of the thesis

With the purposes presented in the section 1.2 in mind. We first present in this thesis the behaviour of rectangular pulse trains in chapter 2. Thus, due to the possibility of defining different values of Duty Cycle (D) for DC/DC converters connected in large numbers through topologies in parallel or series [45], [77], it is necessary to understand the effects of D changing, the displacement of signals with frequency similarities, as well as the processing of these aggregated signals from the time domain to the frequency domain. Chapter 2 covers the expected behaviour model of rectangular pulse trains based on RanM and DetM. Furthermore, the concept of

controlling the switching rate of change from the DC/DC converters, when RanM is considered, is also presented in chapter 2.

Chapter 3 presents a complement to the chapter 2, through the analysis of the conducted EMI measurement standards. Although it seems trivial, the EMI measured level depends on the setting of the EMC-test bench system. Thus, through an introduction of some standardized settings for conducted EMI measurements, based on standards IEC 61000-2-2 [56] and CISPR 16-2-1 [78], chapter 3 highlights the influence of the super-heterodyne frequency band stepping EMI test receivers in the EMI evaluation. It also provides an overview about the settings of the dwell time when assessing DetM and RanM in DC/DC converters.

To prototype an EMC-test bench system controlled by a CPS, chapter 4 primarily introduces the Intel Core i7 embedded controller - NI PXIe-8135 and the FPGA R-Series Multifunction RIO - PXI-7854R. The aptness for the implementation of different PWM techniques, providing high customization and flexibility, makes the proposal EMC-test bench system controlled by a CPS a reliable test set-up. Furthermore, in chapter 4, Probability Density Functions (PDF) are used to analyse and improve RanM. We propose four methods of distribution the PDF in FPGA without arithmetic division and using fixed-point operations. Also, the PWM algorithms are presented and discussed in terms of expected EMI noise shape.

Then, in chapter 5. The LabVIEW-based design of the PWM algorithms presented in chapter 4, as well as the EMC-test bench system validation, were performed with a DC/DC converter. To achieve the EMI noise spreading, i.e., the consciously shaping of the EMI spectrum, it is assumed the DC/DC converter is implemented in its final stage, and unknown parasitics are decreased due to the PCB layout optimization. However, to gain an in-depth comprehension of this investigation, the EMI filter wasn't considered in the experimental setup. The high customization and flexibility of the proposed EMC-test bench system controlled by a CPS are also investigated through a case study with PLC, when the approach of shaping the RanM3 is used.

Finally, the conclusions on the PWM control algorithms, hardware and software details, and conducted EMI measurements, highlighting the paradigms for EMC within smart grids are presented in chapter 6. The directions for further research are also presented in chapter 6.

Controlling the Switching Rate of Change

Chapter 1 of this thesis has emphasized how the noise shape of conducted emissions depends on the EMI source, as well as complex phenomena accompanying the flow of EMI. Since DC/DC converters play a vital role in the operation of modern energy systems, e.g. DC nanogrid [72], solar photovoltaic and thermal energy systems [79], the rectangular pulse trains are used in a wide variety of applications enabling voltage control by the D value specification [77]. The possibility of defining different values of D, for DC/DC converters connected in large numbers through topologies in parallel or series, brings up the debate of time or frequency domain to attest the EMC assurance [80]. Complex phenomena with signals in the time domain might influence the frequency domain assessment and vice-versa.

Therefore, the appendix A, complementary part of this chapter 2, highlights the expected behaviour model of rectangular pulse trains based on two types of switch control strategies, i.e. RanM and DetM. Furthermore, assuming the concept of two identical DC/DC converters, the modelling presented in the appendix A can be used to predict and estimate the conducted EMI noise shape generated in systems using the IPEM. However, in practical applications with DC/DC converters, several conditions might influence the EMI noise shape, such as the switching rate of change.

2.1 Randomization of Rectangular Pulse Trains

The RanM technique has been used in power electronic converters since the 80's [81], [82]. Primarily, the purpose of RanM application was the reduction of an acoustic noise linked with the f_0 of the power electronic converters. Despite significant differences in the frequency domain, the number of the switching actions over long enough time, remains the same for both DetM and RanM, as well as the parameters

of voltage slopes and EMI current paths. However, the use of RanM, may also imply the spreading of the EMI levels in comparison with DetM [82]–[91]. This is why RanM is often treated as EMI mitigation technique for power electronic converters, considering the conducted EMI measurements [84], [85], [87], [89], [91]–[95].

The classical RanM approaches consider Random Carrier Frequency Modulation Fixed Duty (RCFMFD) [96], [97], Random Carrier Frequency Modulation Variable Duty (RCFMVD) [98], [99], Random Pulse Position Modulation (RPPM) [46], [96]–[99], and Random Pulse Width Modulation (RPWM) [100], [101]. Nevertheless, the approach to consolidate the better RanM must consider not only the possibility of EMI noise spreading, but also the hardware resource used. A truly continuous power spectrum is obtained only with a non-periodic signal¹, which, in theory, might be obtained using a true random generator [1]. That is the paradigm for most of the control hardware, such as microcontrollers (μC), Digital Signal Processors (DSP), and FPGA. As the control hardware can only generate pseudo-random sequences, which are periodic in time, even if with an extremely long period of repetitive behaviour. That is why the term pseudo-random is used to refer the Random Stream of Numbers (RSN) generated by the control hardware.

Furthermore, the f_0 randomization is based on Carson's rule [1]. This rule considers the spreading of f_0 within a maximum and minimum defined deviation from it. This deviation can also be represented in terms of onboard clock frequency from the control hardware point of view, i.e. values of clock cycles. For example, assuming that N represents values of clock cycles needed to execute f_0 , the maximum and minimum deviation can be represented by $N_{AV} \pm \delta_N/2$, where δ_N means the defined randomization range². A mathematical expression of RanM can be seen in (2.1):

$$f_{out} = f_0 \pm \frac{\delta_f}{2} \cdot \epsilon(t), \quad (2.1)$$

where the term δ_f is the frequency deviation based on the randomization range defined. The parameter $\epsilon(t)$ is the driving signal which can be triangular, sinusoidal, or e.g. based on random pulse amplitude modulation [1]. The driving signal equation of the RSN based on pulse amplitude modulation is shown in (2.2):

$$\epsilon(t) = \sum_k x_k g(t - kT), \quad (2.2)$$

where $x_k \in [-1, 1] \subset \mathbf{R}$, and represents the transition point between $-1 < t \leq 0$ and $0 \leq t < 1$ of the $g(\cdot)$. $g(\cdot)$ is the normalized rectangular pulse train, where $g(t) = 1$ for

¹Non-periodic signal (also known as aperiodic signal), unlike periodic signal, do not have just one particular frequency. Instead, the non-periodic signal are spread over a continuous range of frequencies.

²The randomization process, i.e. the definition of δ_N and the concept of $N_{AV} \pm \delta_N/2$, is discussed in depth in the subsection 4.2.

$0 < t < 1$ and 0 elsewhere, and T is the duration of the pulse. Also, the summation represented by (2.2) is defined by k .

From a control hardware point of view, for each $\epsilon(t)$ one iteration count (i) is performed, as illustrated in Figure 2.1 (for further information about the MATLAB script used, please see B.3). The i is used to define the total value of N needed to generate one unique f_{out} [65].

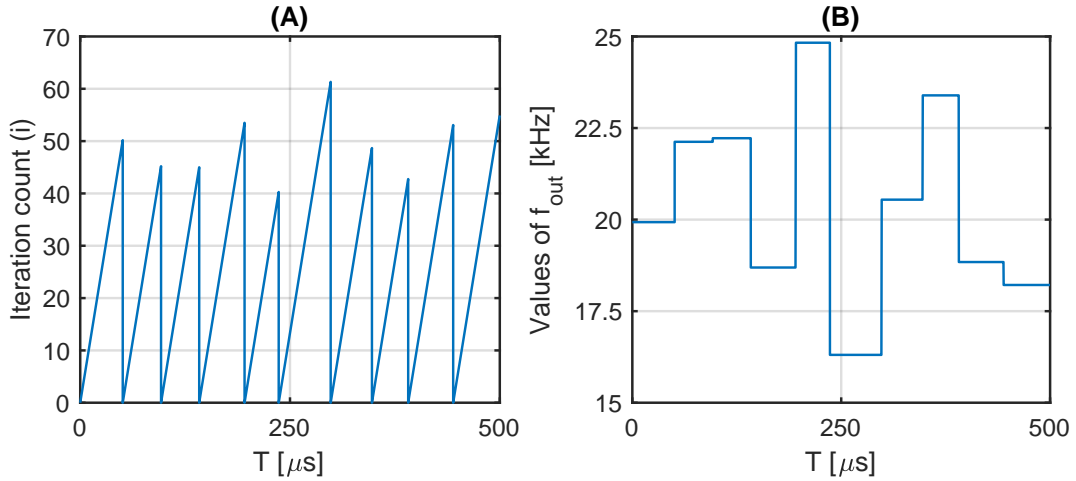


Figure 2.1: The relation between i (A) and f_{out} (B) for a set of 10 $\epsilon(t)$. The Δf_{out} is approximately 20 kHz, and the ΔT is approximately 50 μs . Also, considering in both cases $k=1$, and $f_0=20$ kHz with a $\delta_f=10$ kHz.

The execution rate of i is related to the control hardware feature available. Thus, aiming to explain the concept of RanM repetition rate control, it's assumed that $k=1$ means allocating all control hardware features to execute just one i . In this context, (2.2) shows that when considering constant but broader values for k , one unique $\epsilon(t)$ can be repeated more times, i.e. broader values for k make the i slow.

Nonetheless, implementing a RanM technique can make use of several i , and for different purposes. For example, Figure 2.2-B illustrates how the i becomes slow for $k=3$, in cooperation with and Figure 2.2-A. For one period of $T=1500$ μs with $k=1$, the set of 10 $\epsilon(t)$ was performed three times, in the case of Figure 2.2-A. On the other hand, for the same period of $T=1500$ μs , however with $k=3$, the same set of 10 $\epsilon(t)$ was performed just one time, in the case of Figure 2.2-B.

Nevertheless, once the Δf_{out} and ΔT must remain approximately the same as a single values, i.e. $f_{out}=20$ kHz and $T=50$ μs (see also Figure 2.1). Figure 2.2-C shows that regardless of the influence of k in the set of 10 $\epsilon(t)$, the number of turn-on and turn-off switching actions, consequently the Δf_{out} and ΔT are not drastically changed in both approaches, i.e. thirty switching actions for the RanM with $k=1$ and for the RanM with $k=3$.

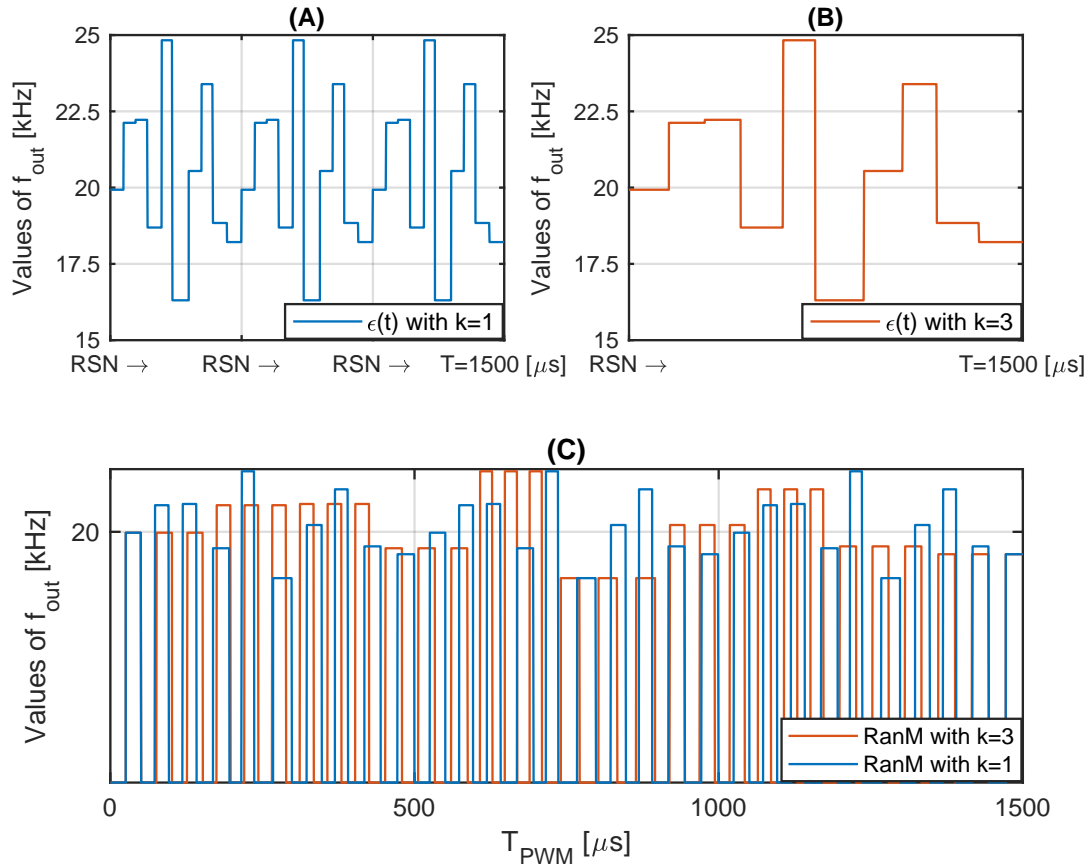


Figure 2.2: The RanM repetition rate control based on k value: (A) $\epsilon(t)$ with $k=1$, (B) $\epsilon(t)$ with $k=3$, and (C) both RanM with $k=1$ and $k=3$.

Furthermore, Figure 2.2-C also shows that instead of thirty turn-on and turn-off switching actions, where each one is based on one $\epsilon(t)$ of the RSN (case of RanM with $k=1$). The RanM with $k=3$ assumes the same $\epsilon(t)$ value for a set of three turn-on and turn-off switching actions, consecutively. In other words, the broader the range of values assigned to k , the longer it takes to randomly alternate the frequencies considered in the RSN of the RanM.

Therefore, assuming the RSN based on pulse amplitude modulation [1] (see Figure 2.2), which define $\epsilon(t)$ as (2.2), is a crucial approach to establish the RanM repetition rate control. From a practical point of view, implementing the RanM repetition rate control means controlling the switching rate of change from the DC/DC converters. Furthermore, to control the switching rate of change, the control hardware must assume that one i is dedicated to $\epsilon(t)$, and another i is dedicated to turn-on and turn-off switching actions. Thus, the PWM time (T_{PWM}) is not influenced by k .

To illustrate the concept presented in the Figure 2.2-C, the Figure 2.3, Figure 2.4, and Figure 2.5 presents $X(t)$ for the conditions of $k=1$, $k=2$, and $k=3$. For further information about the MATLAB script used, please see B.3.

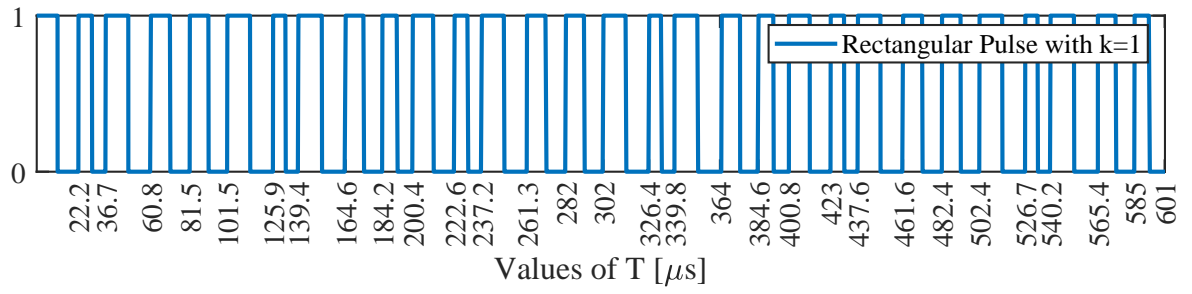


Figure 2.3: The set of ten random periods (T) of $X(t)$, for $k=1$.

Figure 2.3 shows that by using the minor period of k , each random period (T) is kept for as shorter as possible period of time (t), and then the randomization process is repeated (pseudo-random sequences concept). Furthermore, considering that $t = 601\mu s$, the set of ten random periods (T) is repeated three times. Each time with an approximate ten switches, $\Delta f_0 = 50kHz$ (the same applies for Figure 2.4 and Figure 2.5). This supports the claims that the number of switching which operates over a long enough time remains the same if compared with DetM. On the other hand, as previously defined in Figure 2.2-C. Figure 2.4 and Figure 2.5 show that by increasing the value of k , one specific random period T can be maintained for more extended periods of time (t), which defines the switching rate of change.

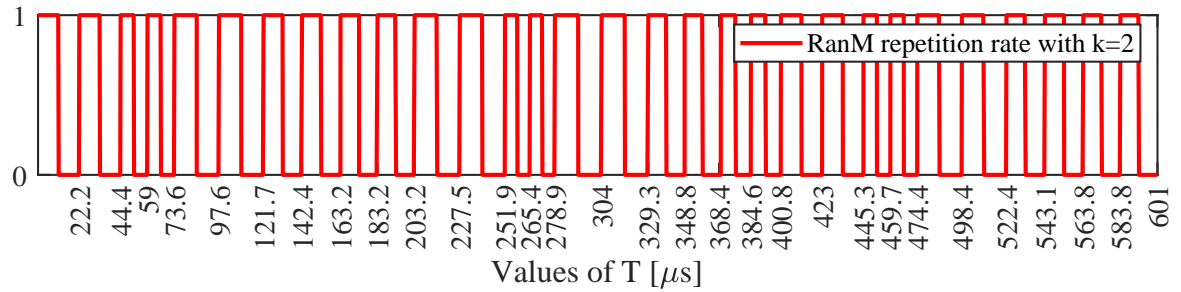


Figure 2.4: The set of ten random periods (T) of $X(t)$, for $k=2$.

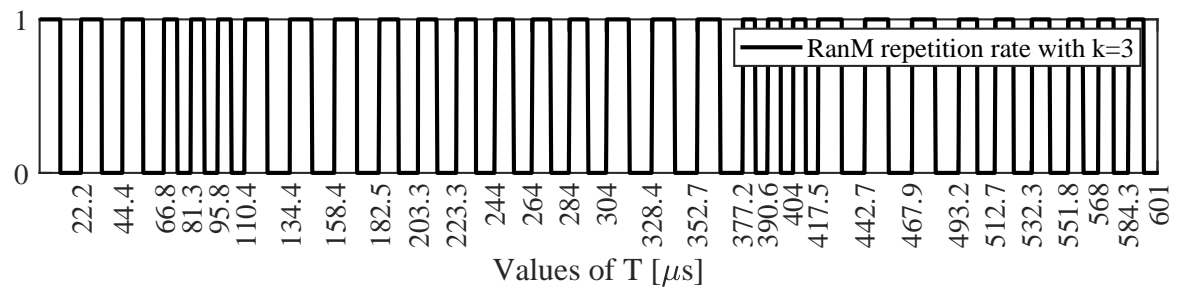


Figure 2.5: The set of ten random periods (T) of $X(t)$, for $k=3$.

Therefore, unequivocally, the index of sum k represented in (2.2) enables the

control of the switching rate of change. The broader the range of values assigned to k the more time required to modulate the pulse amplitude of the RSN. From another perspective, the broader the range of values assigned to k , the longer it takes to randomly alternate the frequencies considered in the RSN of the RanM.

2.2 Summary

This chapter 2 has been dedicated to describing the expected behaviour model of rectangular pulse trains based on two types of switch control strategies, i.e., RanM and DetM. Initially, appendix A introduces the modelling and simulation of waveforms, such as $X(t)$, based on the Fourier series's trigonometric form. Also, the complex exponential Fourier series was used to model and simulate the Fourier series's coefficients (C_n). Thus, it was evidenced that DetM can introduce specific phenomena, mainly considering the aggregation of rectangular pulse trains $X(t)_\Sigma$, due to the variation in the frequency of each $X(t)$, as presented in section A.3. Furthermore, section A.3 highlights the importance of dealing with improper integrals when considering the $X(t)_\Sigma$.

Section 2.1 introduces the concept of RanM. In order to exemplify how the RanM might contribute to spreading the EMI noise over frequency range, in comparison with DetM. Figure 2.6 and Figure 2.7 shows the conducted EMI measurement of one DC/DC converter, with the $f_0 = 60$ kHz, $D \neq 50\%$ and with DetM and RanM, respectively [44]. The conducted EMI measurement topic is discussed in depth in the chapter 5.

Figure 2.7 presents a "reduction" at the $f_0 = 60$ kHz of just over 20 dB, in comparison with Figure 2.6. A truly continuous power spectrum, which in theory provides the best spread of spectrum components, is obtained only with a non-periodic signal. The control hardware only can generate pseudo-random sequences, which are periodic in time, even if with an extremely long period related to the randomization process. How would it be possible to reduce the EMI noise power spectrum if there is no change in the DC/DC converter energy process?

As discussed and presented in the subsection 2.1, the RanM implementation must consider the available hardware resources and capability. Each control hardware can provide functions and have specific features, making implementation difficult or easier, e.g., enabling or not the control of the switching rate of change. That particular topic will be deeply analyzed in chapter 4 of this thesis.

Finally, based on the conducted EMI measurements point of view, it's crucial to understand the signal processing techniques of the super-heterodyne frequency band stepping EMI test receiver. For example, assuming to control the switching rate of change (see section 2.1), it is understood that one specific random period T

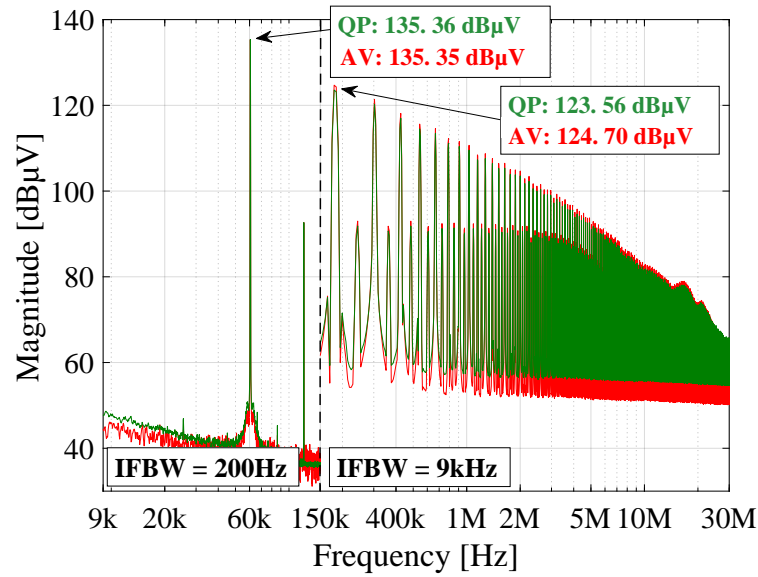


Figure 2.6: The conducted EMI measurement of one DC/DC converter, with $f_0 = 60$ kHz, $D \neq 50\%$ and DetM [44].

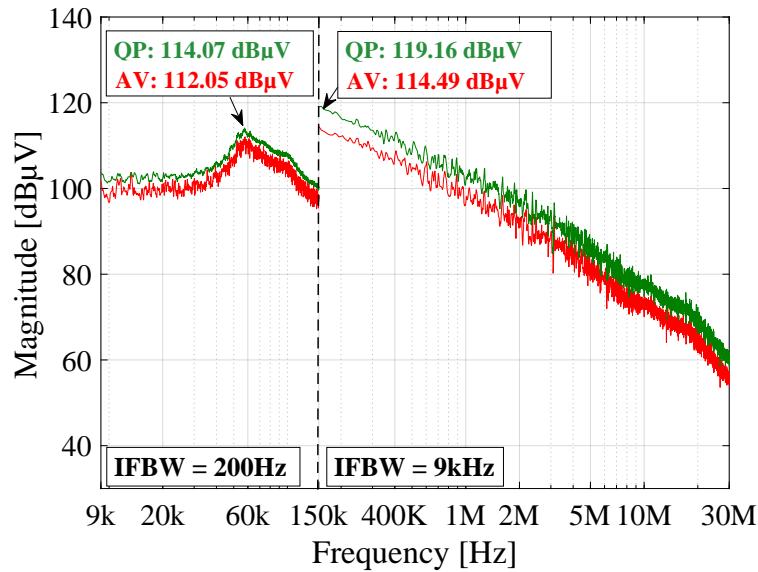


Figure 2.7: The conducted EMI measurement of one DC/DC converter, with $f_0 = 60$ kHz, $D \neq 50\%$ and RanM [44].

of one $X(t)$ can be maintained for more extended periods of time (t). From another perspective, by maintaining one specific random period T of one $X(t)$ for more extended periods of time (t), the longer it takes to randomly alternate the frequencies considered in the RSN of the RanM.

Thus, raising the questions: Which switching rate of change is most appropriate to achieve a suitable conducted EMI measurement? Which must be the dwell time

when the RanM is considered? One adequate switching rate of change can give the demodulator of the detector (e.g., Quasi-Peak Detector (QP) or Average Detector (AV)) more time to correctly charge and discharge the envelope detector (frequency demodulator), without considering long dwell times. This is certainly not the case shown in Figure 2.7. A faster switching rate of change may imply the output graph in the frequency domain is almost flat, i.e., spread. However, a slowly switching rate of change may allow the demodulator to read more times the same frequency (narrower equivalent bandwidth), thus covering variations during the dwell time. That particular topic will be deeply analyzed in the next chapter of this thesis, chapter 3.

Measurement Standards for EMI Shaping

In this chapter 3 an introduction to the theoretical knowledge, used by conventional super-heterodyne frequency band stepping EMI test receivers during conducted EMI measurements, is presented. Two different methods used to measure the signal frequency spectrum are considered. The Discrete Fourier Transform (DFT) (presented in section 3.1) and the Short-Time Fourier Transform (STFT) (presented in section 3.2). Since the research presented in the thesis is based on harmonic voltages, the essential theoretical knowledge is based on the power spectrum, i.e., the Fourier transform of the original signal auto-correlation.

The applicability of both DFT and STFT methods, and their influence on the conducted EMI measurements are detailed in section 3.3. The subsection 3.4 details some standardized settings for conducted EMI measurements, based on standards IEC 61000-2-2 [56] and CISPR 16-2-1 [78]. Finally, section 3.5 highlights the influence of the super-heterodyne frequency band stepping EMI test receivers in the EMI evaluation, as well as provides an overview about possible settings when using DetM and RanM for DC/DC converters.

3.1 Discrete-Fourier Transform

The DFT is calculated to obtain the frequency content of signals. Two parameters are used to compute the spectrum:

- The sampling frequency (f_s), which limits the maximum harmonic (between 0 and $\frac{f_s}{2}$) due to the Nyquist–Shannon sampling theorem¹;

¹The Nyquist–Shannon sampling theorem is fundamental for information theory, telecommunications and signal processing. Sampling is the process of converting a signal (e.g., a continuous function in time or space) into a numerical sequence (e.g., a discrete function in time or space).

- The DFT time window, which directly specifies the frequency resolution (the space between two successive spectral lines). Suppose the size of the DFT time window is bigger or smaller than the duration of the signal. In that case, leakage on the spectrum² can appear.

The DFT is applied on the sequence of samples $x_n := x_0, x_1, \dots, x_{N-1}$, into complex numbers written, $X_k := X_1, X_2, \dots, X_{N-1}$, define as in (3.1):

$$X_k = \sum_{n=0}^{N-1} x_n \cdot e^{-\frac{i2\pi kn}{N}}, \quad (3.1)$$

where N is the number of times samples, n is the current sample ($0, \dots, N-1$), x_n is the value of the signal at time n , k is the current frequency (0 Hertz up to $N-1$), and X_k is the magnitude at frequency k (amplitude and phase).

When DFT is used, the Fourier series coefficients are defined. In fact, any periodic function $f(t)$ of period T can be written as (3.2):

$$f(t) = a_0 + a_1 \sin(\omega t) + b_1 \cos(\omega t) + a_2 \sin(2\omega t) + b_2 \cos(2\omega t) + \dots, \quad (3.2)$$

where the coefficients a_n and b_n (see also subsection A.1 to refer to the sum of the cosines of various frequencies), are linked to a time function $f(t)$.

Due to the Shannon-Nyquist theorem, the spectrum is symmetric from 0 to f_s^3 . It is noteworthy that, in our case, considering the central motivation of this thesis (see section 1.1) related to the low frequency range. The sampling rate of 1 MHz/s should be enough, once the maximum frequency under interest is 150 kHz.

Since each standard used to conducted EMI measurements might specifies different parameters for computing the DFT, the results might be different. This comes from the fact that if the time window on which the DFT is calculated does not cover an integer multiple of signals periods, the spectrum is spread on the side peaks (concept of spectral leakage), which gives a less accurate result.

As presented in [102], the DFT operates on a finite length time sequence to compute its spectrum. For a continuous signal like a rectangular pulse train (see appendix A), it is needed to capture a segment of the signal to perform the DFT. Usually, it is also required to apply a window function to the captured signal before taking the DFT (see Figure 3.4). There are many different window functions, and each one produces a distinct approximation of the spectrum. Figure 3.1 shows eight window functions generated by the Window Designer app from MATLAB.

²More explicitly called spectral leakage, leakage is the smearing of power across a frequency spectrum that occurs when the signal being measured is not periodic in the sample interval.

³The one-sided spectrum concept, e.g., presented in Figure 3.3-B.

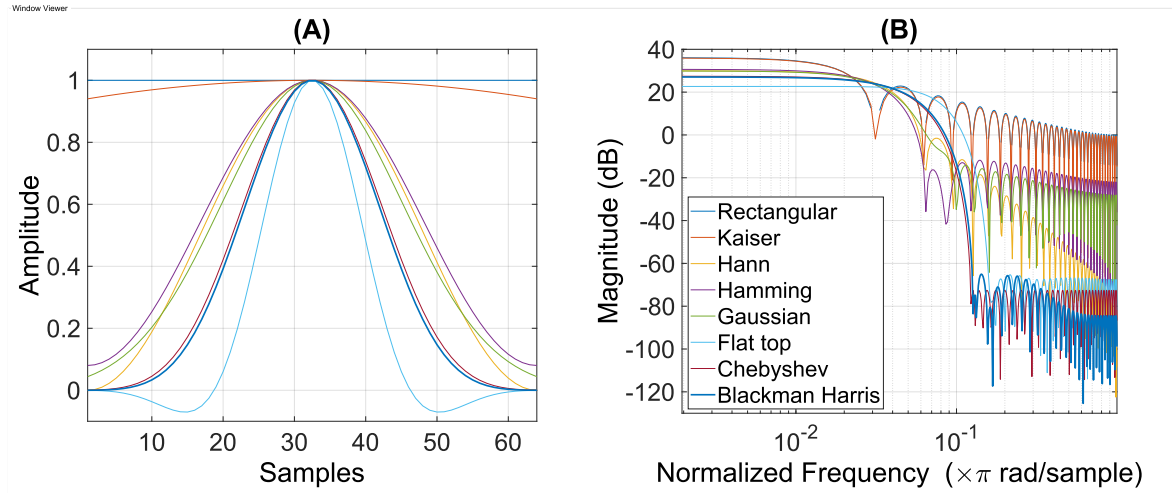


Figure 3.1: Eight window functions generated by the Window Designer app from MATLAB: (A) time domain, and (B) frequency domain.

Nevertheless, in the subsection 3.1.1 for didactic purposes, only the spectrum of windowed sinewaves⁴ for a Hanning window⁵ function will be presented. However, the windowing process (see subsection 3.1.2) is the same for all windows presented in Figure 3.1.

3.1.1 Spectrum of the Hanning Window

The Hanning window is defined by (3.3) [103]:

$$w[n] = 0.5 \left(1 - \cos \left(\frac{2\pi n}{N} \right) \right), n = 0, \dots, N. \quad (3.3)$$

The first and last elements of $w[n]$ are zero. Note that limiting n to $1, \dots, N$ removes the zero-valued elements. The removal of zero-value is done automatically by the MATLAB hanning function, as illustrated in Figure 3.2-A for $N=32$.

Furthermore, as presented in Figure 3.2-B for $N=32$, $L=32$ and $f_s=16$ Hz. It is possible to approximate the Fourier Transform of the Hanning window by appending zeros to the window (zero-padding) and taking the DFT. If we zero-pad such that N is increased by a factor of L , then the DFT frequency spacing (DFT time window) is a product of L , without any change in the N points of the DFT. The MATLAB fft function automatically appends zeros to the hanning function.

On the other hand, Figure 3.3 shows the one-sided spectrum of Hanning window for FFT length of $N=32$, i.e., where there is no frequency spacing. For further

⁴A rectangular pulse train is composed of the sinewaves aggregation of odd and even harmonics. For further information, see section A.2

⁵The Hanning window touches zero at both ends of the signal, removing any discontinuity.

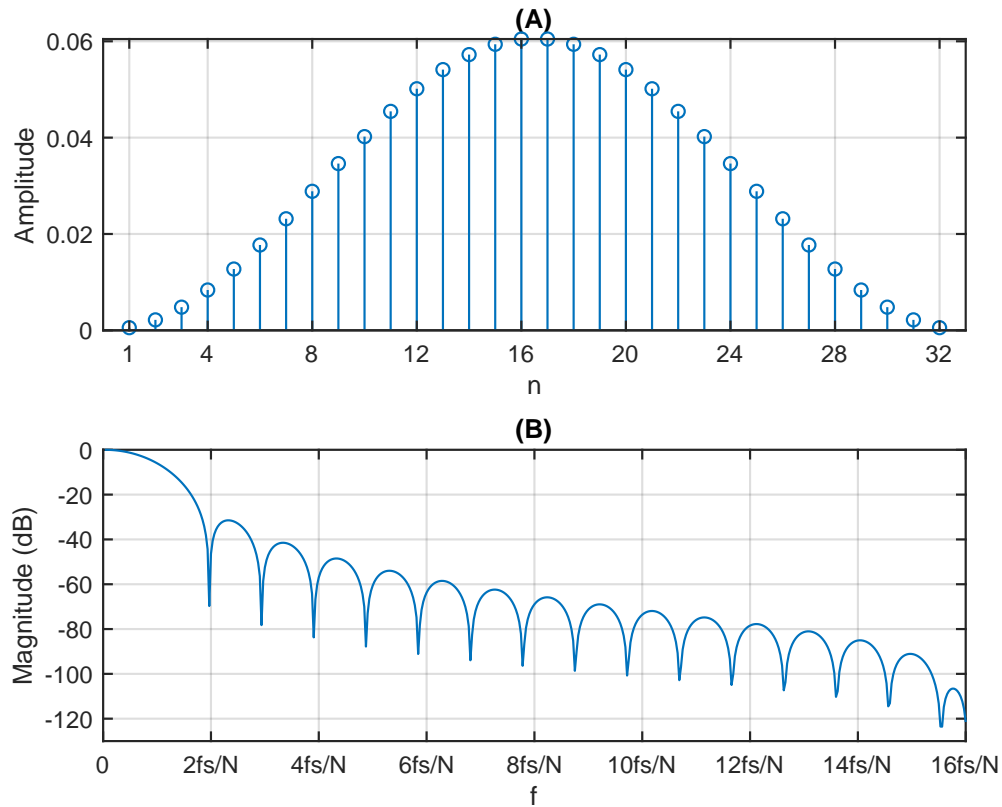


Figure 3.2: Hanning window and one-sided spectrum for $f_s=16$ Hz. (A) Hanning window for $N=32$, and (B) the one-sided spectrum of Hanning window for FFT length = $N \cdot L$.

information about the MATLAB script used in this section 3.1, please see B.4.

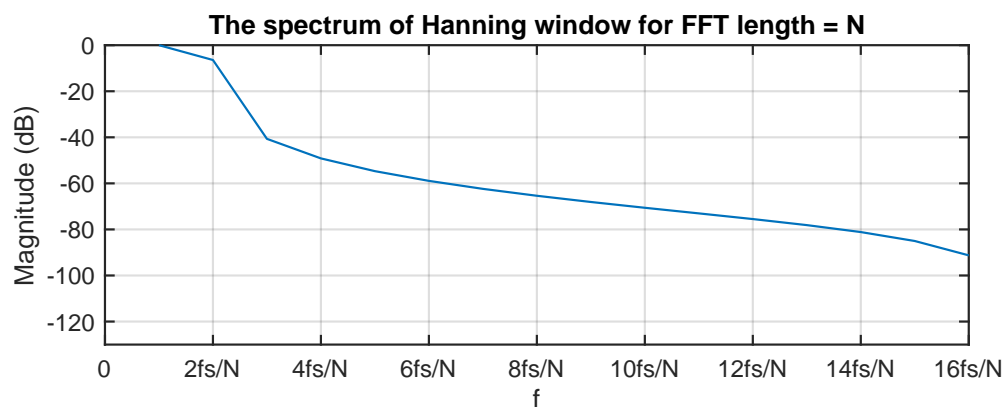


Figure 3.3: The one-sided spectrum of Hanning window for FFT length of $N=32$.

3.1.2 Windowing a Sinewave

Once the Hanning window is defined (see section 3.1.1), the next step is windowing the sinewave and careful track of the power of the signal and its spectrum. Thus, the sinewave presented in Figure 3.4-A will be scaled in such a way that the power of the window function is 1 watt at $f=2$ Hz for a one-sided spectrum with $N=32$. Figure 3.4-B shows the windowed sinewave with Hanning function (refer to Figure 3.2-A).

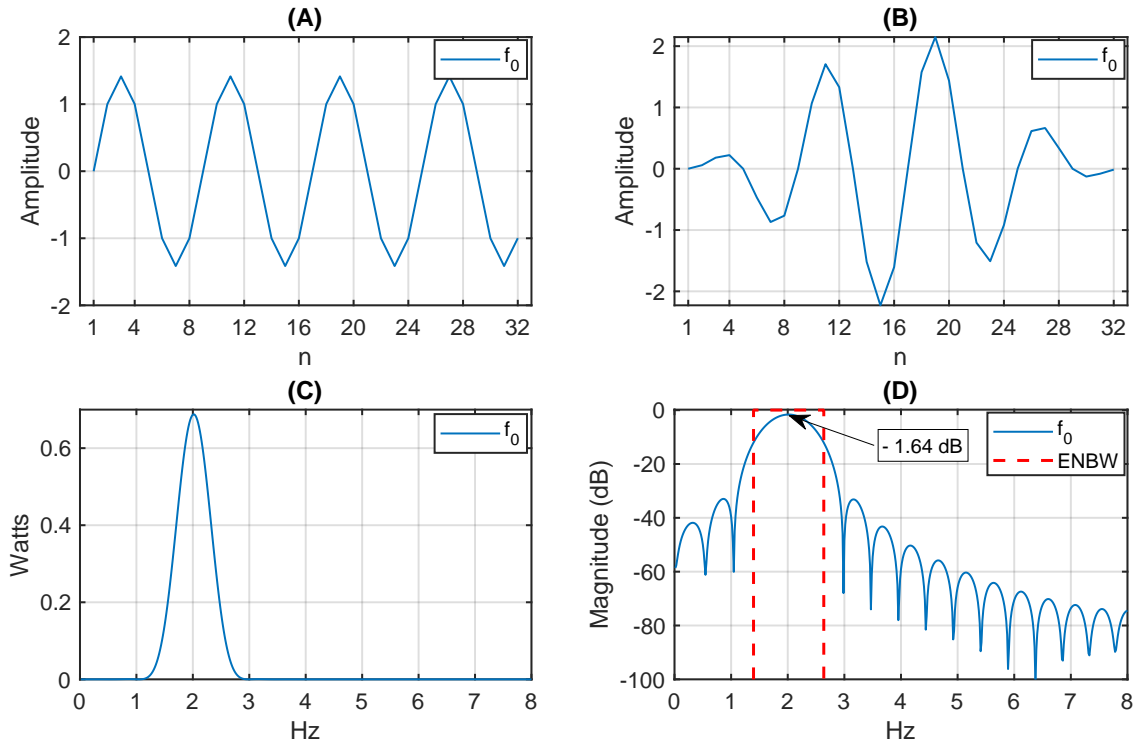


Figure 3.4: Windowing a sinewave with Hanning window. (A) Sinewave with $N=32$, (B) windowed sinewave with Hanning function (refer to Figure 3.2-A), (C) the one-sided power spectrum of 1 watt at $f=2$ Hz, and (D) the one-sided spectrum of windowed sinewave with Hanning window for FFT length = $N \cdot L$ (refer to Figure 3.2-B).

Figure 3.4-A shows the sine frequency $f_0 = 4 \cdot f_s / N = 4 \cdot 16 / 32 = 2$ Hz. This sinewave has approximately 4 of periods over $N=32$, and f_0 falls on a DFT frequency sample, i.e. approximately the center of a DFT bin (see Figure 3.4-B). Although the sinewave is not a full 2 Hz, the process of the windowed sinewave with the Hanning function forced the signal to touch zero at both ends of the signal, removing any discontinuity (see in Figure 3.4-B).

The one-sided spectrum of windowed sinewave presented in Figure 3.4-D is the Hanning window of Figure 3.2-B convolved with the sinewave at 2 Hz (see Figure 3.4-B). Unlike the ideal sine spectrum, the windowed spectrum has a finite bandwidth and sidelobes (see Figure 3.4-D). Also, it is expect the spectral peak

to be 0 dB (1 watt into 1 ohm) for an windowed sine at the DFT bin center. However, the peak of the spectrum using the Hanning window is -1.64 dB (see Figure 3.4-D), once the power is spread over several samples instead of all being contained in one sample (see Figure 3.4-C). If the power of a narrowband spectral component is essential, this reduction of the peak level, called processing loss, should be taken into account.

Processing loss is proportional to the RBW of the window, also named Equivalent Noise Bandwidth (ENBW)⁶ (see red dashed line in Figure 3.4-D). As a practical matter, higher processing loss makes it harder to discern a low-level signal in the presence of noise (it gets hidden by the noise floor) and degrades the ability to resolve signals that are closely spaced in frequency.

3.2 Short-Time Fourier Transform

The STFT is a methodology used by the CISPR 16-2-1 standard [78]. This type of Fast Fourier Transform (FFT) is used to determine the sinusoidal frequency and phase content of local sections of a signal as it changes over time. Thus, considering that the FFT coefficients can represent the harmonic components of a rectangular pulse train in the frequency domain (for further information, please see Figure A.8 and Figure A.9 of subsection A.2). The STFT breaks up the rectangular pulse train in the time domain, and then transforms each FFT coefficients for the frequency domain. The discrete STFT can be defined by (3.4):

$$X_k = \sum_{n=0}^{N-1} x[n-m] \cdot w[n] \cdot e^{-j2\pi kn/N} \quad (3.4)$$

where the parameters are given by $x[n-m]$ as the sampled signal measured in time domain, $w[n]$ is the discretized window, N is the length of a DFT signal calculation, n is an integer ranging from 0 to $N-1$. Finally, k is an integer from 0 to $N-1$ that stores the element number of the spectrogram $Z[m, k]$ in the frequency domain and m is the integer value of the element number for the spectrogram.

The time-frequency resolution of the STFT is usually defined as the product of the time resolution and the frequency resolution. The type and length of the window used affect the time-frequency resolution of the STFT. The window effect phenomenon can be summarized as (refer to Figure 3.1):

- A narrow window results in a shorter time resolution. However, a coarse frequency resolution because narrow windows have a short time duration but a

⁶ENBW, can be considered the ideal bandwidth of a selective filter (intermediate frequency filter) used by the EMI receiver, which allows the same amount of noise as a window function [78].

wide bandwidth. For instance, see the case of Flat top window presented in Figure 3.1;

- A wide window results in a shorter frequency resolution. However a coarse time resolution because wide windows have a long-time duration but a narrow frequency bandwidth. For instance, see the case of Rectangular window and Kaiser window, both presented in Figure 3.1.

3.3 Measurement Standards

To assess the conducted emission following EMC standards [78], one needs to use a super-heterodyne frequency band stepping EMI test receiver, which are micro voltmeters that perform selective measurements in the frequency domain⁷. Therefore EMI receiver measures a voltage, but after connecting auxiliary transducers like probes or antennas one may measure other quantities like an electromagnetic fields.

The EMI receivers have to meet many requirements related to selectivity, pulse response, intermodulation effects, noises and internal unwanted signals and shielding [78]. To explain the principle of its operation, we can assume that the EMI receiver only consists of few main blocks. The block diagram of the super-heterodyne frequency band stepping EMI test receiver [104], can be seen in Figure 3.5, which includes six stages for providing the detector measurements.

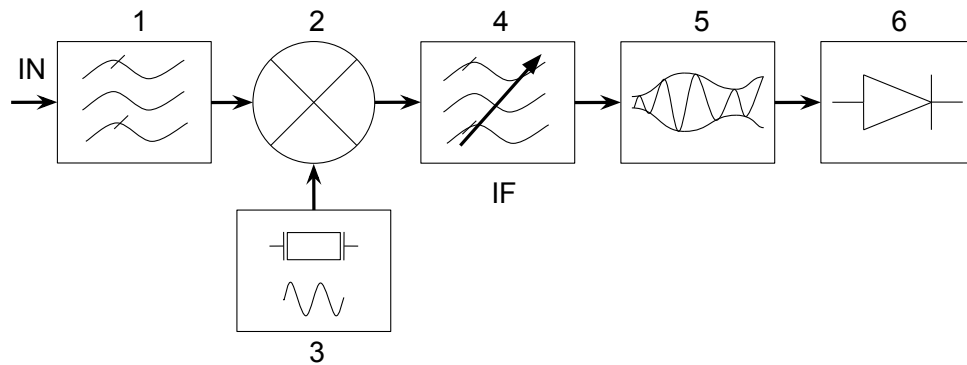


Figure 3.5: The block diagram of the super-heterodyne frequency band stepping EMI test receiver.

The summarized explanation about Figure 3.5 is as follows:

- **Input filter (1):** determines the selectivity of the frequency band to be used according to the standards, e.g., CISPR 16-2-1 [78];
- **Mixer point (2):** accounts for the total energy of the broadband spectrum;

⁷Parts of this section 3.3 are published in [46].

- **Local oscillator (3):** determines the sampling frequency to measure the input signal;
- **Tunable Intermediate Frequency (IF) Filter (4):** extracts the fragment of the signal, and determines the length of the window (see Figure 3.1). The main parameter of the Intermediate Frequency Bandwidth (IFBW) filter varies depending on the scanned frequency range [78];
- **Envelope detector (5):** determines the frequency demodulation⁸ for the detectors;
- **EMI detectors (6):** provides the weighted value for the detectors such as Peak, QP, and AV.

Block (4) of Figure 3.5 plays a crucial role in the entire process developed by the super-heterodyne frequency band stepping EMI test receiver. Once this block (4) delivers the product of the discretized window function sampled w_n to the discretized time-domain signal sampled x_n , in which n is the integer that represents the number of the data measured.

Figure 3.6 shows a classic procedure of measuring the spectrum by the super-heterodyne frequency band stepping EMI test receiver. In the first step, the EMI receiver tunes to the required frequency in a similar way to a radio receiver (sets the frequency of super-heterodyne). In the second step, the selective, IF filter passes the narrow part of the signal. Then the detector measures the signal parameter, e.g. the average value. After the measurement, super-heterodyne changes the frequency (receiver tunes to next frequency point). Typically, the measurement step is related with the IFBW (should be no bigger than half of the IFBW).

The described measurement procedure by Figure 3.5 and Figure 3.6 define the measurement of EMI emission following EMC standards. Therefore, by measuring a signal of a given frequency, we obtain the image of the IF filter instead of the single spectral line expected from the Fourier theorem (see Figure 3.4-D and Figure 3.6).

On the other hand, spectrum measurement in the full range of frequency involves a lot of single measurements. For example, if the objective is to have one narrower RBW, one needs to use a narrower IF filter. However, adopting a narrow IF filter, the super-heterodyne frequency band stepping EMI test receiver must use long dwell times⁹ for every frequency [105].

⁸Frequency demodulation is a key process in the reception of a frequency modulated signal. Once the signal has been received, filtered and amplified, it is necessary to recover the original modulation from the carrier. It is this process that is called demodulation or detection.

⁹Both commercial and military EMC testing standards require specific amounts of measurement time, in order to ensure that impulsive signals are appropriately characterized.

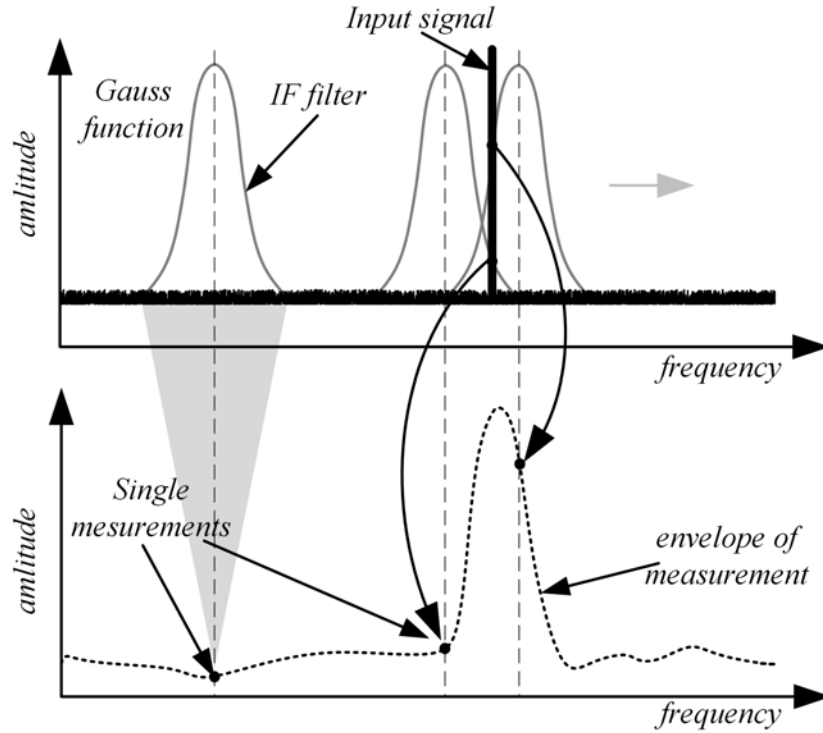


Figure 3.6: The scheme depicting the process of spectrum measurements by the super-heterodyne frequency band stepping EMI test receiver (input signal, IF filter and measurement result) [46].

Furthermore, a super-heterodyne frequency band stepping EMI test receiver may not catch the signal whose frequency varies in time when the dwell time is not precisely defined. I.e., the spectrum spreading effect (for further information, please see section 2.1) may occur when the signal frequency varies during the dwell time. To demonstrate such an effect, let us analyze the simple example. The sinusoidal signal with amplitude one changes from $f_1 = 10$ kHz to $f_2 = 20$ kHz during the observation period of 2 ms, as shown in Figure 3.7-A and described by (3.5):

$$y(t) = \text{rect}(t) \cdot \sin(2 \cdot \pi \cdot f_1 \cdot t) + \text{rect}(t)(t - T/2) \cdot \sin(2 \cdot \pi \cdot f_2 \cdot t), \quad (3.5)$$

where $\text{rect}(t) = 1$ for $0 < t < T/2$, and $\text{rect}(t) = 0$ for $T/2 < t < T$.

The spectrum of (3.5) may be described by (3.6):

$$Y(f) = \mathcal{F}(y(t)) = 0.5 \cdot \text{sinc}(\pi \cdot (f - f_1) \cdot T/2) + 0.5 \cdot \text{sinc}(\pi \cdot (f - f_2) \cdot T/2). \quad (3.6)$$

The spectrum, obtained by means of FFT (Figure 3.7-B) largely corresponds to that given by (3.6). Also the spectrum has a resolution Δf which is related to the dwell time (T_m) according to (3.7):

$$\Delta f = 1/T_m = f_s/N, \quad (3.7)$$

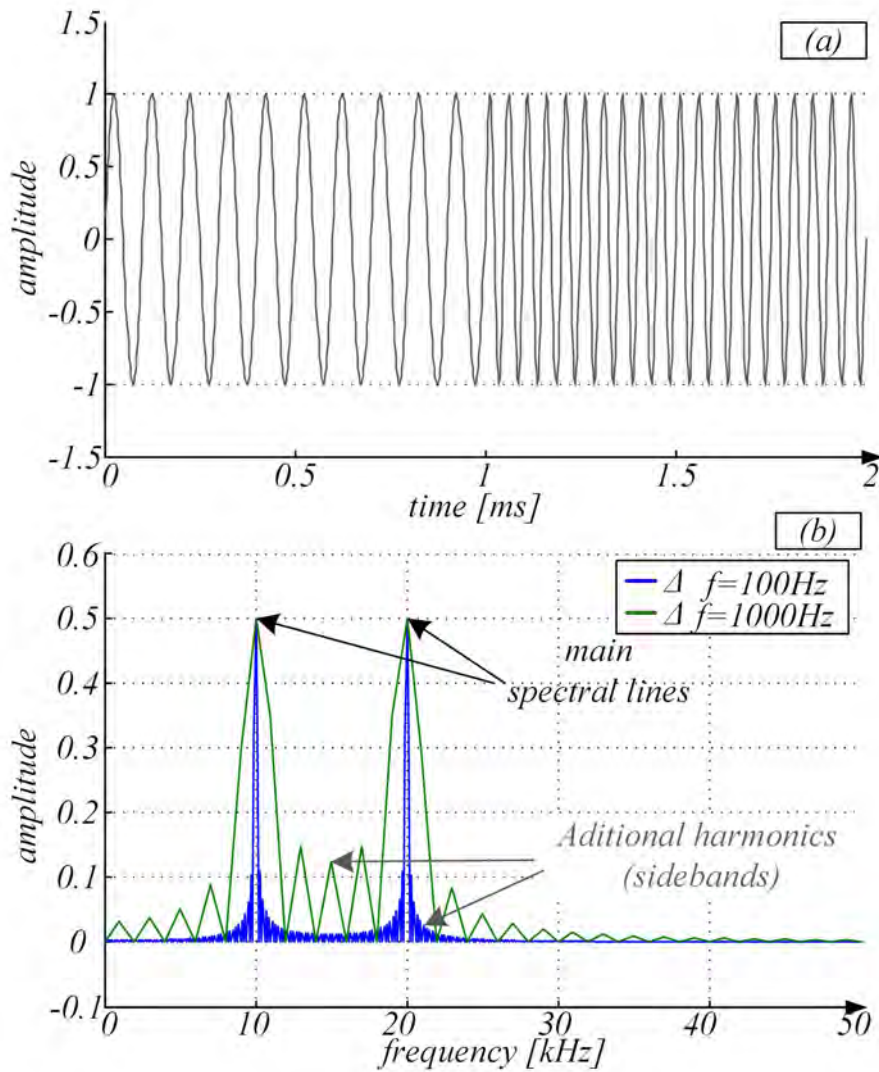


Figure 3.7: The example of signal representation from (3.5): (a) time domain, (b): frequency domain obtained by FFT [46].

where N is the number of samples and f_s is the sampling frequency. In the spectrum represented by Figure 3.7-B, one may see the two main spectral lines (the green and blue) with amplitude equal to 0.5. The amplitude of these spectral lines does not depend on the RBW or T_m . The primary spectral lines amplitude (the green and blue) are proportional to the signal amplitude (observed in the time domain, Figure 3.7-A) and its duration. Furthermore, more sideband spectral lines (additional harmonics) with a lower amplitude occur when a signal frequency varies more times during the T_m , i.e., $\Delta f = 100 \text{ Hz}$.

Through Figure 3.7-B, it is possible to conclude that when the T_m increases, the RBW is narrower. Nevertheless, from another perspective, let's us assume the sinusoidal signal with amplitude one (3.5), now changing from $f_1 = 10 \text{ kHz}$ to $f_2 = 25 \text{ kHz}$, then to $f_3 = 50 \text{ kHz}$ and finally to $f_4 = 100 \text{ kHz}$. Where the change between fre-

quencies is determined¹⁰ during the T_m . Also, consider that the observation period (equal to 20 s), will be measured four times, where each measurement considers a different T_m , as presented by Figure 3.8. For further information about the MATLAB script used in this section 3.3, please see B.5.

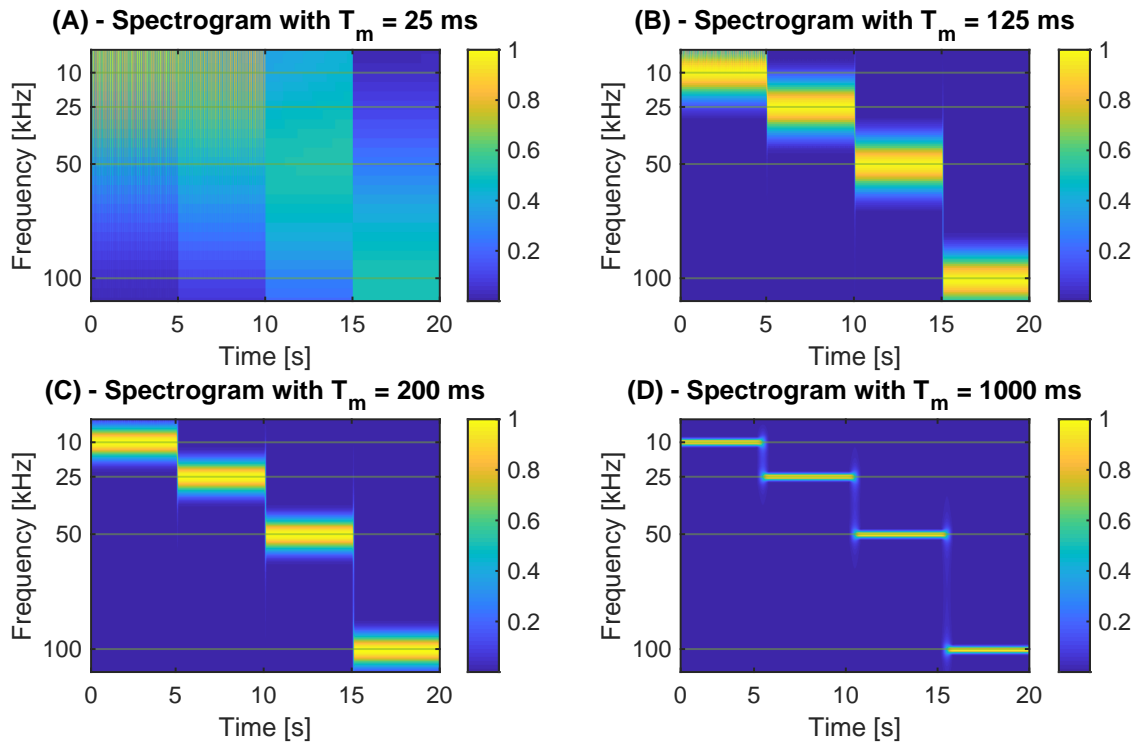


Figure 3.8: MATLAB simulation of STFT for a sinusoidal signal with amplitude one, determinedly changing from $f_1 = 10$ kHz to $f_2 = 25$ kHz, then to $f_3 = 50$ kHz and finally to $f_4 = 100$ kHz. (A) $T_m = 25$ ms, (B) $T_m = 125$ ms, (C) $T_m = 200$ ms and (D) $T_m = 1000$ ms.

Thus, Figure 3.8-D reinforces the relation: the narrower the IF filter, the narrower RBW is, and the longer it is T_m . On the other hand, through the STFT considered in the MATLAB simulation presented in Figure 3.8, especially Figure 3.8-A. It is possible to conclude that if a small value of T_m is considered for a signal whose frequency varies over time, the representation of this signal in the frequency domain will not be realistic. Corroborating the claim that the EMI receiver may not catch the signal whose frequency varies in time when the T_m is not precisely defined.

¹⁰In the case of the RanM, the change between frequencies can also be randomized. For further information, see section 2.1.

3.4 Standardized settings for EMI measurements

The CISPR 16-2-1 standard specifies three EMI detectors: Peak, AV and QP. Furthermore, four bands of frequency, see Table 3.1 [78]. Nevertheless, considering the central motivation of this thesis (see section 1.1), which is related to the low frequency range. The CISPR A frequency band, from 9 kHz to 150 kHz with IFBW filter equal to 200 Hz is considered.

Table 3.1: CISPR 16-2-1 bandwidths for different measurements ranges [78].

CISPR Band	A	B	C	D
Frequency range	9 kHz - 150 kHz	150 kHz - 30 MHz	30 MHz - 300 MHz	300 MHz - 1000 MHz
IFBW filter	200 Hz	9 kHz	120 kHz	120 kHz
QP charge time	45 ms	1 ms	1 ms	1 ms
QP discharge time	500 ms	160 ms	550 ms	550 ms

When considering to measure the EMI of a DetM, the EMI detectors follow this given rule $Peak = QP = AV$. On the other hand, when considering to measure the EMI of a RanM the rule might or might not change to $Peak > QP > AV$. This possible difference that relates the EMI detectors with DetM and RanM, is due to the spreading effect of the EMI spectrum components, as well as the lack of precision in the definition of the T_m and RBW.

However, it is essential to emphasize that the beforehand definition of the T_m and RBW for DetM is more flexible. Once there are no changes in the frequency of a given signal during the EMI measurements for DetM. The challenge arises to define the T_m and RBW for a RanM, which not only provide changes in the frequency of a given signal but also provides random changes between the frequencies of this signal (both cases during the EMI measurements).

The definition of the T_m value is a current debate [105]. Different EMC standards might consider different requirements of T_m . On average, when considering power electronic systems operating in the low frequency range, the IEC 61000-4-7 standard is used as a reference, although it does not cover DC/DC systems [106]. The IEC 61000-4-7 specify for frequency band A (see Table 3.1), $T_m = 200$ ms, i.e. 5 Hertz, which means that five cycles of a given signal should be enough to characterize it appropriately (see Figure 3.8-C).

Peak detector

The Peak detector considers the maximum value of the peak for a measured signal over a short time constant. This means that in time domain the Peak detector works

independently of the Pulse Repetition Frequency (PRF)¹¹ [107].

Average detector

The AV detector demonstrates the mean value of the demodulated IFBW over the time interval measured. Generally, this detector is not suitable for impulsive disturbances [107].

Quasi-peak detector

The QP detector works in a different form when compared to the Peak detection. The main parameters for this detector are given by the charge and discharge time of the circuit, these were shown in Table 3.1 [78]. To this matter, the PRF will have a significant influence on the measured QP value. The more pulses repeated over a particular time, the higher the QP value will be [107].

3.5 Summary

In this chapter 3, essential aspects of the theoretical knowledge used by conventional super-heterodyne frequency band stepping EMI test receivers, during conducted EMI measurements were presented.

Initially, section 3.1 presents two of the main parameters to calculate the DFT, the sampling frequency (f_s) and the DFT time window. Then it is understood that once the DFT operates on a finite length time sequence to compute its spectrum. For a continuous signal like a rectangular pulse train (see appendix A), it is needed to capture a segment of the signal to perform the DFT. Usually, it is also required to apply a window function to the captured signal before taking the DFT (see Figure 3.4-B of the subsection 3.1.2). The window effect phenomenon was summarized by section 3.2 as (refer to Figure 3.1):

- A narrow window results in a shorter time resolution. However, a coarse frequency resolution because narrow windows have a short time duration but a wide bandwidth. For instance, see the case of Flat top window presented in Figure 3.1;
- A wide window results in a shorter frequency resolution. However a coarse time resolution because wide windows have a long-time duration but a narrow

¹¹The PRF is the number of pulses of a repeating signal in a specific time unit, typically measured in pulses per second.

frequency bandwidth. For instance, see the case of Rectangular window and Kaiser window, both presented in Figure 3.1.

The section 3.2 also introduces how the STFT breaks up the rectangular pulse train in the time domain and then transforms each FFT coefficients for the frequency domain. Considering that the FFT coefficients can represent the harmonic components of a rectangular pulse train in the frequency domain (for further information, please see Figure A.8 and Figure A.9 of subsection A.2).

The section 3.3 show the applicability of both DFT and STFT methods, and their influence on the conducted EMI measurements. Assuming that the EMI receiver is based on the calculation given by the STFT and the slices of data according to a specific time window, i.e., IF filter (see the example provided by Figure 3.6). Therefore, by measuring a signal of a given frequency, we obtain the image of the IF filter instead of the single spectral line expected from the Fourier theorem (see Figure 3.4-D and Figure 3.6).

On the other hand, spectrum measurement in the full range of frequency involves a lot of single measurements. For example, if the objective is to have a narrower RBW, one needs to use a narrower IF filter. However, adopting a narrow IF filter, the super-heterodyne frequency band stepping EMI test receiver must use long dwell times (T_m) for every frequency [105]. The MATLAB simulation presented in Figure 3.8-D of the section 3.3 reinforces this relation: the narrower the IF filter, the better RBW is, and the longer is T_m .

Nevertheless, an interesting point, mentioned in both section 3.3 and subsection 3.4 is the tradeoffs between RanM, T_m and RBW. The beforehand definition T_m and RBW for DetM is more flexible. As there are no changes in the frequency of a given signal during the EMI measurements for DetM. The challenge arises to define the T_m and RBW for a RanM, which not only provide changes in the frequency of a given signal but also provides random changes between the frequencies of this signal (both cases during the EMI measurements). A graphical explanation of the tradeoffs for a fixed RBW is shown in Figure 3.9.

In the top panel of Figure 3.9, three cases are shown. The first one is when f_{b1} is less than the RBW. In this case, the spreading effects due to the different frequencies of the signal will appear. Also, the EMI receiver has enough T_m to appropriately characterize the given signal (see Figure 3.8-D). In the second case, the f_{b2} is equal to RBW, then a stable EMC measurement is achieved.

In the third case presented in the top panel of Figure 3.9. The f_{b3} is larger than the RBW. The spreading effects due to the different frequencies of the signal will also appear. However, unlike the first case with f_{b1} , the signal will never complete a frequency period, and the spectrogram will not be realistic. Once the T_m is not enough to characterize the signal appropriately, in the case of f_{b3} . This might induce

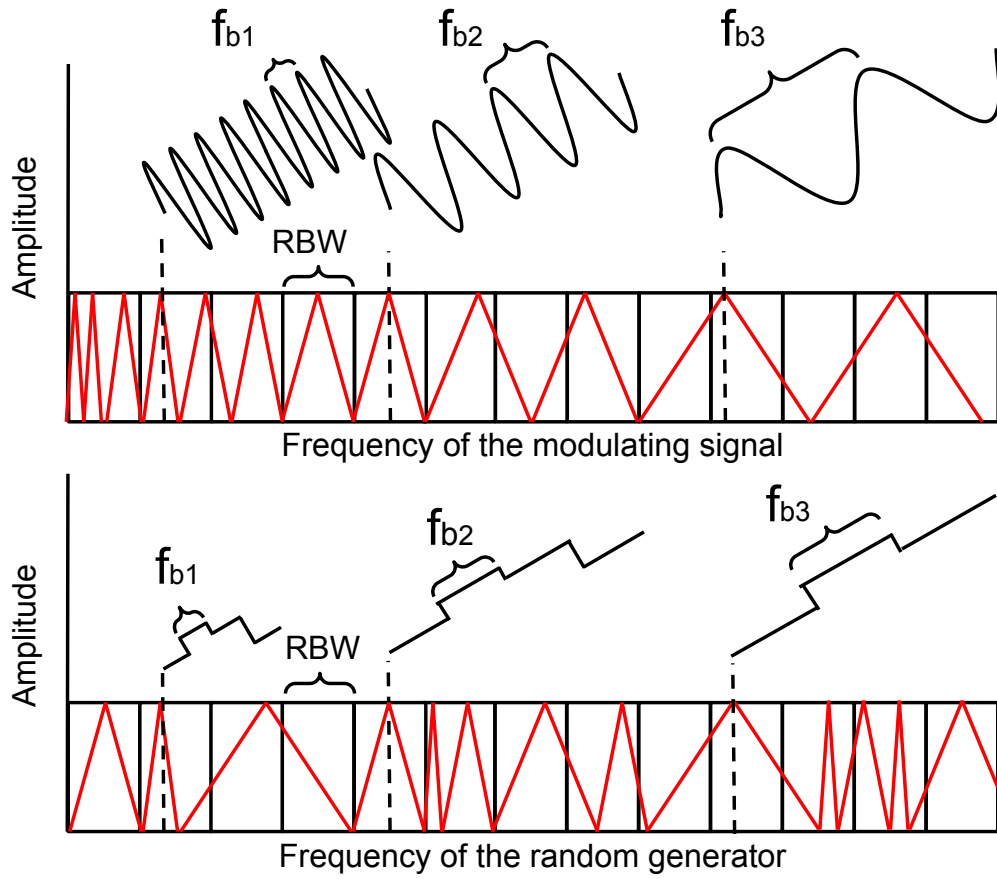


Figure 3.9: The influence of the frequency of the modulating signal (top panel) and frequency of the random generator used by RanM (bottom panel). The RBW is represented with a rectangle, while the frequency of the signal to be measured by the T_m is represented by the red triangles.

a conclusion of EMI noise level reduction (see for example the Figure 2.7 of the section 2.2). When actually what is happening, it is a mismatch between the given signal, T_m , and RBW.

It is noteworthy that for all cases presented in the top panel of Figure 3.9. The RanM only provides changes in the frequency of the signal. On the other hand, for the three cases presented in the bottom panel of Figure 3.9. The RanM provides changes in the frequency of the signal but also provides random changes between the frequencies of this signal. The RanM represented in the bottom panel of Figure 3.9, was conceptually defined as controlling the switching rate of change by the section 2.1 and implemented such as RanM3, as presented in subsection 4.2.6.

Obviously, due to the complexity of establishing the tradeoffs between a RanM using the control of the switching rate of change, T_m , and RBW, as represented in the bottom panel of Figure 3.9. A premise might consider the shorter T_m possible, which in theory can be more problematic to catch the frequency changes and

adapts the switching rate of change to match the RBW (For further information see section 2.1 and subsection 4.2.6). Thus, it is assumed that even in a highly complex case with a shorter T_m , it's possible to have the stable EMC measurements. The conducted EMI measurement topic is discussed in depth in the chapter 5.

Cyber-Physical System for Evaluation of PWM Techniques

CPS is a physical mechanism controlled and monitored by computer based algorithms. CPS can ensure operational and regulatory compliance within smart grids. For instance, in power electronic systems and infrastructures such as IPEM, it is highly necessary to ensure EMC. Consequently, CPS might play an essential role in the design, prototyping, and testing phases of the power electronic converters, explicitly due to their convergence of computing, networking, and control of physical processes [108], enabling high customization and flexibility to the design process of the PWM technique, e.g. used by DC/DC converters. Essentially the CPS can be considered as one fundamental part of the moderns EMC-test bench systems, where one typical control hardware is the FPGA. The FPGA is widely used to enable the configuration by a customer or a designer of parameters such as D and fundamental switching frequency (f_0) [43], [44], [65].

Thus, the challenge can be found in establishing a PWM technique that is "EMC friendly" with the miscellaneous systems associated with smart grids applications. The modern High-Level Graphical Synthesis (HLS) programming tools, such as LabVIEW, may facilitate the design process of the PWM technique, however, some issues connected with the FPGA-based design, such as matching the range of fixed-point numbers [65], and limitations in arithmetic operations [43] might be challenging to implement the concept of controlling the switching rate of change (previously described in subsection 2.1 and subsection 3.5). This is especially true when the communication environment between the FPGA and Integrated Development Environment (IDE) is not available at the EMC-test bench system.

This chapter 4 introduces the Intel Core i7 embedded controller - NI PXIe-8135 and the FPGA R-Series Multifunction RIO - PXI-7854R. PDF are used to analyse and improve RanM. The PWM algorithms are presented and discussed in terms of expected conducted EMI shape.

4.1 Cyber-Physical System

Nowadays, with the advent of smart grids, the demand for CPS [108] and the growth in DC/DC converter applications [109]–[113], EMC issues are becoming more and more significant [114]. The increasingly smart grids demand systems and infrastructures adaptable to inherent challenges, often not foreseen during the development phase, such as a new requirement of regulatory compliance [115]. In this context, CPS have gained notoriety, providing the fusion between computing and communication interacting closely with physical processes [116]. Definitely changing how systems and infrastructures interact with the physical world into smart grids [117].

Recent advances in smart grids enabled by CPS technologies [118], have led to more resilient systems in respect of coding and operation [119] and, ultimately, to an innovative system with adaptable features [120]. Nevertheless, among the various factors influencing smart grids, EMC stands out. The philosophy of the standardization of EMI emissions levels, aims to regulate and certify that an environment ensures the EMC between all the systems and infrastructures installed [44]. Thus, due to their convergence of computation, networking, and control of physical processes [121], the CPS has been frequently used as a integrated control system for bench level testing for one of the big EMI sources in the smart grids, i.e., power electronic converters [122].

In a situation where discussion about the EMI emission levels is important, and before implementing or adopting EMI filters [123], solutions can be accomplished in terms of switch control strategies [65]. The aptness into implementation of different PWM techniques, providing high customization and flexibility, makes CPS a reliable bench test set-up for power electronic converters. Fundamentally, this is due to the need for an early indication of the EMI emission levels that power electronic converters could generate when installed in an environment with EMC standard.

In a typical PWM algorithm, the customer or a designer may set the f_0 and the D. The parameter D controls the output voltage of the power electronic converters and thus affects the energy conversion process. The f_0 of the PWM signal is practically irrelevant to the voltage transfer function of the converter, and of the primary energy conversion. However, it affects the losses in the DC/DC converter, and the parameters of the reactance elements. Since the conducted EMI generated by the DC/DC converter are grouped around the f_0 and its harmonics [24], [124]. Thus, any modification of f_0 also leads to changes in the EMI noise shape.

As presented in subsection 2.1 through the RanM, the f_0 of the PWM signal is randomly changed in the defined randomization range¹. The concept of controlling the switching rate of change (previously described in subsection 2.1 and subsection

¹The randomization range concept of f_0 is discussed in depth in the subsection 4.2.

3.5) define a specific combination of changes for the f_0 (or period T) of the PWM signal. Nevertheless, the RSN used by the RanM must also be designed to the specific hardware platform, thus avoiding issues such as matching the range of fixed-point numbers. One way to better understand and scale the RSN is through PDF.

Therefore, in the following subsections 4.1.1 and 4.1.3 the hardware and resource details of the Intel Core i7 embedded controller - NI PXIe-8135, used in the research presented in this thesis, as well as about the FPGA R-Series Multifunction RIO - PXI-7854R, will be presented. Beyond the knowledge base relating to the LabVIEW projects presented in the subsection 4.1.2. The proposed PWM modulator algorithm will be presented in the subsection 4.1.4 and the Random Number Generator presented in the subsection 4.1.5.

4.1.1 Intel Core i7 embedded controller - NI PXIe-8135

This thesis considers the NI PXIe-8135 embedded control system as the IDE. The NI PXIe-8135 is an Intel Core i7 embedded controller with the HLS - LabVIEW, which enables the PWM techniques' rapid prototyping capabilities. Moreover, the NI PXIe-8135 provides a bespoke integration for FPGA target programming based on the parallelism and data flow with LabVIEW. Furthermore, the choice of the NI PXIe-8135 is due to its high customization and flexibility. The NI PXIe-8135 is compatible with the PXI Express chassis enabling easy interfacing (adjustment of physical parameters, reading of test data, and diagnostics) with the DC/DC converter through the FPGA. Figure 4.1 illustrates the NI PXIe-8135 embedded controller.

Figure 4.2 illustrate the block diagram of the NI PXIe-8135. Thus, based on Figure 4.2, the following highlights provide a brief description of the logic blocks connected with the Central Processing Unit (CPU) module, through the Direct Media Interface (DMI):

- The Small Outline Dual In-line Memory Module (SO-DIMM) block consists of two 64-bit Double Data Rate (DDR)3 Synchronous Dynamic Random-Access Memory (SDRAM) sockets that can hold up to 8 GB each, for a total of 16 GB;
- The Server Message Block (SMB) to PXI Express trigger provides a routable connection of the PXI Express triggers to/from the SMB on the front panel;
- The ATI Radeon E4690 Embedded Graphics Processing Unit (GPU) drives the graphics;
- The watchdog timer block consists of a watchdog timer that can reset the controller or generate a trigger;



Figure 4.1: NI PXIe-8135 embedded controller illustration [125].

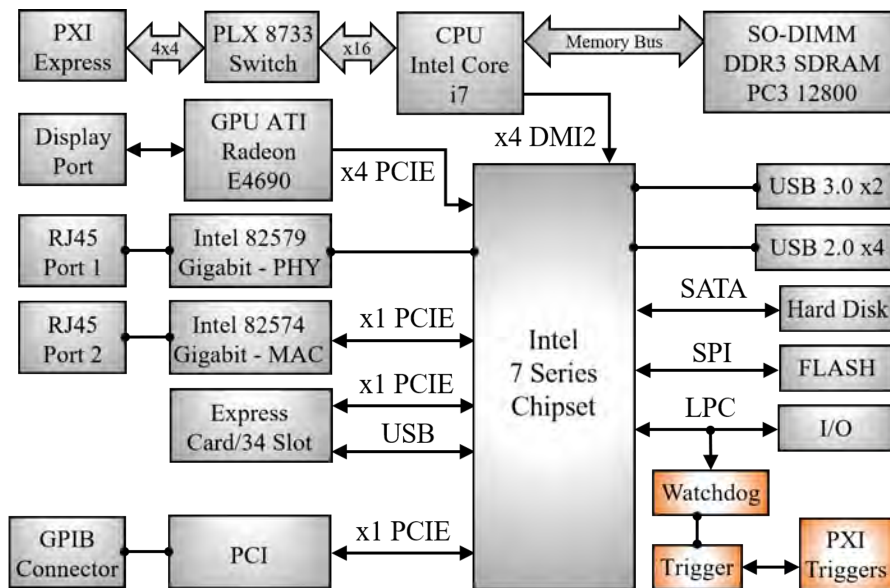


Figure 4.2: NI PXIe-8135 block diagram and application logic interface [125].

- The Intel 7 series chipset connects to the Peripheral Component Interconnect (PCI), Universal Serial Bus (USB), Serial Advanced Technology Attachment (SATA), Serial Peripheral Interface (SPI), PCI-Express (PCIE), and Low Pin Count (LPC) buses;
- The USB connectors connect the Intel 7 Series chipset to the Hi-Speed USB 2.0 interface and USB 3.0 interfaces;

- The SATA Hard Disk is a 250 GB or larger notebook hard disk. The SATA interface enables transfer rates up to 600 MB/s. The hard disk also supports Native Command Queuing (NCQ);
- The PLX 8733 switch processor connects the NI PXIe-8135 to the PXI Express - Compact PCIE backplane;
- The Input/Output (I/O) block represents the other peripherals supplied by the NI PXIe-8135. The NI PXIe-8135 has one serial port, and an Enhanced Parallel Port/Enhanced Capability Port (EPP/ECP) parallel port;
- The 82579 Gigabit Ethernet Physical Layer (PHY) and 82574I Gigabit Ethernet Media Access Controller (MAC) ports connect to either 10 Mbit, 100 Mbit, or 1,000 Mbit Ethernet interfaces. Both ports are housed in a dual-stacked Ethernet connector;
- The General Purpose Interface Bus (GPIB) block contains the GPIB interface. The ExpressCard/34 slot accommodates an ExpressCard/34 module.

Whereas the NI PXIe-8135 embedded controller can be used as an IDE for EMC-test bench system considering several DC/DC converters. In some cases, that system needs to run several LabVIEW FPGA programs simultaneously. Among all the illustrated logical blocks in Figure 4.2, the *watchdog* and *trigger* blocks have a highly relevant role for timing and synchronization of multiple FPGAs. From the LabVIEW project point of view, the *watchdog* and *trigger* blocks represents the hardware path enabling the timing and synchronization function (*TSF*) of several application instances based on Transistor-Transistor Logic (TTL) triggers (see the *PXI Triggers* path of Figure 4.2, Figure 4.3 and Figure 4.6).

In addition, as illustrated in Figure 4.3, the *TSF* are supported by the standardized integrated features of PXI Express chassis, such as: PXI 10 MHz backplane clock, the star trigger bus, PXI Express 100 MHz differential clock and three differential star trigger buses. Additionally, it is noteworthy that the PXI Express Hybrid Peripheral slots are commonly allocated to FPGAs. Also, to ensure conformity between these features, the SYNC 100 was introduced to synchronize the 10 MHz and 100 MHz clocks within a PXI Express chassis.

4.1.2 LabVIEW projects

LabVIEW creates an application instance for each target (hardware resource, i.e., FPGA) in a project. Normally, each application instance is attributed to one Virtual Instruments (VI), where the HLS is used for coding (The LabVIEW Environment

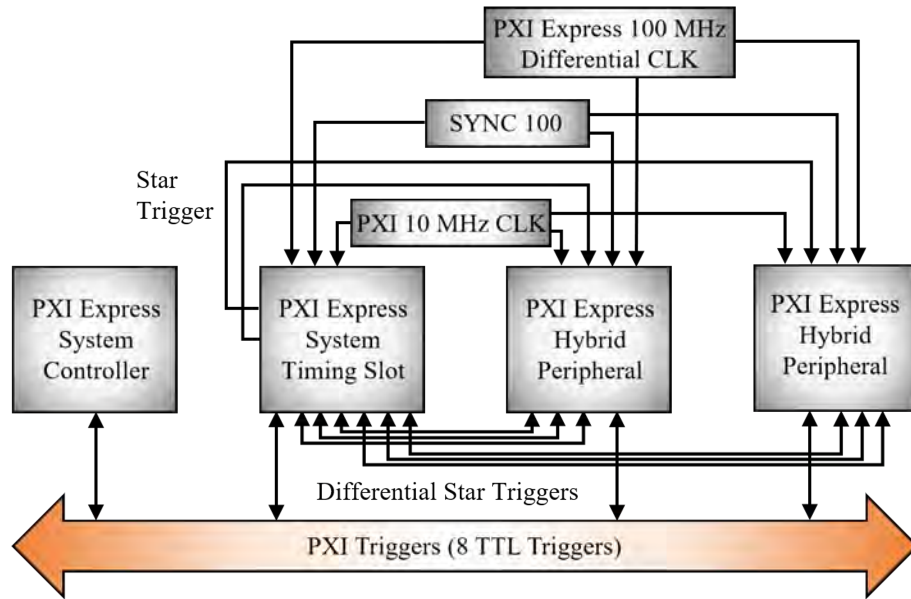


Figure 4.3: Standardized integrated features of PXI Express chassis. [126].

"VI" = program or function, "Front Panel" = user interface, and "Block Diagram" = code). However, also through the LabVIEW it is possible to open one VI on the NI PXIe-8135 embedded controller and control multiple FPGAs application instances simultaneously. For example, it is possible to open the same VI in two different LabVIEW projects or from two different FPGA targets within a LabVIEW project.

Thus, to enable *TSF*, the command must be specified using the LabVIEW project, synchronizing all the FPGAs target application instances. In this thesis, we assume to work with LabVIEW 8.5 and above. Therefore, from the hardware point of view, the *TSF* activation is possible due to the *PXI Triggers*, see Figure 4.2, Figure 4.3 and Figure 4.6.

Figure 4.4 highlights some of the main LabVIEW features related to the possibilities of coding customization and flexibility in the interface, e.g. data acquisition, with the different embedded platforms.

4.1.3 FPGA R-Series Multifunction RIO - PXI-7854R

The development environment mentioned in subsections 4.1.1 and 4.1.2, also include the FPGA R-Series Multifunction RIO - PXI-7854R card (illustration in Figure 4.5) with VIRTEX-5 LX110. As illustrated in Figure 4.3, the FPGA PXI-7854R is allocated at the PXI Express Hybrid Peripheral slots. FPGA is an integrated circuit with an array of programmable logic blocks; each processing task is independently assigned to a dedicated chip section (VIRTEX-5 LX110). Therefore, each chip section of the VIRTEX-5 LX110 may provide the ability to function autonomously without

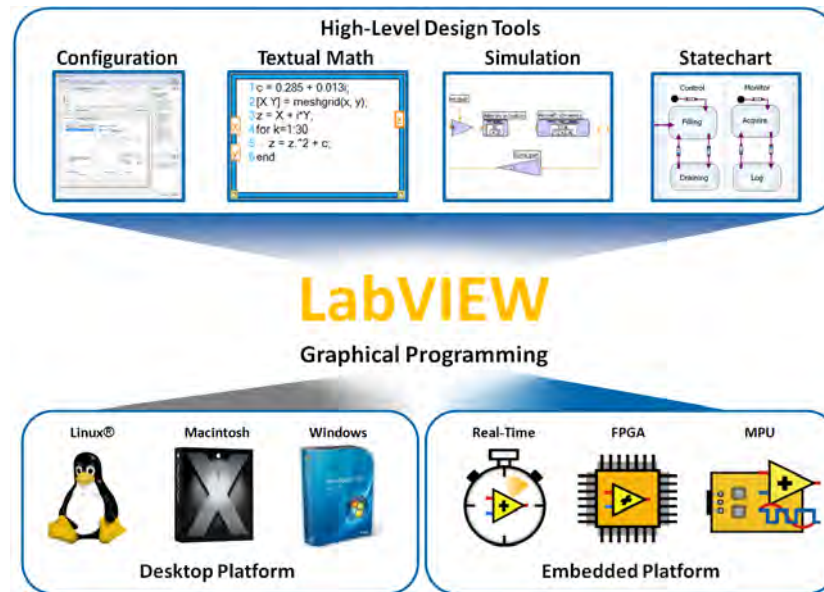


Figure 4.4: LabVIEW features illustration [127].

any influence from other logic blocks [128]. As a result, the performance of a chip section cannot be affected as further processing is added. Also, one benefit of FPGAs over processor-based systems is that the application logic is implemented in hardware circuits rather than running on an operating system, drivers, and application software [65].



Figure 4.5: FPGA PXI-7854R illustration [128].

The FPGA PXI-7854R consists of a few dozen I/O resources, which include

Analog/Digital Converters (ADCs), Digital/Analog Converters (DACs), and digital I/O lines as illustrated in Figure 4.6.

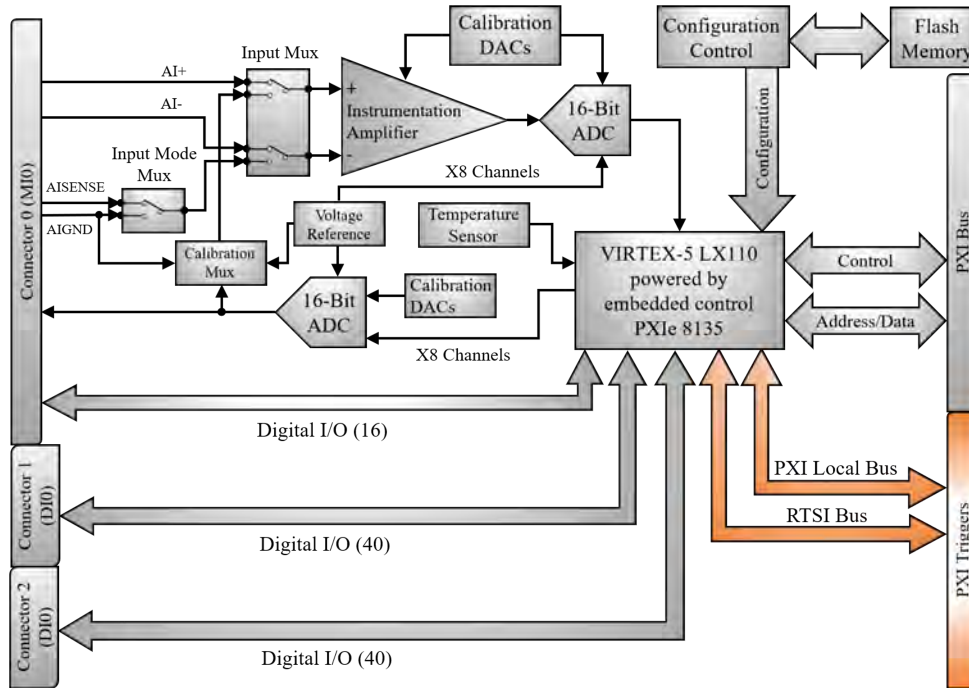


Figure 4.6: FPGA PXI-7854R block diagram and application logic interface [128].

The design tool LabVIEW accesses the VIRTEX-5 LX110 through the bus interfaces *PXI Triggers* (see Figure 4.6). The VIRTEX-5 LX110 is responsible for connecting the bus interfaces and fixed I/O resources. This connection makes possible timing, triggering, processing, and custom I/O measurements. Nevertheless, the number of FPGA slices, used for logical and arithmetic operations, may indicate the algorithmic complexity. Each FPGA PXI-7854R slice contains four look-up tables and four flip-flops. The VIRTEX-5 LX110 has a total number of slices available equal to 17,280. Therefore, the number of slices might be considered as one essential parameter to evaluate the PWM techniques implemented in FPGA PXI-7854R.

Additionally, the FPGA PXI-7854R clock on the NI PXIe-8135 embedded controller is always synchronized to the PXI Express 100 MHz differential clock (see Figure 4.3). However, by default, the FPGA (allocated in the PXI Express Hybrid Peripheral slots, please see Figure 4.3) is not synchronized to the PXI 10 MHz backplane clock. The PXI 10 MHz backplane clock and the PXI Express 100 MHz differential clock (please see Figure 4.3) have a fixed phase relationship as described in [125].

Thus, a Phase-Locked Loop (PLL) of the FPGA clock to the PXI 10 MHz backplane clock automatically creates a fixed phase relationship to the PXI Express 100 MHz differential clock. The PXI 10 MHz backplane clock could be used as a base

level onboard clock with the FPGAs. This is analogous to deriving a 10 MHz clock from the 40 MHz onboard oscillators [125].

4.1.4 PWM Modulator Algorithm

Figure 4.7 shows the main flowchart of the PWM modulator. For better visualization, we divide all operations into three (III) parts. In part I, the customer or a designer may set the main user parameters f_0 and D of the PWM signal. Then, the program calculates the required number of clock cycles for the period (N) and the duration of high state (N_d) according to the equations (4.1) and (4.2).

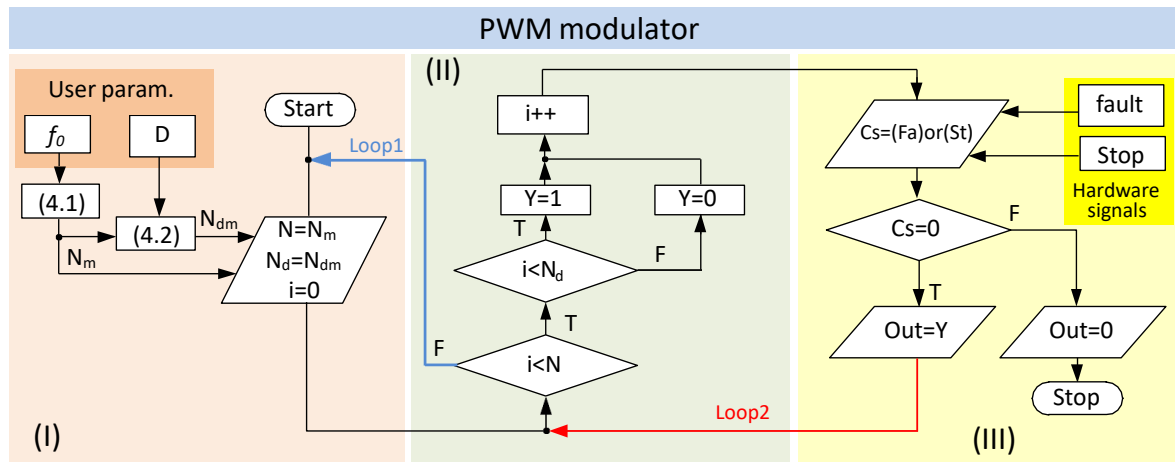


Figure 4.7: The main flowchart of the PWM modulator, providing parameters (I), counter ramp (II), and generation of output signal (III).

$$N = f_{FPGA} / (f_0 \cdot SC_{TL}), \quad (4.1)$$

$$N_d = D \cdot N, \quad (4.2)$$

where f_{FPGA} - onboard available clock frequency, f_0 - fundamental switching frequency, and SC_{TL} - single cycle timed loop (in clock cycles).

The index m (in Figure 4.7 - part I) means that the N_{dm} and N_m value is taken and recalculated for the m 'th PWM period. The presented modulator can, therefore, cooperate with an external voltage control system and dynamically change the factor D . The duration of the period, represented by N_m , may be constant for DetM or may be changed randomly for RanM case.

Part II of Figure 4.7 illustrated the iteration counter represented by the variable i (previously discussed in Figure 2.1). Parameters N and N_d are compared with the variable i to determine the value of output signal Y and control the loop I execution.

Also, Part III of Figure 4.7 presents the generation of control (output) signal and the interaction of the PWM modulator with a C_s function. In the presence of hardware signals of fault (Fa) and the stop button (St), the function C_s returns 1, and the PWM modulator operation is interrupted. The Fa signal is typically generated by DC/DC converter hardware in any emergency, while the St is from the customer or a designer. Figure 4.8 shows the PWM modulator operation based on FPGA.

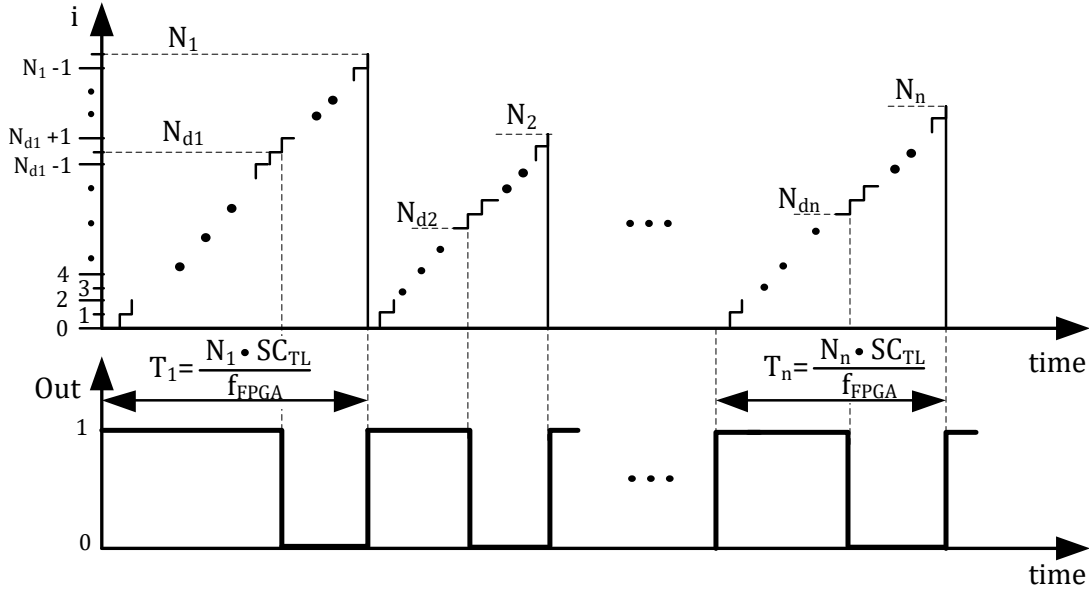


Figure 4.8: The principle of PWM modulator operation based on FPGA.

On the other hand, it is noteworthy that the PWM modulator presented in Figure 4.8 does not enable the control of the switching rate of change (concept presented in the subsection 2.1, discussed in Figure 2.1). The FPGA implementation of the switching rate of change control is presented in the subsection 4.2.6.

4.1.5 Random Number Generator

The random number generator is crucial to the operation of RanM control algorithms. We assume to generate the random stream based on a Linear Congruential Generator (LCG). The LCG is a modular arithmetic algorithm, which provides a RSN calculated with a discontinuous linear equation (4.3).

$$RN_m = (\alpha \cdot RN_{m-1} + c) \bmod n, \quad (4.3)$$

where RN_m - the m 'th random number provided by LCG, α , c , n - LCG coefficients.

The values of coefficients configured for the FPGA PXI-7854R implementation were $\alpha = 17$ and $RN_0 = 17$, $c = 0$, and $n = 2^{32}$. The modulo operation is made automatically due to the use of long integer variables with 32 bits of storage. For RanM, the generation of RSN is done in a loop to get a new pseudo-random number for each PWM signal period. The presented LCG generates pseudo-random numbers with a period of 2^{31} and a normal distribution. To show the property of a RSN, Figure 4.9 shows the 10,000 numbers RN_m generated by LCG and their histogram/distribution.

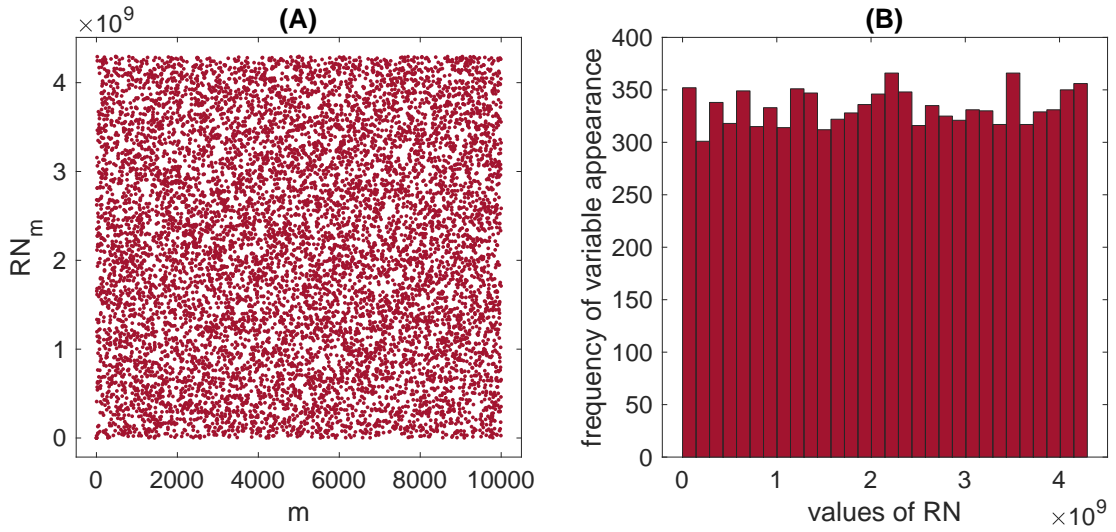


Figure 4.9: RN_m distribution (A) and histogram (B).

4.2 Several FPGA-based RanM approaches

The subsections presented in section 4.1 reinforce how CPS might increase the reliability and robustness of the PWM control algorithms. Especially, since it becomes possible to establish the data transfers between the control hardware and the IDE (see subsection 4.1.1). Through the HLS programming approach, it is possible to develop precise and unrestricted PWM control algorithms in the IDE and then control the physical process that interfacing the control hardware.

Therefore, the next parts of this section 4.2² demonstrate how to provide an LabVIEW FPGA-based control system for a DC/DC converter that randomize the harmonics components, hence, spread the level of conducted EMI. The presented PWM control algorithms are not proposed to change the essential functions or parameters of the DC/DC converter. Moreover, during the design of PWM control algorithms, we take into account the PDF of frequency changes.

²Parts of this section 4.2 are published in [43] and [65] respectively.

In addition, we propose four methods of distribution the PDF in FPGA without arithmetic division and using fixed point operations, presented in the subsections 4.2.1, 4.2.2, 4.2.3, and 4.2.4. The FPGA implementation is presented in subsection 4.2.5. Furthermore, considering the hardware resources presented in subsection 4.1.1, the FPGA implementation of the switching rate of change control is presented in the subsection 4.2.6. Finally, the last RanM proposal is presented in subsection 4.2.7, considering the ability to shaping the PDF, hence, the EMI noise shape.

4.2.1 Single Randomization

Traditionally, during LabVIEW FPGA programming, we use modules with palettes of structures and functions. The number of such functions in LabVIEW FPGA Module is much smaller than for typical control devices with a microprocessor. Furthermore, available functions can only operate on integer variables. Despite this drawback, the LabVIEW FPGA program implementation allows full control of the PWM modulator execution and high speed calculation (see Figure 4.8). For instance, the LabVIEW FPGA Module has access to Single-Cycle Timed Loops (SCTL).

The SCTL is a unique loop structure that executes all functions inside within one fixed time period (SCTL). The SCTL may be defined by the customer or a designer as a time period or in cycles of the FPGA clock. In the FPGA PXI-7854R used, see section 4.1.3, the maximum clock frequency is 40 MHz.

To illustrate the execution of the proposed PWM modulator algorithm from Figure 4.7. Figure 4.10 presents the generation of a PWM signal with digital levels 1 and 0, considering $D=50\%$ and $f_0 = 80$ kHz. For further information about the MATLAB script, hence, the While and For Loops implementation, please see B.3.

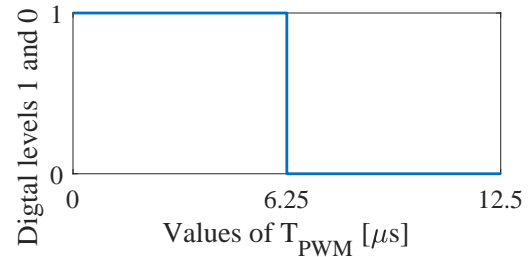


Figure 4.10: PWM signal based on Figure 4.7.

To execute the PWM modulator algorithm from Figure 4.7 in LabVIEW FPGA, the While Loop structure with a sub-system For Loop was chosen. The For Loop corresponds to the Loop2 in Figure 4.7 and is executed N times. The While Loop corresponds to the Loop1 in Figure 4.7. The While Loop is performed until the C_s function is activated.

Conveniently, for DetM we consider the $SC_{TL} = 1$ cycle, and the number $N = N_m$ is constant. For RanM the number N_m is randomly changed for each PWM period using the RSN provided by the LCG (see section 4.1.5). However, due to

the use of fixed-point operations in FPGA PXI-7854R, the resulting RSN must be scaled (reduction of bit precision) to make it suitable for N_m calculation. Figure 4.11 illustrates in the part I how to scale the RN_m using the Reshaped Array Function (R_{AF}) which is available in the LabVIEW environment.

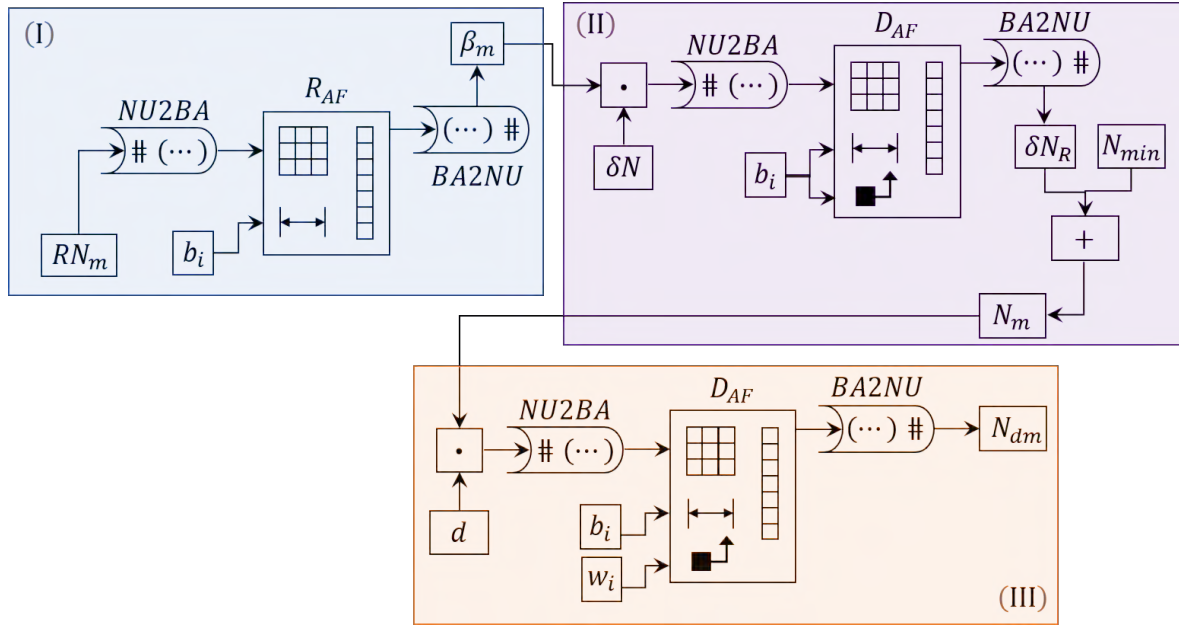


Figure 4.11: The scheme of the RN_m scaling process, led to lower bit precision (I), and for calculating the RSN of N_m (II) and N_{dm} (III).

Figure 4.11 shows in part I the parameter b_i , which is responsible for providing the length of the output array and must be numeric³. Before resizing, the number RN_m is converted to a Boolean Array by the $NU2BA$ function. After resizing, the Boolean Array is converted to a number again by the $BA2NU$ function. As a result, a RSN, β_m from 0 to $2^{b_i} - 1$ is obtained.

The next task is to calculate N_m and N_{dm} (from Figure 4.7), to change randomly according to β_m number for each PWM period. The changes of the N_m and N_{dm} should also take place within the assumed range from the N maximum and minimum values. These operations should be performed with the appropriate precision in fixed-point arithmetic. However, LabVIEW FPGA module does not allow direct actions of the mathematical division. The solution to the stated problem for N_m calculation is shown in part II of the Figure 4.11. The δ_N describes the maximum

³The LabVIEW FPGA design process considers unsigned integer 32 bits as the data type. An unsigned integer is a 32-bit data that encodes a nonnegative integer in the range [0 to 4,294,967,295]. The number 4,294,967,295, equivalent to the hexadecimal value FFFF, FFFF₁₆, is the maximum value for a 32-bit unsigned integer in computing.

assumed changes in the PWM period and may be calculated as:

$$\delta_N = N_{max} - N_{min} + 1. \quad (4.4)$$

The δ_N can be also represented relative to the average value of N , e.g. $\delta_N = 50\% \cdot N_{AV} + 1$. Thus, the first interaction illustrated in Figure 4.11, part II, consider the multiplication of the β_m by δ_N . Since a divide operation is not available, the Delete from Array Function (D_{AF}) is applied to provide δ_{NR} , a RSN that corresponds to the range between the 0 and the value of $\delta_N - 1$. In this step, the N_m value is calculated using (4.5). The final expression for calculating N_m according to the concept from Figure 4.11, part II, is presented in (4.6).

$$\delta_{NR} = ((RN_m \gg (32 - b_i)) \cdot \delta_N) \gg b_i, \quad (4.5)$$

$$N_m = \delta_{NR} + N_{min}. \quad (4.6)$$

Although equation (4.6) accurately describes random changes in the N value (which corresponds to the PWM period - T_{PWM}), it does not provide information on the average value. Therefore, next in this subsection 4.2.1, discussing RanM properties, we will give the average value of N (N_{AV}), and δ_N , thus the variation range of N is equal to $N_{AV} \pm \delta_N/2$. Choosing the right δ_N is not apparent and will be a subject of a broader analysis in subsection 4.2.7. However, we will show in this subsection 4.2.1 the basic challenges that face when choosing parameters for RanM.

We can take δ_N value based on expected frequency randomization. For instance, if we assume that $f_0 = 80$ kHz and this frequency may change $\pm 50\%$, we will obtain $\max(f_0) = 80 \text{ kHz} + 50\% = 120 \text{ kHz}$, $\min(f_0) = 80 \text{ kHz} - 50\% = 40 \text{ kHz}$. The N_{min} value will be related to 120 kHz and N_{max} to 40 kHz (based on expression (4.1)), so $\delta_N = 1000 - 333 + 1 = 668$. However, the value of $N_{AV} = 667$ does not correspond to a frequency of 80 kHz. Figure 4.12 shows the histogram of randomized N_m values and the histogram of randomized frequencies f_0 related to N_m , for $N_{AV} = 667$ with $\delta_N = 668$.

Figure 4.12-B shows that f_0 varies within the assumed range from 40 to 120 kHz. Despite this, the frequency distribution is not uniform and the average frequency is not equal to 80 kHz. Adopting the δ_N in such a way is therefore not particularly useful. Another possible approach to selecting δ_N value may be made based on a relative change in time. Figure 4.13 shows the histogram of N_m values and histogram of f_0 , for $N_{AV}=500$ (value related to $f_0 = 80$ kHz) with $\delta_N = 331$ so $N \in \langle N_{AV} \pm 33\% \rangle$. In such a case the average value of the frequency is closer to that intended, but the frequency distribution is still strongly non-linear.

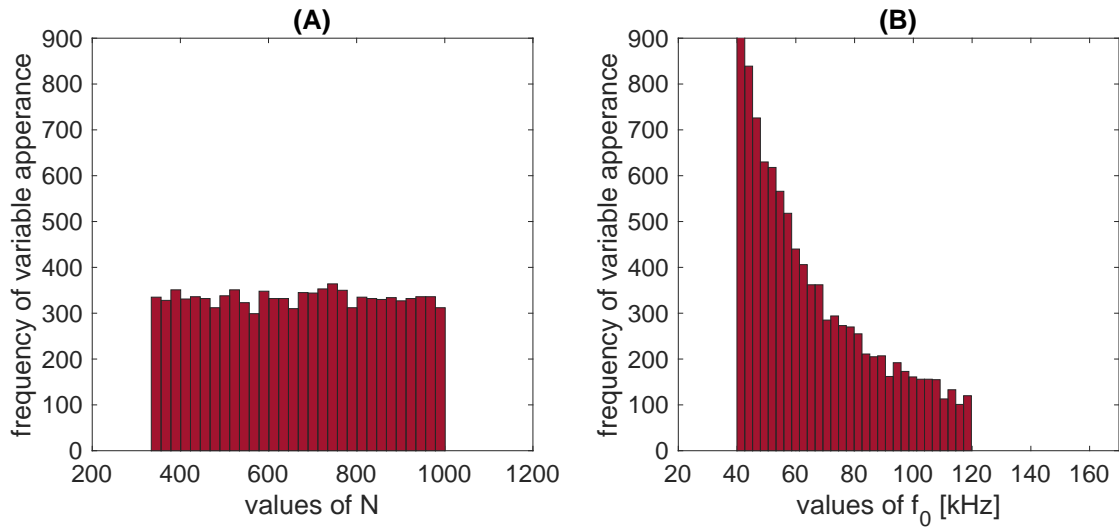


Figure 4.12: Histogram of N_m ticks distribution (A) and histogram of frequency distribution (B), for $N_{AV} = 667$ and $\delta_N = 668$.

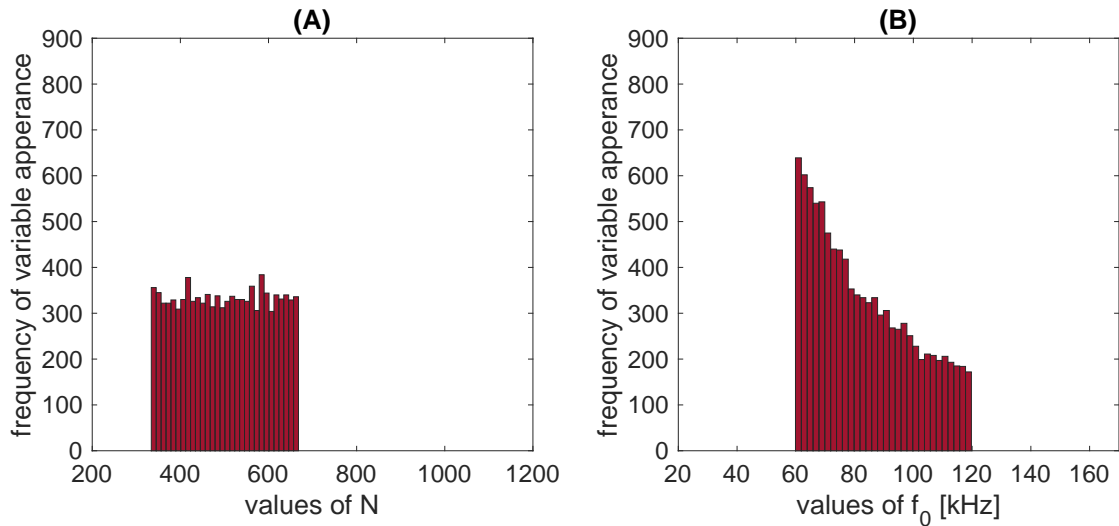


Figure 4.13: Histogram of N_m ticks distribution (A) and histogram of frequency distribution (B), for $N_{AV} = 500$ and $\delta_N = 331$.

On the other hand, the parameter b_i is considered in (4.5) as a numeric value for providing the dimension size (length an index) of D_{AF} . However, for D_{AF} function, it is possible to set up different parameters for the length and index of the array. Figure 4.11 shows in part III the D_{AF} function with consideration of the set up of length and index of array, to provide calculation of N_{dm} . We assumed that the coefficient d , represented as an 8 bit integer will be proportional to duty cycle factor D . The FPGA implementation considers the index value (w_i) equal to 8, and the b_i equal to 23. Thus, the final value of N_{dm} is configurable, maintaining the proportionality with

N_m , within a range defined by d , as follows (4.7).

$$N_{dm} = D \cdot N_m = ((d \cdot N_m) >> w_i) \approx \frac{d \cdot N_m}{2^{w_i}}. \quad (4.7)$$

To calculate the period of PWM signal and its D for RanM, we use (4.6) and (4.7) respectively. These equations are computed in the fixed cycle of a one loop execution - SCTL. However, as presented in the next subsection 4.2.2, we may consider the situation, in which the SCTL is also changed randomly (RSC_{TL}).

4.2.2 RanM with RSCTL—Additional Randomization

When we randomly change both the number of periods of the For Loop - N_m (concept illustrated at Figure 4.8), and the duration of this loop - SC_{TL} , we can talk about an additional randomization (RanM with RSC_{TL}). Basically, for RSC_{TL} generation, we assume the same principle, as illustrated in Figure 4.11, part I and part II, however instead of $SC_{TL} = 1$ cycle we generate random value from 7 to 13. The m 'th PWM period T_{PWMm} is equal to $(N_m \cdot SC_{TLm})/f_{FPGA}$. Figure 4.14 shows the histogram of the T_{PWMm} and histogram of related f_0 , for $N = 50$, $\delta_N = 34$, and $RSC_{TL} \in \langle 7, 13 \rangle$.

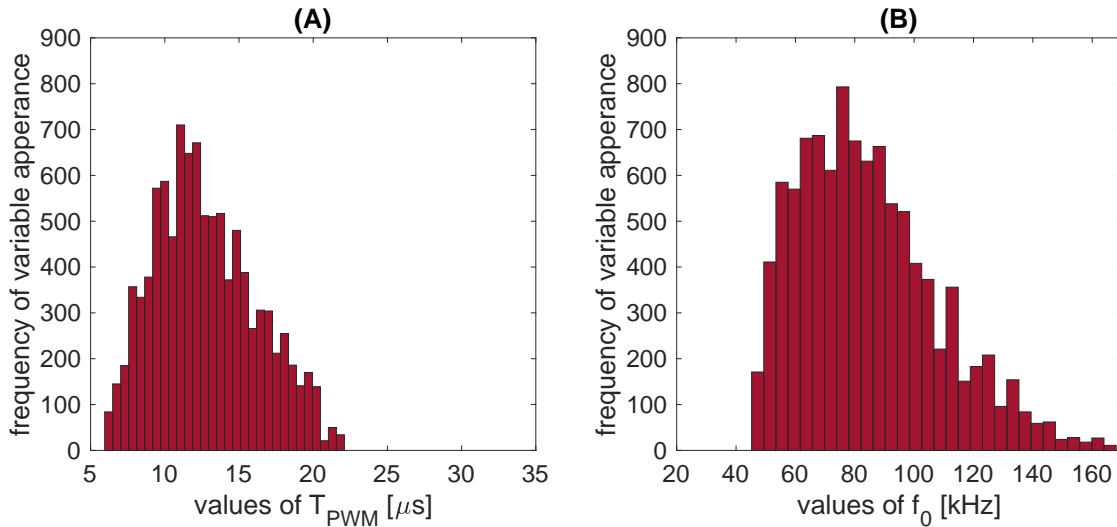


Figure 4.14: Histogram of T_{PWMm} distribution (A) and histogram of frequency distribution (B), for $N_{AV} = 50$ with $\delta_N = 34$, and $RSC_{TL} \in \langle 7, 13 \rangle$.

Figure 4.14 shows that when we consider N_m and RSC_{TL} , the density distribution in both cases, (A) and (B), is changed. Thus, this approach of N_m and RSC_{TL} randomization gives us the possibility of shaping the density distribution of the RSN used by the RanM. The frequency distribution is closer to the Gaussian distribution⁴,

⁴Normal distribution, also known as the Gaussian distribution, is a symmetric probability distribu-

which should be more favourable in terms of the average frequency and converter losses. In the case of Figure 4.14, the expected average is for $f_0 = 80$ kHz and $T_{PWMm} = 12.5 \mu s$.

The shape of the density distribution of the RSN used by the RanM can be changed by assuming a range of different numbers or different types of numbers, e.g. integers and primes, for RSC_{TL} . However, the elementary number theory⁵ is not an investigation target of this thesis. Therefore, the conditional of $RSC_{TL} \in \langle 7, 13 \rangle$ will be considered as standard.

4.2.3 RanM2—Split Distribution of Variable

The other method to shape the T_{PWMm} and f_0 distributions is to split the N_m distribution to a few sub-ranges into the entire N_m range. For the presented LabVIEW FPGA implementation, we propose to use two predefined RSN as the sub-ranges into the entire N_m range.

The RSN generation follows the presented at Figure 4.11 - part I. Then we consider using 1 bit, digital levels 1 and 0, to choose between the sub-ranges of N_m . The FPGA implementation is executed with a selection function (SF), which is available in the LabVIEW environment. The parameter S determines whether the SF returns the value wired to true (T) or false (F).

Thus, we assign one of the predefined RSN for each parameter, F or T. Figure 4.15 illustrating the proposed LabVIEW FPGA implementation, denoted as RanM2, and based on the Figure 4.11.

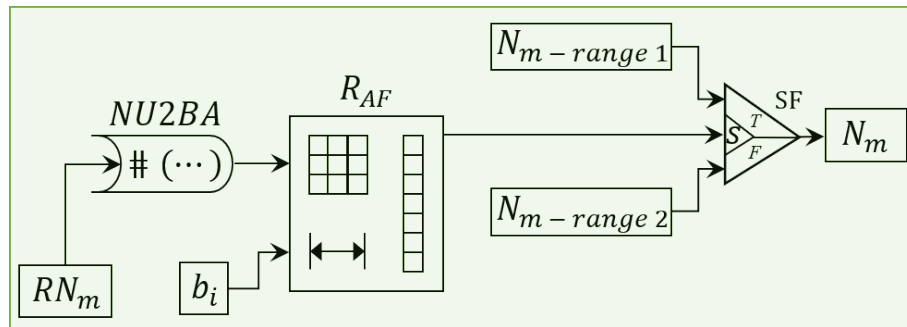


Figure 4.15: Illustration of N_m generation by the RanM2 proposal.

The Figure 4.16 shows the histograms of N_m values and their corresponding f_0 values, for $N_{AV1} = 750$ with $\delta_{N1} = 500$ and $N_{AV2} = 416$ with $\delta_{N2} = 167$ (The same randomization approach assumed in the subsection 4.2.1).

tion about the mean, showing that data near the mean are more frequent in occurrence than data far from the mean. In graph form, the normal distribution will appear as a bell curve.

⁵Elementary number theory is the branch of number theory in which elementary methods (i.e., arithmetic, geometry, and algebra) are used to solve equations with integer or rational solutions.

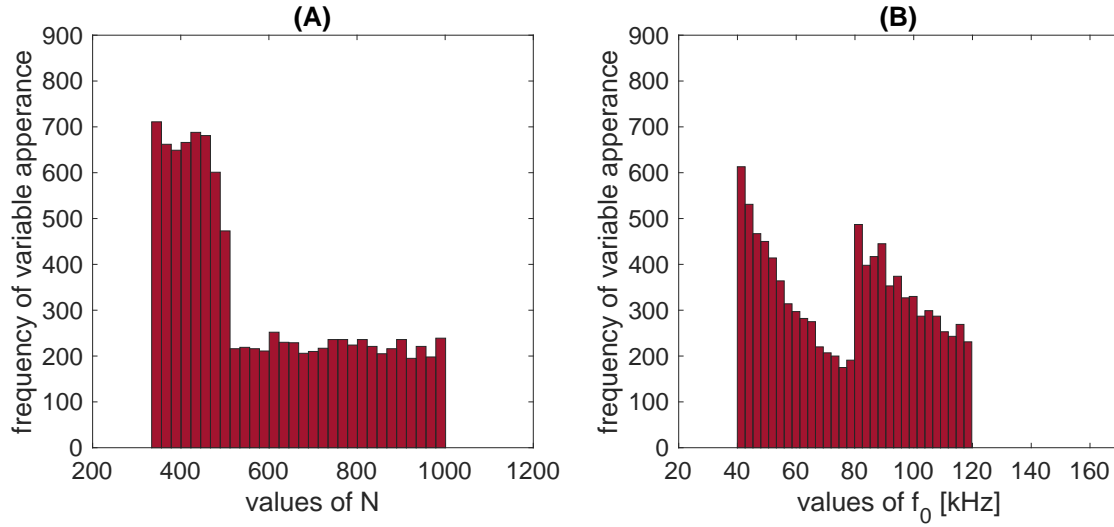


Figure 4.16: Histogram of N_m ticks distribution (A) and histogram of frequency distribution (B), for RanM2 with parameters: $N_{AV1} = 750$ with $\delta_{N1} = 500$ and $N_{AV2} = 416$ with $\delta_{N2} = 167$.

As one can see in the case of Figure 4.16, the use of two density distributions for a PWM period (which is proportional to N_m) produces an equal alignment of the frequency distribution.

Therefore, in such a manner, there is a possibility to control the shaping of frequency, i.e., preventing the occurrence of frequencies (EMI noise) in certain parts of the frequency spectrum.

4.2.4 RanM2 with RSCTL

The presented concept in subsection 4.2.3 may be linked with the concept of additional randomization RSC_{TL} presented in subsection 4.2.2. Figure 4.17 considers such a case with $RSC_{TL} \in \langle 7, 13 \rangle$ and for $N_{AV1} = 75$ with $\delta_{N1} = 50$ and $N_{AV2} = 42$ with $\delta_{N2} = 17$.

The obtained histograms of Figure 4.17 are more smooth than histograms in Figure 4.16, which can be an advantage. However, the use of RSC_{TL} increases the frequency spread, e.g., whether we compare Figure 4.17 with Figure 4.14.

Through the adoption of the RanM2 with RSC_{TL} , the T_{PWMm} changes randomly depending on the random variables N_m and RSC_{TL} . Assuming that these variables (N_m and RSC_{TL}) have uniform distributions, i.e.: $N_m \sim \cup(N_{min}, N_{max})$, $RSC_{TL} \sim \cup(RSC_{TLmin}, RSC_{TLmax})$, and $RSC_{TLmin}, N_{min} > 0$. With the simplifying assumption $N_{min} \cdot RSC_{TLmax} < N_{max} \cdot RSC_{TLmin}$, then the $T_{PWMm} = N_m \cdot RSC_{TL}$, has a probability

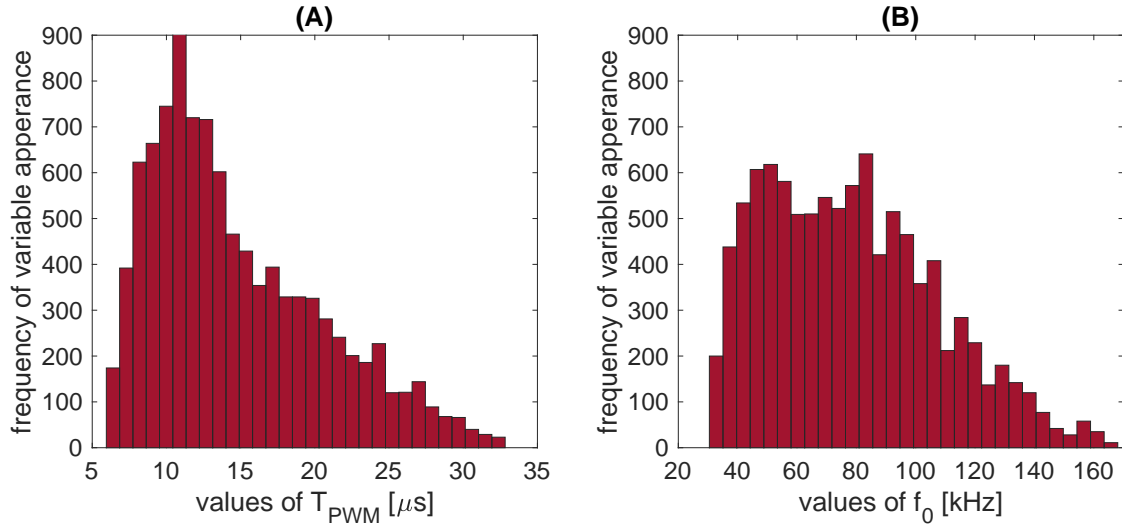


Figure 4.17: Histogram of T_{PWMm} ticks distribution (A) and histogram of frequency distribution (B), for RanM2 with RSC_{TL} based on the parameters: $RSC_{TL} \in \langle 7, 13 \rangle$, $N_{AV1} = 75$, $\delta_{N1} = 50$, $N_{AV2} = 42$, and $\delta_{N2} = 17$.

density distribution (D_{TPWM}):

$$D_{TPWM} = \frac{1}{(N_{max} - N_{min})(RSC_{TLmax} - RSC_{TLmin})} \cdot \begin{cases} 0 \equiv T_{PWMm} < N_{min} \cdot RSC_{TLmin}, \\ \ln \left(\frac{T_{PWMm}}{N_{min} \cdot RSC_{TLmin}} \right) \equiv N_{min} \cdot RSC_{TLmin} < T_{PWMm} < N_{min} \cdot RSC_{TLmax}, \\ \ln \left(\frac{RSC_{TLmax}}{RSC_{TLmin}} \right) \equiv N_{min} \cdot RSC_{TLmax} < T_{PWMm} < N_{max} \cdot RSC_{TLmin}, \\ \ln \left(\frac{N_{max} \cdot RSC_{TLmax}}{T_{PWMm} \cdot N_{min} \cdot RSC_{TLmin}} \right) \equiv N_{max} \cdot RSC_{TLmin} < T_{PWMm} < N_{max} \cdot RSC_{TLmax}, \\ 0 \equiv T_{PWMm} > N_{max} \cdot RSC_{TLmax}. \end{cases} \quad (4.8)$$

Although the presented equation (4.8) seems complicated, it presents a probability distribution resembling a trapezoid, which makes it more similar to the Gaussian distribution. It should be noted that such a distribution is obtained by a simple operation, which is easy to implement in FPGA without arithmetic division and using fixed point operations.

4.2.5 FPGA PXI-7854R Implementation

Figure 4.18 shows the LabVIEW general program implemented in FPGA PXI-7854R. This FPGA PXI-7854R implementation includes the strategies described in the sections 4.2.1, 4.2.2, 4.2.3, and 4.2.4. In Figure 4.18, the parts corresponding to (I)

and (II) refer to the basic PWM modulator configuration (Figure 4.7). Therefore, it is applicable to both DetM and RanM.

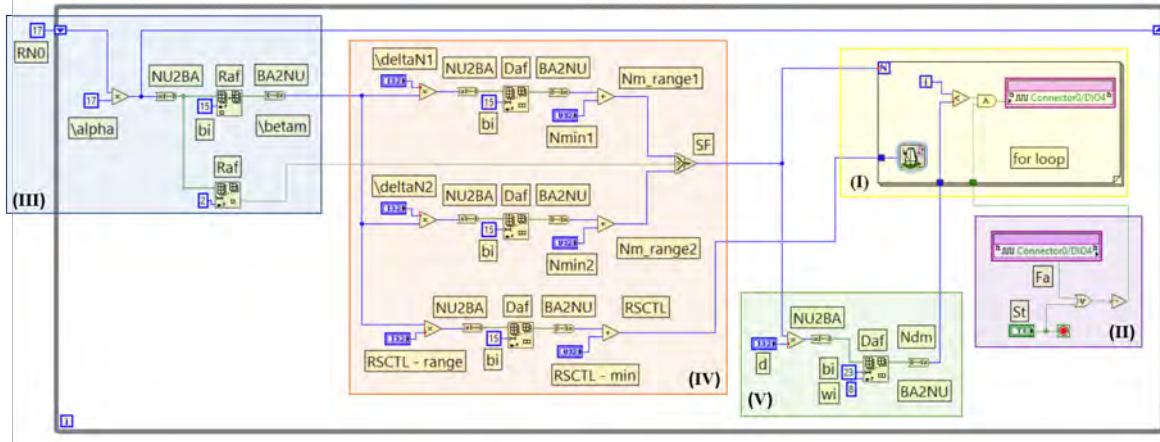


Figure 4.18: LabVIEW implementation in FPGA PXI-7854R. For loop (counter ramp) and output signal generation (I), conditions for stopping the program (II), pseudorandom number generator (III), N_m , SC_{TL} and RSC_{TL} calculation (IV), and N_{dm} calculation (V).

Part (III) of Figure 4.18 presents the RSN generator with a number scaling block, corresponding to part I of Figure 4.11 and is used only for RanM, for all the approaches of randomization presented in the sections 4.2.1, 4.2.2, 4.2.3, and 4.2.4. Parts (IV) and (V) of the Figure 4.18 correspond to part II and part III of Figure 4.11, respectively. Since the FPGA needs to execute predefined RSN (the concept of RanM2 - Split Distribution of Variable, see subsection 4.2.3 and RanM2 with RSC_{TL} , see subsection 4.2.4), the D_{AF} function proportionally increases as illustrated in Figure 4.18 - part (IV).

4.2.6 RanM3—Controlling the Switching Rate of Change

Based on the presented in subsections 4.2.1, 4.2.2, 4.2.3, 4.2.4 and 4.2.5. It's observed that although the FPGA PXI-7854R enables the options for the building of PWM hardware circuits, the FPGA-based coding must overcome hurdles such as fixed-point operations, matching the range of the fixed-point numbers, and limitations in arithmetic operations [65]. Furthermore, as an FPGA-based system is chosen, certain limits are imposed in terms of the amount of memory, DSP slices, and Look up Table (LUT)s. That is evidence of how the controller hardware features influence coding the pseudo-random algorithm, regardless of the RanM approach used [11].

Nevertheless, through the CPS concept described in section 4.1, it becomes possible to consider the hardware and software resources of the IDE NI PXIe-8135,

as well as of the FPGA PXI-7854R. Thus, by means of the transfer of data to the IDE, it is possible to develop precise and unrestricted PWM control algorithms.

Therefore, to implement the concept of controlling the switching rate of change, as previously described in subsection 2.1. Figure 4.19 presents a LabVIEW implementation in IDE NI PXIe-8135 embedded controller, denoted as RanM3.

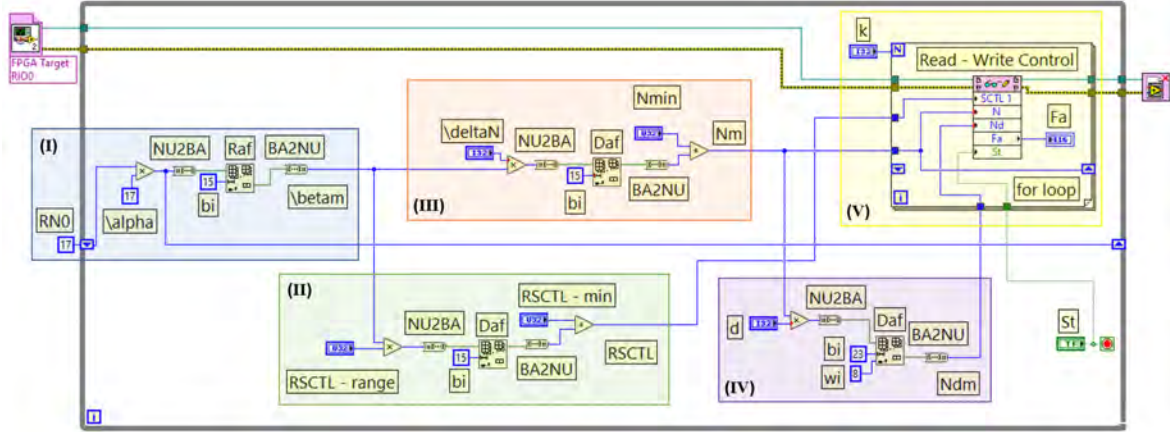


Figure 4.19: LabVIEW implementation in IDE NI PXIe-8135 - RanM3. Pseudorandom number generator (I), RSC_{TL} calculation (II), N_m calculation (III), N_{dm} calculation (IV), and the for loop structure responsible for reading or writing values to the PWM modulator into the FPGA PXI-7854R target (V).

As mentioned in subsection 2.1, the index of sum k represented in (2.1) enables the control of the switching rate of change. Hence, the entire process related to the RanM3 strictly depends on the execution of an additional For loop structure, with the index k , represented by Figure 4.19-V.

Thus, to establish the bespoke interface between the control hardware FPGA PXI-7854R and the IDE NI PXIe-8135. The RSN generated in the IDE NI PXIe-8135 are transferred to the FPGA PXI-7854R through the *Read - Write Control* command (illustrated in Figure 4.19-V inside the For loop structure).

The *Read - Write Control* command can read or write multiple controls and indicators through IDE NI PXIe-8135. As default, the FPGA PXI-7854R implementation presented in subsection 4.2.5, provides the parameters N , N_d , SC_{TL} , and S_t to be manipulated in the IDE NI PXIe-8135 (the basic PWM modulator configuration, see Figure 4.7). The parameter F_a is made available only as an indicator. Therefore, the IDE NI PXIe-8135 needs to provide and manipulate the random parameters N_m , N_{dm} and RSC_{TL} , addressing the calculations to the PWM modulator of the FPGA PXI-7854R (see Figure 4.8).

Once included in the For loop structure (Figure 4.19-V), the *Read - Write Control* command time of execution becomes dependent on the magnitude of the k index

value. In other words, the T_{PWMm} time of execution becomes dependent on the magnitude of the k value. This being a fundamental condition to implement the concept of controlling the switching rate of change (see Figure 2.2). Since in the case of Figure 4.19-V, the *Read - Write Control* command is dedicated to operating the PWM modulator (see Figure 4.8).

Furthermore, the RanM3 implementation is only possible because each environment considers one iteration count (i). As illustrated in Figure 4.20, the i_{IDE} is first evaluated by the IDE NI PXIe-8135 controlled by k (Figure 4.20-part I), and secondly the i_{FPGA} is evaluated by the FPGA PXI-7854R controlled by N (Figure 4.20-parts II and III). In both cases, k and N are the required number of clock cycles for the period, i.e., T_{PWMm} in case of N , and T_{PWMm} time of execution in case of k .

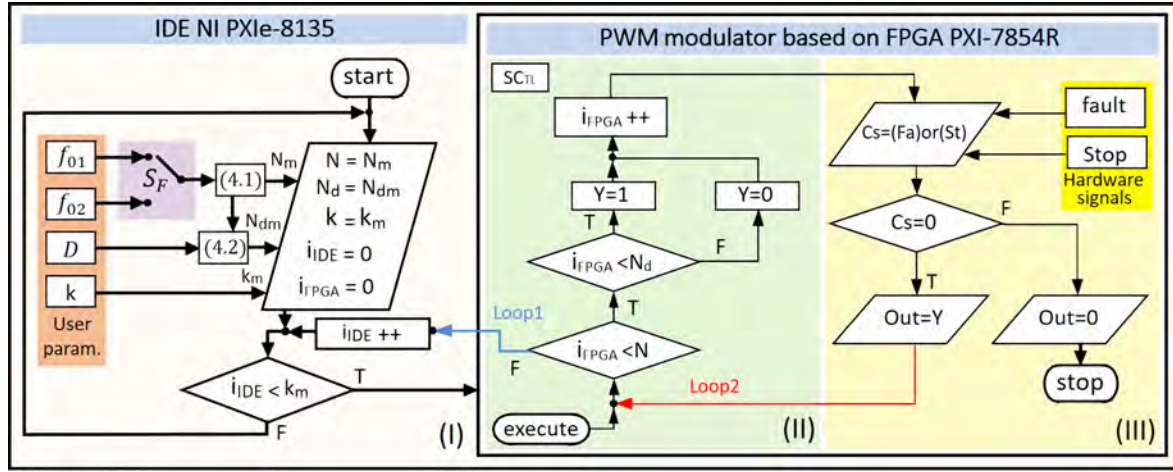


Figure 4.20: RanM3 execution flow.

Figure 4.20-parts II and III, show that the execution of the PWM modulator based on FPGA PXI-7854R remains the same, as previously defined in Figure 4.7. Figure 4.20-part I illustrate the transfer of data between the FPGA PXI-7854R and the IDE NI PXIe-8135, highlighting how the T_{PWMm} time of execution becomes dependent on the magnitude of the k value. The index m associated with the variable k means that the km value is taken and recalculated for each T_{PWMm} time of execution (see MATLAB simulation presented in Figure 2.3, Figure 2.4 and Figure 2.5).

4.2.7 Shaping the RanM3

This subsection 4.2.7 presents a method that also split the distribution of N_m to sub-ranges, as previously presented in subsection 4.2.3. The central approach is the strategic increase of the N_m calculation blocks, as illustrated in Figure 4.15. Each new sub-range of N_m calculation block starts to consider a specific and different range of the entire sequence of N_m .

However, contrary to what is presented in the subsection 4.2.3, the method proposed in this subsection 4.2.7 is based on the RanM3 implementation (see subsection 4.2.6). Thus, the entire calculation is performed by the IDE NI PXIe-8135, which provides the possibility to manipulate the variable δ_N within a range from 10% to 50%. Consequently generating a "gap" between the sub-ranges of N_m defined. Evidently, assuming the design of sub-ranges of N_m , where each sub-range considers $\delta_N > 50\%$, is not recommended due to the phenomenon of overlap with the multiple harmonics components [65].

Furthermore, it is noteworthy that the RanM3 (see subsection 4.2.6) consider the $RSC_{TL} \in \langle 7, 13 \rangle$. Thus, it is essential to pay attention to the fact that even considering a short RSN, e.g. $\delta_N < 10\%$ (remembering that $N_{AV} \pm \delta_N/2$, see subsection 4.2.1), the RSN attributed to N_m and N_{dm} will have their frequency spread increased (see subsection 4.2.4).

Therefore, the question arises as to which part of the frequency spectrum needs to get rid of EMI noise, i.e., make use of the "gap." Considering the central motivation of this thesis (see section 1.1), which is related to the low frequency range, a potential case is the PLC system. For instance, considering that some technologies of the PLC system, such as G3-PLC protocol, operate with frequencies from 35 kHz to 95 kHz, and are highly sensitive to EMI noise around 60 kHz [52], [129].

Assuming 60 kHz as the frequency to avoid, i.e., where it is necessary to provide the "gap" in the frequency spectrum. Then, the next step with shaping the RanM3 is to define the % to be considered by the variable δ_N . This concept is illustrated in Figure 4.20-part I as the use of the selection function (S_F) between two central frequencies. Thus, Figure 4.21, Figure 4.22, Figure 4.23, Figure 4.24 and Figure 4.25, presents a MATLAB simulation considering the concept of $N_{AV} \pm \delta_N/2$, and respectively each of these figures considers a % of δ_N within a range from 10% to 50%. Also, each figure, from Figure 4.21 to Figure 4.25, considered the $N_m - range1$ calculation block equal to $f_0 = 95$ kHz, and the $N_m - range2$ calculation block equal to $f_0 = 35$ kHz. For further information about the MATLAB script, please see B.6.

From Figure 4.21 to Figure 4.25 is exemplified the relationship between δ_N and sub-ranges for N_m , assuming one frequency to avoid, in that case 60 kHz. It is noteworthy that the choice of sub-ranges for N_m and the % of δ_N depend on the expected EMI noise shape, i.e., EMC compliance. Obviously, there is a drawback to considering sub-ranges for N_m from the power electronic converter point of view. Since obtaining a single frequency becomes unlikely. However, the adoption of an approach that shapes the RanM3 is not critical to the execution of any PWM algorithm. This is an additional feature that shows how the EMC-test bench system, primarily controlled by a CPS, can be considered a reliable and "EMC-friendly" controller.

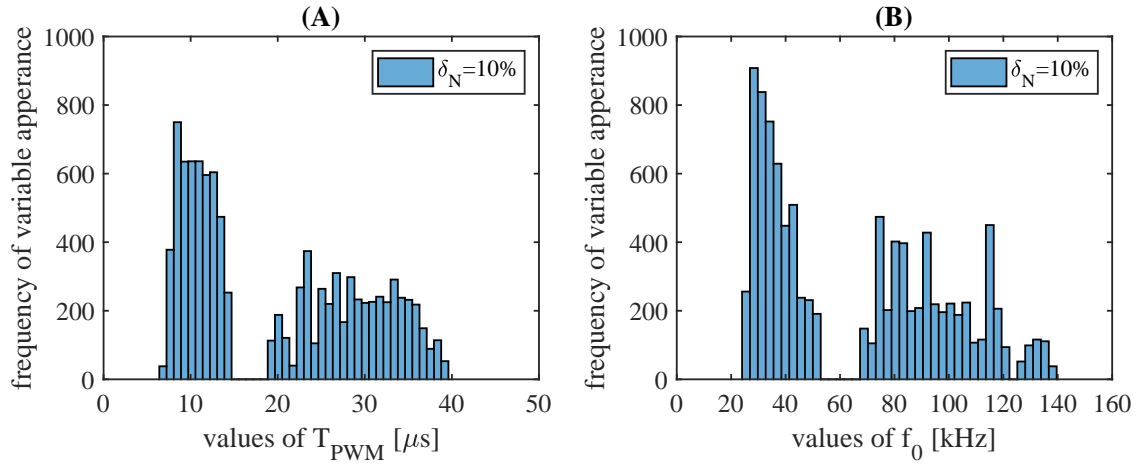


Figure 4.21: Histogram of T_{PWMm} ticks distribution (A) and histogram of frequency distribution (B), for shaping the RanM3 and considering $\delta_N = 10\%$.

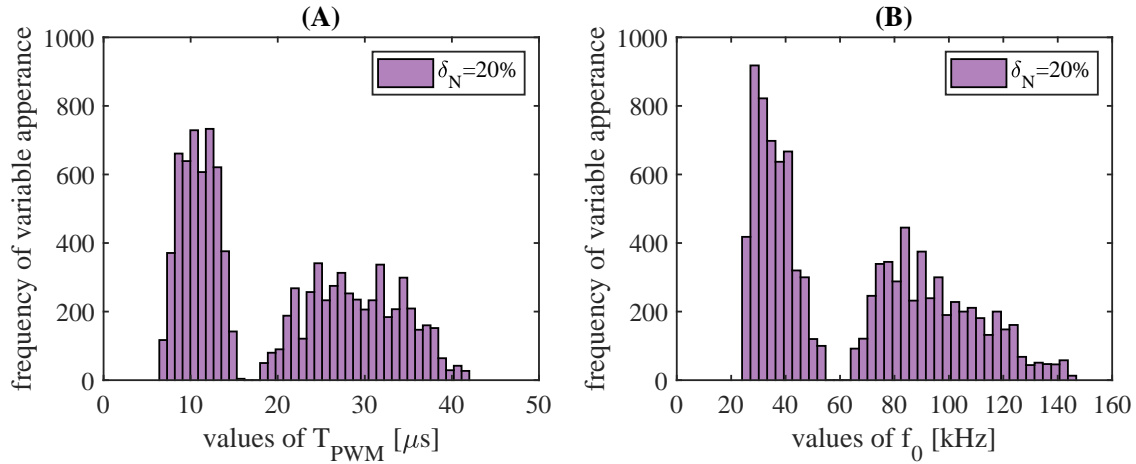


Figure 4.22: Histogram of T_{PWMm} ticks distribution (A) and histogram of frequency distribution (B), for shaping the RanM3 and considering $\delta_N = 20\%$.

4.3 Summary

In this chapter 4, the subsections 4.1.1 and 4.1.3 presented all the hardware and resource details of the IDE NI PXIe-8135, as well as of the FPGA PXI-7854R. Beyond the knowledge base relating to the LabVIEW projects presented in the subsection 4.1.2. The proposed PWM modulator algorithm was presented in the subsection 4.1.4 and the Random Number Generator presented in the subsection 4.1.5.

Since there are some FPGA software limitations (fixed-point operation, and a lack of basic arithmetic functions), it may become challenging to develop the RanM and the DetM implementation. Therefore, a part of the section 4.2 was dedicated to demonstrating how to provide a LabVIEW FPGA-based control system for a DC/DC

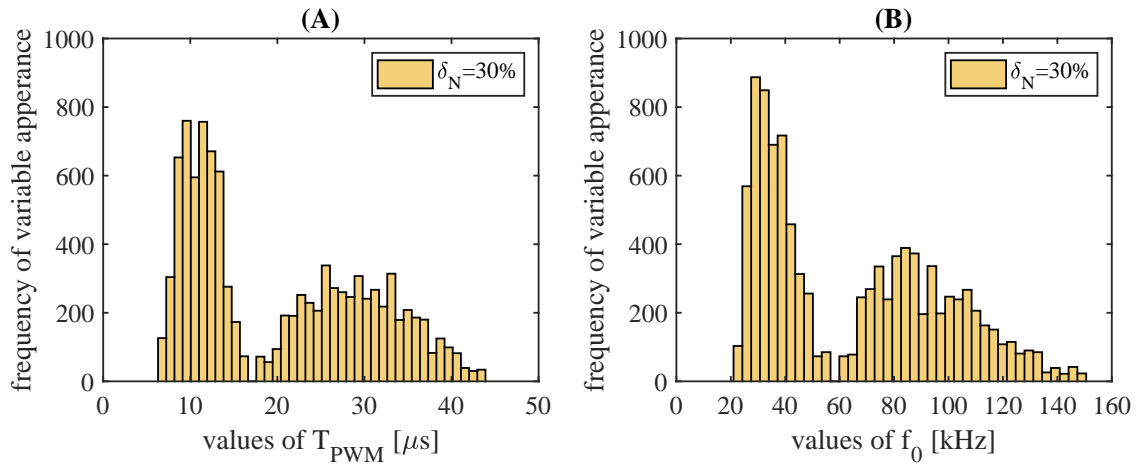


Figure 4.23: Histogram of T_{PWMm} ticks distribution (A) and histogram of frequency distribution (B), for shaping the RanM3 and considering $\delta_N = 30\%$.

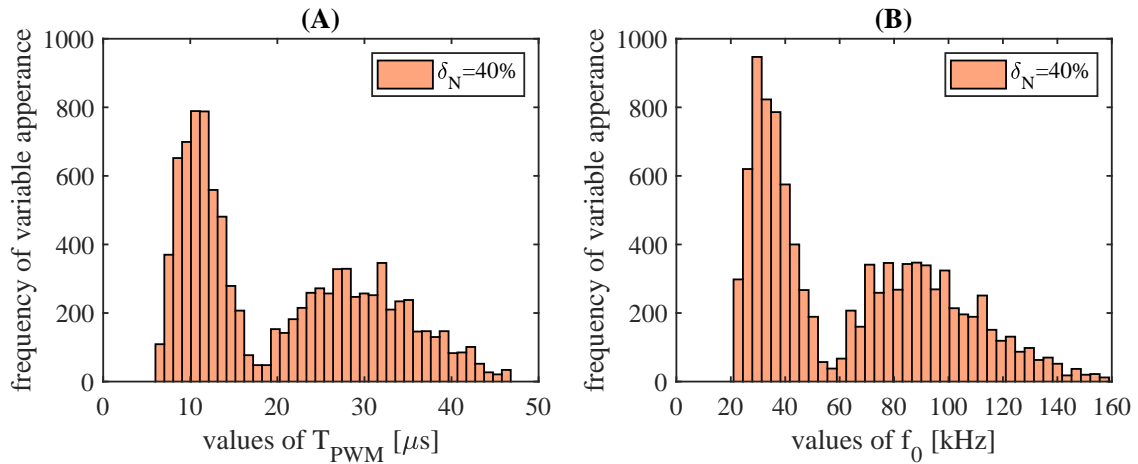


Figure 4.24: Histogram of T_{PWMm} ticks distribution (A) and histogram of frequency distribution (B), for shaping the RanM3 and considering $\delta_N = 40\%$.

converter that randomizes the harmonics components, hence, spread the level of conducted EMI. The novelty of the proposed development lies in the ability to handle the fixed-point processor. Since, we proposed four methods of distribution the PDF in FPGA without arithmetic division and using fixed-point operations, presented in the subsections 4.2.1, 4.2.2, 4.2.3, and 4.2.4. The FPGA implementation is presented in subsection 4.2.5, and the most extensive version of the algorithm (RanM2 with RSC_{TL}) used only 5.5% of FPGA resources.

Furthermore, considering the hardware resources presented in section 4.1, it becomes possible to the transfer of data from FPGA PXI-7854R to IDE NI PXIe-8135. These resources were used for the concept of controlling the switching rate of change, implementation as RanM3 (see subsection 4.2.6). The RanM3 imple-

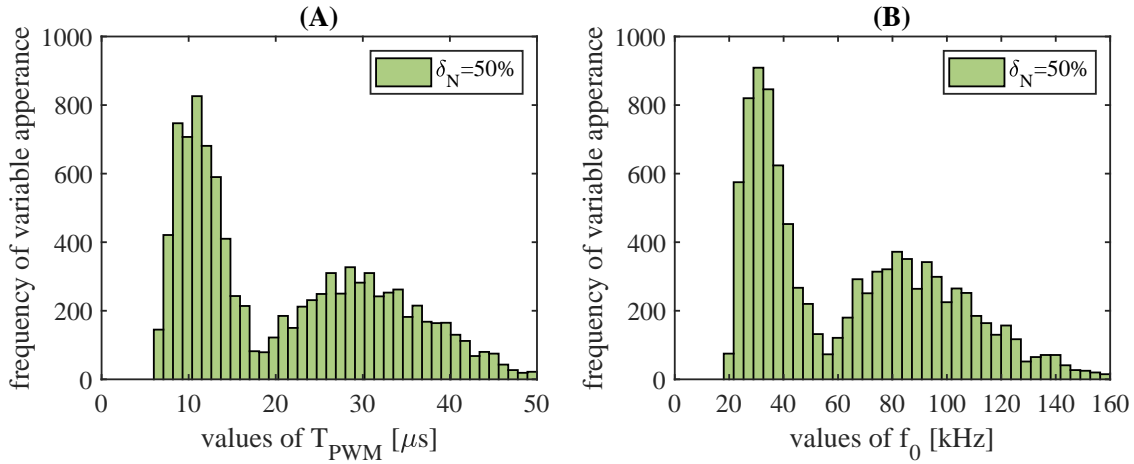


Figure 4.25: Histogram of T_{PWMm} ticks distribution (A) and histogram of frequency distribution (B), for shaping the RanM3 and considering $\delta_N = 50\%$.

mentation was only possible because each environment, i.e., the FPGA PXI-7854R and IDE NI PXIe-8135, considers an independent iteration count (i) process. As illustrated in Figure 4.20-part I, the i_{IDE} is first evaluated by the IDE NI PXIe-8135 controlled by k , and secondly the i_{FPGA} is evaluated by the FPGA PXI-7854R controlled by N (Figure 4.20-parts II and III).

Finally, the last RanM proposed was presented in subsection 4.2.7, considering the ability to shaping the PDF, hence, the EMI noise. The approach of shaping the RanM3 is flexible, and the choice of sub-ranges for N_m and the % of δ_N depend on the expected EMI noise shape, i.e., EMC compliance. Basically, the approach of shaping the RanM3, proposes to model the EMI noise shape according to the imposed needs of spectrum utilization by the possible victims [52]–[55]. Obviously, there is a drawback to considering sub-ranges for N_m from the power electronic converter point of view. Since obtaining a single frequency becomes unlikely. However, the adoption of the approach that shapes the RanM3 is not critical to the execution of any PWM algorithm.

Additionally, it is essential to highlight that although the research presented in this thesis is premised on DC/DC converters. All the presented modulation algorithms in this chapter 4 can be adapted and used in half-bridge or full-bridge typologies of converters, as well as multi-level or multi-phase systems. The FPGA calculation and implementation were developed to be dependent on the internal clock frequency of the control hardware. Thus, increasing possible switching speeds and output frequencies is as simple as interchanging the FPGA by one that runs on a higher internal clock frequency.

For all the presented PWM control algorithms in this chapter 4, the conducted EMI evaluation was carried out and further details are available in the chapter 5.

The Validation of PWM Algorithms

The RanM techniques presented in the chapter 4 are focused on spreading the EMI noise without modifying any critical design parameters of a DC/DC converters, e.g., efficiency, energy density, cost of components, or reliability. Nevertheless, as mentioned in section 4.1, the D and f_0 parameter behaviors were considered in the RanM design process. Primarily, due to the fact that the frequency changes of a given signal might affect the losses in the DC/DC converter, and the parameters of the reactance elements. Theoretically, the frequency changes of a given signal would not affect the cost of components. On the other hand, future studies regarding efficiency, energy density, and reliability are needed [11].

In the chapter 1, more specifically in the section 1.1 and section 1.2, descriptions were given about the purpose to consider DC/DC converters, mostly in context of DC micro-grids [11], DC nano-grids [72], solar photovoltaic and thermal energy systems [79]. In all the cases mentioned in the section 1.1 and section 1.2, DC/DC converters often act as power electronic interfaces and can be characterized as sub-modules that are part of a larger power electronic infrastructure, e.g., IPEM [11], [130], [131]. Furthermore, investigations of the generated EMI by IPEM remain challenging due to the complexity of the total system and the dependency on (often unpredictable) parasitics [132]–[134].

Thus, considering that the functionality of any IPEM depends heavily on the switching behavior of each sub-modules, i.e., of each DC/DC converters [11], [130], [131]. This chapter 5 presents the conducted EMI measurements for all PWM control algorithms described in chapter 4, considering a two-transistor step-down DC/DC converter operating at the low frequency range (the central motivation of this thesis, for further information see section 1.1). Through the assessment of the output harmonic voltage, it gives possibilities to understand the EMI noise behavior at the very origin, as well as to shape it accurately. To recognize and validate the behaviour model of the rectangular pulse trains discussed in depth in chapter 2 as well as the PWM control algorithms proposed and discussed in chapter 4, the conducted EMI

measurements of the two-transistor step-down DC/DC converter are in consonance with EMI's standardized measurement procedures presented in chapter 3.

Thus, firstly in this chapter 5, the entire description of the EMC-test bench system used to carry out the conducted EMI measurements is presented in section 5.1. The analyzed two-transistor step-down DC/DC converter is a sub-module integrating an inverter hardware system, as presented in [24].

Then, the Conducted Emission (CE) behaviour is assessed in section 5.2, intending to broaden the understanding of the DC/DC converters behaviour when is considered the D variation and f_0 with different frequency stabilities¹. The conducted EMI measurements results and statistical analysis are presented in section 5.3.

5.1 EMC-Test Bench System

The conducted EMI measurements presented in this section 5.1, firstly, concern a two-transistor step-down DC/DC converter, where both transistors type are C2-class high speed IGBT. Figure 5.1 shows the schematic diagram of the EMC-test bench system and Figure 5.2 shows the respective EMC-test bench system implemented.

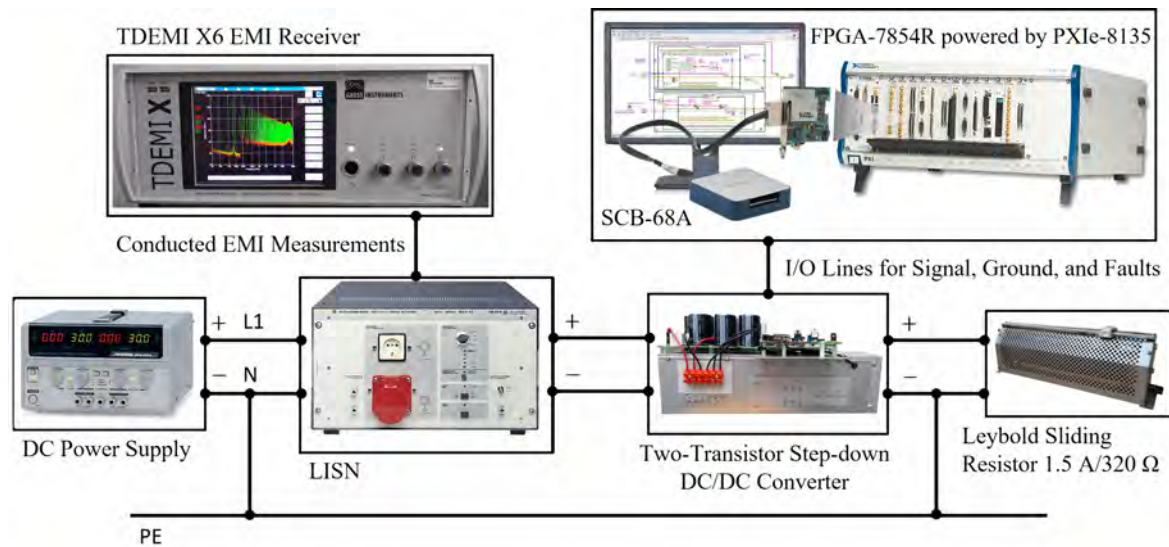


Figure 5.1: The schematic diagram of the EMC-test bench system of a single two-transistor step-down DC/DC converter.

The hardware interfaces of the PWM control signals (RanM or DetM), stop button (S_t) and fault (F_a) (for further information see subsection 4.1.4) were established

¹Frequency stability, also called frequency drift, represents the variation of the output frequency of a crystal oscillator due to external conditions like temperature variation, voltage variation, output load variation, and frequency aging.

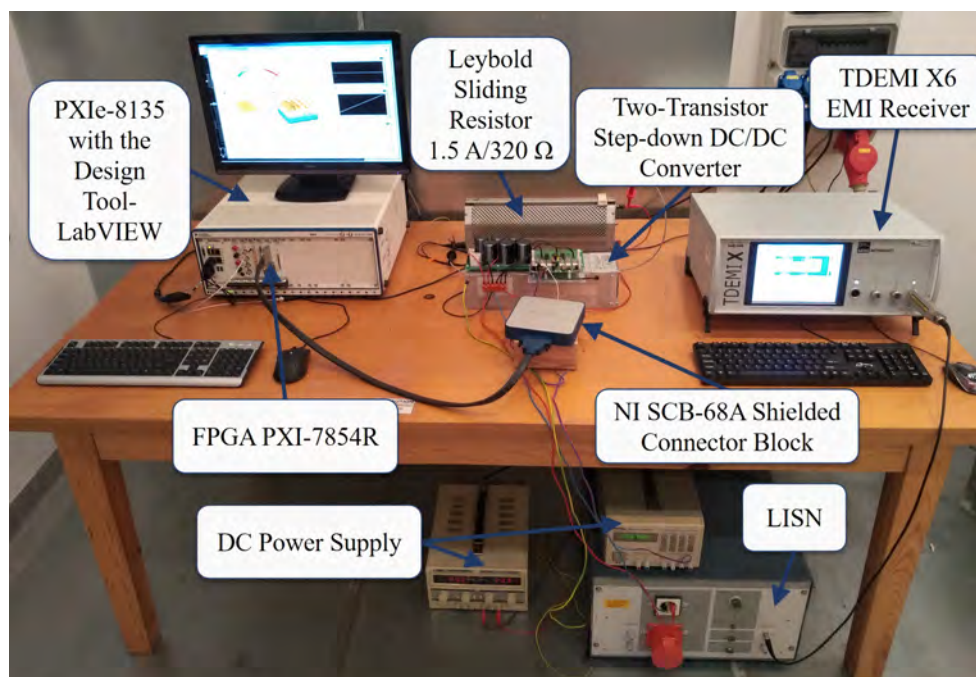


Figure 5.2: The EMC-test bench system implemented for a single two-transistor step-down DC/DC converter.

between the two-transistor step-down DC/DC converter and the FPGA PXI-7854R through the NI SCB-68A shielded connector block. Since the NI SCB-68A is combined with shielded cables, then it provides rugged and very low-noise signal termination to both IGBT gate drives. Furthermore, as also illustrated by Figure 5.1 and Figure 5.2, a Leybold sliding resistor of 320Ω and $1.5A$ was connected as load for the two-transistor step-down DC/DC converter output.

The principle of our CE assessment [78], [106], [135], is to find how much conducted EMI can be generated by the Equipment Under Test (EUT), i.e., the two-transistor step-down DC/DC converter. The CE represents Common-Mode (CM) and Differential-Mode (DM) emissions. Also, the $50\Omega/50\mu H$ LISN was connected to a DC power supply, providing a pure DC supply to the two-transistor step-down DC/DC converter (see Figure 5.1 and Figure 5.2).

Within its specified frequency range, a LISN can provide a stable input impedance for EMI measurement in spite of variations of the mains impedance. The LISN acts as Low Pass Filter (LPF) to ensure that the DC power is transferred to the load device yet uncoupling the TDEMI X6 EMI test receiver from the high-frequency noise coming from the main utility supply. In this way, only the EMI generated by the EUT are measured at the LISN over the specified frequency range.

The minus of the DC power supply was connected to the Protective Earth (PE) and basically to the Ground Reference Plane (GRP) of the EMC-test bench system in a way quite often found in EMC tests (see Figure 5.1). This situation occurs e.g.

in automotive applications where the negative potential is combined with the car's chassis. The negative line was also connected to PE to simulate the circuit for EMI current (i_{CM} illustrated in Figure 5.3).

The two-transistor step-down DC/DC converter is controlled by the drive circuit, interfacing the PWM control signals provided by the FPGA PXI-7854R. The PWM control signals have a 180-degree lag and a dead time of 50% between the two IGBT. Thus, through the assessment of the output harmonic voltage (the *Out* represented in Figure 5.3), with the LISN, it gives possibilities to understand the EMI noise behavior at the very origin, as well as to shape it accurately.

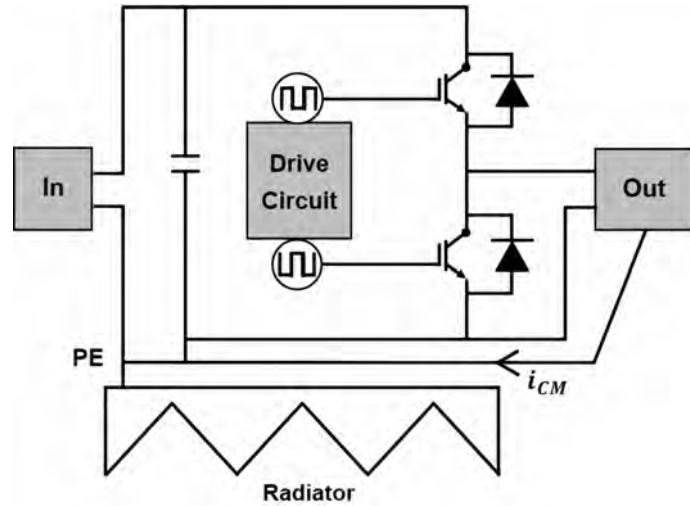


Figure 5.3: The schematic diagram of the two-transistor step-down DC/DC converter.

A review of the operation, control, and applications of DC/DC converters is provided in [130]. In an ideal situation, DC/DC converters might presuppose no inductances in their path. However, in real applications (as discussed in section 1.1 and section 1.2), the inductances must be considered [136].

In the case of a two-transistor step-down DC/DC converter (Figure 5.3), it should be noted that the dead time was a constant set in the LabVIEW FPGA program. We always considered a dead time of 50% of the total switching period, i.e., 50% of the clock cycles needed to generate the PWM signal (N value). Independent of D changing. Thus, adopting this approach, since the analyzed two-transistor step-down DC/DC converter is a sub-module integrating an inverter hardware system. We expected a lower impedance path than the parallel diode of the IGBT.

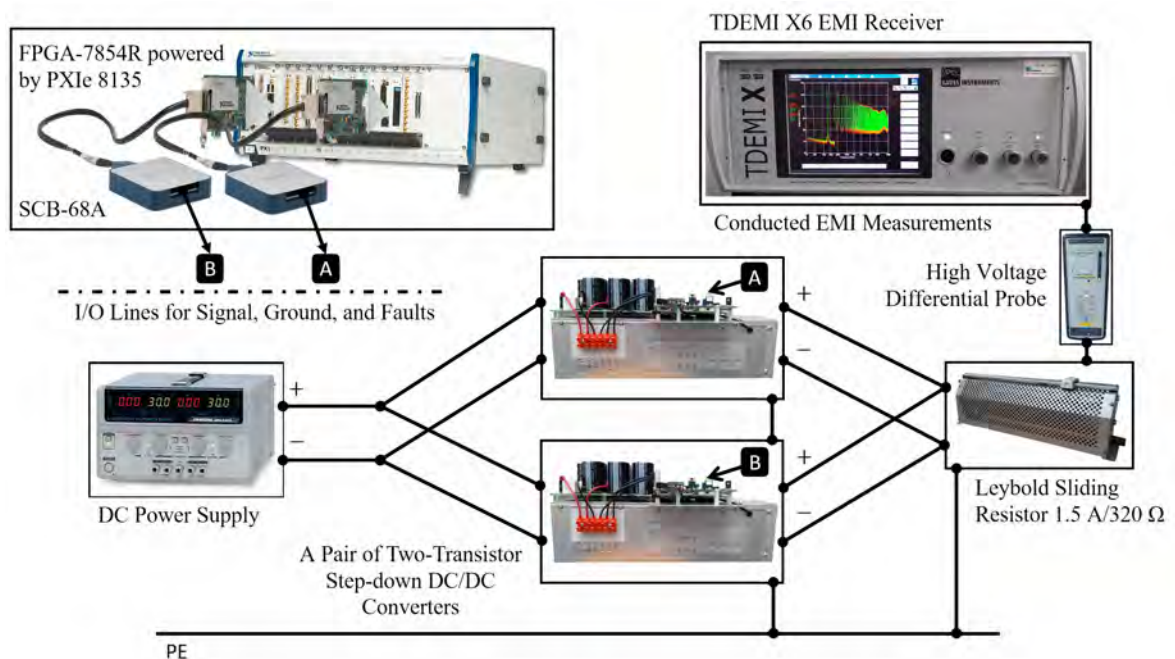
Therefore, evaluating the output harmonic voltage becomes essential since the PWM techniques determine the moments of switching actions. The important parameters of the two-transistor step-down DC/DC converter are summarized in Table 5.1. The speed of transistors is above the frequency $\frac{f_{on}}{f_{off}} = \frac{1}{2 \cdot \pi \cdot \frac{T_{on}}{T_{off}}}$, which in our case exceeds 0.88 MHz. Therefore, the switching speed of transistors does not affect the spectrum in the analyzed CISPR-A frequency band.

Additionally, considering to evaluate the effects in IPPEM due to the typologies that consider different DC/DC converters, where each f_0 of each DC/DC converter may

Table 5.1: The main parameters of the two-transistor step-down DC/DC converter.

Component/function	Specification
Transistors type	IXGH40N60C2D1
I_C (max)	40 A
t_{on}	40 ns
t_{off}	180 ns
Transistor Gate Drivers	HCPL-316J
Diode rectifier	KBPC3506
Converter Power	1800 W (max)
Capacitor	1 μ F
Max DC voltage	450 V
Load	Leybold sliding resistor 320 Ω , 1.5A

present different frequency stabilities. Figure 5.4 presents the schematic diagram of the EMC-test bench system for a pair of two-transistor step-down DC/DC converters. Furthermore, Figure 5.5 presents the EMC-test bench system implemented for a pair of two-transistor step-down DC/DC converters.

**Figure 5.4:** The schematic diagram of the EMC-test bench system for a pair of two-transistor step-down DC/DC converters.

The conducted EMI measurement through the LISN was not considered in the case of Figure 5.4 and Figure 5.5. Once, the target was to assess the influence of the low-frequency envelope only in the output harmonic voltage, instead of the entire

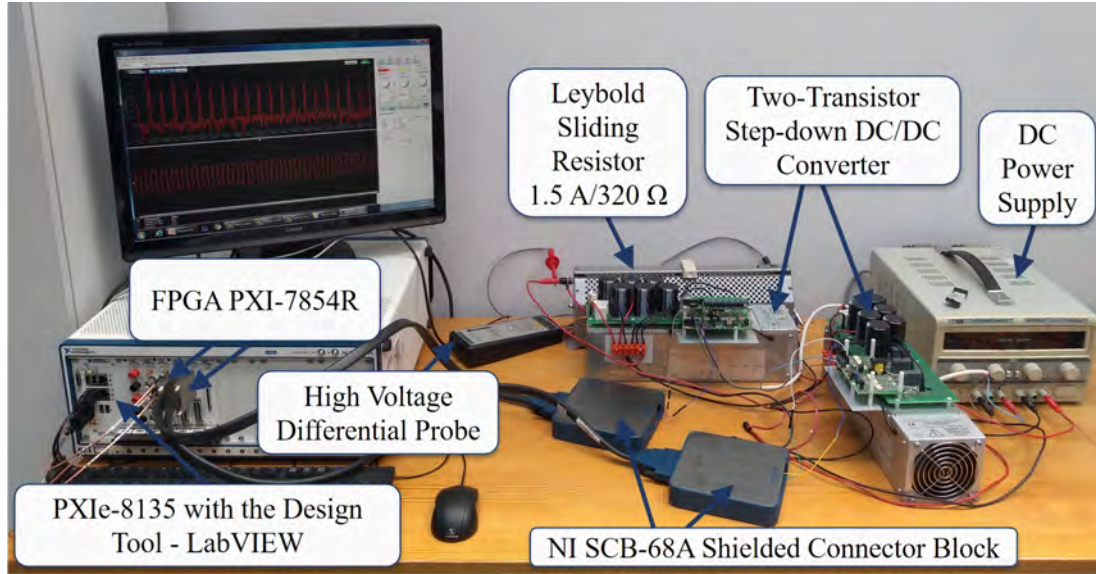


Figure 5.5: The EMC-test bench system implemented for a pair of two-transistor step-down DC/DC converters.

i_{CM} behavior (the case of Figure 5.1 and Figure 5.2). Thus, the output harmonic voltage was measured with the probe SI-9010A from Sapphire Instruments (40 dB of attenuation level), and the attenuation rate was configured 1/100.

5.2 Conducted Emission Behaviour

Fundamentally, however much one expects rectangular pulses trains (as discussed extensively in chapter 2). The PWM control signals, as well as the output harmonic voltage, behave like trapezoidal waveforms. Thus, harmonic frequencies will be produced across the frequency spectrum, with multiples of harmonic frequencies [137]. Therefore, understanding CE behaviours of the two-transistor step-down DC/DC converter due to the D variation and f_0 with different frequency stabilities is essential, mainly in the systems that employ wired communication, e.g., in electric vehicles [138].

Thus, Figure 5.6 presents three cases where the voltage waveforms were measured within the D variation of 12.5%, 50%, and 87.5%, considering DetM and $f_0 = 100 \text{ kHz}^2$. Figure 5.6 shows the output harmonic voltage of the two-transistor step-down DC/DC converter with different D settings, indicating that a larger D has a longer turn-on duration (see Figure 5.6-C). Furthermore, as presented by [139] the highest CE at $f_0 = 100 \text{ kHz}$ occurs when the $D \approx 50\%$. The same principle, can be seen in Figure A.8 of the subsection A.2, and in the Figure 5.10 of the section 5.3.

²Parts of this section 5.2 are published in [139].

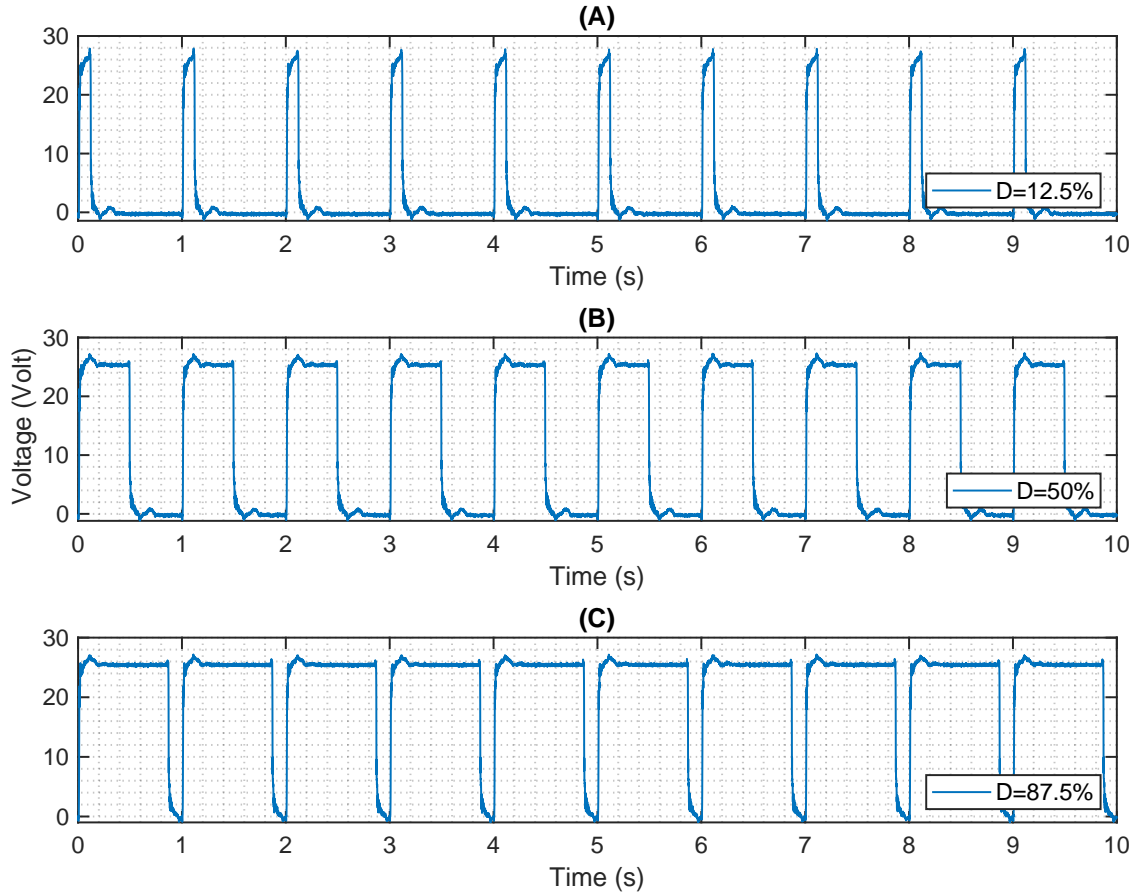


Figure 5.6: The voltage waveforms at the converter output for several selected duty cycle factors D : (A) 12%, (B) 50%, and (C) 87.5% [139].

Figure 5.7, also considered in [139], indicates that the D effects at the f_0 , is not linear but resembles a quadratic function. It is noteworthy that the effects presented by Figure 5.7 only occurs at the f_0 . However, in the Figure 5.9, Figure 5.10, and Figure 5.11 of the section 5.3 is possible to see the effects of the D variation in the another harmonic components, as predicted by the Figure A.8 and Figure A.9 of the subsection A.2.

Moreover, according to the measurement data (blue line) presented by Figure 5.7. The behaviour model that represents the effect of D variation on the f_0 amplitude can be generated using the 2^{nd} order polynomial quadratic regression approach (5.1):

$$y = a + bx + cx^2, \quad (5.1)$$

where a , b , and c coefficients are generated from the obtained measurement data (blue line) presented at Figure 5.7. The parameter y is the CE level and x is the D . Therefore, the behaviour model that represents the effect of D variation on the f_0

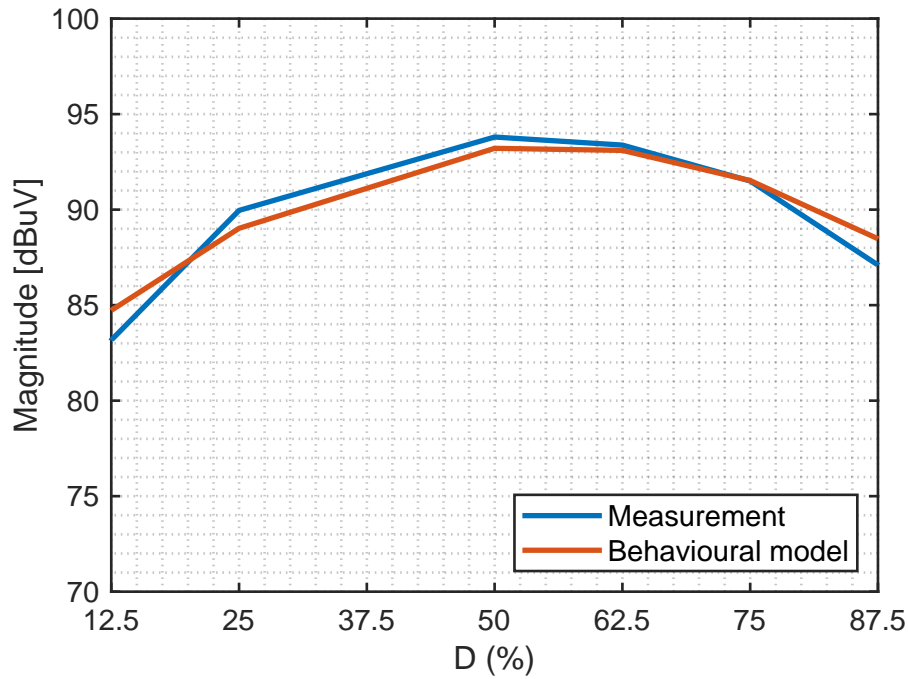


Figure 5.7: The behavior of f_0 amplitude with D variation [139].

amplitude, orange line presented at Figure 5.7, can be expressed by (5.2) [139].

$$y = 78.96 + 0.52x + 0.0047x^2. \quad (5.2)$$

Nevertheless, an interesting point that reinforces the need to understand the CE behaviour of a two-transistor step-down DC/DC converter is related with the EUT and the measurements procedures. In the case presented by [139] the EUT is a DC motor as illustrated by Figure 5.8.

In the case of the EUT presented at Figure 5.8, the principle introduced by Figure 5.7 means that the highest EMI occurs at 50% of the DC motor speed. Thus, from the practice point of view with EMC testing, the maximum speed test condition according to the CISPR 14-1:2020 recommendation [135], is not a correct choice to capture the worst CE profile [139].

On the other hand, if it is considered a IPEM, e.g., multiples DC/DC converters in parallel topology, beyond the CE behaviours presented above (see Figure 5.7). The low frequency envelope provided by the frequency beat might appear [44]. As discussed in depth in section A.3 this phenomenon might be attributed to the f_0 with different frequency stabilities. When two signals of the same type (frequency and instances of time) pass simultaneously through the same point in space, the individual signal displacements add. Also, their respective amplitudes add linearly, and the beat occurs at times of maximum sum signal amplitude [140], see Figure A.10 of the section A.3. The evaluation of this particular topic is based on Figure 5.4 and

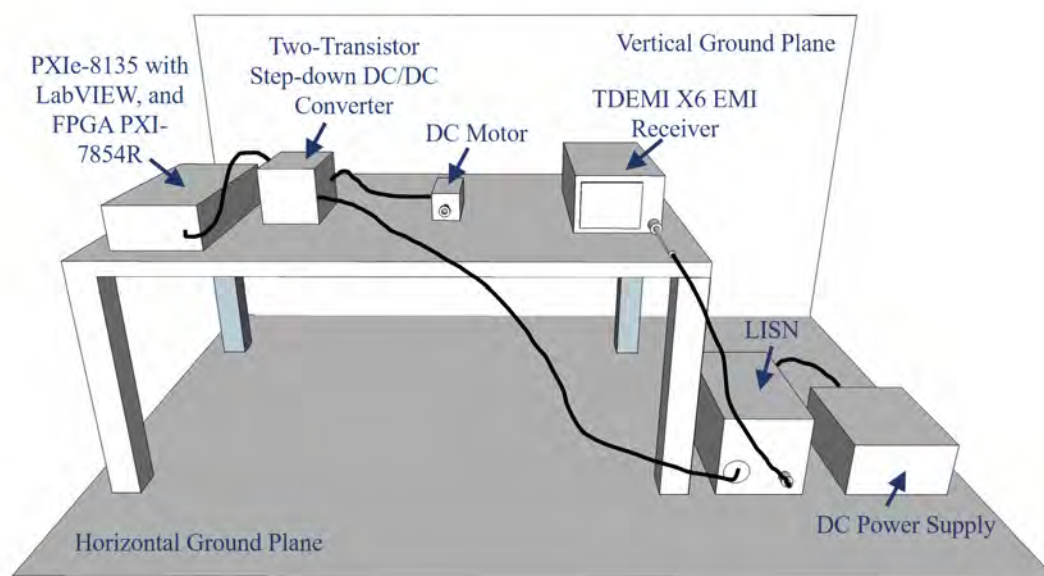


Figure 5.8: The EMI measurement setup used by [139] to assess the CE from the two-transistor step-down DC/DC converter to a DC motor.

Figure 5.5, and the EMI measurements are presented in subsection 5.3.4.

5.3 The Measurements of Conducted Emissions for DC-DC Converter

All the EMI's standardized measurement procedures presented in this section 5.3³ are based on [78] as also described in chapter 3. Firstly was considered to assess the two-transistor step-down DC/DC converter for 24V and using the EMC-test bench system highlighted at Figure 5.2. Nevertheless, to visualize the harmonic components distribution.

The frequency range considered in Figure 5.9, Figure 5.10 and Figure 5.11 was from 50 kHz to ≈ 1 MHz (similar to the subsection 5.3.4), with the IFBW filter equal to 200 Hz (see Table 3.1 in the subsection 3.4). In the subsection 5.3.1, subsection 5.3.2, and subsection 5.3.3 only the CISPR A frequency band was considered. Also, to carry out the EMI measurements presented in this section 5.3, the TDEMI X6 EMI test receiver was adopted (see Figure 5.1).

Figure 5.9 consider $D \approx 30\%$, Figure 5.10 consider $D \approx 50\%$, and Figure 5.11 consider $D \approx 70\%$. In all the cases, from Figure 5.9 to Figure 5.11 the $f_0 = 62.5$ kHz and the AV and QP detectors were considered, since them better characterize the EMI

³Parts of this section 5.3 are published in [44], [65].

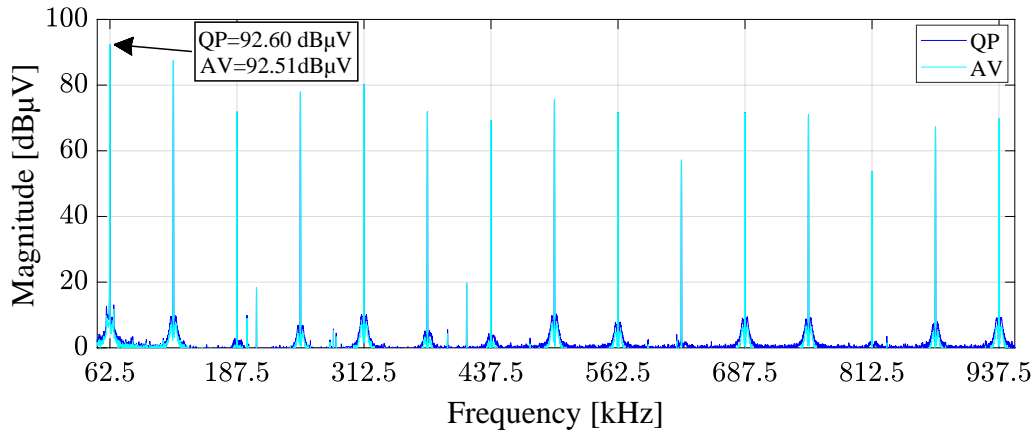


Figure 5.9: The conducted EMI measurements with $D \approx 30\%$ and $f_0 = 62.5$ kHz.

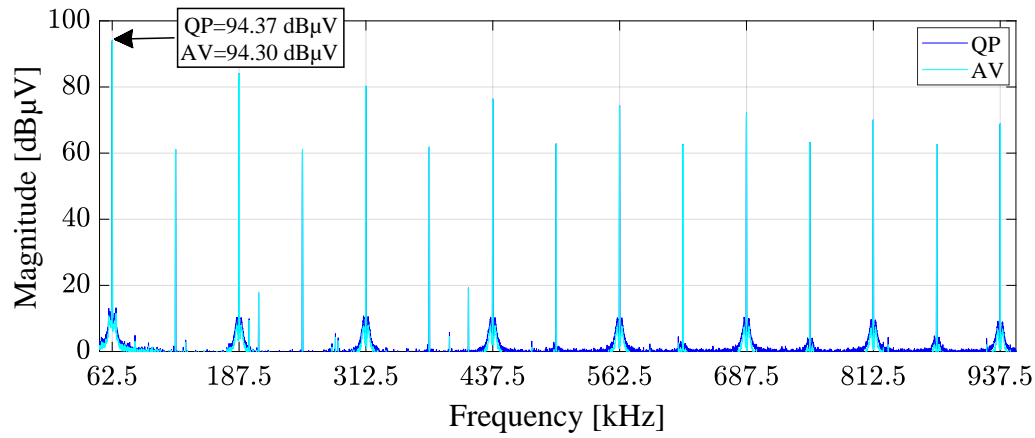


Figure 5.10: The conducted EMI measurements with $D \approx 50\%$ and $f_0 = 62.5$ kHz.

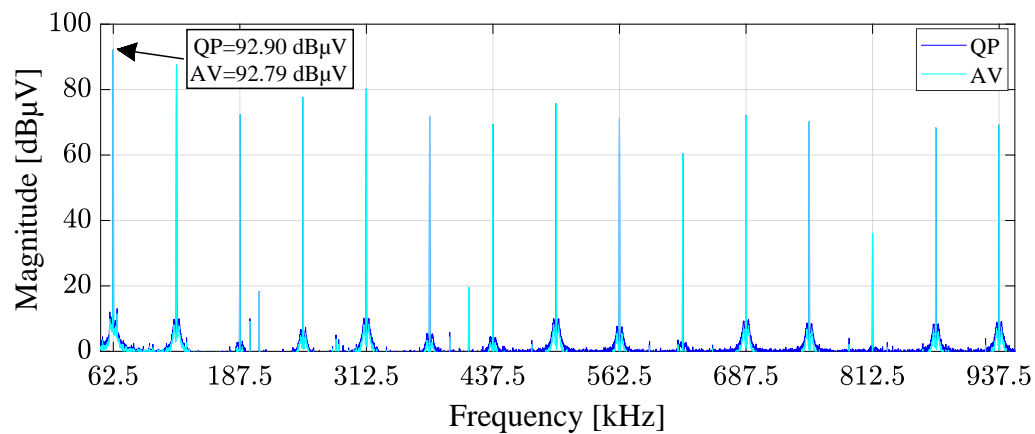


Figure 5.11: The conducted EMI measurements with $D \approx 70\%$ and $f_0 = 62.5$ kHz.

currents [104]. In all the conducted EMI measurements presented in Figure 5.9, Figure 5.10 and Figure 5.11 it is possible to observe the expected behavior of DetM, as

previously presented in subsection A.2 of the chapter 2, and especially highlighted in Figure A.8 and Figure A.9. As also presented in the subsection 5.2, Figure 5.7. Figure 5.9 and Figure 5.11 show that since the voltage variation is more rapid in time, compared with the case of $D \approx 50\%$ (Figure 5.10). Thus, the conducted EMI measurements in both cases of Figure 5.9 and Figure 5.11 contain a wider distribution of the C_n to allow for rapid change (see Figure A.8).

Furthermore, Figure 5.10 shows the expected constant value of the even harmonics, since the $D \approx 50\%$. Also, Figure 5.10 shows that from $n=15$, the odd and even harmonics become similar in amplitude, analogous to the modeling shown in Figure A.8.

5.3.1 The Deterministic and Pseudo-random Modulation

Initially in this subsection 5.3.1, the conducted EMI measurements relative a DetM will be presented, in order to provide a comparative base with the others conducted EMI measurements also presented in this subsection 5.3.1, however relative a RanM. Thus, Figure 5.12 and Figure 5.13 show the measurements obtained by means of the TDEMI X6 EMI test receiver, which provided a 3D spectrogram for both AV and QP detectors, considering CISPR A frequency band. In both cases of Figure 5.12 and Figure 5.13 the $f_0 = 80$ kHz and $D \approx 50\%$.

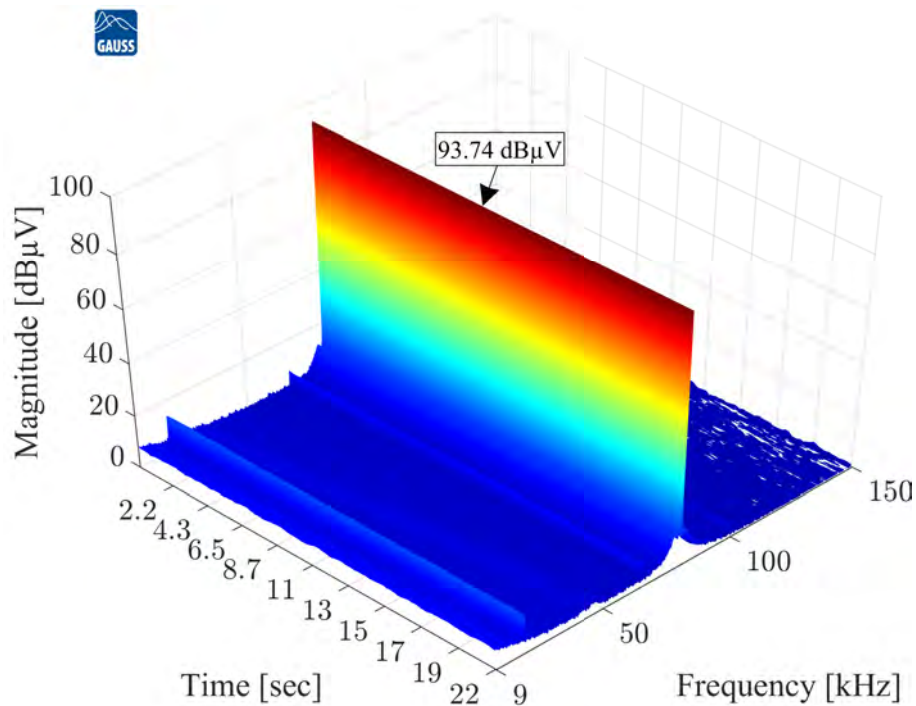


Figure 5.12: The EMI shape of DetM: $f_0=80$ kHz and AV detector.

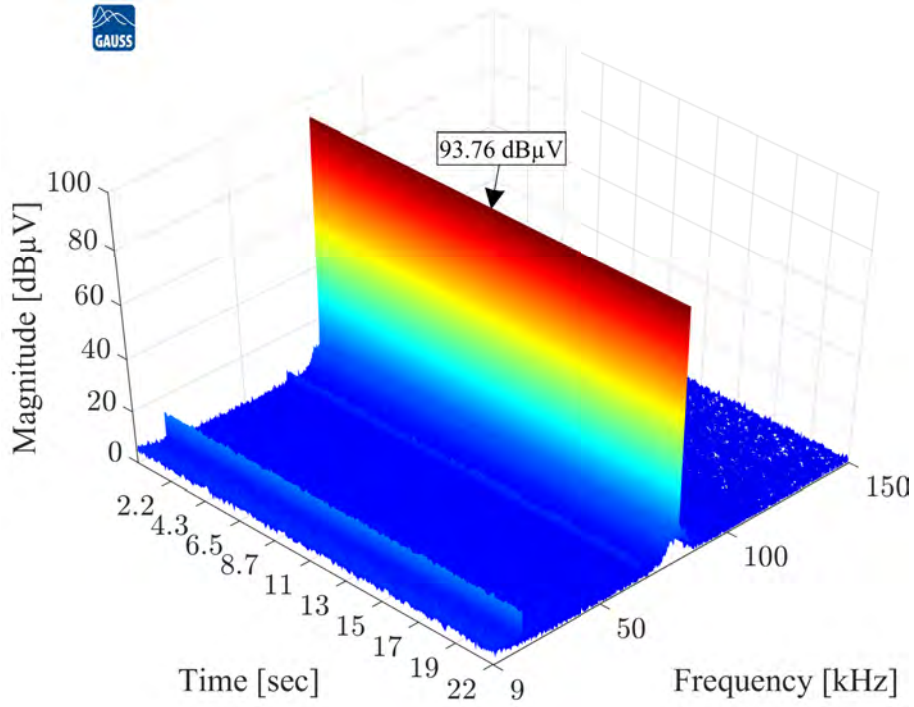


Figure 5.13: The EMI shape of DetM: $f_0=80$ kHz and QP detector.

It is noteworthy that the $D \approx 50\%$ represents the worst CE behavior, as presented in Figure A.8 and Figure A.9, in Figure 5.7, and in Figure 5.10. Thus, condition $D \approx 50\%$ is adopted as the default for all conducted EMI measurements presented in the section 5.3.

Figure 5.12 and Figure 5.13 refers to the AV and QP detectors measurement for DetM with $N_m = N_{AV} = 500$ and $\delta_N = 0$. For further information on the PWM modulation algorithm see subsection 4.1.4. The first harmonic magnitude (occurring at 80 kHz) is the most significant one overall in the whole frequency spectrum in both cases of Figure 5.12 and Figure 5.13. The second harmonic is expected to appear at 160 kHz, which is outside the CISPR A frequency band (see Table 3.1 in the subsection 3.4). The EMI measurements presented in Figure 5.12 and Figure 5.13 corroborate the EMI shape for DetM, as deeply discussed in chapter 2. Also, in the entire chapter 3 and in the chapter 4, subsection 4.1.4.

The Figure 5.14 and Figure 5.15 refer to the AV and QP detectors measurement for RanM with $N_{AV} = 667$, $\delta_N = 668$ and SC_{TL} . The completed details of the used RanM approach are presented in the subsection 4.2.1, Figure 4.12.

As presented in Figure 4.12, in the case of Figure 5.14 and Figure 5.15, the f_0 varies within the assumed δ_N range. Despite this, the frequency distribution is not uniform, and the average frequency is not equal to 80 kHz. Furthermore, as discussed in section 3.5. Once the RanM provides changes in the frequency of a given PWM signal and also provides random changes between the frequencies consid-

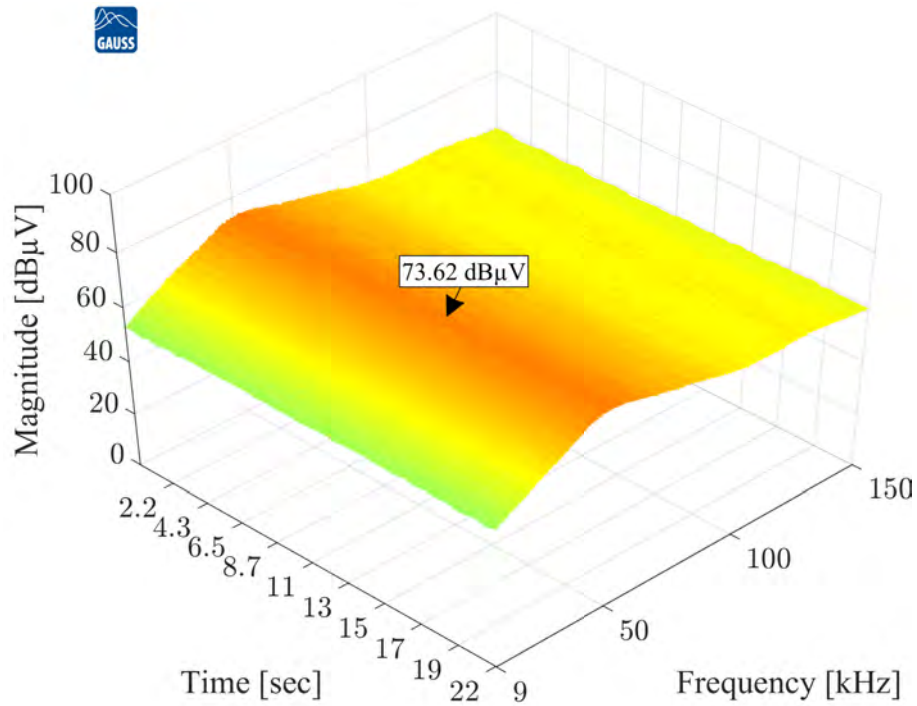


Figure 5.14: The EMI shape of RanM with $N_{AV} = 667$, $\delta_N = 668$ and AV detector.

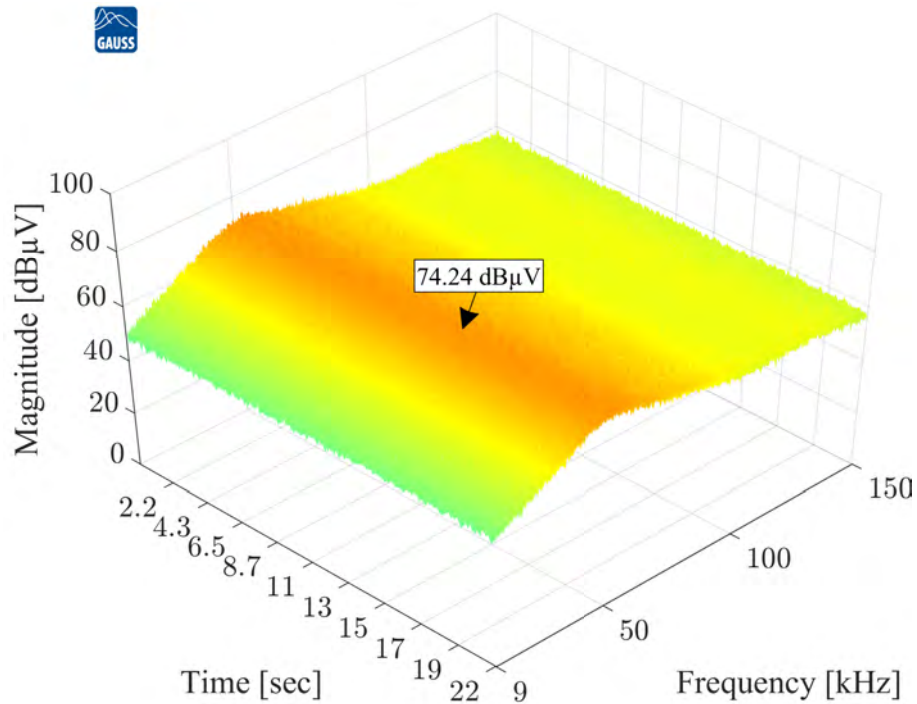


Figure 5.15: The EMI shape of RanM with $N_{AV} = 667$, $\delta_N = 668$ and QP detector.

ered in this PWM signal. The spreading effects appeared, as well as in Figure 5.16 and Figure 5.17. Figure 5.16 and Figure 5.17 refer to the AV and QP detectors measurement for RanM with $N_{AV} = 500$, $\delta_N = 331$ and SC_{TL} .

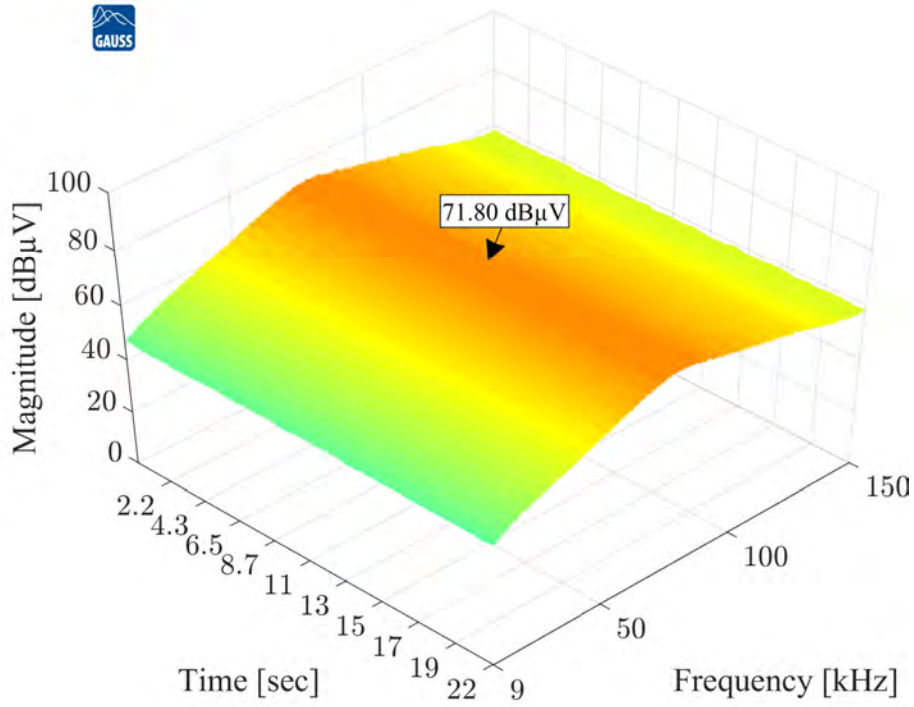


Figure 5.16: The EMI shape of RanM with $N_{AV} = 500$, $\delta_N = 331$ and AV detector.

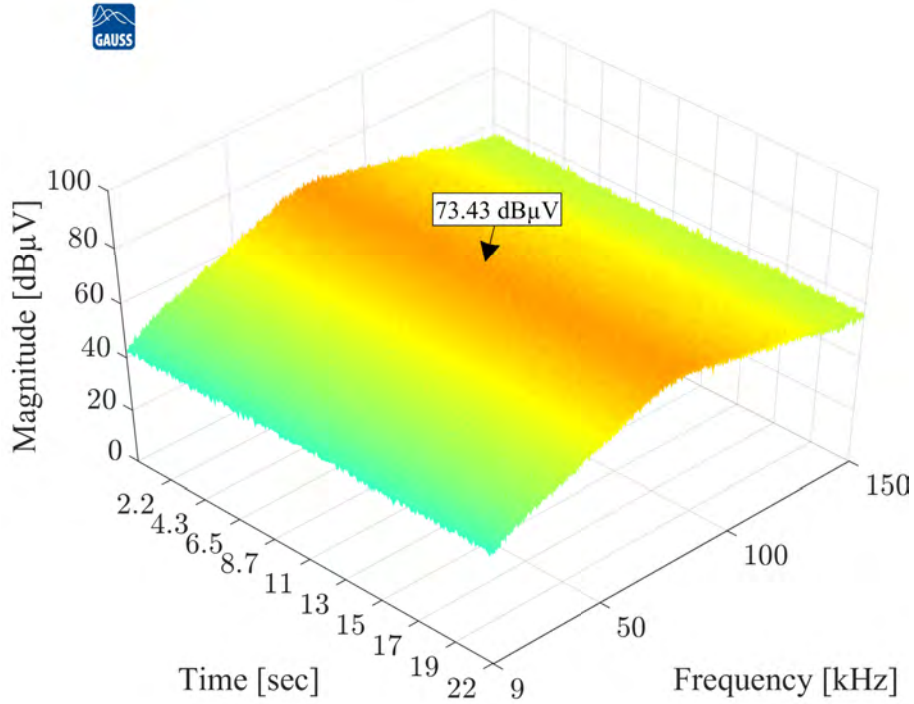


Figure 5.17: The EMI shape of RanM with $N_{AV} = 500$, $\delta_N = 331$ and QP detector.

Figure 5.16 and Figure 5.17 shows the average value of the f_0 closer to that intended, i.e., $f_0 = 80$ kHz, but the frequency distribution is still strongly non-linear. The details of the used RanM are presented in the subsection 4.2.1, Figure 4.13.

Therefore, as proposed in the subsection 4.2.2 of the chapter 4. The RanM with RSC_{TL} was adopted. This means randomly changing both the number of periods of the For Loop - N_m (concept illustrated at Figure 4.8), and the duration of this loop - SC_{TL} . Figure 5.18 and Figure 5.19 refer to the AV and QP detectors measurement for RanM with $N_{AV} = 50$, $\delta_N = 34$, and $RSC_{TL} \in \langle 7, 13 \rangle$. The completed details of the used RanM approach are presented in the subsection 4.2.2, Figure 4.14.

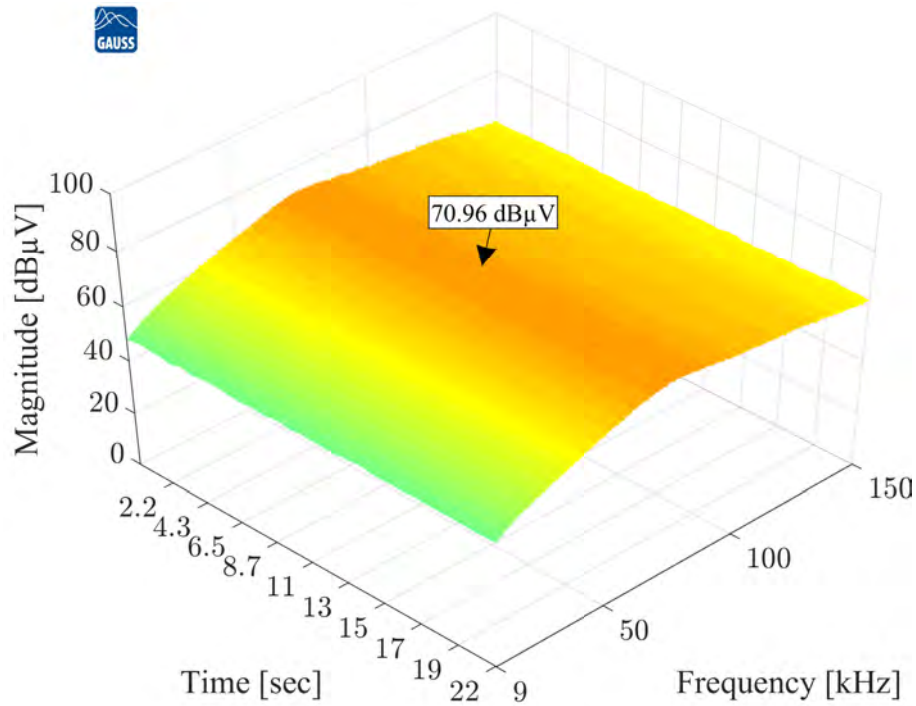


Figure 5.18: The EMI shape of RanM with $N_{AV} = 50$, $\delta_N = 34$, $RSC_{TL} \in \langle 7, 13 \rangle$ and AV detector.

Figure 5.18 and Figure 5.19 show that when we consider N_m and RSC_{TL} , the power spectral density changes, especially from f_0 to higher frequencies. Thus, this approach of N_m and RSC_{TL} randomization gives us the possibility to shape the EMI noise (clearer results are presented in the next subsection 5.3.2 and subsection 5.3.3). The frequency distribution is closer to a Gaussian distribution, as is also possible to see in Figure 4.14, which should be more favourable in terms of the average frequency and converter losses.

Furthermore, a little increase in the EMI noise spreading is provided, whether compared Figure 5.18 and Figure 5.19 with Figure 5.16 and Figure 5.17.

Additionally, in chapter 4, two more RanM approaches were proposed, as presented in subsection 4.2.3 and subsection 4.2.4. Figure 5.20 and Figure 5.21 refer to the AV and QP detectors measurement for RanM2 proposed in the subsection 4.2.3, considering the parameters: $N_{AV1} = 750$ with $\delta_{N1} = 500$, $N_{AV2} = 416$ with $\delta_{N2} = 167$, and SC_{TL} .

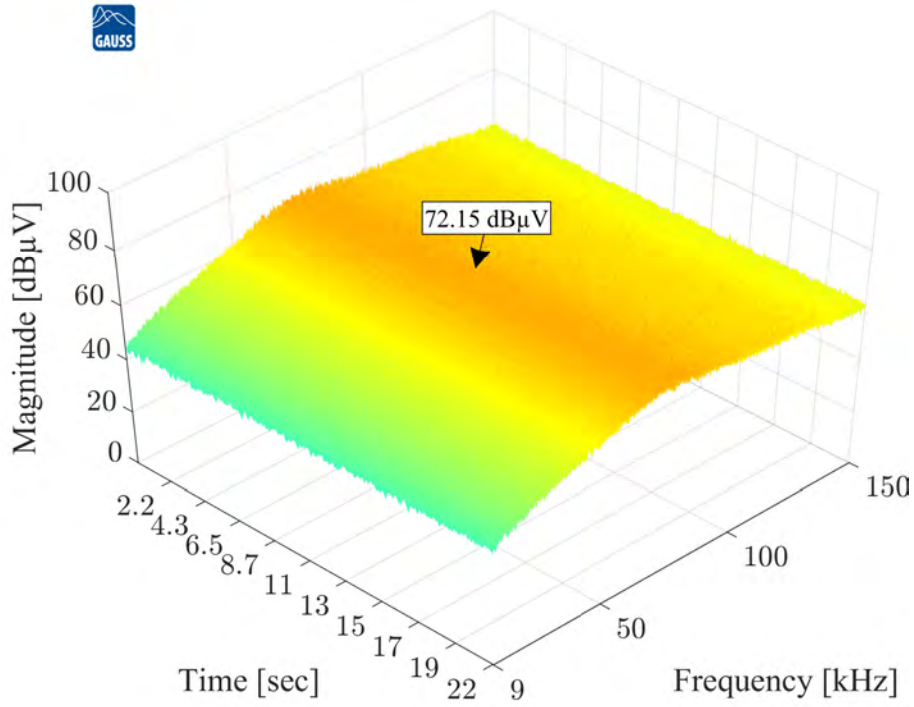


Figure 5.19: The EMI shape of RanM with $N_{AV} = 50$, $\delta_N = 34$, $RSC_{TL} \in \langle 7, 13 \rangle$ and QP detector.

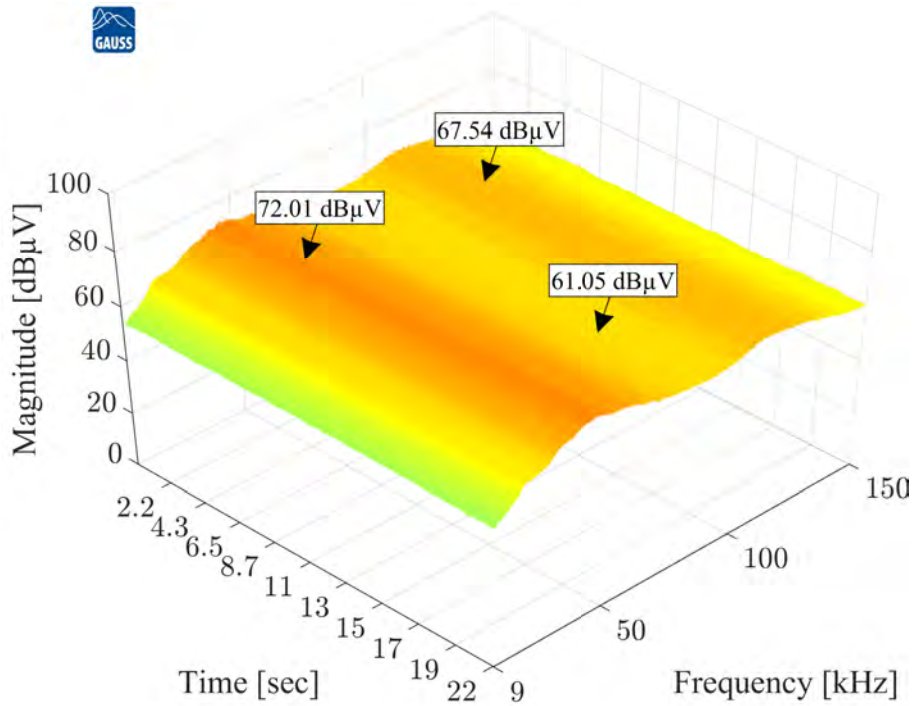


Figure 5.20: The EMI shape of RanM2 with $N_{AV1} = 750$, $\delta_{N1} = 500$, $N_{AV2} = 416$, $\delta_{N2} = 167$, SC_{TL} , and AV detector.

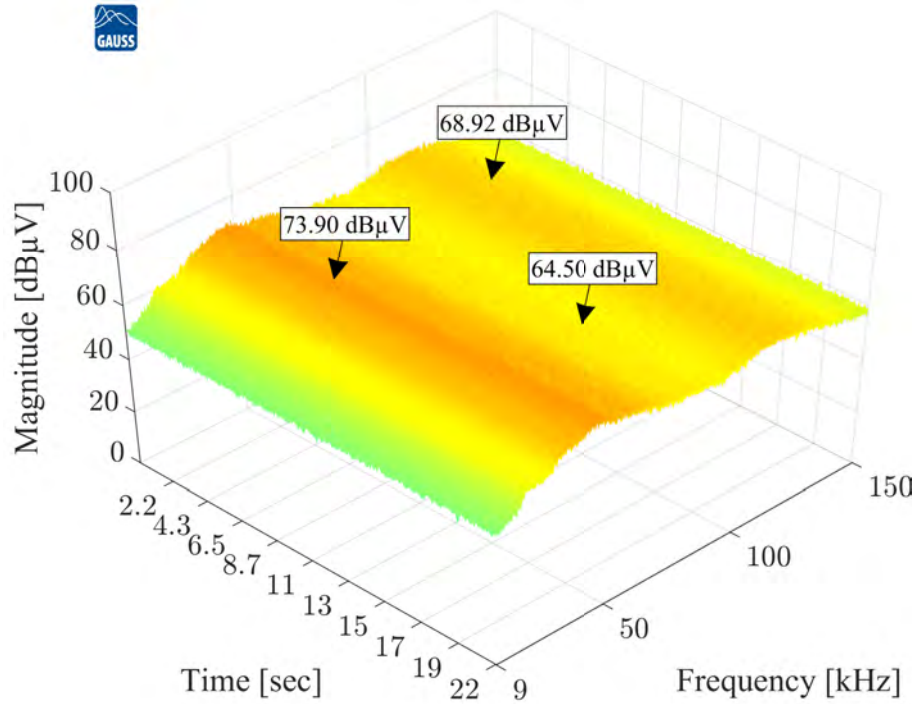


Figure 5.21: The EMI shape of RanM2 with $N_{AV1} = 750$, $\delta_{N1} = 500$, $N_{AV2} = 416$, $\delta_{N2} = 167$, SC_{TL} and QP detector.

Two higher EMI noise levels are visible in the CISPR A frequency spectrum presented in both Figure 5.20 and Figure 5.21. Once the RanM2 approach considers shaping the T_{PWMm} and f_0 by splitting the N_m distribution to a few sub-ranges into the entire N_m range. For further information about the LabVIEW FPGA implementation, based on the RSN generation presented at Figure 4.11 - part I, see subsection 4.2.3 and subsection 4.2.5. Therefore, through the RanM2 approach, there is a possibility to control the shaping of frequency, i.e., controlling the occurrence of frequencies in certain parts of the RSN used by RanM.

Figure 5.22 and Figure 5.23 refer to the AV and QP detectors measurement for RanM2 with RSC_{TL} proposed in the subsection 4.2.4, considering the parameters: $RSC_{TL} \in \langle 7, 13 \rangle$, $N_{AV1} = 75$, $\delta_{N1} = 50$, $N_{AV2} = 42$, and $\delta_{N2} = 17$. Figure 5.22 and Figure 5.23 show a EMI noise better spread than the RanM proposed in subsection 4.2.1 (the EMI measurements in Figure 5.16 and Figure 5.17), in subsection 4.2.2 (the EMI measurements in Figure 5.18 and Figure 5.19), and in subsection 4.2.3 (the EMI measurements in Figure 5.20 and Figure 5.21).

Through the evaluation of all conducted EMI measurements presented in this subsection 5.3.1, and based on the LabVIEW FPGA implementation presented in subsection 4.2.5, the following observations can be made:

- The spreading of the spectrum components will always be a consequence of the RanM utilization. The more appropriate the PDF used to generate the

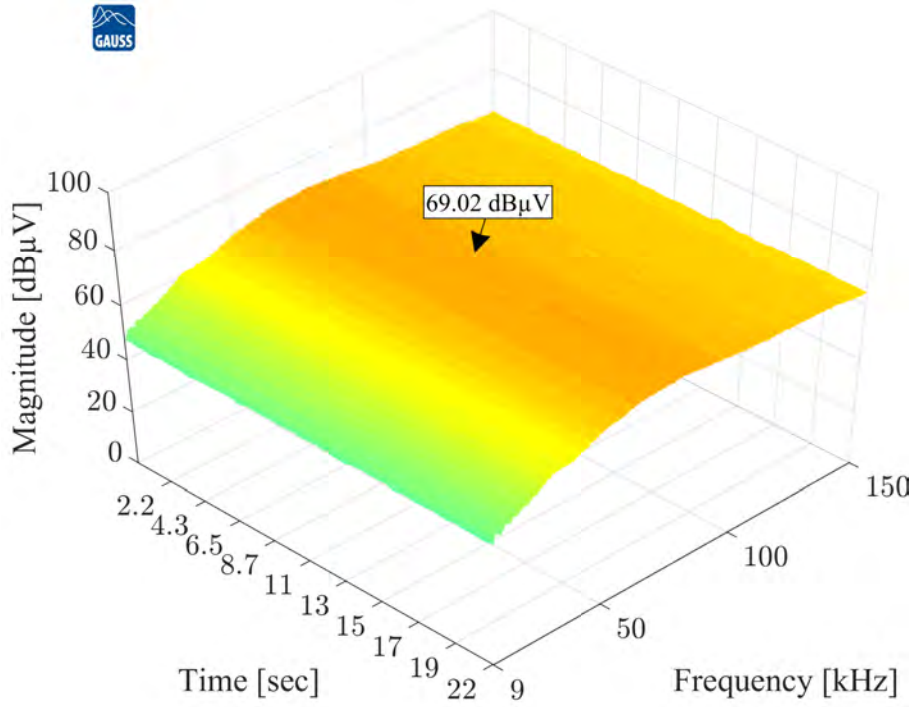


Figure 5.22: The EMI shape of RanM2 with $RSC_{TL} \in \langle 7, 13 \rangle$, $N_{AV1} = 75$, $\delta_{N1} = 50$, $N_{AV2} = 42$, $\delta_{N2} = 17$, and AV detector.

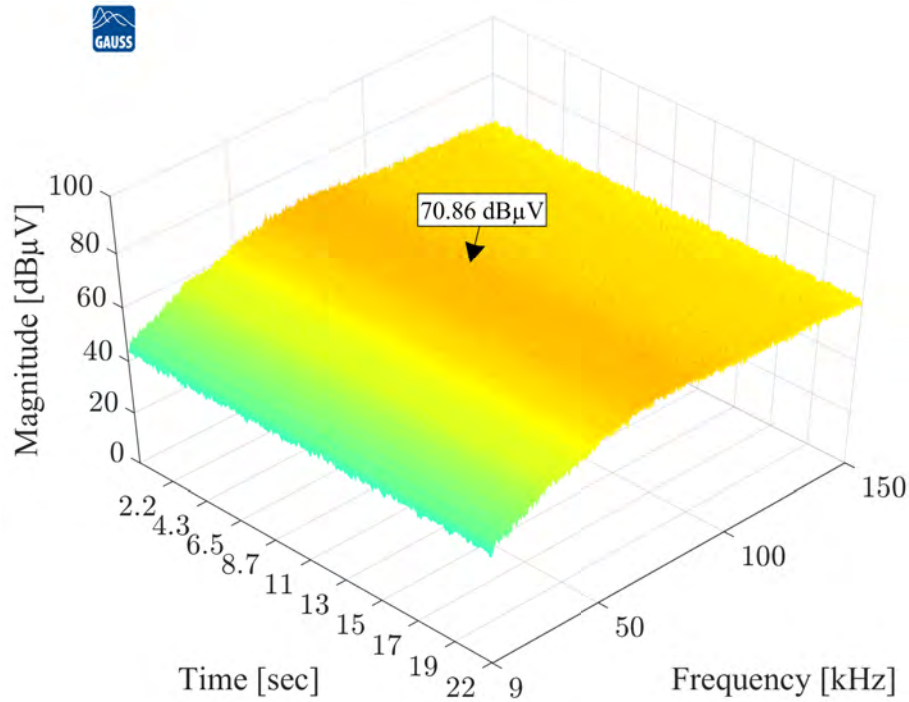


Figure 5.23: The EMI shape of RanM2 with $RSC_{TL} \in \langle 7, 13 \rangle$, $N_{AV1} = 75$, $\delta_{N1} = 50$, $N_{AV2} = 42$, $\delta_{N2} = 17$, and QP detector.

PWM signal, the greater the spreading effect becomes, as in the case of the Figure 5.22 and Figure 5.23;

- However, the EMI noise spreading as presented in this subsection 5.3.1 does not mean an EMI noise level reduction or even power spectrum lowering;
- Once the RanM provides changes in the frequency of a given PWM signal and also provides random changes between the frequencies considered in this PWM signal. It becomes imperative to find the tradeoffs between RanM, dwell time (T_m) and RBW to achieved a stable EMI measurement, as dicussed in chapter 3, subsetion 3.5.

5.3.2 The Pseudo-random Modulation 3

This subsection 5.3.2 aims to investigate the RanM3 proposed in the subsection 4.2.6. Through the CPS concept described in section 4.1, it becomes possible to control the switching rate of change. Figure 4.19 presents the LabVIEW implementation in the IDE NI PXIe-8135, denoted as RanM3, and the one considered in the EMC-test bench system (see Figure 5.2). Thus, considering the principle that the broader the range of values assigned to k , the longer it takes to randomly alternate the frequencies considered in the RSN used by RanM (see MATLAB simulation presented in Figure 2.3, Figure 2.4 and Figure 2.5).

Furthermore, considering that presented in section 3.5 where, there is a complexity of establishing the tradeoffs between RanM3, dwell time (T_m) and RBW, a premise could assume the shorter T_m possible and adapt the switching rate of change to match the RBW. Let's consider again the parameters used by LabVIEW FPGA implementation presented in subsection 4.2.4, which resulted in the conducted EMI measurments presented in Figure 5.22 and Figure 5.23. However, using the LabVIEW implementation in the IDE NI PXIe-8135, denoted as RanM3, as presented in Figure 4.19.

Figure 5.24 and Figure 5.25 refer to the AV and QP detectors measurement for RanM3 proposed in the subsection 4.2.6, considering the parameters: $RSC_{TL} \in \langle 7, 13 \rangle$, $N_{AV1} = 75$, $\delta_{N1} = 50$, $N_{AV2} = 42$, $\delta_{N2} = 17$, and $k = 1$. Also, with the $T_m = 100$ ms. The $T_m = 100$ ms was also considered for the conducted EMI measurements presented in subsection 5.3.1.

Figure 5.24 and Figure 5.25 show that assuming $k=1$ means allocating all control hardware features to execute just one iteration count (i) of the PWM signal (see subsection 4.2.6). Therefore, the random alternation of the frequencies considered in the RSN used by RanM3 is speedy. Furthermore, considering a $T_m = 100$ ms, there is not enough time for the TDEMI X6 EMI test receiver to properly characterize

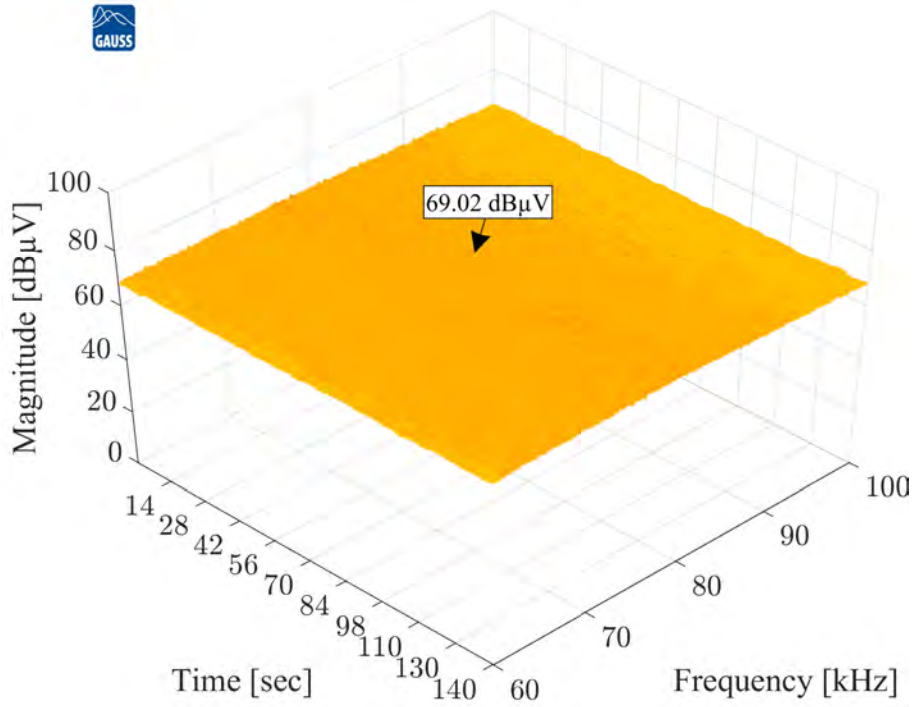


Figure 5.24: The EMI shape of RanM3 with $RSC_{TL} \in \langle 7, 13 \rangle$, $N_{AV1} = 75$, $\delta_{N1} = 50$, $N_{AV2} = 42$, $\delta_{N2} = 17$, $k = 1$ and AV detector.

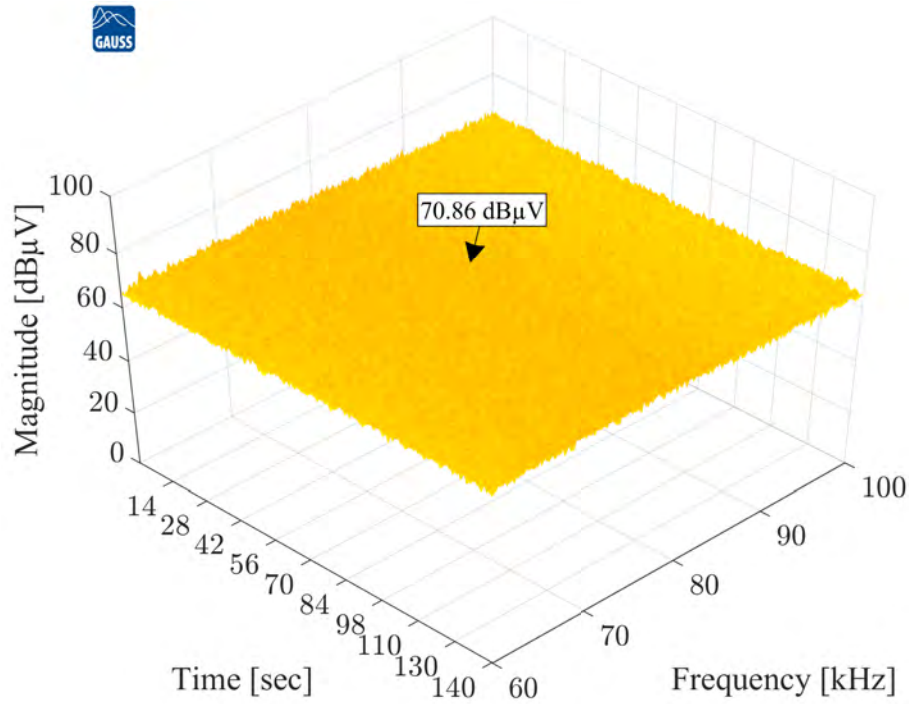


Figure 5.25: The EMI shape of RanM3 with $RSC_{TL} \in \langle 7, 13 \rangle$, $N_{AV1} = 75$, $\delta_{N1} = 50$, $N_{AV2} = 42$, $\delta_{N2} = 17$, $k = 1$ and QP detector.

the PWM signal generated by the RanM3. Corroborating the claim highlighted in subsection 3.5 of the chapter 3: the TDEMI X6 EMI test receiver may not catch the signal whose frequency varies in time when the T_m is not precisely defined.

As also mentioned in chapter 3, subsection 3.3, based on Figure 3.8-D: the narrower the IF filter, the narrower the RBW is, and the longer is T_m . However, since we assume to keep the $T_m = 100$ ms, let's adapt the switching rate of change to match the RBW. Figure 5.26 and Figure 5.27 refer to the RanM3 presented in Figure 5.24 and Figure 5.25, respectively, however in both cases with $k = 4 \times 10^5$.

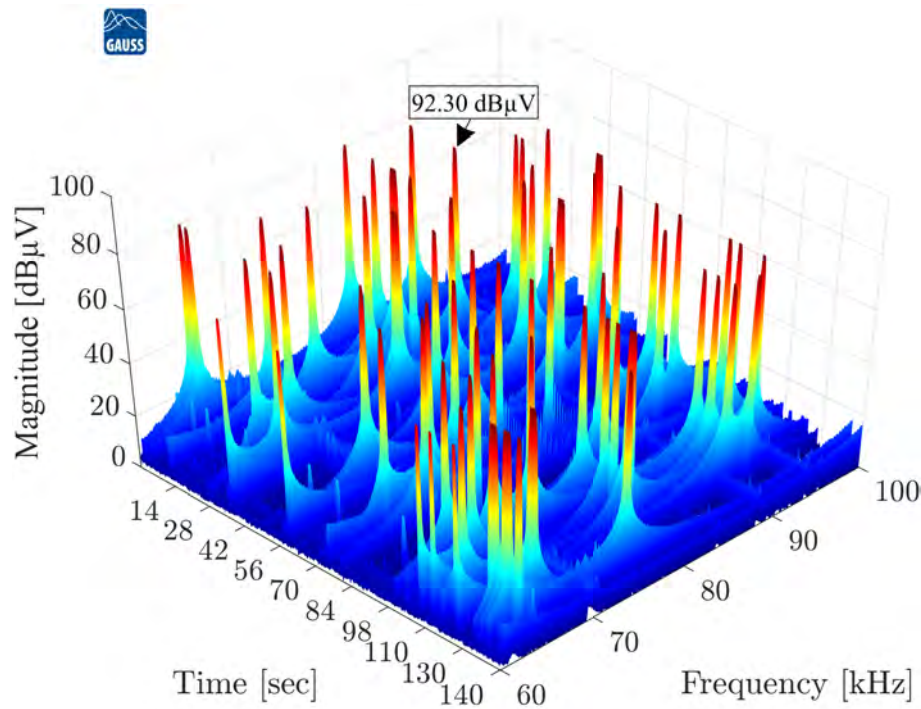


Figure 5.26: The RanM3 presented in Figure 5.24, however with $k = 4 \times 10^5$.

Therefore by using $k = 4 \times 10^5$, it takes longer to randomly alternate the frequencies considered in the RSN used by RanM, as is possible to see in Figure 5.26 and Figure 5.27. This effect in the time-domain can be seen in the MATLAB simulation presented in Figure 2.3, Figure 2.4 and Figure 2.5.

Thus, even in a complex case with $T_m = 100$ ms, it's possible to have the stable EMI measurements. Changing the understanding that the EMI measurements such as presented in Figure 5.24 and Figure 5.25 show a reduction of the EMI noise level, whether compare with Figure 5.12 and Figure 5.13. When actually what is happening in the case of Figure 5.24 and Figure 5.25, it's a mismatch between the PWM signal generated by the RanM, T_m , and RBW. It should be noted that in both cases of Figure 5.26 and Figure 5.27, the time range of the EMI measurements was increased to see better the RanM3 performance, as well the narrow range of frequencies assessed was considered around the $f_0 = 80$ kHz.

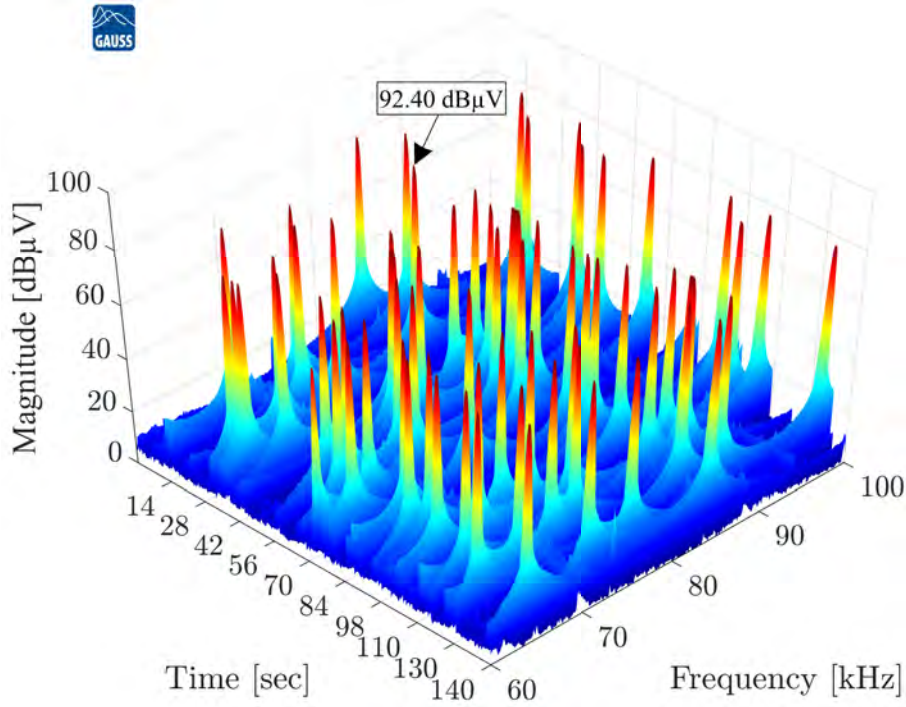


Figure 5.27: The RanM3 presented in Figure 5.25, however with $k = 4 \times 10^5$.

5.3.3 Shaping the Pseudo-random Modulation 3

This subsection 5.3.3 is based on the subsection 4.2.7, which presents a method that also split the distribution of N_m to sub-ranges, as previously presented in subsection 4.2.3. However, the central approach is the strategic increase of the N_m calculation blocks, as illustrated in Figure 4.15, based on the RanM3 implementation (see subsection 5.3.2). Thus, the calculation is performed by the IDE NI PXIe-8135, which provides the possibility to manipulate the δ_N within a range from 10% to 50%, consequently generating a "gap" between the sub-ranges of N_m defined. The opposite approach of the one presented by the Figure 5.20 and Figure 5.21.

Furthermore, it is noteworthy that the RanM3 (see subsection 5.3.2) consider the $RSC_{TL} \in \langle 7, 13 \rangle$. Thus, it is essential to pay attention to the fact that even considering a short RSN, e.g. $\delta_N < 10\%$ (remembering that $N_{AV} \pm \delta_N/2$, see subsection 4.2.1), this RSN once attributed to N_m and N_{dm} will have their frequency spread increased (see subsection 4.2.4). The question arises as to which part of the frequency spectrum needs to get rid of EMI noise, i.e., make use of the "gap."

The central motivation of this thesis (see section 1.1), is related to the low frequency range, a potential case could be related with PLC system [52], [129]. Assuming 63 kHz as the frequency to avoid, i.e., where it is necessary to provide the "gap" in the frequency spectrum, then, the next step with shaping the RanM3 approach is to define the % to be considered by the variable δ_N . This concept is illustrated

in Figure 4.20-part I as the use of the selection function (S_F) between two central frequencies. Figure 5.28 illustrates the possibilities for δ_N definition and splitting.

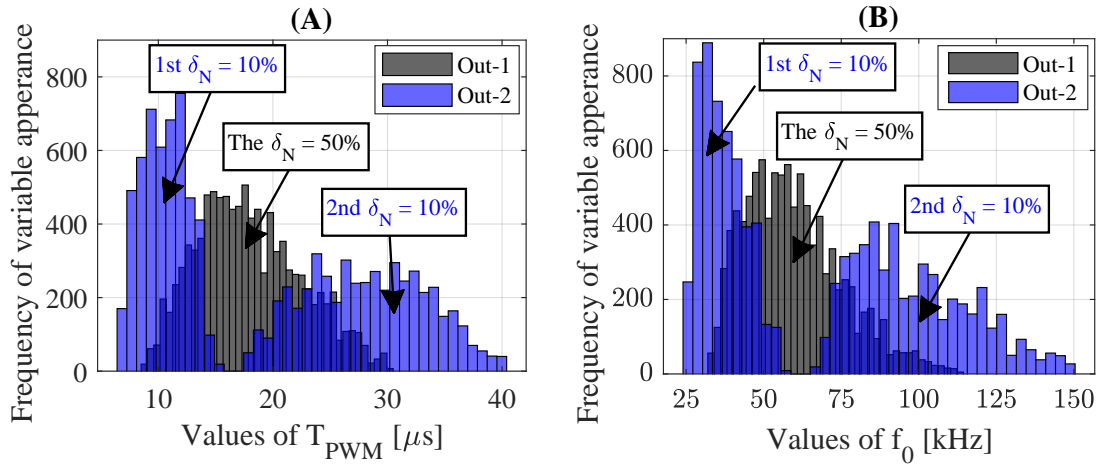


Figure 5.28: Illustration for δ_N definition and splitting.

In both cases of Figure 5.28-A and Figure 5.28-B two MATLAB simulated *Out* are presented. The *Out* – 1 considers a single range of N_m with $\delta_N=50\%$ around 63 kHz, i.e., from ≈ 47 kHz to ≈ 79 kHz. On the other hand, the *Out* – 2 considers two sub-ranges of N_m , each one with $\delta_N=10\%$. The first sub-range of N_m is around 36 kHz, i.e., from ≈ 34 kHz to ≈ 38 kHz, and the second sub-range of N_m is around 98 kHz, i.e., from ≈ 93 kHz to ≈ 103 kHz.

It is noteworthy that even considering $\delta_N=10\%$ and getting the density distribution closer to the Gaussian, the random stream N_m have their frequency spread increased due to the multiplication with the additional random stream RSC_{TL} . Nevertheless, by adopting two sub-ranges of N_m , each one with $\delta_N=10\%$ as presented in Figure 5.28, the narrow band of frequencies around the 63 kHz gets rid of EMI.

Therefore, the proposal of δ_N definition and splitting illustrated by Figure 5.28, was consider by the LabVIEW implementation in the IDE NI PXIe-8135 with the EMC-test bench system (see Figure 5.2). The Figure 5.29, Figure 5.30 and Figure 5.31 refer only to the QP detector measurements, since there was no great variation between the conducted EMI measurements with AV and QP detectors as presented in the subsection 5.3.1 and subsection 5.3.2.

From the EMC assurance point of view, Figure 5.31 presents the results of shaping the RanM3 approach. Assuming that the EMI removal can increase the PLC system reliability. Figure 5.31 shows a 66 dB reduction around 63 kHz, when comparing the two indexes presented by the same Figure 5.31.

Furthermore, by increasing the k values, the switching rate of change begins to adapt to the RBW, consequently to the dwell time ($T_m = 100$ ms) used by the TDEMI X6 EMI test receiver. Moreover, in the case of shaping the RanM3 approach,

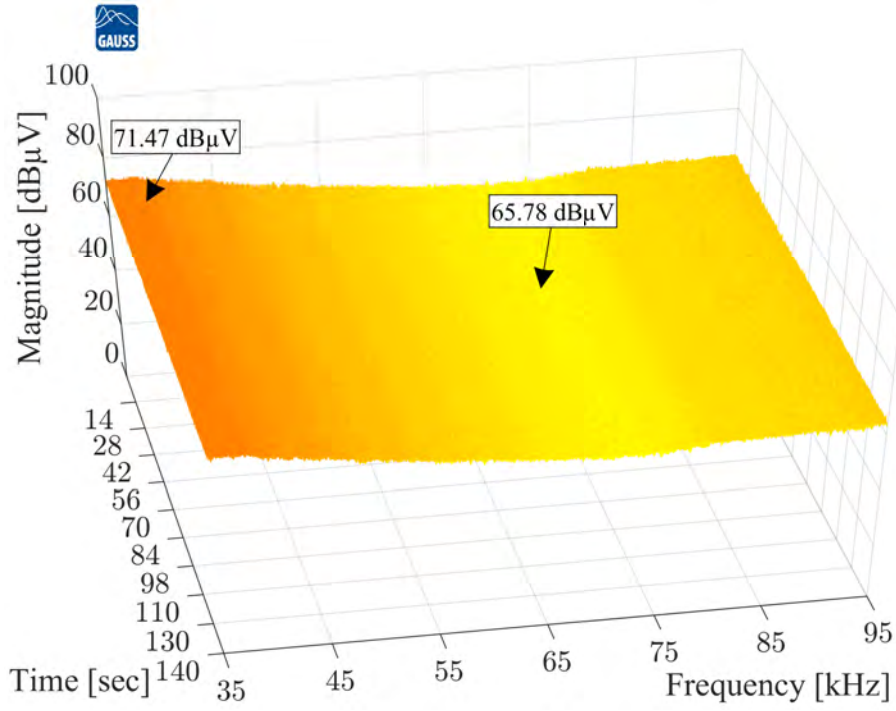


Figure 5.29: The EMI shape with two $\delta_N=10\%$ and $k=1$. Shaping the RanM3 approach with QP detector.

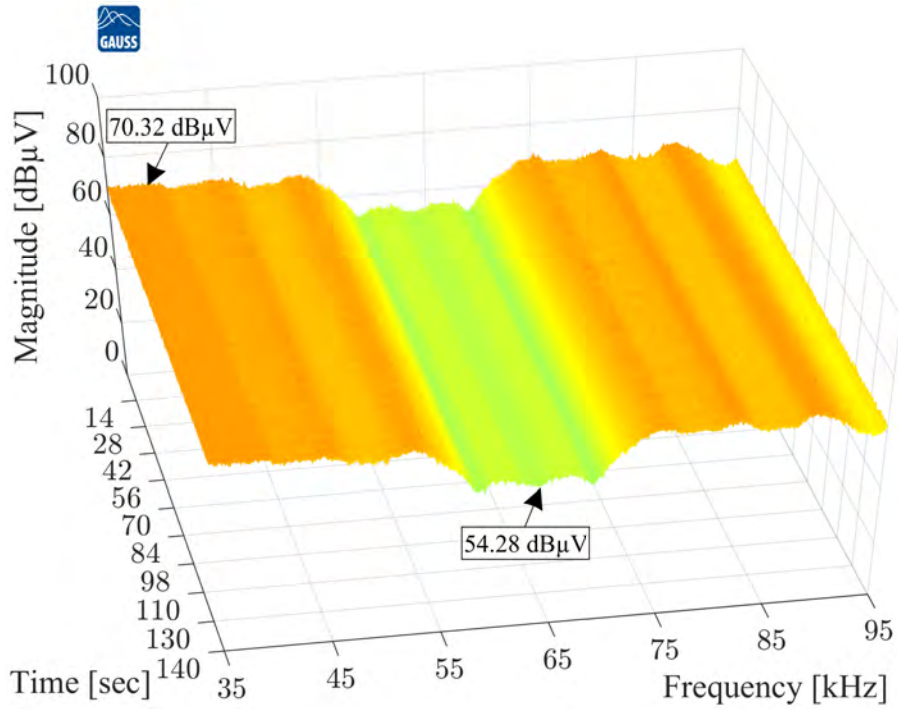


Figure 5.30: The EMI shape with two $\delta_N=10\%$ and $k=100$. Shaping the RanM3 approach with QP detector.

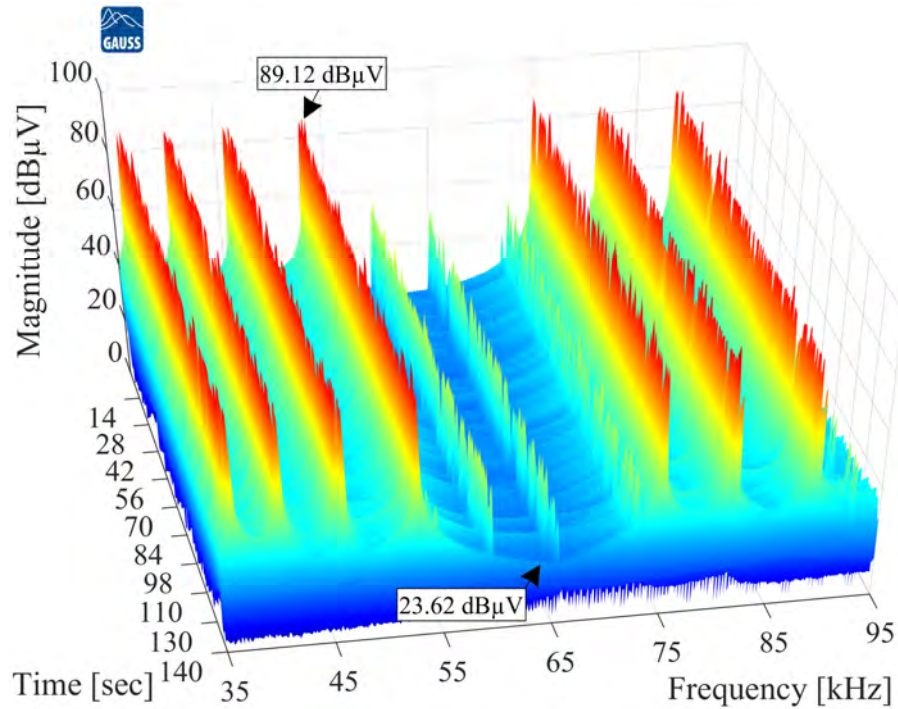


Figure 5.31: The EMI shape with two $\delta_N=10\%$ and $k = 4 \times 10^4$. Shaping the RanM3 approach with QP detector.

by increasing the k values, also means the possibility to see the v -shape in the frequency spectrum, e.g., as compared with Figure 5.29 with Figure 5.31. Therefore, from Figure 5.29 to Figure 5.31 is exemplified the relationship between δ_N and sub-ranges for N_m , assuming the frequency to avoid is 63 kHz. It is noteworthy that the choice of sub-ranges for N_m and the % of δ_N depend on the expected EMI noise shape, i.e., EMC compliance. There is a drawback to considering sub-ranges for N_m from the power electronic converter point of view, as obtaining a single frequency becomes unlikely. However, this is an additional feature that shows how the EMC-test bench system, primarily controlled by a CPS, can be considered a reliable and "EMC-friendly" controller.

The section 5.4 presents further investigations on the benefits of using shaping the RanM3 approach from the PLC system point of view.

5.3.4 Aggregated Conducted EMI with Deterministic and Pseudo-random Modulation

As mentioned through chapter 2, chapter 3 and chapter 4, as well as discussed in section 1.1 of chapter 1. EMC issues due to the EMI generated by single DC/DC converter, or by IPEM systems, operating in the CISPR A frequency band (from 9 kHz to 150 kHz) become a real predicament [11], [72], [79]. Also, in some situations,

the DC/DC converters or the IPEM systems must operate for the concept of parallel electrical installations' topologies [45]. Thus, the low frequency envelope provided by the frequency beat might appear [44], [140]. As discussed in depth in section A.3 (see Figure A.10) and in section 5.2, this phenomenon might be attributed to the f_0 with different frequency stabilities.

Therefore, to evaluate the IPEM system where each DC/DC converters has a f_0 with its own frequency stability, the EMC-test bench system implemented for a pair of two-transistor step-down DC/DC converters, highlighted in Figure 5.4 and Figure 5.5 was considered. It is noteworthy that even the two-transistor step-down DC/DC converter being a sub-module that integrates an inverter hardware system, as presented in [24]. It was necessary to consider two inverter hardware systems, each one with a dedicated FPGA PXI-7854R, to assess the low frequency envelope (see also appendix C). Furthermore, for comparison purposes, Figure 5.32 and Figure 5.33 firstly presents the AV and QP detectors measurement for a single two-transistor step-down DC/DC converter with DetM.

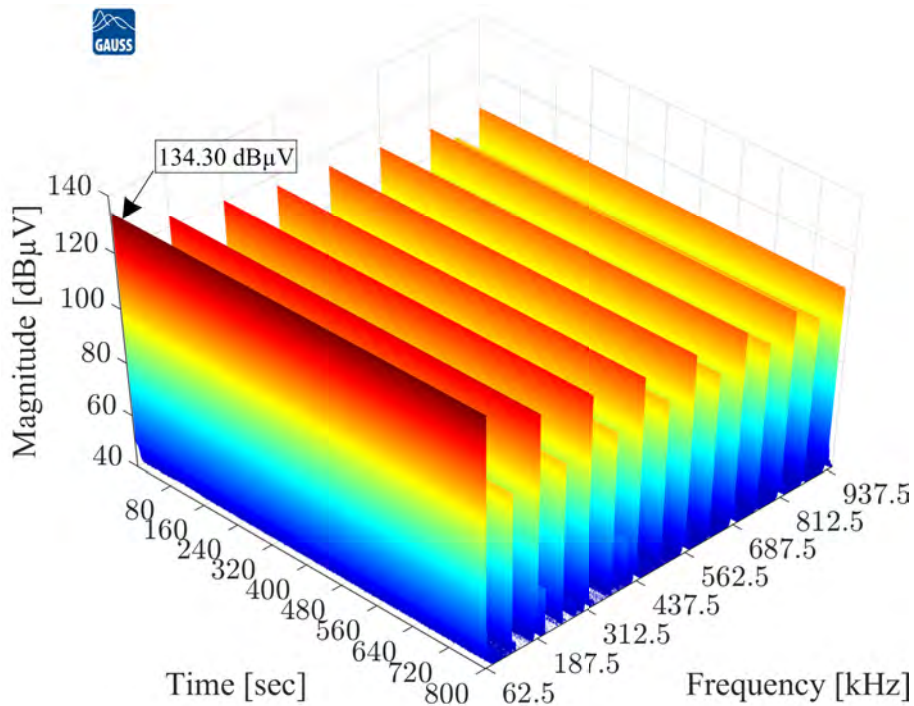


Figure 5.32: The EMI shape of a single two-transistor step-down DC/DC converter with DetM, $D \approx 50\%$, $f_0 = 62.5$ kHz and AV detector.

Figure 5.32 and Figure 5.33 first reinforce the EMI measurements presented in the section 5.3, Figure 5.10 for a $D \approx 50\%$. However, it is important to note that in the case of Figure 5.32 and Figure 5.33, the EMC-test bench system highlighted in Figure 5.4 and Figure 5.5 was considered. Therefore, due to the use of the high voltage differential probe SI-9010A, the EMI noise base level starts at 40 dB.

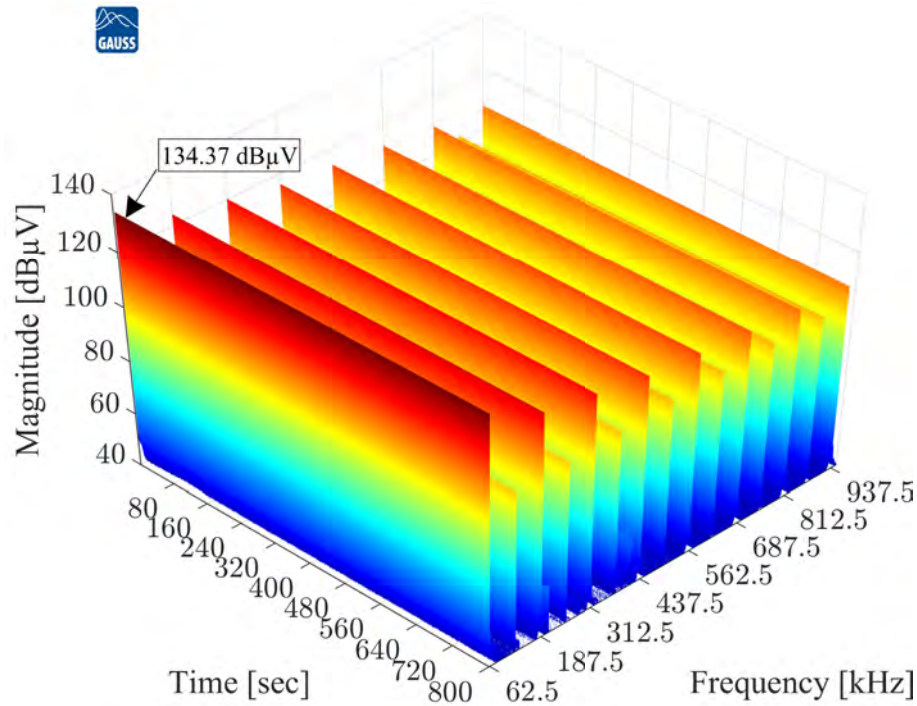


Figure 5.33: The EMI shape of a single two-transistor step-down DC/DC converter with DetM, $D \approx 50\%$, $f_0 = 62.5$ kHz and QP detector.

Nevertheless, the magnitude range of the EMI noise level is the same between Figure 5.32, Figure 5.33 and Figure 5.10, for AV and QP detectors.

Furthermore, to provide a more straightforward analysis of low frequency envelopes phenomenon under the spectrum. In the case of Figure 5.32, Figure 5.33, Figure 5.34 and Figure 5.35, it was considered to assess harmonics components distribution until the 15th harmonic order.

The other parameters used in the EMI measurements presented in Figure 5.32, Figure 5.33, Figure 5.34 and Figure 5.35, follow the CISPR 16-2-1 standard (see Table 3.1 of the subsection 3.4) [78]. Figure 5.34 and Figure 5.35 refer to the AV and QP detectors measurement for a pair of two-transistor step-down DC/DC converters, where both considered DetM, $D \approx 50\%$ and $f_0 = 62.5$ kHz. The low frequency envelope due to the frequency beat phenomenon is noticed in all the 15th harmonic orders, where the highest EMI noise level is related with the $f_0 = 62.5$ kHz.

Furthermore, as previously discussed in the section A.3 of the chapter 2. Since each f_0 of each two-transistor step-down DC/DC converter has its own frequency stability, there is a time displacement between the PWM signals (see Figure A.10-C). This situation was presented in the section A.3 of the chapter 2 as improper integration, and treated with the Lebesgue integral, and as is possible to observe by comparing the Figure 5.34 and Figure 5.35 with the Figure A.12, the TDEMI X6 EMI test receiver presents the expected EMI noise shape. Once regardless of the value

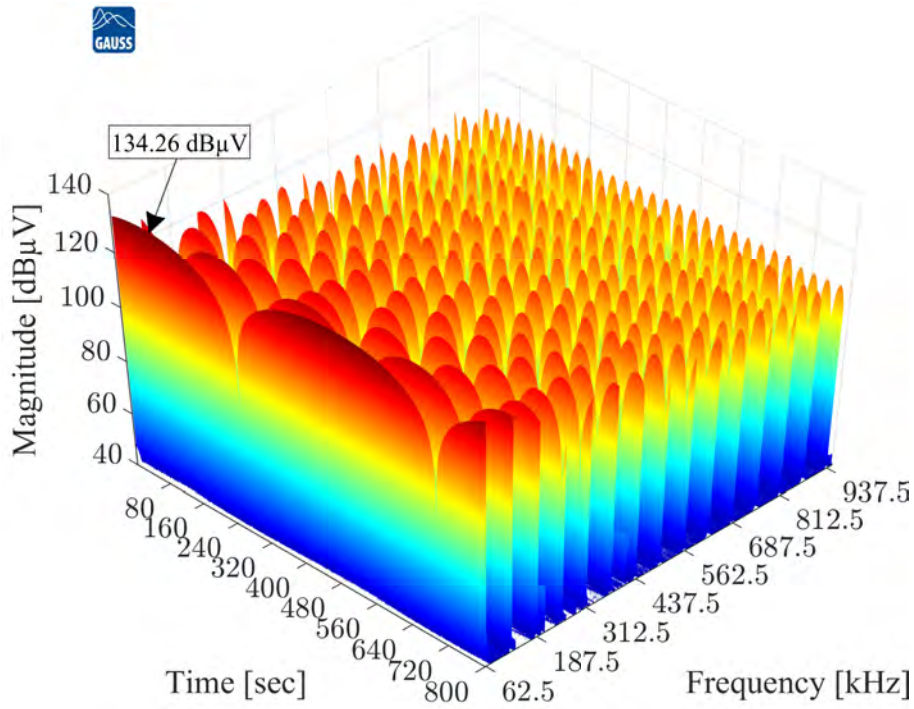


Figure 5.34: The EMI shape of a pair of two-transistor step-down DC/DC converters, where both consider DetM, $D \approx 50\%$, $f_0 = 62.5$ kHz and AV detector.

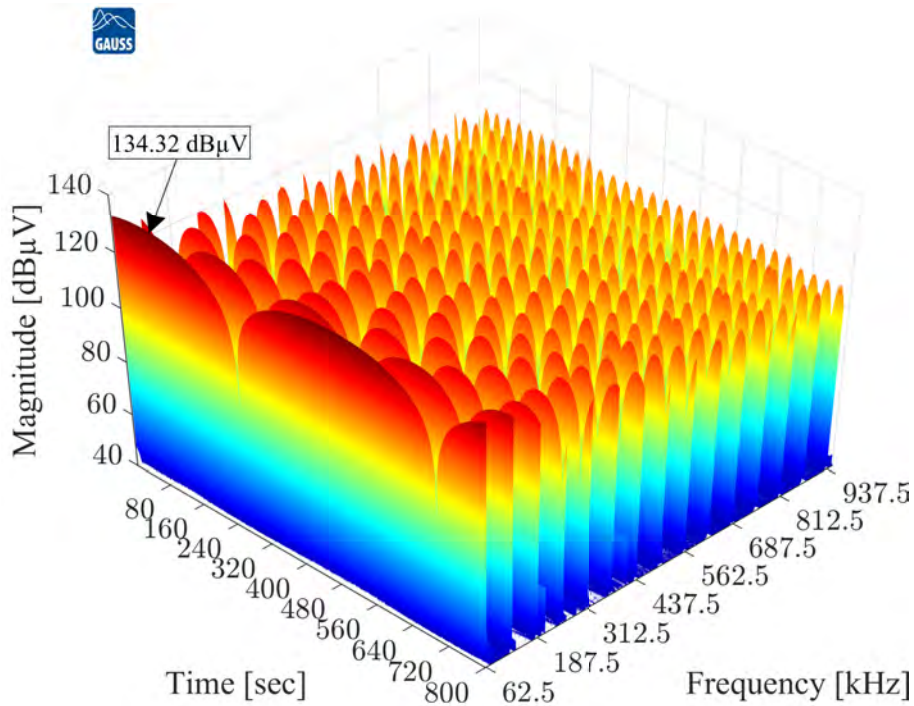


Figure 5.35: The EMI shape of a pair of two-transistor step-down DC/DC converters, where both consider DetM, $D \approx 50\%$, $f_0 = 62.5$ kHz and QP detector.

of harmonic order, the change due to the frequency beat only affects EMI noise amplitude over time, i.e., a constant decrease of the spectrum power density as the harmonic order values increase was expected (see also appendix C).

In the case of Figure 5.34 and Figure 5.35, the frequency beat is strictly due to the FPGA PXI-7854R. In other words, the frequency stability of each crystal oscillator within the FPGA PXI-7854R controller, which is usually represented in ppm (parts per million). According to the presented in Figure A.10-C, the frequency beat might appear at $\left| -\frac{1}{(f_0-f_1)} < t < \frac{1}{(f_0-f_1)} \right|$. The term $|f_0 - f_1|$ can be considered such as $|f_0 - f_1| = (f_0 \cdot ppm)/10^6$. Thus, in the case of the FPGA PXI-7854R, considering $f_0=62.5$ kHz and ± 100 ppm, the frequency beat might appear at $t=0.32$ s. Nevertheless, the frequency stability variation of the f_0 depends on external conditions like temperature variation, voltage variation, output load variation, and frequency aging. In the case of Figure 5.35 (the same applies for Figure 5.34), Figure 5.36 shows the frequency beat with $t=420$ s, i.e., $f_0=62500$ Hz ± 0.00476 Hz.

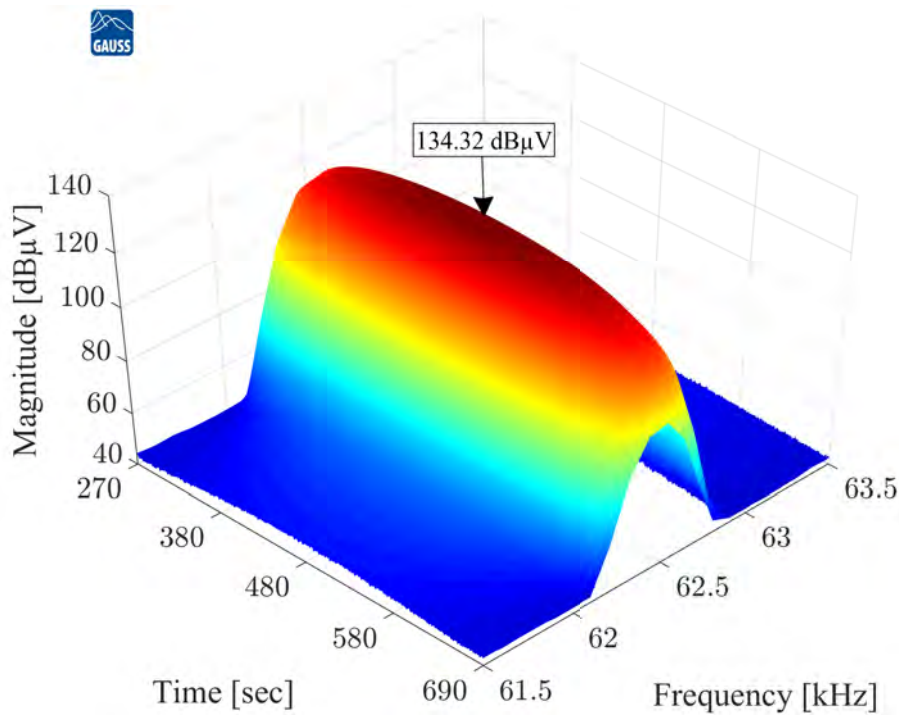


Figure 5.36: The frequency beat with $t=420$ s and $f_0=62500$ Hz ± 0.00476 Hz, in the case of Figure 5.35.

Additionally, as presented in subsection 4.1.1 of the chapter 4, the IDE NI PXIe-8135 can be used in the EMC-test bench system considering several DC/DC converters. Thus, among all the illustrated logical blocks in Figure 4.2, the *watchdog* and *trigger* blocks have a highly relevant role for timing and synchronization of multiple FPGAs. From the LabVIEW project point of view, the *watchdog* and *trigger* blocks represents the hardware path enabling the timing and synchronization func-

tion (TSF) of several application instances based on TTL triggers (see the *PXI Triggers* path of Figure 4.2, Figure 4.3 and Figure 4.6).

To illustrate the TSF , Figure 5.37 show the QP detector measurement, based on the EMC-test bench system implemented for a pair of two-transistor step-down DC/DC converters, highlighted in Figure 5.4 and Figure 5.5. The TSF was deactivated at the $t \approx 150$ s. Then, clearly, it is possible to observe the low frequency envelope.

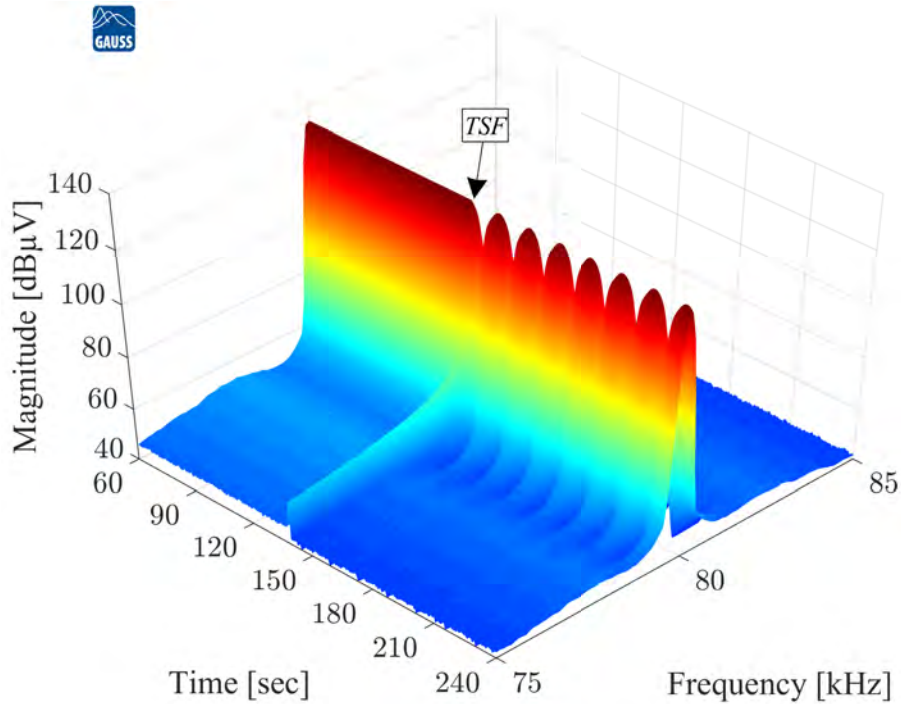


Figure 5.37: The EMI shape of a pair of two-transistor step-down DC/DC converters, where both considered DetM, $D \approx 50\%$, $f_0 = 80$ kHz, and QP detector. The TSF deactivation at the $t \approx 150$ s.

Therefore, Figure 5.37 reinforces how the TSF function made possible by the CPS hardware and software infrastructure is essential for the execution of a reliable EMC analysis. Once regardless of the increase in the number of control hardware, i.e., DC/DC converters, it is possible to establish clock synchronization between all the application instances.

Based on Figure 5.37, the Figure 5.38 shows the TSF implemented in the LabVIEW project, with two application instances, each one dedicated for one DetM. As a drawback of the TSF implementation, just one application instance, i.e., one VI can execute both VI (the message highlighted in the error list box, details field, in the lower center of the Figure 5.38). Nevertheless, by accepting synchronization, both VI operate properly and synchronized.

On the other hand, RanM can also be used in IPeM systems where each DC/DC

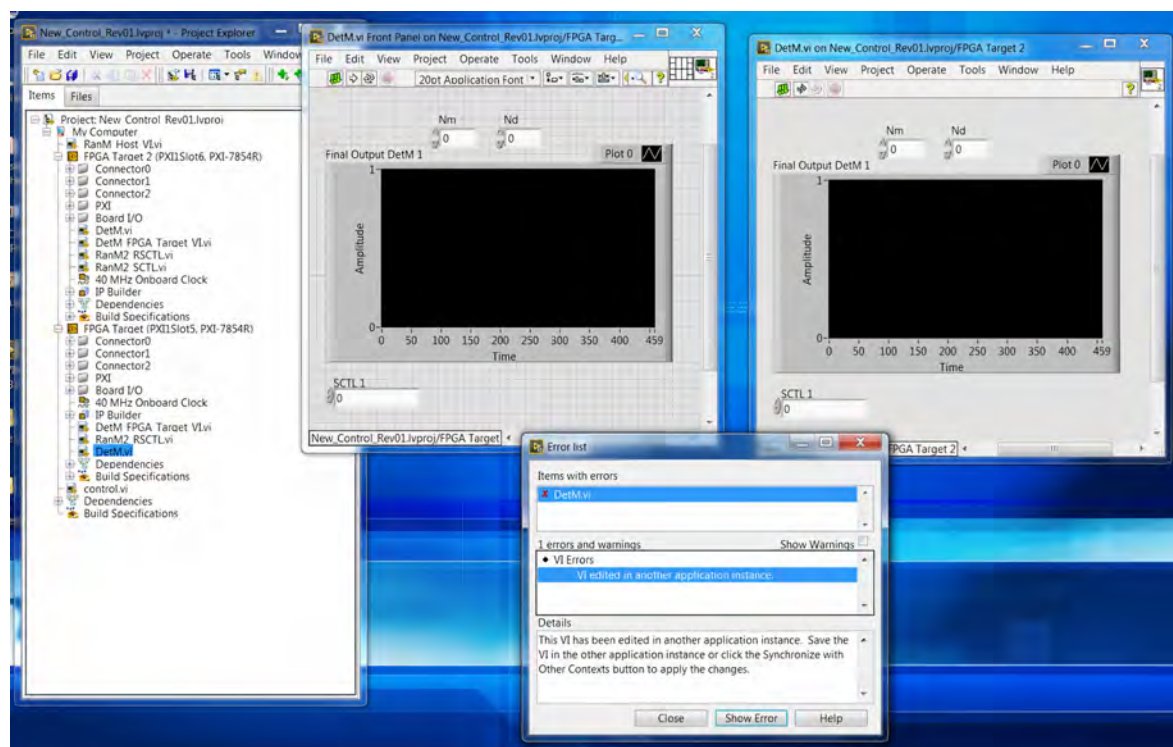


Figure 5.38: The TSF implemented in the LabVIEW project with two VI.

converters has a f_0 with its own frequency stability. Based on [44], both the Figure 5.39 and Figure 5.40 in the form of box-and-whisker plots, presents the results for AV detector measurement, comparing DetM with the RanM2 with RSC_{TL} (see subsection 4.2.4). For each investigated case 1,000 final measurements during 1 s were taken [44], [141].

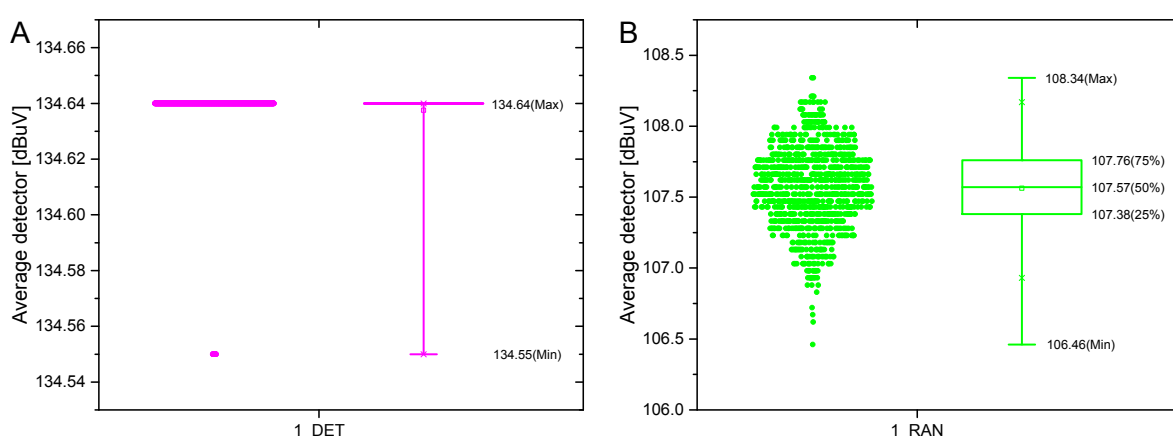


Figure 5.39: Box-and-whisker plots of 1,000 AV detector 1 s measurements for one two-transistor step-down DC/DC converter with: (A) DetM and (B) RanM2 with RSC_{TL} (see subsection 4.2.4).

Since the conducted EMI standards consider one final measurement for one

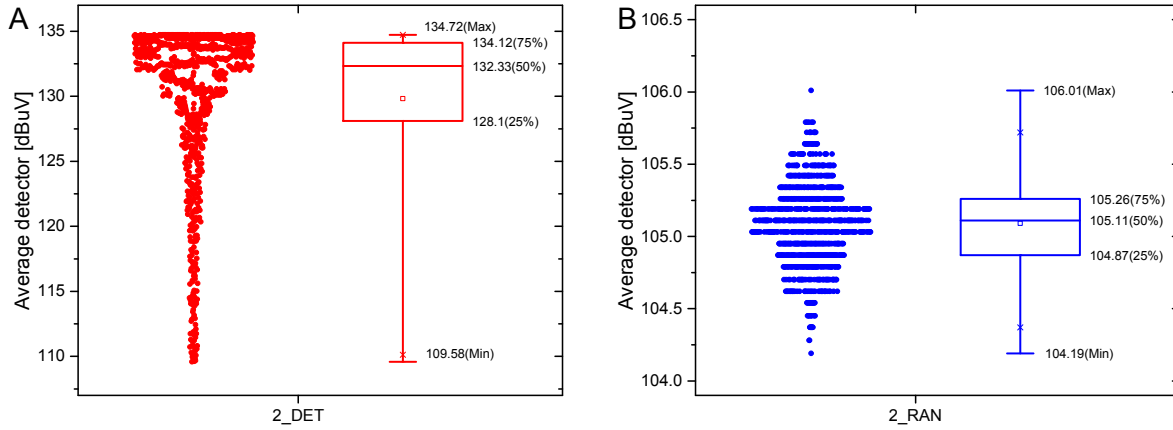


Figure 5.40: Box-and-whisker plots of 1,000 AV detector 1 s measurements for a pair of two-transistor step-down DC/DC converters with: (A) DetM and (B) RanM2 with RSC_{TL} (see subsection 4.2.4).

selected frequency as sufficient [78]. The distribution of the results obtained for the two-transistor step-down DC/DC converter with DetM, in Figure 5.39-A, confirms that such an approach is reasonable.

However, low frequency envelopes, linked with the frequency beat phenomenon and accompanying aggregation of EMI introduced by a pair of two-transistor step-down DC/DC converters with DetM, caused a significant increase in the range of measured levels. The observed differences reached 25 dB (18 times), Figure 5.40-A. Thus, this difference between each measurement of 25 dB makes EMC assessment unreliable for a pair of DC/DC converters with DetM.

The comparison between Figure 5.39-B and Figure 5.40-B, shows a 2 dB dispersion remained unchanged in the case of aggregated EMI introduced by the two-transistor step-down DC/DC converters with RanM2 with RSC_{TL} (see subsection 4.2.4). However, as discussed in subsection 5.3.1 and presented in subsection 5.3.2, the spreading of the spectrum components will always be a consequence of the RanM utilization.

Therefore, It becomes imperative to find the tradeoffs between RanM, dwell time (T_m) and RBW to achieved a stable EMI measurement, as dicussed in subsection 3.5 and reached through RanM3, see Figure 5.26 and Figure 5.27. Otherwise, the RanM approaches can lead to wrong conclusions about one EMI noise level reduction, when actually what is happening is a mismatch between the RanM, T_m , and RBW.

5.4 EMI Noise Shaping with Power Line Communication System

In this section 5.4, the EMI effects generated by a two-transistor step-down DC/DC converter with shaping the RanM3 approach (see subsection 5.3.3), in the PLC system through inductive coupling is evaluated ⁴.

5.4.1 Experimental Setup Description

Considering that many PLC systems operate in the CENELEC frequency band (from 3 kHz to 150 kHz). The PLC technology must consider a robust modulation to establish the sending data process, such as Orthogonal Frequency Division Multiplexing (OFDM). The main advantage of using OFDM over techniques that use a single carrier is that it can achieve a high transfer rate, due to the parallelism of subcarriers, with greater resistance to EMI in the communication channel [142].

The OFDM principle to establish the sending data process is the conversion of a N serial data symbols into multiple N parallel data symbols. For example, as illustrated in Figure 5.41, a set of N serial data symbols is transformed into an OFDM symbol, representing N data in parallel. After serial-parallel conversion, each sub-stream of N data is modulated on a subcarrier, such as $f_0, f_1, \dots, f_{N-2}, f_{N-1}$.

The core idea of OFDM-based spectrum sharing is to make the width of the PLC system band an integer multiple of the space Δf (as illustrated in Figure 5.41) used by each subcarrier of the PLC system. Thus, in order to investigate the EMI effects generated by a two-transistor step-down DC/DC converter with shaping the RanM3 approach (see subsection 5.3.3) in the PLC system. The connection diagram presented in Figure 5.42 was established as the experimental setup, as presented in Figure 5.43.

The EM represented by Figure 5.42 and Figure 5.43 shows both communication and power electronic circuits of the experimental setup. The communication circuit consists of two PL360 Microchip modems, used as the transmitter (PLC Tx) and the receiver (PLC Rx). The PL360 is a programmable modem with state-of-the-art narrow-band PLC standards ITU G.9903 (G3-PLC). The two PL360 Microchip modems are connected by a 42 m single-phase cable representing the PLC system's point-to-point connection. Table 5.2 shows the G3-PLC specification used in the experimental setup (Figure 5.42 and Figure 5.43).

The LISN and an isolation transformer illustrated in Figure 5.42 and Figure 5.43 are utilized to isolate the communication and power electronic circuits from grid dis-

⁴Parts of this section 5.4, at the time of writing this PhD thesis, are being used for a journal paper proposal.

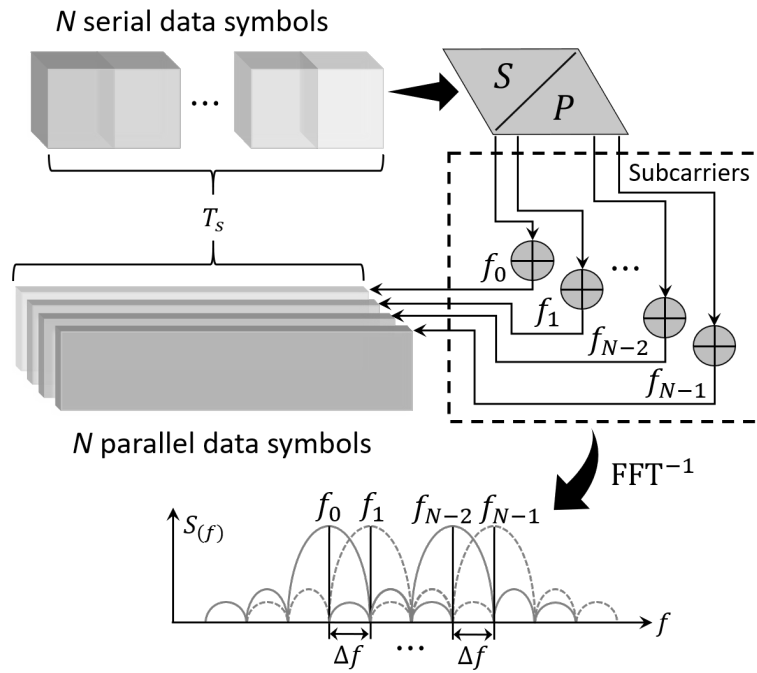


Figure 5.41: A simple idealized OFDM system model (transmitter) highlighting the conversion of N serial data symbols into N parallel data symbols.

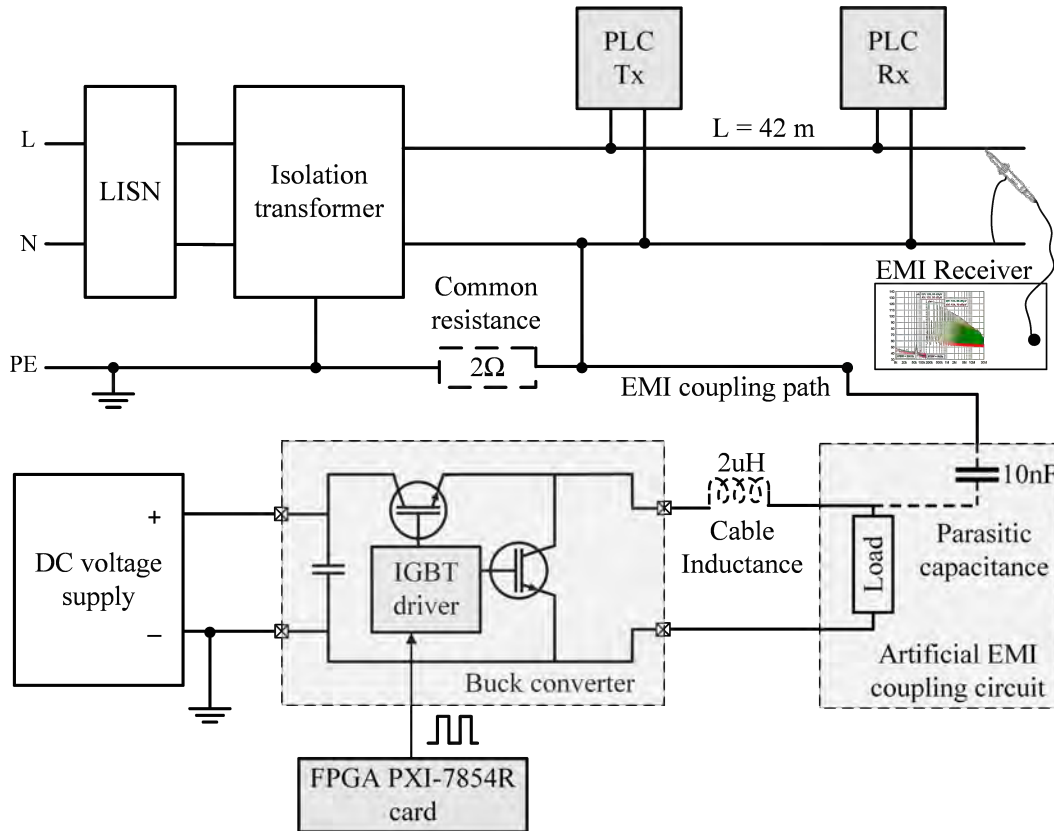


Figure 5.42: Connection diagram of the experimental setup.

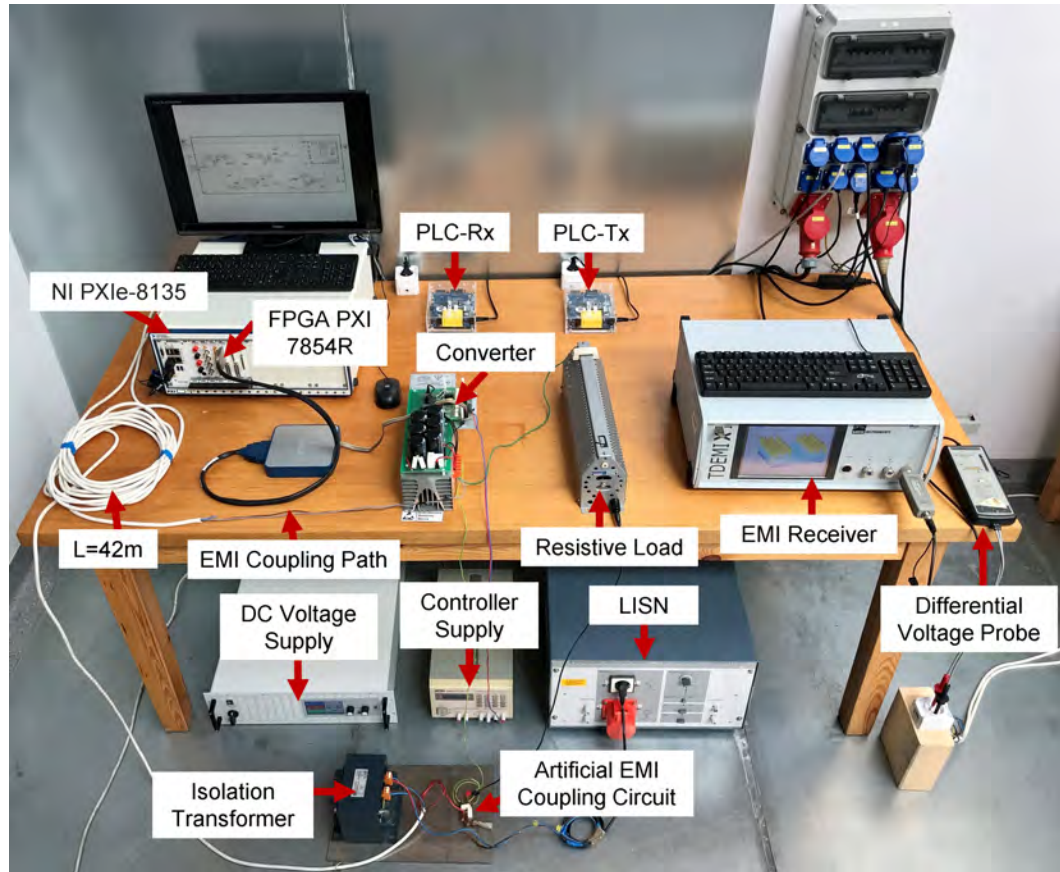


Figure 5.43: The experimental setup.

Table 5.2: The G3-PLC specification used in the experimental setup.

G3-PLC	Specification
Narrow-band	From 35 kHz to 91 kHz
Sampling Frequency	400 kHz
Subcarrier Spacing	1.5625 kHz
No. of Carriers Used	36
Length of Cyclic Prefix	30
Modulation Scheme	DBPSK
Total Sent Frames	3000
Frame Interval	100 ms

turbances. Both circuits are connected to the same ground through a common resistor. The power electronic circuit is inductively coupled with the communication circuit through the EMI coupling path, and as the source of conducted EMI was considered the two-transistor step-down DC/DC converter, operating at 24V.

The two-transistor step-down DC/DC converter affects the communication circuit through an artificial EMI coupling circuit, considering a parasitic capacitance

as shown in Figure 5.42 and Figure 5.43. The parasitic capacitance could appear because of the load enclosure or any other reason. Usually, the two-transistor step-down DC/DC converter contain an EMI filter. However, to gain an in-depth comprehension of this investigation, the EMI filter wasn't considered in the experimental setup. Further information about the EMI's standardized measurement procedures can be found in section 5.1 and section 5.3.

5.4.2 Data analysis

Assuming the narrow-band from 35 kHz to 91 kHz, the two-transistor step-down DC/DC converter was programmed to operate with a $f_0=63$ kHz, i.e., in the intermediate frequency of the G3-PLC channel. Two operating conditions were analyzed. The first one considers the no shaping approach (see subsection 5.3.2), as presented by the Figure 5.44-A, Figure 5.44-B and Figure 5.44-C. The second one considers the shaping approach (see subsection 5.3.3), as presented by the Figure 5.44-D, Figure 5.44-E and Figure 5.44-F.

It should be noted that once the output harmonic voltage measured and presented in Figure 5.44 considered the probe SI-9010A from Sapphire Instruments (see in Figure 5.43), and the attenuation rate was configured 1/100, the amplitude noise level measured by the EMI receiver started in 40 dB.

From the EMC assurance point of view, it is clearly possible to observe the benefits of the shaping approach. Assuming that the EMI removal around the intermediate frequency of the G3-PLC channel can contribute to the PLC system reliability. Figure 5.44-F shows a 71 dB reduction around 63 kHz compared to Figure 5.44-C. The premise of two sub-ranges of N_m , each one with $\delta_N=10\%$ contributed to the v -shape in the frequency spectrum as expected and presented in Figure 5.44-E and Figure 5.44-F. Thus, finding that it is possible to develop new, dedicated converter control algorithms that allow shaping the spectrum of disturbances to meet standardization or technical requirements.

Furthermore, the larger the k values, the lower the RanM switching rate of change. From the point of view of conducted EMI measurements, the larger the k values, the longer it takes for the EMI receiver demodulation process to correctly charge and discharge the QP envelope detector. The effect of changing the k values can be seen in all cases (from Figure 5.44-A to Figure 5.44-F), for both shaping and no shaping approaches.

To evaluate the FER of the PLC system, the PLC system performance was assessed considering the k values from 1 tick to 40000 ticks (i.e., with Γ values from 0.1 kHz to 4 MHz, see Figure 5.45). Further information about k values can be found in subsection 4.2.6. Since k represents onboard clock frequency values, i.e.,

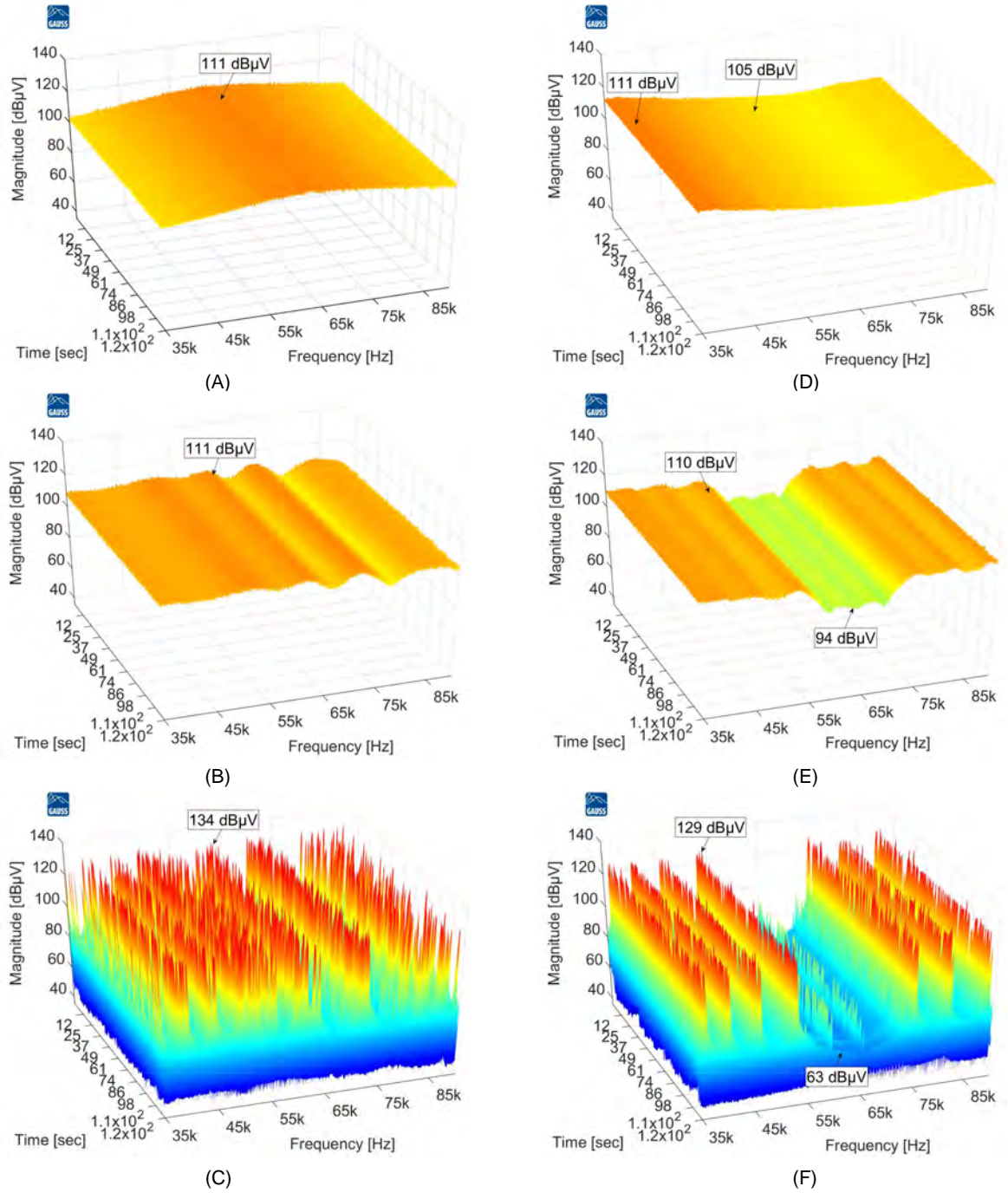


Figure 5.44: EMI shape according to δ_N and k for: **1. No shaping approach:** (A) $\delta_N = 50\%$ and $k = 1$; (B) $\delta_N = 50\%$ and $k = 100$; (C) $\delta_N = 50\%$ and $k = 40000$, and; **2. Shaping approach:** (D) $\delta_N = 10\%$ and $k = 1$; (E) $\delta_N = 10\%$ and $k = 100$; (F) $\delta_N = 10\%$ and $k = 40000$.

clock cycles, its value in frequency can be calculated considering the equation (4.1). Thus, for $k=1$, considering $f_{FPGA}=40$ MHz and $SC_{TL}=10$, then $\Gamma=4$ MHz.

The FER represents the proportion of data received with errors to the total data received. FER is used to determine the quality of a signal connection, if the FER is too high the PLC system connection may drop. When PLC reliability is under investigation, it means ensuring that the quality of the PLC system is consistently performing well under the induced EMI; which fundamentally depends on low FER. However, it should be noted that this thesis does not quantify the EMI-based risk, i.e., whether or not the measured FER can drop the signal connection, as this depends on several aspects such as whether PLC technology considers error correction protocol, which was not the scope of this thesis.

The choice of analyzing the data considering the Γ values from 0.1 kHz to 4 MHz, is properly related to PLC subcarrier spacing ($\Delta f=1.5625$ kHz) and multiples values, e.g. 3 kHz. Also, as mentioned in Table 5.2, the PLC system communication channel assumes a narrow-band from 35 kHz to 91 kHz. Therefore, the EMI noise shaping was designed to provide the *v*-shape in the frequency spectrum from ≈ 34 kHz to ≈ 103 kHz (as mentioned in subsection 5.3.3), and considering the RanM switching rate of change ranging from 0.1 kHz to 4 MHz.

Figure 5.45 shows the FER reaching a value of 73% for the no shaping approach between the Γ values from 1.5 kHz to 3 kHz. On the other hand, to the shaping approach, the FER increases linearly between the Γ values from 0.3 kHz to 3 kHz, reaching a maximal value of 58%.

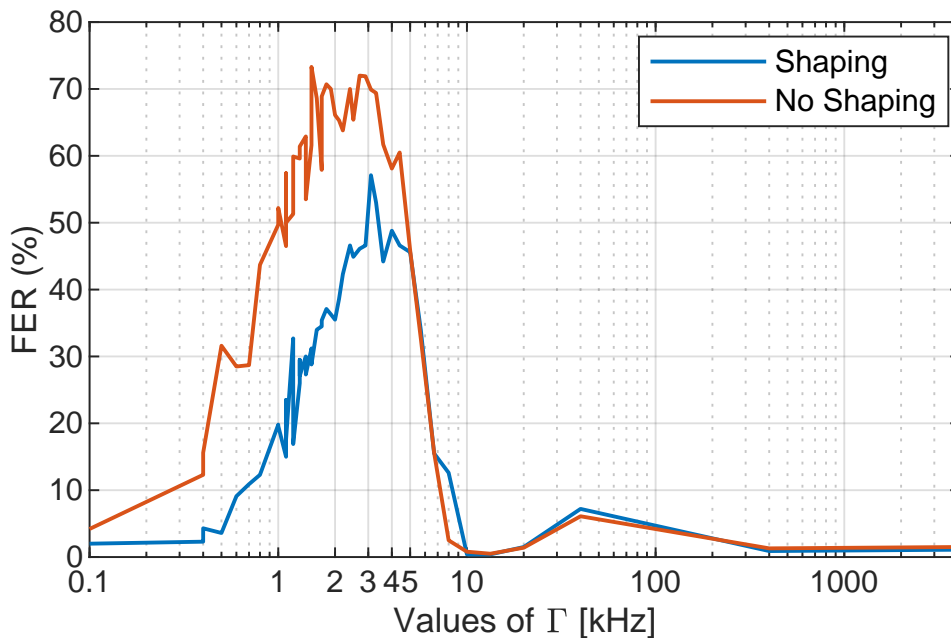


Figure 5.45: FER evaluation under the influence of Γ values from 0.1 kHz to 4 MHz. In both shaping and no shaping approaches.

Plainly, it is possible to observe in Figure 5.45 that according to the Γ values are

closing to the G3-PLC subcarrier spacing ($\Delta f=1.5625$ kHz) and multiples values, e.g. 3 kHz, the FER increases. Figure 5.46 shows the influence of Γ values from 1 kHz to 10 kHz to the PLC system.

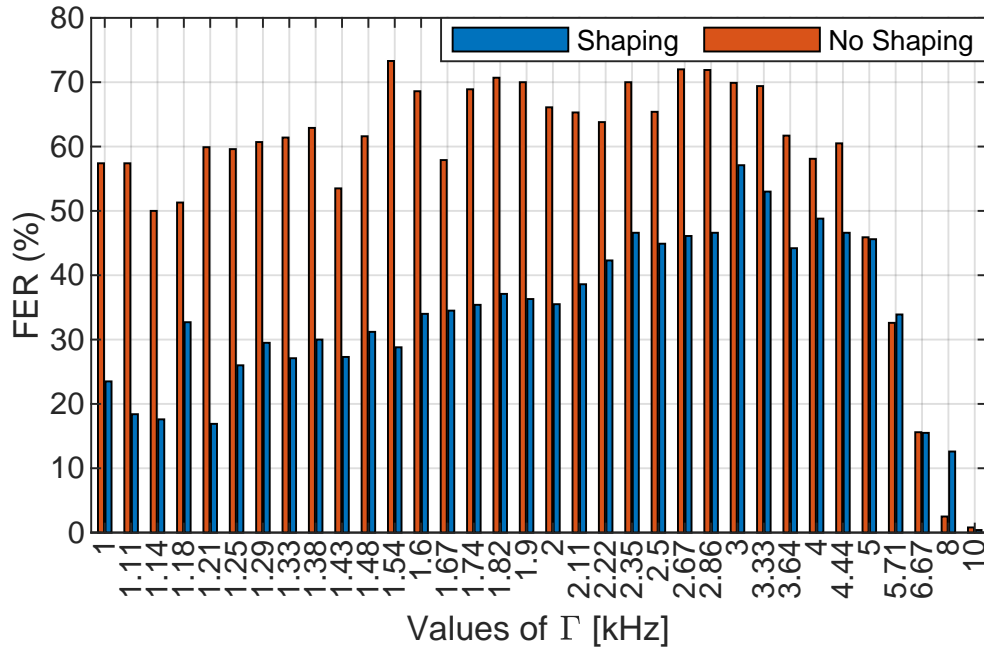


Figure 5.46: FER evaluation under the influence of Γ values from 1 kHz to 10 kHz. In both shaping and no shaping approaches.

Figure 5.46 reinforces the finding that according to the Γ values are closing to the G3-PLC subcarrier spacing ($\Delta f=1.5625$ kHz) and multiples values, e.g. 3 kHz, the FER increases. For example, for the Γ value equal to 1.54 kHz the FER is 73% in the case of no shaping approach (the case presented in Figure 5.44-A, Figure 5.44-B and Figure 5.44-C). Figure 5.46 also shows that for the Γ value equal to 1.54 kHz, however considering the shaping approach, the FER is 29% (the case presented in Figure 5.44-D, Figure 5.44-E and Figure 5.44-F). Therefore, the EMI noise shaping as a method to mitigate induced EMI in PLC system, achieved 61 % reduction in FER for the most sensitive communication frequency band, i.e., around the G3-PLC subcarrier spacing ($\Delta f=1.5625$ kHz). On the other hand, the difference between the shaping approach to the no shaping approach is decreased to 18 % reduction in FER when considered the G3-PLC subcarrier spacing multiples values, e.g. Γ value equal to 3 kHz. Thus, Figure 5.46 shows that, on average for all the Γ value, the shaping approach provides up to 30 % reduction in FER.

The Figure 5.44, Figure 5.45 and Figure 5.46 reinforce the finding that it is possible to develop new, dedicated converter control algorithms that allow shaping the spectrum of disturbances to meet standardization or technical requirement. Since from the point of view of standardization requirements, it becomes possible to re-

duce the level of EMI noise, and on the other hand from the point of view of technical requirements, it becomes possible to decrease the level of interference for the PLC system. Thus, the concept of EMI noise shaping provides an alternative to the debates dealt with in the literature on the use of DetM or RanM modulation as EMI mitigation techniques [143].

Figure 5.47 presents the probability for normal distribution, aiming to assess the similarities between some of the Γ values presented in Figure 5.45 and Figure 5.46 with the G3-PLC subcarrier spacing and multiple values.

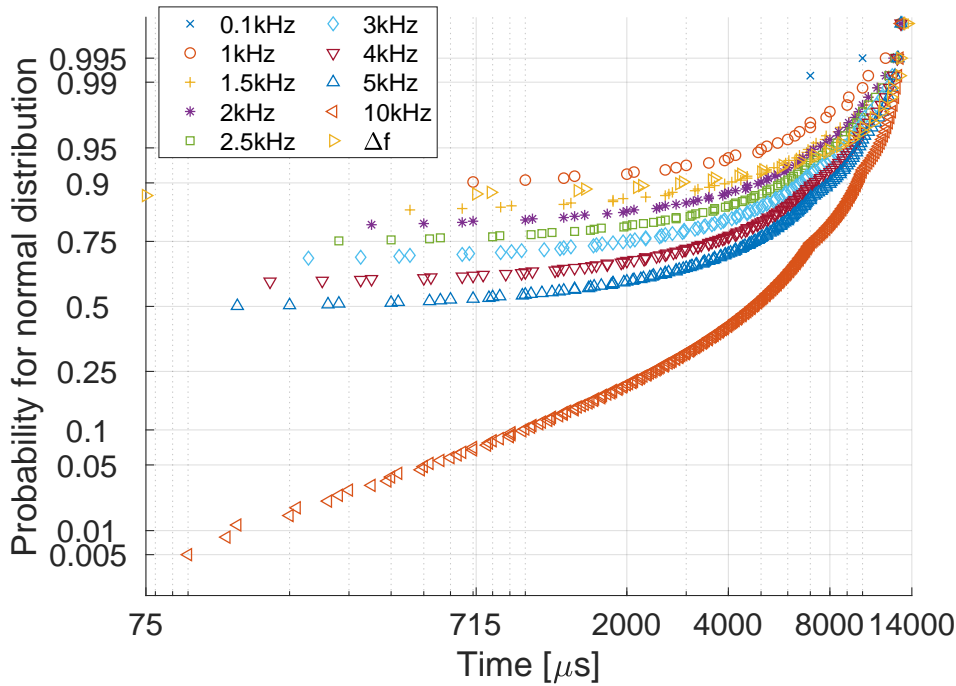


Figure 5.47: Probability for normal distribution of the G3-PLC subcarrier spacing and multiple values with the Γ values presented in Figure 5.45 and Figure 5.46.

Through the analysis of the probability for normal distributions presented by Figure 5.47, it becomes possible, firstly, to observe the probability of the Γ values appearing at the same time as the G3-PLC subcarrier spacing ($\Delta f = 1.5625$ kHz) and multiple values. Figure 5.47 starts in time with the value of $75 \mu s$, which is the cyclic prefix length used by the G3-PLC system. Then, from $75 \mu s$ to $715 \mu s$ is the first G3-PLC data sending process hypothetical at $\Delta f = 1.5625$ kHz (which is repeated over time, as presented in Figure 5.47). Thus, as the Γ values are closing to the 1.5 kHz and multiples values, e.g. 3 kHz, the greater is the probability of its appearing at the same time as the G3-PLC subcarrier spacing ($\Delta f = 1.5625$ kHz). However, Figure 5.47 reinforces that it is not enough just to appear at the same instant of time, which indeed happens with all Γ values presented in Figure 5.47, but the normal

distribution must have the same probability. For example, both the Γ values of 1.5 kHz and 10 kHz appear at or near the instant of time that $\Delta f = 1.5625$ kHz appears, nevertheless, the probability of normal distribution of the $\Gamma = 1.5$ kHz at $715 \mu s$ is ≈ 0.86 , i.e., similar to the probability of normal distribution of $\Delta f = 1.5625$ kHz. On the other hand, the probability of normal distribution of the $\Gamma = 10$ kHz at $715 \mu s$ is ≈ 0.075 , thus, even appearing at the same instant of time as $\Delta f = 1.5625$ kHz, the probability of the norm distributions converge is low.

5.5 Summary

This chapter 5 presented the conducted EMI measurements for all modulation algorithms described in chapter 4. The main assumption considered that the functionality of any IPEM depends heavily on the switching behavior of each sub-modules, i.e., of each DC/DC converters [11], [130], [131]. The EMC-test bench systems used to carry out the conducted EMI measurements were presented in section 5.1, as highlighted in Figure 5.1, Figure 5.2, Figure 5.4 and Figure 5.5.

Thus, firstly, to recognize and validate the behaviour model of the rectangular pulse trains discussed in depth in chapter 2 as well as the modulation algorithms proposed and discussed in chapter 4. The CE behaviour is assessed in section 5.2, intending to broaden the understanding of the DC/DC converters behaviour when is considered the D variation and f_0 with different frequency stabilities. Then, the other standardized EMI measurement procedures were presented in the section 5.3.

All the conducted EMI measurements presented in subsection 5.3.1 stand under the assumption that the bandwidth in which the spectrum components are spread by the adopted RanM techniques is much larger than the RBW and dwell time (T_m) used by the TDEMI X6 EMI test receiver. Thus, through the evaluation of all conducted EMI measurements presented in subsection 5.3.1, and based on the LabVIEW FPGA implementation presented in subsection 4.2.5, the following observations can be made:

- The spreading of the spectrum components will always be a consequence of the RanM utilization. The more appropriate the PDF used to generate the PWM signal, the greater the spreading effect becomes, as in the case of the Figure 5.22 and Figure 5.23;
- However, the EMI noise spreading as presented in subsection 5.3.1 does not mean an EMI noise level reduction or even power spectrum lowering;
- Once the RanM provides changes in the frequency of a given PWM signal and also provides random changes between the frequencies considered in

this PWM signal. It becomes imperative to find the tradeoffs between $RanM$, T_m and RBW to achieved a stable EMC measurement, as dicussed in chapter 3, subsetion 3.5.

Consequently, as introduced by Figure 5.18 and Figure 5.19, which show that when we consider N_m and RSC_{TL} , the power spectral density changes. Furthermore, as also presented by Figure 5.20 and Figure 5.21, where through the $RanM2$ approach, there is a possibility to control the occurrence of frequencies in certain parts of the RSN used by $RanM$. The $RanM3$ was proposed and presented in subsection 5.3.2.

For the conducted EMI measurements presented in subsection 5.3.2, a premise was assumed to consider the shorter T_m possible and adapt the switching rate of change to match the RBW. Therefore by using $k = 4 \times 10^5$, it takes longer to random alternate the frequencies considered in the RSN used by $RanM3$, as is possible to see in Figure 5.26 and Figure 5.27. Thus, even in a complex case with $T_m = 100$ ms, it's possible to have the stable EMI measurements. Changing the understanding that the EMI measurements such as presented in Figure 5.24 and Figure 5.25 show a reduction of the EMI noise level, whether compare with Figure 5.12 and Figure 5.13 (see also the discussion in subsection 5.3.4 about the Figure 5.39 and Figure 5.40).

Once controlling the occurrence of frequencies in certain parts of the RSN used by $RanM3$ becomes possible, it is unavoidable not to think about EMC compliance issues. Thus, the subsection 5.3.3 presented how to shape the $RanM3$ approach. From Figure 5.29 to Figure 5.31 is exemplified the relationship between δN and sub-ranges for N_m . Furthermore, the results presented in Figure 5.44, Figure 5.45, Figure 5.46 and Figure 5.47, reinforce the finding that it is possible to develop new, dedicated converter control algorithms that allow shaping the spectrum of disturbances to meet standardization or technical requirement. Since from the point of view of standardization requirements, it becomes possible to reduce the level of EMI noise, the EMI noise shaping method allowed the removal of its level around 71 dB from the critical fault areas of the PLC system. On the other hand, from the point of view of technical requirements, it becomes possible to decrease the level of interference for the PLC system, achieving on average up to 30 % reduction in FER.

Despite huge potential for use in the context of EMC compliance (see section 5.4), there is a drawback to considering sub-ranges for N_m from the power electronic converter point of view, since obtaining a single frequency becomes unlikely. However, this is an additional feature that shows how the EMC-test bench system, primarily controlled by a CPS, can be considered a reliable and "EMC-friendly" controller.

On the other hand, subsection 5.3.4 presented the aggregated conducted EMI with $DetM$ and $RanM$, considering as a premise such a situation where the DC/DC

converters or the IPEM systems must operate into the concept of parallel electrical installations' topologies [45].

Therefore, since each f_0 of each two-transistor step-down DC/DC converter has its own frequency stability, there is a time displacement between the PWM signals (see Figure A.10-C). This situation was presented in the section A.3 of the chapter 2 as improper integration, and as is possible to observe by comparing the Figure 5.34 and Figure 5.35 with the Figure A.12, the TDEMI X6 EMI test receiver presents the expected EMI noise shape. Once regardless of the value of harmonic order, the change due to the frequency beat only affects EMI noise amplitude over time, i.e., a constant decrease of the spectrum power density as the harmonic order values increase was expected (see also appendix C).

Additionally, as presented in subsection 4.1.1 of the chapter 4. The IDE NI PXIe-8135 can be used in the EMC-test bench system considering several DC/DC converters. Thus enabling the timing and synchronization function (*TSF*) of several application instances, as presented in Figure 5.37.

Conclusions and Directions for Further Research

Firstly, this chapter 6 will briefly recap that the central motivation of the research carried out and presented in this thesis is based on the emission and immunity aspect (limit lines) of the EMI level assessment process. Figure 1.2 showed that the standard considers different limits levels for different frequencies in the spectrum. Thus, a technique that can be used to deal with this situation is adopting switching control strategies that aim to shape the EMI noise. However, even considering recent progress, such as the last amendment included in the IEC 61000-2-2 in 2018 [56]. The dynamics of interoperation required by smart grids make EMC a challenge [57]–[59]. Once smart grids permeate different environments, e.g., industrial, residential, where each environment has its own recommendations on EMC assurance [60].

Thus, EMC issues due to the EMI generated by DC/DC converters operating in the low frequency range (from 9 kHz to 150 kHz) become a real predicament in smart grids. Since situations may arise where best engineering practices, whether from the point of view of power electronic converters [53], [57], [62]–[65] or telecommunications devices [52], [61], [66]–[69], may not be electromagnetically compatible.

Therefore, based on the research carried out and presented in this thesis, confirmed by the experimental results carried out in accordance with technical EMI standards, it becomes possible to confirm the hypothesis: **it is possible to develop new, dedicated converter control algorithms that allow shaping the spectrum of disturbances to meet standardization or technical requirements.**

6.1 Conclusions

The objectives of this thesis were related to the identification and realization of whether it is possible to develop new, dedicated converter control algorithms that

allow shaping the spectrum of disturbances to meet standardization or technical requirements. Briefly, the conclusions of this thesis can be highlighted as:

- Usage of National Instruments PXI with Field-Programmable Gate Array based control hardware with a fixed point processor as a cyber-physical fast prototyping platform enabling electromagnetic compatibility investigations of pseudo-random modulated converters;
- EMC-friendly PWM technique: the control of the pulse width modulation generation scheme, shaping the electromagnetic interference noise from the critical fault areas of the information and communications technology equipment (increasing the effectiveness of an already implemented EMI filter);
- Description of a concept of the control algorithm for power electronic converters, enabling electromagnetic interference shaping, providing 30% reduction of Frame Error Rate in Power Line Communication;
- Case study showing possibility of development of new, dedicated converter control algorithms that allow shaping of the spectrum of disturbances to meet standardization or technical requirements as well as presentation of the system for flexible implementation and validation of developed concepts.

6.1.1 Chapter 2

The chapter 2 was devoted to describing the expected behaviour model of rectangular pulse trains based on two types of switch control strategies, i.e., RanM and DetM. A more theoretical approach was presented in the appendix A, introducing the modelling and simulation of rectangular pulse trains, based on the Fourier series's trigonometric form. Also, the complex exponential Fourier series was used to model and simulate the Fourier series's coefficients. Section A.3 also introduced some specific phenomena, mainly considering the aggregation of rectangular pulse trains $X(t)_{\Sigma}$. Furthermore, section A.3 highlights the importance of dealing with improper integrals when considering the $X(t)_{\Sigma}$ with DetM.

The section 2.1 introduces the concept of RanM, that paved the way for the contributions of this thesis. How would it be possible to reduce the EMI noise power spectrum if there is no change in the DC/DC converter energy process?

Thus, from the point of view of modulation algorithms and the point of view of the EMI measurement procedures. It can be concluded that a faster switching rate of change may imply the output graph in the frequency domain is almost flat, i.e., evenly spread. However, a slowly switching rate of change may allow the super-heterodyne frequency band stepping EMI test receiver to read more times the same

frequency. Thus covering variations during the dwell time. Therefore, the challenge changed, and it became challenging to implement a modulation algorithm to identify and achieve the EMI noise spreading through the EMI spectrum shaping consciously.

The use of RanM spreads the maximum level of EMI but does not change the aggregate/total power of the disorders. Many of the adverse effects caused by electromagnetic waves result from the total energy of disturbances. This means that the impact on the EM due to the use of the proposed modulation algorithms is neutral.

6.1.2 Chapter 3

Chapter 3 presented essential aspects of the theoretical knowledge used by conventional super-heterodyne frequency band stepping EMI test receivers, during conducted EMI measurements. Among the topics covered, it is worth mentioning that section 3.1 presented the DFT, the sampling frequency (f_s) and the DFT time window. The window effect phenomenon was summarized by section 3.2.

The section 3.3 showed the applicability of both DFT and STFT methods, and their influence on the conducted EMI measurements. The spectrum measurement in the full range of frequency involves a lot of single measurements. For example, if the objective is to increase the RBW, one needs to use a narrow IF filter. However, adopting a narrow IF filter, the super-heterodyne frequency band stepping EMI test receiver must use long dwell times (T_m) for every frequency.

Nevertheless, an interesting point, mentioned in both section 3.3 and subsection 3.4 is the tradeoffs between RanM, T_m and RBW. The definition of the T_m value is a current debate [105]. Different EMC standards might consider different requirements of T_m . On average, when considering power electronic systems operating in the low frequency range, the IEC 61000-4-7 standard is used as a reference, although it does not cover DC/DC systems [106]. The IEC 61000-4-7 specify for frequency band A (see Table 3.1), $T_m = 200$ ms, i.e. 5 Hertz, which means that five cycles of a given signal should be enough to characterize it appropriately (see Figure 3.8-C).

The beforehand definition T_m and RBW for DetM is more flexible. Once there are no changes in the frequency of a given signal during the EMI measurements for DetM. The challenge arises to define the T_m and RBW for a RanM, which not only provide changes in the frequency of a given signal but also provides random changes between the frequencies of this signal (both cases during the EMI measurements).

Therefore, due to the complexity of establishing the tradeoffs between a RanM, T_m , and RBW, a premise was assumed based on chapter 3. The proposal considered the shorter T_m possible and adapted the switching rate of change to match the

RBW. Thus, it is assumed that even in a highly complex case with a shorter T_m , it's possible to have the stable EMC measurements.

6.1.3 Chapter 4

The chapter 4, and the subsections 4.1.1 and 4.1.3 presented all the hardware and resource details of the IDE NI PXIe-8135, as well as of the FPGA PXI-7854R. The knowledge base relating to the LabVIEW projects was presented in the subsection 4.1.2. The proposed PWM modulator algorithm was presented in the subsection 4.1.4 and the Random Number Generator presented in the subsection 4.1.5.

FPGAs have been found highly suitable for control for a multitude of reasons, like parallelism, speed, reprogram ability, and possible feedback schemes. Since there are some FPGA software limitations when using fixed-point operation, the section 4.2 was dedicated to demonstrating how to provide a LabVIEW FPGA-based control system for a DC/DC converter (the RanM implementation).

The novelty of the proposed development lies in the ability of handle the fixed-point processor. Four methods of distribution the PDF in FPGA without arithmetic division and using fixed-point operations were proposed and presented in the subsections 4.2.1, 4.2.2, 4.2.3, and 4.2.4. The FPGA implementation was presented in subsection 4.2.5, and the most extensive version of the algorithm (RanM2 with RSC_{TL}) used only 5.5% of FPGA resources.

Furthermore, considering the hardware resources presented in section 4.1, it became possible to the transfer of data from FPGA PXI-7854R to IDE NI PXIe-8135. These resources were used for the concept of controlling the switching rate of change, implemented as RanM3 (see subsection 4.2.6). The RanM3 implementation was only possible because each environment, i.e, the FPGA PXI-7854R and IDE NI PXIe-8135, considers an independent iteration count (i) process. As illustrated in Figure 4.20-part I, the i_{IDE} is first evaluated by the IDE NI PXIe-8135 controlled by k , and secondly the i_{FPGA} is evaluated by the FPGA PXI-7854R controlled by N (Figure 4.20-parts II and III).

When considering the use of RanM some care must be reinforced. The minimum frequency affects the current ripple amplitude or the value of reactance elements to smooth the current. Lowering this frequency increases the current amplitude. The average frequency affects the average switching losses and, consequently, the DC/DC converter efficiency. The upper frequency must be matched to the speed of the transistors and drivers. Thus, the proposed RanM3 have a neutral effect on the DC/DC converter energy processes. Indeed, changing the type of modulation and changing the frequency has a significant impact on the operation of the DC/DC converter. In particular, the average switching frequency affects the switching losses

of transistors. However, maintaining the average switching frequency, we do not change the efficiency of the DC/DC converter, and the losses in the system are the same.

Finally, the last RanM proposed was presented in subsection 4.2.7, considering the ability to shaping the PDF, hence, the EMI noise. The approach of shaping the RanM3 is flexible, and the choice of sub-ranges for N_m and the % of δ_N depend on the expected EMI noise shape, i.e., EMC compliance. Basically, the approach of shaping the RanM3, proposes to model the EMI noise shape according to the imposed needs of spectrum utilization by the possible victims. In other words, the precise definition of achieving the optimization of EMI noise spreading through consciously shaping the EMI spectrum.

Additionally, it is essential to highlight that although the research presented in this thesis is premised on DC/DC converters. All the presented modulation algorithms in this chapter 4 can be adapted and used in half-bridge or full-bridge typologies of converters, as well as multi-level or multi-phase systems. The FPGA calculation and implementation were developed to be dependent on the internal clock frequency of the control hardware. Thus, increasing possible switching speeds and output frequencies is as simple as interchanging the FPGA by one that runs on a higher internal clock frequency.

The presented modulation algorithms have been checked in the real DC/DC converter system and implemented in the final FPGA control system. Therefore, it was assessed that offered solutions have reached at least level 7 of Technology Readiness Levels (TRLs).

6.1.4 Chapter 5

The chapter 5 presented the conducted EMI measurements for all modulation algorithms described in chapter 4, considering a two-transistor step-down DC/DC converter operating at the low frequency range (the central motivation of this thesis, for further information see section 1.1). Through the assessment of the output harmonic voltage, it gives possibilities to understand the EMI noise behavior at the very origin, as well as to shape it accurately. The EMC-test bench systems used to carry out the conducted EMI measurements were presented in section 5.1, as highlighted in Figure 5.1, Figure 5.2, Figure 5.4 and Figure 5.5.

Firstly, to recognize and validate the behaviour model of the rectangular pulse trains discussed in depth in chapter 2 as well as the modulation algorithms proposed and discussed in chapter 4, the CE behaviour was assessed in section 5.2, intending to broaden the understanding of the DC/DC converters behaviour when the D variation is considered and f_0 with different frequency stabilities. Then, the

other standardized EMI measurement procedures were presented in section 5.3.

All the conducted EMI measurements presented in subsection 5.3.1 stand under the assumption that the bandwidth in which the spectrum components are spread by the adopted RanM techniques is much larger than the RBW and dwell time (T_m) used by the TDEMI X6 EMI test receiver. Thus, through the evaluation of all conducted EMI measurements presented in subsection 5.3.1, and based on the LabVIEW FPGA implementation presented in subsection 4.2.5, the following observations can be made:

- The spreading of the spectrum components will always be a consequence of the RanM utilization. The more appropriate the PDF used to generate the PWM signal, the greater the spreading effect becomes, as in the case of the Figure 5.22 and Figure 5.23;
- However, the EMI noise spreading as presented in subsection 5.3.1 does not mean an EMI noise level reduction or even power spectrum lowering;
- Once the RanM provides changes in the frequency of a given PWM signal and also provides random changes between the frequencies considered in this PWM signal, it becomes imperative to find the tradeoffs between RanM, T_m and RBW to achieved a stable EMC measurement, as dicussed in chapter 3, subsetion 3.5.

Figure 5.18 and Figure 5.19 show that when we consider N_m and RSC_{TL} , the power spectral density changes. Furthermore, as also presented by Figure 5.20 and Figure 5.21, where through the RanM2 approach, there is a possibility to control the occurrence of frequencies in certain parts of the RSN used by RanM. The RanM3 was proposed and presented in subsection 5.3.2.

For the conducted EMI measurements presented in subsection 5.3.2, a premise was assumed to consider the shorter T_m possible and adapt the switching rate of change to match the RBW. Therefore by using $k = 4 \times 10^5$, it takes longer to random alternate the frequencies considered in the RSN used by RanM3, as is possible to see in Figure 5.26 and Figure 5.27. Thus, even in a complex case with $T_m = 100$ ms, it's possible to have the stable EMI measurements.

Figure 5.26 and Figure 5.27 totally change the understanding that the EMI measurements such as presented in Figure 5.24 and Figure 5.25 show a reduction of the EMI noise level, whether compare with Figure 5.12 and Figure 5.13 (see also the discussion in subsection 5.3.4 about the Figure 5.39 and Figure 5.40). When actually what is happening, it's a mismatch between the given PWM signal, T_m =, and RBW.

Once controlling the occurrence of frequencies in certain parts of the RSN used by RanM3 becomes possible, it is unavoidable not to think about EMC compliance issues. Thus, the subsection 5.3.3 presented how to shape the RanM3 approach. From Figure 5.29 to Figure 5.31 is exemplified the relationship between δN and sub-ranges for N_m . The results presented in Figure 5.44, Figure 5.45, Figure 5.46 and Figure 5.47, reinforce the finding that it is possible to develop new, dedicated converter control algorithms that allow shaping the spectrum of disturbances to meet standardization or technical requirement. Since from the point of view of standardization requirements, it becomes possible to reduce the level of EMI noise, the EMI noise shaping method allowed the removal of its level around 71 dB from the critical fault areas of the PLC system. On the other hand, from the point of view of technical requirements, it becomes possible to decrease the level of interference for the PLC system, achieving on average up to 30 % reduction in FER.

Despite huge potential for use in the context of EMC compliance (see section 5.4), there is a drawback to considering sub-ranges for N_m from the power electronic converter point of view, since obtaining a single frequency becomes unlikely. However, this is an additional feature that shows how the EMC-test bench system, primarily controlled by a CPS, can be considered a reliable and "EMC-friendly" controller.

On the other hand, subsection 5.3.4 presented the aggregated conducted EMI with DetM and RanM, considering as a premise such a situation where the DC/DC converters or the IPEM systems must operate into the concept of parallel electrical installations' topologies [45].

Therefore, since each f_0 of each two-transistor step-down DC/DC converter has its own frequency stability, there is a time displacement between the PWM signals (see Figure A.10-C). This situation was presented in the section A.3 of the chapter 2 as improper integration, and as is possible to observe by comparing the Figure 5.34 and Figure 5.35 with the Figure A.12, the TDEMI X6 EMI test receiver presents the expected EMI noise shape.

Additionally, as presented in subsection 4.1.1 of the chapter 4. The IDE NI PXIe-8135 can be used in the EMC-test bench system considering several DC/DC converters. Thus enabling the timing and synchronization function (*TSF*) of several application instances, as presented in Figure 5.37.

6.2 Directions for Further Research

In addition to attesting that the proposed EMC-friendly PWM technique has proved to be highly advantageous for modern EM. Especially at low frequency, where non-compatibility scenarios were not previously identified due to new device technologies

used by microgrids. This thesis also makes clear that the disturbance spectrum measured by the EMI receiver cannot be taken as the only factor for EMC assurance, since reduced EMI spectrum alone is not the only factor for EMC assurance in EM with interoperating electronic and communication technologies.

The usage of RanM techniques for spreading the spectrum components of a signal in DC/DC converters is a topic that must be considered according to particular needs. In the past, many authors have suggested that it was a fraudulent way of complying with EMC standards. This holds if there is not enough information about all the RanM parameters as well as about the functioning of the super-heterodyne EMI test receiver. In other words, it is not enough to just determine the RanM parameters. In addition, the control of the switching rate of change can be used as a parameter to control the EMI generated by switching power converters. In general, many power electronic researchers are not looking at the EMI potential nor the system emission, which can be considered the main contribution of the modulation algorithms proposed in this thesis.

Furthermore, as was explained in the thesis, the stability of a signal measured by the super-heterodyne EMI test receiver depends on the STFT calculation. The STFT calculation relies on essential parameters like the RBW, dwell time, and the IF filter.

Much remains to be researched in terms of procedures for conducted EMI measurements. Controlling the switching rate of change of RanM is fully justified; If there are options only for lower dwell times values (below 500 ms); Or in the case of shaping the EMI noise to avoid particular areas of the frequency spectrum, thus increasing the EMC. Otherwise, higher dwell times values may be enough to measure RanM. Finding the middle point between dwell times values and random modulated DC/DC converters is missing.

Acknowledgments

It would be impossible to begin the acknowledgment chapter of this thesis without first mentioning those who have always supported me in my existence as a human being, my dear mother, **Maria Aparecida de Santana Loschi**, and my dear and late father, **Clóvis Francisco Loschi**. Among the diverse and valuable lessons learned from my dear parents, the one that necessarily represents the doctoral process (of course, from my point of view) can be translated as "life is unfair," and that is something positive concerning our existence as human beings, not harmful. Because there have always been and always will be injustices, which, given a particular perspective, represent hurdles that need to be overcome. It all boils down to how much you can develop or do given your current situation, not what you could do in other more comfortable situation. Thank you very much, my dear and beloved parents, for this valuable lesson that fundamentally supported all the hours, days, weeks, and months invested in all the processes and stages for realizing this joint doctorate.

This thesis, as well as all the energy and time consumed, must be dedicated to a Wonder Woman **Ana Claudia Galindo Bomfim Loschi**. Life in Poland was not always so fun or easy (culture shock, difficult language, husband doing joint doctorate with 3 universities, etc.). There were many challenges, especially in times of a pandemic. However, this Wonder Woman faced them all, as well as being the stronghold, the foundation of a family that started in the middle of my joint doctorate and in the middle of a pandemic. Not only did we just get pregnant during these difficult times, but she had our beloved daughter in a natural birth (we had no family or friends living nearby). Thank you so much my beloved Ana for always being there.

A valuable lesson learned from my dear **Prof. Yuzo Iano**, to whom I dedicate a paragraph of acknowledgments below, is that: what matters is not the outcome but the process. It is in this sense that today I celebrate, thank, and feel incredibly blessed that the doctoral process has provided me with the experience of becoming a father of my beloved daughter **Julia Galindo Bomfim Loschi**. At the moment I write this thesis, a lot is going through my head about how I can contribute to

your existence as a human being. And at the same time I find myself in a situation of extreme anxiety about all the possible experiences and situations that you will go through in life. I sincerely hope that this entire learning process, which I have been developing intensively since 2009, can somehow be added to your life, to your knowledge, to your existence. I will always be there my dear and beloved Juju.

The beginning of a process is not the most important, however, the process itself is more important than its possible outcome. This is how my dear **Prof. Yuzo**, with this simple and short sentence, summed up all his experience of more than 50 years as a professor at the University of Campinas in Brazil. A lot happened during our more intense coexistence between the end of my bachelor's degree and a year after my master's degree conclusion, and in many situations **Prof. Yuzo Iano** was fundamental for the professional and personal balance. As he also likes to say, the secret is in the balance. The most difficult period of my academic journey occurred during the last years of my master's degree when I was without any form of funding. Which meant not being able to rent a house close to the university. The only solution to continue the academic journey was to spend the nights in the laboratory, which was done! For a year and a half I slept 3 days in the laboratory and then traveled to my mother's house (150 km from the University of Campinas) to shower and rest for 2 days, then back to the laboratory. And during all this time **Prof. Yuzo Iano** was fundamental, he supported me financially (money for the bus), with food and emotionally. If this thesis is possible today, it is largely due to the support of **Prof. Yuzo Iano**.

I would also like to thank many Brazilian colleagues that I met during my bachelor's degree and master's degree who always helped me directly and indirectly with my academic journey, mainly through prospective conversations about technological issues and trends. Among them I would like to, especially thank **Raquel Cardamone, Carlos Bertolassi, Dr. Kelem Jordao, Dr. Silvio Renato Messias de Carvalho, Gabriel Gomes Oliveira, Dr. Navid Razmjooy, Prof. Dr. Vania V. Estrela, Dr. Euclides Chuma, Andre Quaglio, Leonardo Nery, Victor Vellano Neto, Prof. Denito, and Jamilson Evangelista** for always being available for a good and motivating conversation.

The year 2019 was a year of changes; it was a watershed in my life, thanks to the SCENT (Smart Cities EMC Network for Training) project. Initially, a lot is owed to **Prof. David Thomas**, to whom I dedicate a paragraph of acknowledgments below, for having received my application. Thus, I would like to thank the **funding from the European Union's Horizon 2020 research and innovation programme under the Marie-Sklodowska-Curie grant agreement No 812391**. I would also like to thank **Dr. Marco Raaben** for all the support with the organization of the SCENT project and its activities, guidance of the tasks to be performed, and for being a friendly

person who was available to talk, listen to our demands and always meet the best balance point. Thank you so much, Marco, for all the support. I am immensely grateful to all my colleagues on the SCENT and ETOPIA project: **Marshall Choon Lok, Erjon Ballukja, Karol Niewiadomski, Venkatkumar Muneeswaran, Daria Nemashkalo, Abdusalam Hamid Beshir, Lu Wan, Francinei Vieira, Muhammad Septian Alamsyah, Amr Madi, Arun Khilnani** for all their support.

I am also immensely grateful to thank my dear friends from Indonesia **Muhammad Imam Sudrajat** and **Muhammad Ammar Wibisono** and my dear friend from Mexico **Angel Pena Quintal** for everything that we have accomplished during these last years. I am very grateful to you all for the conversations, brainstorming, insights, and publications. Indeed, much of this thesis is due to this cooperation.

In particular, I would like to record my gratitude to two colleagues. Firstly for **Waseem Wafik Elsayed** by the partnership during all the years of the SCENT project. I do not doubt that our collaboration was fundamental for developing all activities. I believe that despite our cultural differences our goal was achieved. We had a good collaboration that resulted in many published papers. Thank you very much, Waseem, for all the support. Secondly, I would like to thank my dear friend **Douglas Aguiar do Nascimento**. Our partnership is already close to completing 8 years, and during all times, Douglas has become an essential person. In difficult times, Douglas was always there to help me and my family, and we managed to maintain this partnership that has been lasting and productive, both personally and academically. Thanks so much, Douglas, for all the help!

Prof. David Thomas was the first person in the SCENT project universe with whom I have contact. Luckily thanks to **Prof. David Thomas** eyes my application was considered. I could then later participate in the interviews and be chosen as the Early-Stage Researcher 2 of the SCENT project. Thanks to you **Prof. David Thomas**, the process of transforming my professional and personal life has begun. Thank you very much **Prof. David Thomas** also for all the support and guidance regarding all the deliverables that we jointly develop, the steps of the admissions processes at the **University of Nottingham**, the papers, and the writing development of my thesis. I would like to take this opportunity to also thank the **University of Nottingham**, and in particular to **Ms. Charlotte Day, Mr. Carys Williams, Mr. James Houston, Dr. Gary Clarke, Prof. Steve Greedy, and Prof. Mark Sumner**, for all their support during the admissions process.

I am also immensely grateful to the **University of Twente**, in particular to **Ms. Lilian Hannink** and **Ms. Lorena Montoya Morales**, for all their support during the admissions process. I also take this opportunity to thank **Prof. Niek Moonen**, and to **Prof. Robert Vogt-Ardatjew** for being a source of inspiration that I look up to a lot. Thank you all for the cooperation and support. I learned a lot from you all.

Some people are naturally a source of inspiration and, over time, become a source of admiration. This is how I get to define **Prof. Frank Leferink**. Since the beginning of the SCENT project, **Prof. Frank Leferink** has taught all the fundamental values to become a researcher, from ethical and academic integrity to cultural and social values. Thank you very much **Prof. Frank Leferink** for all your work, dedication, and contribution to everyone. Thanks for being this rock, the foundation for many young researchers' knowledge. I am eternally grateful for everything you have supported me. Also, thank you very much **Prof. Frank Leferink** for all the support and guidance regarding the steps of the admissions processes at the **University of Twente**, the papers, and the writing development of my thesis

I would also like to thank the **Uniwersytet Zielonogórski** immensely, particularly to **Ms. Anna Ułasik**, **Ms. Joanna Pietrań**, **Ms. Dorota Casti** and **Dr. Jarek Kijak**, **Prof. UZ**, for all their support during the admissions process for both employee and doctoral student positions. I want to thank **Dr. Jacek Bojarski**, **Prof. UZ** and **Dr. Piotr Leżyński** immensely for fundamental review and comments of this thesis. Furthermore, **Dr. Piotr Leżyński** provided fundamental support that enabled and supported many of the activities carried out at **Uniwersytet Zielonogórski**. This collaboration was essential and resulted in developing and publishing many of our conference and journal articles. Thank you very much, **Dr. Piotr Leżyński**. I learned a lot from you.

Finally, I would like to thank the person who made this whole doctoral process possible, **Dr. Robert Smoleński**, **Prof. UZ**. January 14th, 2019, was the day of change; because it was the day we received the acceptance letter from **Dr. Robert Smoleński**, **Prof. UZ**. Thirty days after receiving the acceptance letter, I was married, and eighty days after, I was in Poland. Everything was completely new, from the execution of the SCENT project itself to understanding what would be my role within the SCENT project. However, at all times, **Dr. Robert Smoleński**, **Prof. UZ** was always attentive to the smallest details of our stay, from understanding housing issues to documentation issues necessary both to perform the work as an employee and become a doctoral student, that is, at all important moments, **Dr. Robert Smoleński**, **Prof. UZ** was present and always supported us. **Dr. Robert Smoleński**, **Prof. UZ** has always been a great motivator for publications and thesis development. I do not doubt that our achievements regarding publications and the development of this doctoral thesis are due to the encouragement and motivation provided by **Dr. Robert Smoleński**, **Prof. UZ**. Thank you very much **Dr. Robert Smoleński**, **Prof. UZ** for all your work, dedication, and contribution to my progress. My family and I are forever grateful to you for everything.

I would also like to thank **EMCC Dr. Rasek** for all the support, particularly from **Nathalia Rasek-Abach** and **Dr. Martin Gabrisak**.

Biography and List of my Publications

8.1 Biography

I am an EMC Test Engineer working on R&D and EMC projects at EMCC Dr. Rasek. From 2019 to 2022, I was an Early-Stage Researcher on the SCENT (Smart Cities EMC Network for Training) project. SCENT was a consortium of three universities and has received funding from the European Union's Horizon 2020 Research and Innovation Program under the Marie-Sklodowska-Curie grant agreement No 812391. I was working towards a unique joint Ph.D. degree awarded by the University of Nottingham, the Uniwersytet Zielonogórski, and the University of Twente.



Initially, I'm from São Paulo, Brazil, where I received my master's degree in Electrical Engineering with an emphasis in Telecommunications and Telematics by the University of Campinas (2017), and my bachelor's degree in Control and Automation Engineering by the Paulista University (2014). During my last years of graduation (from 2011 to 2013), I worked as a Technical Analyst in a German company in Brazil responsible for developing high-speed DIESEL engines for marine propulsion systems, drive systems for Oil & Gas, and Power Generation applications. Also, during

my last performances in Brazil (2014 to 2018), I was a student in a research group focused on the development of Smart and Sustainable Cities, where my primary duties included supporting the development of Courses, Lectures, and Outreach activities. Organization of Symposiums and Conferences, Workshops, Technical and Group Meeting. Editorial and Review Activities. Publication of Books, Chapters of Books, Articles in Conference Proceedings, and Articles in Journals.

8.2 List of My Publications

- M. Montagner, M. Mezaroba, C. Rech, E. B. D. Prazeres, D. Nascimento and **H. Loschi**, "Power Flow Numerical Assessment of an iUPQC Utility Interface for Microgrids with STATCOM and PAC Functions," 2022 IEEE 21st Mediterranean Electrotechnical Conference (MELECON), 2022, pp. 1223-1228, <https://doi.org/10.1109/MELECON53508.2022.9842887>.
- W. E. Sayed, **H. Loschi**, M. A. Wibisono, N. Moonerr, P. Lezynski and R. Smolenski, "The Influence of Spread-Spectrum Modulation on the G3-PLC Performance," 2021 Asia-Pacific International Symposium on Electromagnetic Compatibility (APEMC), 2021, pp. 1-4, <https://doi.org/10.1109/APEMC49932.2021.9597060>.
- J. Evangelista, **H. Loschi**, E. T. Costa, R. Smolenski, N. Moonen and R. Vogt-Ardatjew, "Radiated and Conducted EMI by RF Fields at Hospital Environment," 2021 Asia-Pacific International Symposium on Electromagnetic Compatibility (APEMC), 2021, pp. 1-4, <https://doi.org/10.1109/APEMC49932.2021.9597035>.
- W. E. Sayed, **H. Loschi**, A. Madi, N. Moonen, R. Smolenski and F. Leferink, "Low-Frequency Envelope of DC/DC Converters due Differences in the Control Hardware Features," 2021 Asia-Pacific International Symposium on Electromagnetic Compatibility (APEMC), 2021, pp. 1-4, <https://doi.org/10.1109/APEMC49932.2021.9596732>.
- D. Nascimento, R. Smolenski, **H. Loschi**, A. Madi, M. Alamsyah and F. Vieira, "A Simulation for Parameters Extraction of Double-Layer Shielded Power Cable using FEA," 2021 Asia-Pacific International Symposium on Electromagnetic Compatibility (APEMC), 2021, pp. 1-4, <https://doi.org/10.1109/APEMC49932.2021.9596960>.
- D. Nascimento, R. Smolenski, **H. Loschi**, F. Grassi, L. Wan and A. Hamid, "Electromagnetic Fields on 3-Phase Induction Motor Using Finite Element Anal-

- ysis,” 2021 IEEE International Joint EMC/SI/PI and EMC Europe Symposium, 2021, pp. 434-439, <https://doi.org/10.1109/EMC/SI/PI/EMCEurope52599.2021.9559357>.
- Leonardo dos Santos, Yuzo Iano, **Hermes Loschi**, Douglas Nascimento, Navid Razmjoooy, Euclides Chuma, and Carlos Bertolassi (2021) EMC Issues in Grid-Connected Photovoltaic Systems. In: Iano Y., Saotome O., Kemper G., Mendes de Seixas A.C., Gomes de Oliveira G. (eds) Proceedings of the 6th Brazilian Technology Symposium (BTSym'20). BTSym 2020. Smart Innovation, Systems and Technologies, vol 233. Springer, Cham. https://doi.org/10.1007/978-3-030-75680-2_76.
 - Douglas Nascimento, Shady S. Refaat, **Hermes Loschi**, Yuzo Iano, Euclides Chuma, Waseem El-Sayed, Amr Madi, Current Sensor Optimization based on Simulated Transfer Function under Partial Discharge Pulses, Sensors and Actuators A: Physical, Volume 329, 2021, 112825, ISSN 0924-4247. <https://doi.org/10.1016/j.sna.2021.112825>.
 - de Jesus M.A., Estrela V. V., Aroma R. J., Razmjoooy N., da Silva S. E. B., de Almeida A. C., da Hora H. R. M., Deshpande A. , Patavardhan P., Andreopoulos N., Terziev A., Raimond K., and **Loschi H. J.** (2021) Building Bridges and Remediating Illiteracy: How Intergenerational Cooperation Foster Better Engineering Professionals. In: Khelassi A., Estrela V.V. Advances in Multidisciplinary Medical Technologies Engineering, Modeling and Findings. Springer, Cham. https://doi.org/10.1007/978-3-030-57552-6_3.
 - Fernandes S. R., de Assis J. T., Estrela V. V., Razmjoooy N., Deshpande A. , Patavardhan P., Aroma R. J., Raimond K., **Loschi H. J.** and Nascimento D. A. (2021) Nondestructive Diagnosis and Analysis of Computed Microtomography Images via Texture Descriptors. In: Khelassi A., Estrela V.V. (eds) Advances in Multidisciplinary Medical Technologies Engineering, Modeling and Findings. Springer, Cham. https://doi.org/10.1007/978-3-030-57552-6_16.
 - Hamid, A., L. Wan, **H. Loschi**, D. Nascimento, F. Grassi, R. Smolenski, G. Spadacini, Giordano, and S. Pignari, "PSpice-Simulink Co-Simulation of the Conducted Emissions of a DC-DC Converter with Random Modulation," 2020 6th Global Electromagnetic Compatibility Conference (GEMCCON), 2020, pp. 1-4, <https://doi.org/10.1109/GEMCCON50979.2020.9456753>.
 - **H. Loschi**, R. Smolenski, P. Lezynski, W. El Sayed and D. Nascimento, "Reduction of Conducted Emissions in DC/DC Converters with FPGA-based Random Modulation," 2020 International Symposium on Electromagnetic Compati-

bility - EMC EUROPE, Rome, Italy, 2020, pp. 1-6, <https://doi.org/10.1109/EMCEUROPE48519.2020.9245684>.

- W. E. Sayed, **H. Loschi**, C. L. Lok, P. Lezynski and R. Smolenski, "Prospective Analysis of the effect of Silicon based and Silicon-Carbide based Converter on G3 Power Line Communication," 2020 International Symposium on Electromagnetic Compatibility - EMC EUROPE, Rome, Italy, 2020, pp. 1-6, <https://doi.org/10.1109/EMCEUROPE48519.2020.9245727>.
- Lezynski, P., Smolenski, R., **Loschi, H.**, Thomas, D., & Moonen, N. (2020). A novel method for EMI evaluation in random modulated power electronic converters. *Measurement*, 151, 107098. <https://doi.org/10.1016/j.measurement.2019.107098>.
- **Loschi, H.**, Smolenski, R., Lezynski, P., Nascimento, D., & Demidova, G. (2020). Aggregated Conducted Electromagnetic Interference Generated by DC/DC Converters with Deterministic and Random Modulation. *Energies*, 13(14), 3698. <https://doi.org/10.3390/en13143698>.
- **Loschi, H.**, Lezynski, P., Smolenski, R., Nascimento, D., & Sleszynski, W. (2020). FPGA-Based System for Electromagnetic Interference Evaluation in Random Modulated DC/DC Converters. *Energies*. <https://doi.org/10.3390/en13092389>.
- Chuma, E. L., Iano, Y., Fontgalland, G., Roger, L. L. B., & **Loschi, H.** (2020). PCB-integrated Non-destructive Microwave Sensor for Liquid Dielectric Spectroscopy Based on Planar Metamaterial Resonator. *Sensors and Actuators A: Physical*, 112112. <https://doi.org/10.1016/j.sna.2020.112112>.
- **Hermes Loschi**, Vania V. Estrela, Jude Hemanth, [i in.]. Communications requirements, video streaming, communications links, and networked UAVs. *Imaging and Sensing for Unmanned Aircraft Systems Vol. 2: Deployment and Applications*, 2020. / ed. V.V. Estrela, J. Hemanth, O. Saotome et al., London: IET Digital Library, s. 1-10, ISBN: 9781785616440. https://doi.org/10.1049/PBCE120G_ch6.
- Asif Ali Laghari, Asia Khan, Hui He, Vania V. Estrela, Navid Razmjoooy, Jude Hemanth, **Hermes Loschi**, [i in.]. Quality of experience (QoE) and quality of service (QoS) in UAV systems. *Imaging and Sensing for Unmanned Aircraft Systems Vol. 2: Deployment and Applications*, 2020. / ed. V.V. Estrela, J. Hemanth, O. Saotome et al., London: IET Digital Library, s. 1-10, ISBN: 9781785616440. https://doi.org/10.1049/PBCE120G_ch10.

- Vania V. Estrela, Jude Hemanth, **Hermes Loschi**, [i in.]. Computer vision and data storage in UAVs. Imaging and Sensing for Unmanned Aircraft Systems. Volume 1: Control and Performance, 2020. / ed. V.V. Estrela, J. Hemanth, O. Saotome et. al, London: IET Digital Library, s. 23–45, ISBN: 9781785616426. https://doi.org/10.1049/PBCE120F_ch2.
- Razmjooy, N., Ashourian, M., Karimifard, M., Estrela, V. V., **Loschi, H. J.**, do Nascimento, D., and Vishnevski, M. (2020). Computer-aided diagnosis of skin cancer: a review. *Current medical imaging*, 16(7), 781-793. <https://doi.org/10.2174/1573405616666200129095242>.
- Razmjooy, N., Estrela, V. V., & **Loschi, H. J.** (2020). Entropy-Based Breast Cancer Detection in Digital Mammograms Using World Cup Optimization Algorithm. *International Journal of Swarm Intelligence Research (IJSIR)*, 11(3), 1-18. <http://dx.doi.org/10.4018/IJSIR.2020070101>.
- **Hermes LOSCHI**, Robert SMOLEŃSKI, Piotr LEŻYŃSKI, Waseem El SAYED, Choon Long LOK. EMC Issues: Prospective Review on the Switch Control Strategies. 2019 Proceedings of XIV Scientific Conference Control in Power Electronics and Electric Drive "SENE 2019". All Rights Reserved. SENE, 2019. V.1. Łódź, 20-22 November 2019.
- Waseem El SAYED, **Hermes LOSCHI**, Choon Long LOK, Piotr LEŻYŃSKI, Robert SMOLEŃSKI, Performance Evaluation of the Effect of Power Converters Modulation on Power line Communication. 2019 Proceedings of XIV Scientific Conference Control in Power Electronics and Electric Drive "SENE 2019". All Rights Reserved. SENE, 2019. V.1. Łódź, 20-22 November 2019.
- Nascimento, D. A. D., Iano, Y., **Loschi, H. J.**, Razmjooy, N., Sroufe, R., Oliveira, V. D. J. S., & Montagner, M. (2019). Sustainable adoption of Connected Vehicles in the Brazilian landscape: policies, technical specifications and challenges. *Transactions on Environment and Electrical Engineering*, 3. <http://dx.doi.org/10.22149/tee.v3i1.130>.
- Razmjooy, N., Estrela, V. V., & **Loschi, H. J.** (2019). A survey of potatoes image segmentation based on machine vision. In *Applications of Image Processing and Soft Computing Systems in Agriculture* (pp. 1-38). IGI Global. <http://dx.doi.org/10.4018/978-1-5225-8027-0.ch001>.
- Razmjooy, N., Estrela, V. V., & **Loschi, H. J.** (2019). A study on metaheuristic-based neural networks for image segmentation purposes. In *Data Science* (pp. 25-49). CRC Press. <http://dx.doi.org/10.1201/9780429263798-2>.

- Proceedings of the 4th Brazilian Technology Symposium (BTSym'18). Emerging Trends and Challenges in Technology. Yuzo Iano, Rangel Arthur, Osamu Saotome, Vania V. Estrela, **Hermes Loschi**. Springer International Publishing, 2019, XXI, 665 s. ISBN: 9783030160524. Smart Innovation, Systems and Technologies book series (SIST, Vol. 140). <http://dx.doi.org/10.1007/978-3-030-16053-1>.
- Proceedings of the 3rd Brazilian Technology. Emerging Trends and Challenges in Technology. Yuzo Iano, Rangel Arthur, Osamu Saotome, Vania V. Estrela, **Hermes Loschi**. Springer International Publishing, 2019, 332 s. ISBN: 9783319931111. <https://doi.org/10.1007/978-3-319-93112-8>.
- Chuma, Euclides Lourenço, Iano, Yuzo, Cardoso, Paulo Eduardo dos Reis, **Loschi, Hermes José**, Pajuelo, Diego; 2018. Design of Stepped Impedance Microstrip Low-Pass Filter for Coexistence of TV Broadcasting and LTE Mobile System Close to 700 MHz. SET INTERNATIONAL JOURNAL OF BROADCAST ENGINEERING. ISSN Print: 2446-9246 ISSN Online: 2446-9432. <https://doi.org/10.18580/setijbe.2018.7>.
- Padilha, Reinaldo, Iano, Yuzo, Monteiro, Ana Carolina B., **Loschi, Hermes José**; 2018. Improvement of the Content Transmission in Broadcasting Systems: Potential Proposal to Rayleigh and Rician Multichannel MIMO Systems. SET INTERNATIONAL JOURNAL OF BROADCAST ENGINEERING. ISSN Print: 2446-9246 ISSN Online: 2446-9432. <http://dx.doi.org/10.18580/setijbe.2018.3>.
- Ferreira, L. A., **Loschi, H. J.**, Rodriguez, A. A., Iano, Y., & do Nascimento, D. A. (2018). A Solar Tracking System Based on Local Solar Time Integrated to Photovoltaic Systems. Journal of Solar Energy Engineering, 140(2). <https://doi.org/10.1115/1.4039094>.
- Marinho, C. E. V., Estrela, V. V., **Loschi, H. J.**, Razmjooy, N., Herrmann, A. E., Thiagarajan, Y., ... & Iano, Y. (2018, October). A Model for Medical Staff Idleness Minimization. In Brazilian Technology Symposium (pp. 633-645). Springer, Cham. https://doi.org/10.1007/978-3-030-16053-1_62.
- Carreiro, L. S., Estrela, V. V., Vishnevski, M. P., Huacasi, W. D., Herrmann, A. E., **Loschi, H. J.**, ... & Thiagarajan, Y. (2018, October). Poemathics. In Brazilian Technology Symposium (pp. 655-665). Springer, Cham. https://doi.org/10.1007/978-3-030-16053-1_64.
- Razmjooy, N., Ramezani, M., Estrela, V. V., **Loschi, H. J.**, & do Nascimento, D. A. (2018, October). Stability analysis of the interval systems based on lin-

- ear matrix inequalities. In Brazilian Technology Symposium (pp. 371-378). Springer, Cham. https://doi.org/10.1007/978-3-030-16053-1_36.
- Estrela, V.V.; Saotome, O.; **Loschi, H.J.**; Hemanth, J.; Farfan, W.S.; Aroma, J.; Saravanan, C.; Grata, E.G.H. Emergency Response Cyber-Physical Framework for Landslide Avoidance with Sustainable Electronics. *Technologies* 2018, 6, 42. <https://doi.org/10.3390/technologies6020042>.
 - Nascimento, D. A., Iano, Y., **Loschi, H. J.**, de Sousa Ferreira, L. A., Rossi, J. A. D., & Pessoa, C. D. (2018). Evaluation of partial discharge signatures using inductive coupling at on-site measuring for instrument transformers. *International Journal of Emerging Electric Power Systems*, 19(1). <https://doi.org/10.1515/ijeeps-2017-0160>.
 - **H. J. Loschi**, L. A. S. Ferreira, D. A. Nascimento, P. E. R. Cardoso, S. R. M. Carvalho, and F. D. Conte, "EMC Evaluation of Off-Grid and Grid-Tied Photovoltaic Systems for the Brazilian Scenario," *Journal of Clean Energy Technologies* vol. 6, no. 2, pp. 125-133, 2018. <https://doi.org/10.18178/JOCET.2018.6.2.447>.
 - Cardoso, J. M. M., Mota, L. T. M., **Loschi, H. J.**, Oliveira, G. G., Cristina, V., Iano, Y.; Solar Generation Data Acquisition System for Photovoltaic Applications in BAPV. *BTSym 2018 Proceedings*. ISSN 2447-8326. V.1. <https://www.lcv.fee.unicamp.br/images/BTSym18/Papers/017.pdf>.
 - Jordao, K.; I. Yuzo; **Loschi, Hermes José**; Ferreira, L. A. S; Bianchini, D. Smart City IoT model: a prospective analysis considering indicators of social, technical and operational aspects. *International Conference on Information Society and Smart Cities (ISC 2018)*, 2018. *ISC Conference Proceedings* ISBN: 978-1-912532-02-5.
 - Nascimento, D. A. ; Iano, Y. ; **Loschi, Hermes Jose**; Pessoa, C. D. The Using of Sustainable High Voltage Equipment Insulation Materials in Brazilian Scenario. In: 9th Edition of International Conference on Biofuels and Bioenergy, 2018, Endiburgo. v. 2. p. 39-40. ISSN 2572-4657. <https://doi.org/10.21767/2572-4657-C1-002>.
 - **Loschi, Hermes Jose**; Iano, Y. An Algorithm for Development of Transition Probabilities Matrices to Predicting Ramp Events, based on Markov Model. In: 9th Edition of International Conference on Biofuels and Bioenergy, 2018, Edinburgh. 2018. v. 2. p. 38-39. ISSN 2572-4657. <https://doi.org/10.21767/2572-4657-C1-002>.

- Cardoso, Paulo; Iano, Yuzo; Carvalho, Silvio; **Loschi, Hermes**; Magrin, Fabiano; Castro, Diego; Ferreira, Luiz. Reasons for SFN Failure in Broadcast. SET INTERNATIONAL JOURNAL OF BROADCAST. v. 2017, p. 71-76, 2017. <https://doi.org/10.18580/setijbe.2017.10>.
- Padilha, R., Iano, Y., Moschim, E., Monteiro, A. C. B., & **Loschi, H. J.** (2017, December). Computational Performance of an Model for Wireless Telecommunication Systems with Discrete Events and Multipath Rayleigh. In Brazilian Technology Symposium (pp. 193-203). Springer, Cham. https://doi.org/10.1007/978-3-319-93112-8_20.
- **H, J, Loschi**; Iano, Y. Biomass Cogeneration with Green Coconut Husk: an analysis of efficiency energy solutions. In: Euro-Global Summit and Expo on Biomass, 2016, Birmingham. Scientific Tracks Abstracts: Journal of Fundamentals of Renewable Energy and Applications, 2016. v. 6. p. 1-53. <https://www.longdom.org/conference-abstracts-files/2090-4541.C1.014-020.pdf>.
- **Loschi, Hermes José**; Iano, Yuzo ; León, Julio ; Moretti, Angelo ; Conte, Fabrizio Daibert ; Braga, Horácio. A Review on Photovoltaic Systems: Mechanisms and Methods for Irradiation Tracking and Prediction. Smart Grid and Renewable Energy, v. 06, p. 187-208, 2015. <https://doi.org/10.4236/sgre.2015.67017>.
- **Loschi, Hermes José**; Leon, Julio ; Iano, Yuzo ; Filho, Ernesto Ruppert ; Conte, Fabrizio Daibert ; Lustosa, Telmo Cardoso ; Freitas, Priscila Oliveira. Energy Efficiency in Smart Grid: A Prospective Study on Energy Management Systems. Smart Grid and Renewable Energy, v. 06, p. 250-259, 2015. <https://doi.org/10.4236/sgre.2015.68021>.
- T. C. Lustosa, **H. J. Loschi**, Y. Iano and A. Moretti, "The importance of integrated network management and telecom service through time," 2015 International Workshop on Telecommunications (IWT), Santa Rita do Sapucaí, Brazil, 2015, pp. 1-5, <https://doi.org/10.1109/IWT.2015.7224576>.
- Y. Iano, I. T. Lima, **H. J. Loschi**, T. C. Lustosa, O. S. Mesquita and A. Moretti, "Sustainable computing and communications: Internet broadband network of things applied to intelligent education," 2015 International Conference on Smart Cities and Green ICT Systems (SMARTGREENS), Lisbon, Portugal, 2015, pp. 1-7. <http://dx.doi.org/10.5220/0005447303500356>.
- **Loschi, H. J.** (2015). Compreendendo um Sistema Fotovoltaico: uma abordagem didática conceitual. 1. ed. São Paulo: Baraúna, 2015. v. 1. 150p. ISBN: 978-854-370-427-2.

8.3 Articles in Process of Publication

- **Hermes Loschi**, Douglas Nascimento, Robert Smolenski, Waseem El-Sayed, and Piotr Lezynski. “Shaping of Converter Interference for Error Rate Reduction in PLC Based Smart Metering Systems.” Measurements.
- Angel Pena-Quintal, **Hermes Loschi**, Robert Smolenski, Mark Sumner, Dave Thomas, Steve Green, Piotr Lezynski and Frank Leferink. “Impact of Pseudo-Random Modulation on Measured Conducted EMI.” IEEE EMC Magazine.
- Muhammad Imam Sudrajat, Muhammad Ammar Wibisono, **Hermes Loschi**, Niek Moonen and Frank Leferink. “Evaluation of Nonlinear ARX System Identification Technique on Modeling Crosstalk Effect.” 2022 IEEE International Symposium on EMC+SIPI, August 1-5 Spokane, Washington.

Bibliography

- [1] F. Pareschi, R. Rovatti, and G. Setti, "Emi reduction via spread spectrum in dc/dc converters: State of the art, optimization, and tradeoffs," *IEEE Access*, vol. 3, pp. 2857–2874, 2015.
- [2] B. Czerniewski, J.-L. Schanen, H. Chazal, P. Zanchetta, and C. F. d. Freitas, "Identification and validation of a non symmetrical system level emc model for power electronics converter," in *2021 IEEE Energy Conversion Congress and Exposition (ECCE)*, 2021, pp. 2859–2865.
- [3] F. Leferink, C. Keyer, and A. Melentjev, "Static energy meter errors caused by conducted electromagnetic interference," *IEEE Electromagnetic Compatibility Magazine*, vol. 5, no. 4, pp. 49–55, 2016.
- [4] H. Hirsch, S. Jeschke, L. Wei, M. Trautmann, J. Bärenfänger, M. Maarleveld, J. Heyen, and A. Darrat, "Latest development of the national and international emc-standards for electric vehicles and their charging infrastructure," in *2015 IEEE International Symposium on Electromagnetic Compatibility (EMC)*, 2015, pp. 708–713.
- [5] L. Jiang, H. Liu, and C. Wang, "Summary of emc test standards for wireless power transfer systems of electric vehicles," in *2021 Asia-Pacific International Symposium on Electromagnetic Compatibility (AP EMC)*, 2021, pp. 1–4.
- [6] IEEE, "Ieee draft standard for validation of computational electromagnetics computer modeling and simulations," *IEEE P1547.1/D6*, October 2021, pp. 1–50, 2021.
- [7] M. Seddighi, F. Costa, and M. Petit, "Influence of modifying standard emission levels on the sizing of emc filters," in *2021 23rd European Conference on Power Electronics and Applications (EPE'21 ECCE Europe)*, 2021, pp. P.1–P.9.
- [8] S. K. Rönnberg, M. H. Bollen, H. Amaris, G. W. Chang, I. Y. Gu, Łukasz H. Kocewiak, J. Meyer, M. Olofsson, P. F. Ribeiro, and J. Desmet, "On

- waveform distortion in the frequency range of 2kHz–150kHz—review and research challenges,” *Electric Power Systems Research*, vol. 150, pp. 1–10, 2017. [Online]. Available: <https://www.sciencedirect.com/science/article/pii/S0378779617301864>
- [9] R. Smolenski, *Conducted electromagnetic interference (EMI) in smart grids*. Springer Science & Business Media, 1999.
- [10] A. Matthee, N. Moonen, and F. Leferink, “Micro-grid inrush current stability analysis,” in *2021 IEEE International Joint EMC/SI/PI and EMC Europe Symposium*, 2021, pp. 440–444.
- [11] N. Moonen, “Noise control in novel power electronics for smart grid,” Ph.D. dissertation, University of Twente, Netherlands, Oct. 2019.
- [12] D. Nemashkalo, N. Moonen, and F. Leferink, “Multi-channel time-domain emi evaluation of dominant mode interference for optimized filter design in three-phase systems,” in *2020 IEEE International Symposium on Electromagnetic Compatibility Signal/Power Integrity (EMCSI)*, 2020, pp. 205–208.
- [13] F.-Y. Shih, D. Chen, Y.-P. Wu, and Y.-T. Chen, “A procedure for designing emi filters for ac line applications,” *IEEE Transactions on Power Electronics*, vol. 11, no. 1, pp. 170–181, 1996.
- [14] D. Nemashkalo, N. Moonen, and F. Leferink, “Practical consideration on power line filter design and implementation,” in *2020 International Symposium on Electromagnetic Compatibility - EMC EUROPE*, 2020, pp. 1–6.
- [15] M. Hartmann, H. Ertl, and J. W. Kolar, “Emi filter design for a 1 mhz, 10 kw three-phase/level pwm rectifier,” *IEEE Transactions on Power Electronics*, vol. 26, no. 4, pp. 1192–1204, 2011.
- [16] D. Nemashkalo, N. Moonen, and F. Leferink, “Mode decomposition in multi-channel time-domain conducted emission measurements,” in *2021 IEEE International Joint EMC/SI/PI and EMC Europe Symposium*, 2021, pp. 643–647.
- [17] D. Zhao, B. Ferreira, A. Roc’h, and F. Leferink, “New common mode emi filter for motor drive using a fourth leg in the inverter,” in *2008 International Symposium on Electromagnetic Compatibility - EMC Europe*, 2008, pp. 1–6.
- [18] D. Nemashkalo, N. Moonen, and F. Leferink, “Why not(ch)?” in *2021 Asia-Pacific International Symposium on Electromagnetic Compatibility (APEMC)*, 2021, pp. 1–4.

- [19] S. Shahparnia and O. Ramahi, "Electromagnetic interference (emi) reduction from printed circuit boards (pcb) using electromagnetic bandgap structures," *IEEE Transactions on Electromagnetic Compatibility*, vol. 46, no. 4, pp. 580–587, 2004.
- [20] E.-P. Li, X.-C. Wei, A. C. Cangellaris, E.-X. Liu, Y.-J. Zhang, M. D'Amore, J. Kim, and T. Sudo, "Progress review of electromagnetic compatibility analysis technologies for packages, printed circuit boards, and novel interconnects," *IEEE Transactions on Electromagnetic Compatibility*, vol. 52, no. 2, pp. 248–265, 2010.
- [21] M. Ramdani, E. Sicard, A. Boyer, S. B. Dhia, J. J. Whalen, T. H. Hubing, M. Coenen, and O. Wada, "The electromagnetic compatibility of integrated circuits—past, present, and future," *IEEE Transactions on Electromagnetic Compatibility*, vol. 51, no. 1, pp. 78–100, 2009.
- [22] J. D. van Wyk and F. C. Lee, "On a future for power electronics," *IEEE Journal of Emerging and Selected Topics in Power Electronics*, vol. 1, no. 2, pp. 59–72, 2013.
- [23] "Switching control techniques," https://en.wikipedia.org/wiki/Switching_control_techniques, accessed: 2021-06-15.
- [24] P. Lezynski, "Random modulation in inverters with respect to electromagnetic compatibility and power quality," *IEEE Journal of Emerging and Selected Topics in Power Electronics*, vol. 6, no. 2, pp. 782–790, 2017.
- [25] S. A. Q. Mohammed and J.-W. Jung, "A state-of-the-art review on soft-switching techniques for dc–dc, dc–ac, ac–dc, and ac–ac power converters," *IEEE Transactions on Industrial Informatics*, vol. 17, no. 10, pp. 6569–6582, 2021.
- [26] E. Zhong and T. Lipo, "Improvements in emc performance of inverter-fed motor drives," *IEEE Transactions on Industry Applications*, vol. 31, no. 6, pp. 1247–1256, 1995.
- [27] G. Skibinski, R. Kerkman, and D. Schlegel, "Emi emissions of modern pwm ac drives," *IEEE Industry Applications Magazine*, vol. 5, no. 6, pp. 47–80, 1999.
- [28] L. Rossetto, S. Buso, and G. Spiazzi, "Conducted emi issues in a 600-w single-phase boost pfc design," *IEEE Transactions on Industry Applications*, vol. 36, no. 2, pp. 578–585, 2000.

- [29] H. Akagi and T. Shimizu, "Attenuation of conducted emi emissions from an inverter-driven motor," *IEEE Transactions on Power Electronics*, vol. 23, no. 1, pp. 282–290, 2008.
- [30] H.-H. Chang, I.-H. Hua, and S.-I. Liu, "A spread-spectrum clock generator with triangular modulation," *IEEE Journal of Solid-State Circuits*, vol. 38, no. 4, pp. 673–676, 2003.
- [31] S. Johnson and R. Zane, "Custom spectral shaping for emi reduction in high-frequency inverters and ballasts," *IEEE Transactions on Power Electronics*, vol. 20, no. 6, pp. 1499–1505, 2005.
- [32] A. Stankovic, G. Verghese, and D. Perreault, "Analysis and synthesis of randomized modulation schemes for power converters," *IEEE Transactions on Power Electronics*, vol. 10, no. 6, pp. 680–693, 1995.
- [33] K. Tse, H.-H. Chung, S. Huo, and H. So, "Analysis and spectral characteristics of a spread-spectrum technique for conducted emi suppression," *IEEE Transactions on Power Electronics*, vol. 15, no. 2, pp. 399–410, 2000.
- [34] A. M. Stankovic and H. Lev-Ari, "Randomized modulation in power electronic converters," *Proceedings of the IEEE*, vol. 90, no. 5, pp. 782–799, 2002.
- [35] K. Tse, H. S.-H. Chung, S. Ron Hui, and H. So, "A comparative study of carrier-frequency modulation techniques for conducted emi suppression in pwm converters," *IEEE Transactions on Industrial Electronics*, vol. 49, no. 3, pp. 618–627, 2002.
- [36] K. Tse, R.-M. Ng, H.-H. Chung, and S. Hui, "An evaluation of the spectral characteristics of switching converters with chaotic carrier-frequency modulation," *IEEE Transactions on Industrial Electronics*, vol. 50, no. 1, pp. 171–182, 2003.
- [37] J. Balcells, A. Santolaria, A. Orlandi, D. Gonzalez, and J. Gago, "Emi reduction in switched power converters using frequency modulation techniques," *IEEE Transactions on Electromagnetic Compatibility*, vol. 47, no. 3, pp. 569–576, 2005.
- [38] D. Gonzalez, J. Balcells, A. Santolaria, J.-C. Le Bunetel, J. Gago, D. Magnon, and S. Brehaut, "Conducted emi reduction in power converters by means of periodic switching frequency modulation," *IEEE Transactions on Power Electronics*, vol. 22, no. 6, pp. 2271–2281, 2007.

- [39] "On semiconductor. (nov. 2010). low power, reduced emi clock synthesizer." <https://www.onsemi.com/pdf/datasheet/nb2780a-d.pdf>, accessed: 2022-01-20.
- [40] "Mb88155 spread spectrum clock generator, document ds04- 29119-2ea, fujitsu microelectron., nov. 2006." <https://www.cypress.com/file/242586/download>, accessed: 2022-01-20.
- [41] "Multiphase oscillator with spread spectrum frequency modulation, document ltc6902, linear technology, 2003." <http://cds.linear.com/docs/en/datasheet/6902f.pdf>, accessed: 2022-01-20.
- [42] "Lm5088 evaluation board, texas instrum., dallas, tx, usa, appl. note 1913." <https://www.ti.com/tool/LM5088MH-1EVAL>, accessed: 2022-01-20.
- [43] H. Loschi, R. Smolenski, P. Lezynski, W. El Sayed, and D. Nascimento, "Reduction of conducted emissions in dc/dc converters with fpga-based random modulation," in *2020 International Symposium on Electromagnetic Compatibility - EMC EUROPE*, 2020, pp. 1–6.
- [44] H. Loschi, R. Smolenski, P. Lezynski, D. Nascimento, and G. Demidova, "Aggregated conducted electromagnetic interference generated by dc/dc converters with deterministic and random modulation," *Energies*, vol. 13, no. 14, 2020. [Online]. Available: <https://www.mdpi.com/1996-1073/13/14/3698>
- [45] R. Smolenski, P. Lezynski, J. Bojarski, W. Drozd, and L. C. Long, "Electromagnetic compatibility assessment in multiconverter power systems – conducted interference issues," *Measurement*, vol. 165, p. 108119, 2020. [Online]. Available: <https://www.sciencedirect.com/science/article/pii/S0263224120306576>
- [46] P. Lezynski, R. Smolenski, H. Loschi, D. Thomas, and N. Moonen, "A novel method for emi evaluation in random modulated power electronic converters," *Measurement*, vol. 151, p. 107098, 2020.
- [47] M. I. Sudrajat, N. Moonen, H. Bergsma, R. Bijman, and F. Leferink, "Evaluating rapid voltage changes and its propagation effect using multipoint measurement technique," in *2020 International Symposium on Electromagnetic Compatibility - EMC EUROPE*, 2020, pp. 1–6.
- [48] M. I. Sudrajat, N. Moonen, H. Bergsma, and F. Leferink, "Emi mitigation technique for warship power distribution systems in the frequency range below

- 150 khz,” in *2021 Asia-Pacific International Symposium on Electromagnetic Compatibility (APEMC)*, 2021, pp. 1–4.
- [49] K. Hardin, J. Fessler, and D. Bush, “A study of the interference potential of spread spectrum clock generation techniques,” in *Proceedings of International Symposium on Electromagnetic Compatibility*, 1995, pp. 624–629.
- [50] H. Skinner and K. Slattery, “Why spread spectrum clocking of computing devices is not cheating,” in *2001 IEEE EMC International Symposium. Symposium Record. International Symposium on Electromagnetic Compatibility (Cat. No.01CH37161)*, vol. 1, 2001, pp. 537–540 vol.1.
- [51] K. Hardin, R. Oglesbee, and F. Fisher, “Investigation into the interference potential of spread-spectrum clock generation to broadband digital communications,” *IEEE Transactions on Electromagnetic Compatibility*, vol. 45, no. 1, pp. 10–21, 2003.
- [52] W. E. Sayed, H. Loschi, C. Lok, P. Lezynski, and R. Smolenski, “Prospective analysis of the effect of silicon based and silicon-carbide based converter on g3 power line communication,” in *2020 International Symposium on Electromagnetic Compatibility - EMC EUROPE*, 2020, pp. 1–6.
- [53] W. E. Sayed, P. Lezynski, R. Smolenski, N. Moonen, P. Croveti, and D. W. Thomas, “The effect of emi generated from spread-spectrum-modulated sic-based buck converter on the g3-plc channel,” *Electronics*, vol. 10, no. 12, p. 1416, 2021.
- [54] W. El Sayed, P. Croveti, N. Moonen, P. Lezynski, R. Smolenski, and F. Leferink, “Electromagnetic interference of spread-spectrum modulated power converters in g3-plc power line communication systems,” *IEEE Letters on Electromagnetic Compatibility Practice and Applications*, vol. 3, no. 4, pp. 118–122, 2021.
- [55] W. E. Sayed, H. Loschi, M. A. Wibisono, N. Moonerr, P. Lezynski, and R. Smolenski, “The influence of spread-spectrum modulation on the g3-plc performance,” in *2021 Asia-Pacific International Symposium on Electromagnetic Compatibility (APEMC)*, 2021, pp. 1–4.
- [56] IEC, *Electromagnetic compatibility (EMC) - Part 2-2: Environment - Compatibility levels for low-frequency conducted disturbances and signalling in public low-voltage power supply systems*, IEC 61 000-2-2:2002+AMD1:2017+AMD2:2018, 2018.

- [57] S. Gulur, V. Mahadeva Iyer, and S. Bhattacharya, "A cm filter configuration for grid-tied voltage source converters," *IEEE Transactions on Industrial Electronics*, vol. 67, no. 10, pp. 8100–8111, 2020.
- [58] H. Liao, X. Zhang, and H. Ma, "Impedance-shaping based stability control of point-of-load converter integrated with emi filter in dc microgrids," *IEEE Access*, pp. 1–1, 2021.
- [59] L. Zheng, X. Han, Z. An, R. P. Kandula, K. Kandasamy, M. Saeedifard, and D. Divan, "Sic-based 5-kv universal modular soft-switching solid-state transformer (m-s4t) for medium-voltage dc microgrids and distribution grids," *IEEE Transactions on Power Electronics*, vol. 36, no. 10, pp. 11 326–11 343, 2021.
- [60] F. Leferink, "Conducted interference, challenges and interference cases," *IEEE Electromagnetic Compatibility Magazine*, vol. 4, no. 1, pp. 78–85, 2015.
- [61] D. Miller, G. Mirzaeva, C. D. Townsend, and G. C. Goodwin, "The use of power line communication in standalone microgrids," *IEEE Transactions on Industry Applications*, vol. 57, no. 3, pp. 3029–3037, 2021.
- [62] D. Xu, C. K. Lee, S. Kiratipongvoot, and W. M. Ng, "An active emi choke for both common- and differential-mode noise suppression," *IEEE Transactions on Industrial Electronics*, vol. 65, no. 6, pp. 4640–4649, 2018.
- [63] N. Moonen, R. Vogt-Ardatjew, and F. Leferink, "Simulink-based fpga control for emi investigations of power electronic systems," *IEEE Transactions on Electromagnetic Compatibility*, vol. 63, no. 4, pp. 1266–1273, 2021.
- [64] I. Petric, P. Mattavelli, and S. Buso, "Feedback noise propagation in multisampled dc-dc power electronic converters," *IEEE Transactions on Power Electronics*, pp. 1–1, 2021.
- [65] H. Loschi, P. Lezynski, R. Smolenski, D. Nascimento, and W. Sleszynski, "Fpga-based system for electromagnetic interference evaluation in random modulated dc/dc converters," *Energies*, vol. 13, no. 9, 2020. [Online]. Available: <https://www.mdpi.com/1996-1073/13/9/2389>
- [66] Y. Zhu, J. Wu, R. Wang, Z. Lin, and X. He, "Embedding power line communication in photovoltaic optimizer by modulating data in power control loop," *IEEE Transactions on Industrial Electronics*, vol. 66, no. 5, pp. 3948–3958, 2019.
- [67] D. Yu, K. Li, S. Yu, H. Trinh, P. Zhang, A. M. Oo, and Y. Hu, "A novel power and signal composite modulation approach to powerline data communication

- for srm in distributed power grids,” *IEEE Transactions on Power Electronics*, vol. 36, no. 9, pp. 10 436–10 446, 2021.
- [68] A. E. Shadare, M. N. Sadiku, and S. M. Musa, “Electromagnetic compatibility issues in critical smart grid infrastructure,” *IEEE Electromagnetic Compatibility Magazine*, vol. 6, no. 4, pp. 63–70, 2017.
- [69] A. Llano, D. De La Vega, I. Angulo, and L. Marron, “Impact of channel disturbances on current narrowband power line communications and lessons to be learnt for the future technologies,” *IEEE Access*, vol. 7, pp. 83 797–83 811, 2019.
- [70] A. Khilnani, L. Wan, M. Sumner, D. Thomas, A. Hamid, and F. Grassi, “Conducted emissions measurements in dc grids: Issues in applying existing lisp topologies and possible solutions,” in *2021 IEEE 15th International Conference on Compatibility, Power Electronics and Power Engineering (CPE-POWERENG)*, 2021, pp. 1–6.
- [71] IEC, *Photovoltaic power generating systems - EMC requirements and test methods for power conversion equipment.*, Std. IEC 62 920:2017, Ed. 1, Am. 1, 2017.
- [72] X. Yue, D. Boroyevich, F. C. Lee, F. Chen, R. Burgos, and F. Zhuo, “Beat frequency oscillation analysis for power electronic converters in dc nanogrid based on crossed frequency output impedance matrix model,” *IEEE Transactions on Power Electronics*, vol. 33, no. 4, pp. 3052–3064, 2018.
- [73] R. F. Q. Magossi, L. J. Elias, F. A. Faria, R. Q. Machado, and V. A. Oliveira, “An n-pwm dc–dc converter modeling: Switched systems meets fourier series,” *IEEE Transactions on Industrial Electronics*, vol. 69, no. 4, pp. 3255–3265, 2022.
- [74] Q. Li, D. Jiang, Z. Shen, Y. Zhang, and Z. Liu, “Variable switching frequency pwm strategy for high-frequency circulating current control in paralleled inverters with coupled inductors,” *IEEE Transactions on Power Electronics*, vol. 35, no. 5, pp. 5366–5380, 2020.
- [75] R. Faraji, H. Farzanehfard, M. Esteki, and S. A. Khajehoddin, “A lossless passive snubber circuit for three-port dc–dc converter,” *IEEE Journal of Emerging and Selected Topics in Power Electronics*, vol. 9, no. 2, pp. 1905–1914, 2021.
- [76] A. Pena-Quintal, K. Niewiadomski, S. Greedy, M. Sumner, and D. Thomas, “The influence of the number of frequencies and the frequency repetitions rates in spread spectrum sigma-delta modulated dc-dc converters,” in

- 2021 Asia-Pacific International Symposium on Electromagnetic Compatibility (APEMC)*, 2021, pp. 1–4.
- [77] X. Yue, X. Wang, and F. Blaabjerg, “Review of small-signal modeling methods including frequency-coupling dynamics of power converters,” *IEEE Transactions on Power Electronics*, vol. 34, no. 4, pp. 3313–3328, 2019.
- [78] IEC, *Specification for radio disturbance and immunity measuring apparatus and methods - Part 1-1: Radio disturbance and immunity measuring apparatus - Measuring apparatus.*, Std. IEC CISPR 16-1-1, 2015.
- [79] M. Malinowski, J. I. Leon, and H. Abu-Rub, “Solar photovoltaic and thermal energy systems: Current technology and future trends,” *Proceedings of the IEEE*, vol. 105, no. 11, pp. 2132–2146, 2017.
- [80] B. t. Have, T. Hartman, N. Moonen, and F. Leferink, “Why frequency domain tests like iec 61000-4-19 are not valid; a call for time domain testing,” in *2019 International Symposium on Electromagnetic Compatibility - EMC EUROPE*, 2019, pp. 124–128.
- [81] S. Legowski and A. Trzynadlowski, “Hypersonic mosfet-based power inverter with random pulse width modulation,” in *Industry Applications Society Annual Meeting, 1989., Conference Record of the 1989 IEEE*. IEEE, 1989, pp. 901–903.
- [82] A. M. Trzynadlowski, S. Legowski, and R. L. Kirlin, “Random pulse width modulation technique for voltage-controlled power inverters,” in *Industry Applications Society Annual Meeting, 1987., Conference Record of the 1987 IEEE*. IEEE, 1987, pp. 863–868.
- [83] R. Kirlin, S. Legowski, and A. Trzynadlowski, “An optimal approach to random pulse width modulation in power inverters,” in *Power Electronics Specialists Conference, 1995. PESC'95 Record., 26th Annual IEEE*, vol. 1. IEEE, 1995, pp. 313–318.
- [84] R. L. Kirlin, C. Lascu, and A. M. Trzynadlowski, “Shaping the noise spectrum in power electronic converters,” *IEEE Transactions on Industrial Electronics*, vol. 58, no. 7, pp. 2780–2788, 2011.
- [85] C. Liaw, Y. Lin, C. Wu, and K. Hwu, “Analysis, design, and implementation of a random frequency pwm inverter,” *IEEE Transactions on Power Electronics*, vol. 15, no. 5, pp. 843–854, 2000.

- [86] K.-S. Kim, Y.-G. Jung, and Y.-C. Lim, "A new hybrid random pwm scheme," *IEEE Transactions on Power Electronics*, vol. 24, no. 1, pp. 192–200, 2009.
- [87] L. Mathe, F. Lungeanu, D. Sera, P. O. Rasmussen, and J. K. Pedersen, "Spread spectrum modulation by using asymmetric-carrier random pwm," *IEEE Transactions on Industrial Electronics*, vol. 59, no. 10, pp. 3710–3718, 2012.
- [88] Y.-C. Chang and C.-M. Liaw, "A flyback rectifier with spread harmonic spectrum," *IEEE Transactions on Industrial Electronics*, vol. 58, no. 8, pp. 3485–3499, 2011.
- [89] C.-H. Tsai, C.-H. Yang, and J.-C. Wu, "A digitally controlled switching regulator with reduced conductive emi spectra," *IEEE Transactions on Industrial Electronics*, vol. 60, no. 9, pp. 3938–3947, 2013.
- [90] Y.-S. Lai, Y.-T. Chang, and B.-Y. Chen, "Novel random-switching pwm technique with constant sampling frequency and constant inductor average current for digitally controlled converter," *IEEE Transactions on Industrial Electronics*, vol. 60, no. 8, pp. 3126–3135, 2013.
- [91] B. Jacob and M. Baiju, "Vector-quantized space-vector-based spread spectrum modulation scheme for multilevel inverters using the principle of over-sampling adc," *IEEE transactions on Industrial Electronics*, vol. 60, no. 8, pp. 2969–2977, 2013.
- [92] M. M. Bech, F. Blaabjerg, and J. K. Pedersen, "Random modulation techniques with fixed switching frequency for three-phase power converters," in *Power Electronics Specialists Conference, 1999. PESC 99. 30th Annual IEEE*, vol. 1, Aug 1999, pp. 544–551 vol.1.
- [93] D. Jiang, R. Lai, F. Wang, F. Luo, S. Wang, and D. Boroyevich, "Study of conducted emi reduction for three-phase active front-end rectifier," *IEEE Transactions on Power Electronics*, vol. 26, no. 12, pp. 3823–3831, 2011.
- [94] K. Tse, H.-H. Chung, S. Huo, and H. So, "Analysis and spectral characteristics of a spread-spectrum technique for conducted emi suppression," *IEEE Transactions on Power Electronics*, vol. 15, no. 2, pp. 399–410, 2000.
- [95] H. Khan, E.-H. Miliani, and K. E. K. Drissi, "Discontinuous random space vector modulation for electric drives: A digital approach," *IEEE Transactions on Power Electronics*, vol. 27, no. 12, pp. 4944–4951, 2012.

- [96] Y. Lai and B. Chen, "New random pwm technique for a full-bridge dc/dc converter with harmonics intensity reduction and considering efficiency," *IEEE Transactions on Power Electronics*, vol. 28, no. 11, pp. 5013–5023, 2013.
- [97] S. Chatterjee, A. K. Garg, K. Chatterjee, and H. Kumar, "Chaotic pwm spread spectrum scheme for conducted noise mitigation in dc-dc converters," in *2015 International Conference on Energy, Power and Environment: Towards Sustainable Growth (ICEPE)*, 2015, pp. 1–6.
- [98] V. Adrian, J. S. Chang, and B. Gwee, "A randomized wrapped-around pulse position modulation scheme for dc–dc converters," *IEEE Transactions on Circuits and Systems I: Regular Papers*, vol. 57, no. 9, pp. 2320–2333, 2010.
- [99] Y. Lai, Y. Chang, and B. Chen, "Novel random-switching pwm technique with constant sampling frequency and constant inductor average current for digitally controlled converter," *IEEE Transactions on Industrial Electronics*, vol. 60, no. 8, pp. 3126–3135, 2013.
- [100] G. Marsala and A. Ragusa, "Spread spectrum in random pwm dc-dc converters by pso ga optimized randomness levels," in *2017 IEEE 5th International Symposium on Electromagnetic Compatibility (EMC-Beijing)*, 2017, pp. 1–6.
- [101] Y. Lim, S. Wi, J. Kim, and Y. Jung, "A pseudorandom carrier modulation scheme," *IEEE Transactions on Power Electronics*, vol. 25, no. 4, pp. 797–805, 2010.
- [102] S. Rapuano and F. J. Harris, "An introduction to fft and time domain windows," *IEEE Instrumentation Measurement Magazine*, vol. 10, no. 6, pp. 32–44, 2007.
- [103] A. V. Oppenheim, *Discrete-time signal processing*. Pearson Education India, 1999.
- [104] T. Karaca, B. Deutschmann, and G. Winkler, "Emi-receiver simulation model with quasi-peak detector," in *2015 IEEE International Symposium on Electromagnetic Compatibility (EMC)*, 2015, pp. 891–896.
- [105] T. Hartman, R. Grootjans, N. Moonen, and F. Leferink, "Time-domain emi measurements using a low cost digitizer to optimize the total measurement time for a test receiver," in *2020 International Symposium on Electromagnetic Compatibility - EMC EUROPE*, 2020, pp. 1–6.

- [106] IEC, *Electromagnetic compatibility (EMC) – Part 2-2: Environment – Compatibility levels for low frequency conducted disturbances and signalling in public low-voltage power supply systems*., Std. IEC 61 000-4-7, 2018.
- [107] W. Li, G. Wei, X. Pan, H. Wan, and C. Qi, “Quasi-peak — one of sensitive parameters of electromagnetic interference in communication equipment,” in *2017 International Applied Computational Electromagnetics Society Symposium (ACES)*, 2017, pp. 1–2.
- [108] V. V. Estrela, O. Saotome, H. J. Loschi, J. Hemanth, W. S. Farfan, J. Aroma, C. Saravanan, and E. G. Grata, “Emergency response cyber-physical framework for landslide avoidance with sustainable electronics,” *Technologies*, vol. 6, no. 2, p. 42, 2018.
- [109] R. Smoleński, “Selected conducted electromagnetic interference issues in distributed power systems,” *Bulletin of the Polish Academy of Sciences: Technical Sciences*, vol. 57, no. 4, pp. 383–393, 2009.
- [110] Q. Peng, Q. Jiang, Y. Yang, T. Liu, H. Wang, and F. Blaabjerg, “On the stability of power electronics-dominated systems: Challenges and potential solutions,” *IEEE Transactions on Industry Applications*, vol. 55, no. 6, pp. 7657–7670, 2019.
- [111] B. Yuan, M.-X. Liu, W. T. Ng, and X.-Q. Lai, “Hybrid buck converter with constant mode changing point and smooth mode transition for high-frequency applications,” *IEEE Transactions on Industrial Electronics*, vol. 67, no. 2, pp. 1466–1474, 2019.
- [112] T. Arunkumari and V. Indragandhi, “An overview of high voltage conversion ratio dc-dc converter configurations used in dc micro-grid architectures,” *Renewable and Sustainable Energy Reviews*, vol. 77, pp. 670–687, 2017.
- [113] H. Loschi, L. Ferreira, D. Nascimento, P. Cardoso, S. Carvalho, and F. Conte, “Emc evaluation of off-grid and grid-tied photovoltaic systems for the brazilian scenario,” *Journal of Clean Energy Technologies*, vol. 6, no. 2, pp. 125–133, 2018.
- [114] J. Bojarski, R. Smolenski, P. Lezynski, and Z. Sadowski, “Diophantine equation based model of data transmission errors caused by interference generated by dc-dc converters with deterministic modulation,” *Bulletin of the Polish Academy of Sciences Technical Sciences*, vol. 64, no. 3, pp. 575–580, 2016.

- [115] I. Lamrani, A. Banerjee, and S. K. S. Gupta, "Operational data-driven feedback for safety evaluation of agent-based cyber-physical systems," *IEEE Transactions on Industrial Informatics*, vol. 17, no. 5, pp. 3367–3378, 2021.
- [116] C. Sonntag, S. Engell, and T. Samad, *Challenges and Potential for EU-US Collaboration at the Intersection of the Internet of Things and Cyber-physical Systems*, 2020, pp. 111–144.
- [117] R. Heartfield, G. Loukas, A. Bezemskij, and E. Panaousis, "Self-configurable cyber-physical intrusion detection for smart homes using reinforcement learning," *IEEE Transactions on Information Forensics and Security*, vol. 16, pp. 1720–1735, 2021.
- [118] S. Yoo, Y. Jo, and H. Bahn, "Integrated scheduling of real-time and interactive tasks for configurable industrial systems," *IEEE Transactions on Industrial Informatics*, pp. 1–1, 2021.
- [119] S. Kim, Y. Eun, and K.-J. Park, "Stealthy sensor attack detection and real-time performance recovery for resilient cps," *IEEE Transactions on Industrial Informatics*, pp. 1–1, 2021.
- [120] E. G. Kaigom and J. Roßmann, "Value-driven robotic digital twins in cyber-physical applications," *IEEE Transactions on Industrial Informatics*, vol. 17, no. 5, pp. 3609–3619, 2021.
- [121] A. Termehchi and M. Rasti, "Joint sampling time and resource allocation for power efficiency in industrial cyber-physical systems," *IEEE Transactions on Industrial Informatics*, vol. 17, no. 4, pp. 2600–2610, 2021.
- [122] I. Stevanović, B. Wunsch, G. L. Madonna, and S. Skibin, "High-frequency behavioral multiconductor cable modeling for emi simulations in power electronics," *IEEE Transactions on Industrial Informatics*, vol. 10, no. 2, pp. 1392–1400, 2014.
- [123] Z. Zhang, Y. Hu, X. Chen, G. W. Jewell, and H. Li, "A review on conductive common-mode emi suppression methods in inverter fed motor drives," *IEEE Access*, vol. 9, pp. 18 345–18 360, 2021.
- [124] Z. Kubík and J. Skála, "Electromagnetic interference from dc/dc converter of photovoltaic system," in *2019 International Conference on Applied Electronics (AE)*. IEEE, 2019, pp. 1–4.
- [125] C. H. National Instruments, "Pxi express: Ni pxie-8135 user manual," 2012–2013 National Instruments Corporation., Tech. Rep.

- [126] SlideToDoc, "Readout with lab view arun veeramani national instruments," Access in 23-03-2021 in <https://slidetodoc.com/readout-with-lab-view-arun-veeramani-national-instruments/>, 2021.
- [127] L. C. of Mechatronics, "Labview - ni - software," Access in 23-03-2021 in <https://www.lcm.at/en/project/labview-ni-software/>, 2021.
- [128] C. H. National Instruments, "Ni r series multifunction rio user manual ni 781xr, ni 783xr, ni 784xr, and ni 785xr devices," 2003–2009 National Instruments Corporation., Tech. Rep.
- [129] C. Cano, A. Pittolo, D. Malone, L. Lampe, A. M. Tonello, and A. G. Dabak, "State of the art in power line communications: From the applications to the medium," *IEEE Journal on Selected Areas in Communications*, vol. 34, no. 7, pp. 1935–1952, 2016.
- [130] K. Huang and J. A. Ferreira, "Two operational modes of the modular multilevel dc converter," in *2015 9th International Conference on Power Electronics and ECCE Asia (ICPE-ECCE Asia)*, 2015, pp. 1347–1354.
- [131] S. Debnath, J. Qin, B. Bahrani, M. Saeedifard, and P. Barbosa, "Operation, control, and applications of the modular multilevel converter: A review," *IEEE Transactions on Power Electronics*, vol. 30, no. 1, pp. 37–53, 2015.
- [132] S.-P. Weber, E. Hoene, S. Guttowski, J. John, and H. Reichl, "Predicting parasitics and inductive coupling in emi-filters," in *Twenty-First Annual IEEE Applied Power Electronics Conference and Exposition, 2006. APEC '06.*, 2006, pp. 4 pp.—.
- [133] S. Weßling and S. Dickmann, "Predicting the conducted emissions of switched-mode power converters including component and printed circuit board parasitics," in *2015 IEEE International Symposium on Electromagnetic Compatibility (EMC)*, 2015, pp. 1406–1411.
- [134] N. Moonen, F. Buesink, and F. Leferink, "Unexpected poor performance of presumed high-quality power line filter, and how it improved," in *2015 IEEE International Symposium on Electromagnetic Compatibility (EMC)*, 2015, pp. 382–385.
- [135] IEC, *Electromagnetic compatibility - Requirements for household appliances, electric tools and similar apparatus - Part 1: Emission.*, Std. IEC CISPR 14-1, 2020.

- [136] "Ieee recommended practice and requirements for harmonic control in electric power systems," *IEEE Std 519-2014 (Revision of IEEE Std 519-1992)*, pp. 1–29, 2014.
- [137] M. A. Wibisono, T. Hartman, N. Moonen, D. Hamdani, and F. Leferink, "The effect of the current pulse width from leds on narrowband power line communication and its analysis in time and frequency domain," in *2020 International Symposium on Electromagnetic Compatibility - EMC EUROPE*, 2020, pp. 1–6.
- [138] S. Rinaldi, F. Bonafini, P. Ferrari, A. Flammini, M. Pasetti, E. Sisinni, G. Artale, A. Cataliotti, V. Cosentino, D. D. Cara, N. Panzavecchia, and G. Tinè, "An experimental characterization of time of arrival accuracy for time synchronization of medium voltage smart grid solutions," in *2019 IEEE 10th International Workshop on Applied Measurements for Power Systems (AMPS)*, 2019, pp. 1–6.
- [139] M. I. Sudrajat, M. A. Wibisono, H. Loschi, N. Moonen, and F. Leferink, "Capturing the worst conducted emission behavior of two-transistor converters motor-operated equipment." in *International Symposium and Exhibition on Electromagnetic Compatibility September 5-8, 2022, Gothenburg (EMC Europe 2022)*, 2022.
- [140] V. Quintard, H. Issa, and A. Pérennou, "Dynamic behavior of a multi-wavelength acousto-optic filter," *Physics Procedia*, vol. 70, pp. 770–773, 2015.
- [141] A. Ferrero, D. Petri, P. Carbone, and M. Catelani, *EMC Measurements*, 2015, pp. 317–351.
- [142] T. Weiss and F. Jondral, "Spectrum pooling: an innovative strategy for the enhancement of spectrum efficiency," *IEEE Communications Magazine*, vol. 42, no. 3, pp. S8–14, 2004.
- [143] K. Niewiadomski, R. Smolenski, P. Lezynski, J. Bojarski, D. W. P. Thomas, and F. Blaabjerg, "Comparative analysis of deterministic and random modulations based on mathematical models of transmission errors in series communication," *IEEE Transactions on Power Electronics*, vol. 37, no. 10, pp. 11 985–11 995, 2022.
- [144] F. G. Stremler, *Introduction to communication systems*, 1990.
- [145] G. Dolling, C. Enkrich, M. Wegener, C. M. Soukoulis, and S. Linden, "Simultaneous negative phase and group velocity of light in a metamaterial," *Science*, vol. 312, no. 5775, pp. 892–894, 2006.

- [146] R. Baillie, D. Borwein, and J. Borwein, "Surprising sinc sums and formulas," *The American Mathematical Monthly*, vol. 115, no. 10, pp. 888–901, 2008.
- [147] K. R. Stromberg, *An Introduction to Classical Real Analysis*, Wadsworth, 1981.
- [148] E. Titchmarsh, *Introduction to the Theory of Fourier Integrals* Oxford University Press, 1937.
- [149] D. Borwein and J. M. Borwein, "Some remarkable properties of sinc and related integrals," *The Ramanujan Journal*, vol. 5, no. 1, pp. 73–89, 2001.
- [150] J. M. Borwein, D. H. Bailey, and R. Girgensohn, *Experimentation in mathematics: Computational paths to discovery*. CRC Press, 2004.
- [151] D. Borwein, J. M. Borwein, and B. A. Mares, "Multi-variable sinc integrals and volumes of polyhedra," *The Ramanujan Journal*, vol. 6, no. 2, pp. 189–208, 2002.
- [152] W. E. Sayedl, H. Loschi, A. Madi, N. Moonen, R. Smolenski, and F. Leferink, "Low-frequency envelope of dc/dc converters due differences in the control hardware features," in *2021 Asia-Pacific International Symposium on Electromagnetic Compatibility (AP EMC)*, 2021, pp. 1–4.

Appendix A

Rectangular Pulse Trains

An ideal periodic rectangular pulse train $X(t)$ is illustrated in Figure A.1. The period (T) determines the pulse spacing of the signal instantaneously, transitions between low and high states, whose amplitudes are 0 and A , respectively.

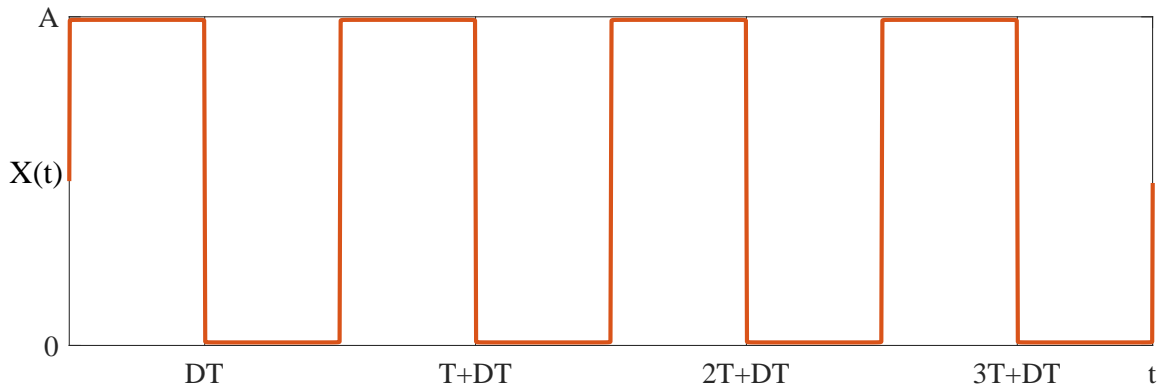


Figure A.1: An Ideal periodic rectangular pulse train, with instantaneous transitions between 0 and A at perfectly regular intervals.

Figure A.1 shows the time width (DT) as a product of the period T and fractional D . The fractional D , is the fraction of the time where the signal dwells in A . Thus, the $X(t)$ must contain an instantaneous transition between 0 and A at perfectly rectangular intervals. Therefore, considering A centered around the origin, i.e. 0, the function $X(t)$ can be expressed as (A.1):

$$X(t) = \begin{cases} A, & |t| \leq \frac{DT}{2} \\ 0, & |t| > \frac{DT}{2} \end{cases}, -\frac{T}{2} < t < \frac{T}{2}. \quad (\text{A.1})$$

However, in practical applications with DC/DC converters, several conditions might influence the shape of $X(t)$, such as the switching rate of change. The switching rate of change can be defined as the ability to keep the period T , hence the

fundamental frequency f_0 , for more extended periods of time t , when using RanM. Those conditions are based on the user specification or in the requirements of the application [44].

Nevertheless, from the modelling point of view, the waveforms, such as $X(t)$, that is periodic in time t can be represented using the trigonometric form of the Fourier series [144], as expressed by (A.2):

$$X(t) = A_0 + \sum_{n=1}^{\infty} (A_n \cos(n2\pi f_0 t) + B_n \sin(n2\pi f_0 t)). \quad (\text{A.2})$$

The first term in (A.2), A_0 , is a constant amplitude calculated using the fractional D. The summation in the second term extends to infinity. Each sine (sin) and cosine (cos) function in the summation is multiplied by a Fourier coefficient (A_n and B_n), which depends on the index of harmonic summation (n).

Also, in the summation included in (A.2), the oscillation frequency of each trigonometric term is the f_0 multiplied by n , which is a positive integer. The first harmonic frequency is equal to the f_0 : the first harmonic frequency is found by multiplying the f_0 by one, i.e., $n = 1$. Furthermore, an ideal $X(t)$ must consider a D between 0 and t , in the case of a sinusoidal pulse of the fundamental frequency $n = 1$ if we consider the positive values to be the high state then $D = \frac{T}{2}$.

The trigonometric form of the Fourier series [144], is strictly based on the concept of even and odd function. An even function $X_e(t)$, is symmetric about $t = 0$, i.e. $X_e(t) = X_e(-t)$. An odd function $X_o(t)$, is antisymmetric about $t = 0$, i.e. $X_o(t) = -X_o(-t)$. (note: this implies that $X_o(0) = 0$).

Other important facts about $X_e(t)$ and $X_o(t)$:

- The product of two even functions is an even function. Given two even functions $X_{e1}(t)$ and $X_{e2}(t)$, their product $Y_e(t) = X_{e1}(t) \cdot X_{e2}(t)$ is even;
- The product of two odd functions is an even function. Given two odd functions $X_{o1}(t)$ and $X_{o2}(t)$, their product $Y_e(t) = X_{o1}(t) \cdot X_{o2}(t)$ is even;
- The product of an even function and an odd function is an odd function. Given an even function, $X_e(t)$ and an odd function $X_o(t)$, their product $Y_o(t) = X_e(t) \cdot X_o(t)$ is odd;
- The integral of an odd function, $X_o(t)$, from $t = -A$ to $t = A$ is equal to zero. The same is not generally true for even functions. In other words, the integral of an even function, $X_e(t)$, from $t = -A$ to $t = A$ is not generally equal to zero.

A.1 Fourier Transform Approach

The $X(t)$ can be considered as a sum of cosines of various frequencies, thus, only A_n are considered, as expressed by (A.3):

$$X(t) = A_0 + \sum_{n=1}^{\infty} (A_n \cos(n2\pi f_0 t)) . \quad (\text{A.3})$$

The equation (A.3) is called the "synthesis" equation because it shows how it might create or synthesize the function $X(t)$ by adding up cosines. The A_0 is expressed by (A.4):

$$A_0 = A \frac{DT}{T} . \quad (\text{A.4})$$

The other terms of the (A.3) follow (A.5). To facilitate the modelling, it's assumed that $\omega_0 = 2\pi f_0$. Then, both sides of the partial Fourier sum from (A.3) are multiplied by $\cos(m\omega_0 t)$:

$$X(t) \cos(m\omega_0 t) = \sum_{n=1}^{\infty} A_n \cos(n\omega_0 t) \cos(m\omega_0 t). \quad (\text{A.5})$$

Then integrating over the period defined by (A.1):

$$\int_{-\frac{T}{2}}^{\frac{T}{2}} X(t) \cos(m\omega_0 t) dt = \int_{-\frac{T}{2}}^{\frac{T}{2}} \sum_{n=1}^{\infty} A_n \cos(n\omega_0 t) \cos(m\omega_0 t) dt. \quad (\text{A.6})$$

Also, switching the order of summation and integrating on the right-hand side (A.7), followed (A.8) by identity application $\cos(a) \cos(b) = \frac{1}{2}(\cos(a+b) + \cos(a-b))$:

$$\int_{-\frac{T}{2}}^{\frac{T}{2}} X(t) \cos(m\omega_0 t) dt = \sum_{n=1}^{\infty} A_n \int_{-\frac{T}{2}}^{\frac{T}{2}} \cos(n\omega_0 t) \cos(m\omega_0 t) dt, \quad (\text{A.7})$$

$$\int_{-\frac{T}{2}}^{\frac{T}{2}} X(t) \cos(m\omega_0 t) dt = \frac{1}{2} \sum_{n=1}^{\infty} A_n \int_{-\frac{T}{2}}^{\frac{T}{2}} (\cos((n+m)\omega_0 t) + \cos((n-m)\omega_0 t)) dt. \quad (\text{A.8})$$

It's possible to consider only the cases when $m \geq 0$, then the function $\cos((n+m)\omega_0 t)$ has exactly $(n+m)$ complete oscillations in the interval of integration (A.1). When we integrate the function $\cos((n+m)\omega_0 t)$, the result is zero since we integrate over an integer (greater than or equal to one) number of oscillations. This simplifies our development to:

$$\int_{-\frac{T}{2}}^{\frac{T}{2}} X(t) \cos(m\omega_0 t) dt = \frac{1}{2} \sum_{n=1}^{\infty} A_n \int_{-\frac{T}{2}}^{\frac{T}{2}} \cos((n-m)\omega_0 t) dt. \quad (\text{A.9})$$

Once (A.9) presents \cos as a function of the $X_o(t)$, i.e., $\cos(m\omega_0 t) = \cos((n - m)\omega_0 t)$, time-varying and with exactly $|n - m|$ complete oscillations in the interval of integration (A.1), except when $n = m$ in which $\cos((n - m)\omega_0 t) = \cos(0) = 1$, thus:

$$\int_{-\frac{T}{2}}^{\frac{T}{2}} \cos((n - m)\omega_0 t) dt = \begin{cases} \int_{-\frac{T}{2}}^{\frac{T}{2}} \cos((n - m)\omega_0 t) dt = 0, n \neq m, \\ \int_{-\frac{T}{2}}^{\frac{T}{2}} 1 \cdot dt = T, n = m. \end{cases} \quad (\text{A.10})$$

Therefore, considering (A.9), and that n goes from 1 to ∞ , every term in the summation (except when $n = m$) will be zero. The only term that contributes to the summation is $n = m$, when the integral equals T . Thus, the entire summation expressed by (A.9) reduces to (A.13):

$$\int_{-\frac{T}{2}}^{\frac{T}{2}} X(t) \cos(m\omega_0 t) dt = \frac{1}{2} A_n T, \quad (\text{A.11})$$

$$A_n = \frac{2}{T} \int_{-\frac{T}{2}}^{\frac{T}{2}} X(t) \cos(m\omega_0 t) dt, \quad (\text{A.12})$$

$$A_n = \frac{2}{T} \int_{-\frac{T}{2}}^{\frac{T}{2}} X(t) \cos(n2\pi f_0 t) dt, n \neq 0. \quad (\text{A.13})$$

Nonetheless, $X(t) = A$ between $-\frac{DT}{2}$ to $\frac{DT}{2}$ and zero elsewhere. Thus, the integral represented in (A.13) simplifies and can be solved, as follow:

$$A_n = \frac{2}{T} \int_{-\frac{DT}{2}}^{\frac{DT}{2}} A \cos(n2\pi f_0 t) dt, \quad (\text{A.14})$$

$$A_n = \frac{2}{T} \frac{A}{n2\pi f_0} \sin(n2\pi f_0 t) \Bigg|_{-\frac{DT}{2}}^{+\frac{DT}{2}}, \quad (\text{A.15})$$

$$A_n = \frac{2}{T} \frac{A}{n2\pi f_0} \left(\sin\left(n2\pi f_0 \frac{DT}{2}\right) - \sin\left(n2\pi f_0 \frac{DT}{2}\right) \right). \quad (\text{A.16})$$

Once (A.16) presents the \sin as a function of the $X_e(t)$, i.e., $\sin(a) - \sin(a) = 2 \sin(a)$, and using the fact that $f_0 = \frac{1}{T}$, the (A.16) can be expressed by (A.17)

$$A_n = \frac{4}{T} \frac{A}{n2\pi f_0} \sin\left(n2\pi f_0 \frac{DT}{2}\right) = 2 \frac{A}{n\pi} \sin\left(n\pi \frac{DT}{T}\right). \quad (\text{A.17})$$

Thus, the Fourier sum from (A.3), from $n = 1$ to ∞ can be expressed by (A.18):

$$X(t) = A_0 + \sum_{n=1}^{\infty} 2 \frac{A}{n\pi} \sin\left(n\pi \frac{DT}{T}\right) \cos(n2\pi f_0 t). \quad (\text{A.18})$$

A.2 Even and Odd Harmonics

Based on the interval of integration defined by (A.1), $f_0 = 20$ Hz ($T=0.05$ s) and $A = 1$, Figure A.2 and Figure A.3 shows the performance of (A.18) with $D= 50\%$. For further information about the MATLAB script used, please see B.1 and B.2.

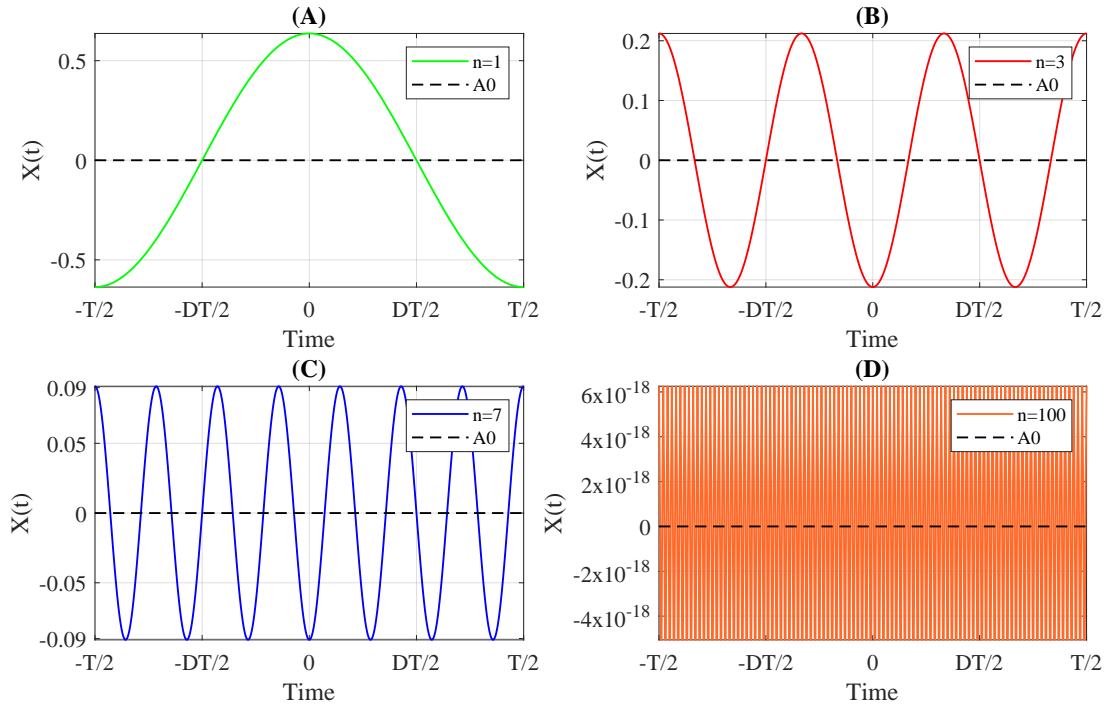


Figure A.2: Rectangular Pulse with Individual Odd Harmonics: (A) $n = 1$ and $D= 50\%$, (B) $n = 3$ and $D= 50\%$, (C) $n = 7$ and $D= 50\%$, and (D) $n = 100$ and $D= 50\%$.

Figure A.2 shows the highest harmonic component for $n = 1$ (Figure A.2-A). The lower harmonic components are obtained according to the increase of the odd number related to n (Figure A.2-D). On the other hand, Figure A.3 shows that according to the adding of \sin waves of increasingly higher frequency, e.g. $n = 1 \times 10^4$, the approximation to the expected $X(t) = A$, with D equal to 50% improves and tracks the rapid changes, i.e., the discontinuity (Figure A.3-D). Thus, since Gibb's overshoot exists on either side of the discontinuity, only odd harmonics (1, 3, 5, ...) are needed to approximate the $X(t)$ function (Figure A.3-D), and the even harmonics may be considered as nonexistent. However, that is not totally true for cases where $D \neq 50\%$.

Figure A.4 and Figure A.5 shows the performance of (A.18) with $D= 30\%$. Moreover, Figure A.6 and Figure A.7 shows the performance of (A.18) with $D= 70\%$. All the cases presented by Figure A.4, Figure A.5, Figure A.6, and Figure A.7 consider the interval of integration defined by (A.1), $f_0 = 20$ Hz ($T=0.05$ s) and $A = 1$.

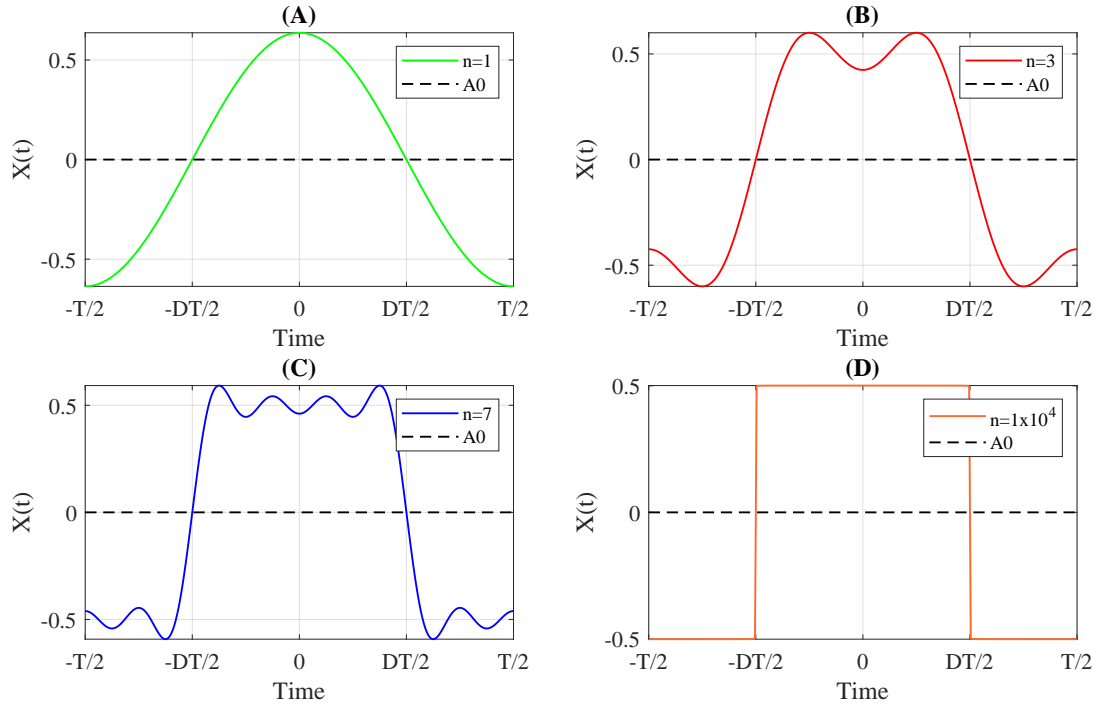


Figure A.3: Rectangular Pulses with Aggregated (Summation) Odd Harmonics: (A) $n = 1$ and $D = 50\%$, (B) $n = 3$ and $D = 50\%$, (C) $n = 7$ and $D = 50\%$, and (D) $n = 1 \times 10^4$ and $D = 50\%$.

Figure A.4, Figure A.5, Figure A.6, and Figure A.7 shows that the coefficients of the Fourier series (C_n) are no longer equal to zero for even harmonics, in the cases where the $D \neq 50\%$.

Therefore, in this subsection A.2, it's also assumed to modeling C_n based on the complex exponential Fourier series [144]. Thus, considering the pulse $\frac{DT}{2}$ described in (A.1) scaled in t by DT , the interval of integration can be expressed by (A.19):

$$X(t) \left(\frac{t}{DT} \right) = \begin{cases} A, & |t| \leq \frac{DT}{2} \\ 0, & |t| > \frac{DT}{2} \end{cases}, \quad -\frac{T}{2} < t < \frac{T}{2}. \quad (\text{A.19})$$

Thus, the C_n are given by:

$$X(t) \left(\frac{t}{DT} \right) = \sum_{n=-\infty}^{+\infty} C_n e^{jn\omega_0 t}, \quad (\text{A.20})$$

$$C_n = \int_T X(t) \left(\frac{t}{DT} \right) e^{-jn\omega_0 t} dt. \quad (\text{A.21})$$

Considering the interval of integration defined by (A.19) and make use of the facts that $X(t) \left(\frac{t}{DT} \right)$ is constant for $|t| \leq \frac{DT}{2}$ and zero elsewhere (A.22). Also, considering

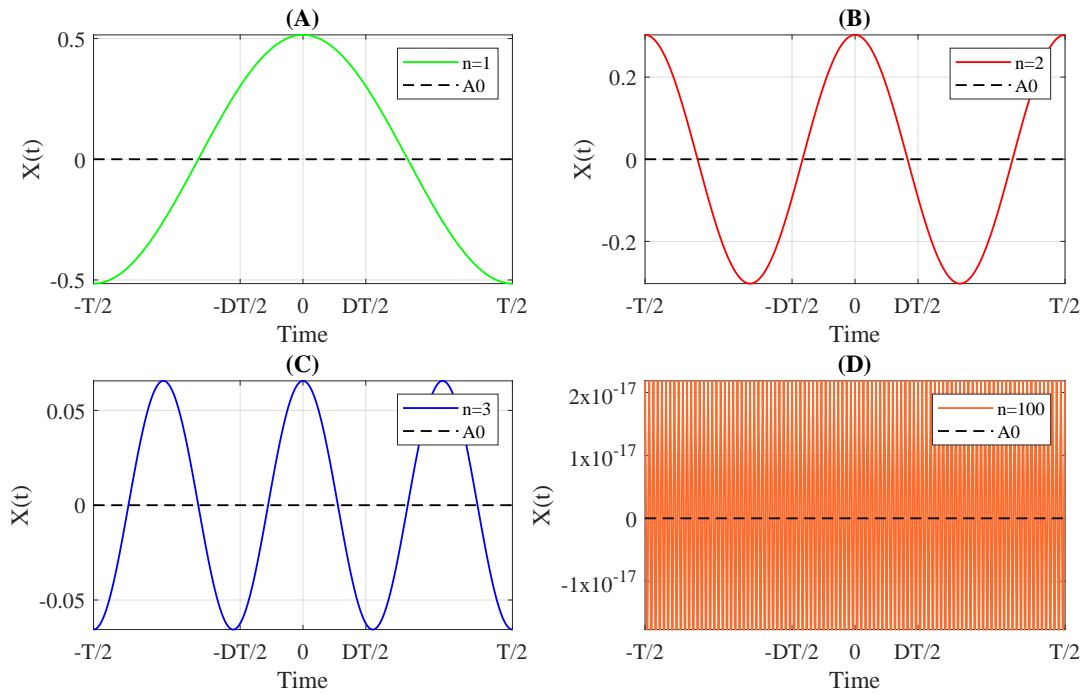


Figure A.4: Rectangular Pulses with Individual Odd and Even Harmonics: (A) $n = 1$ and $D = 30\%$, (B) $n = 2$ and $D = 30\%$, (C) $n = 3$ and $D = 30\%$, and (D) $n = 100$ and $D = 30\%$.

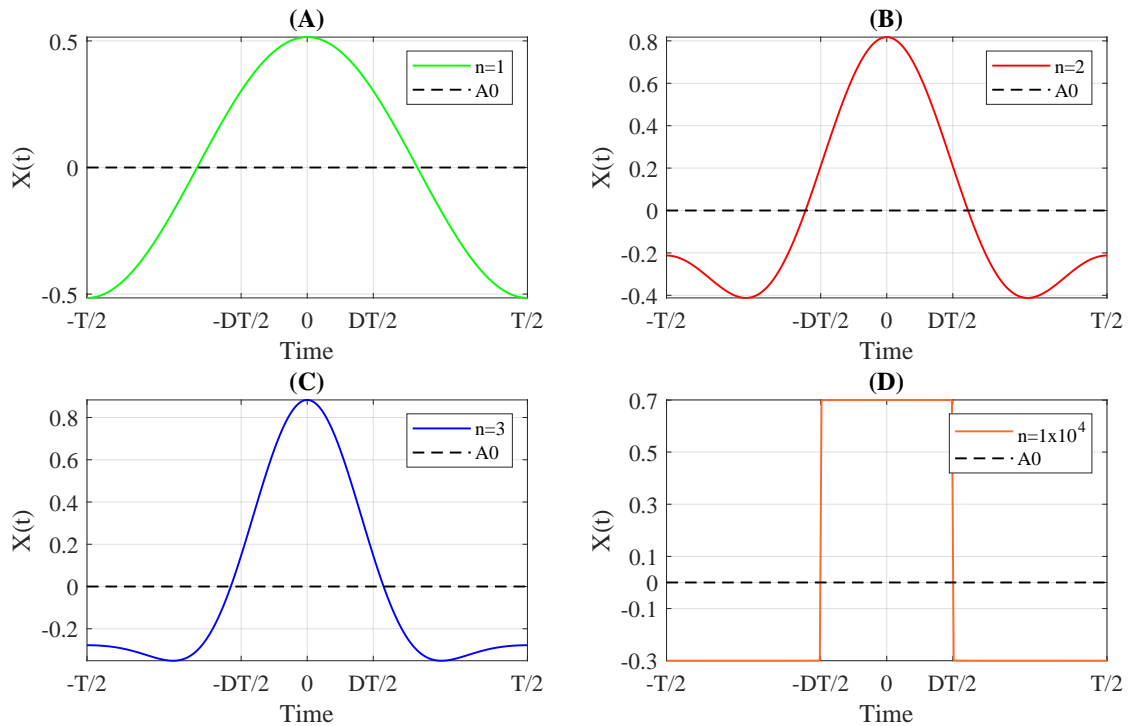


Figure A.5: Rectangular Pulses with Aggregated (Summation) Odd and Even Harmonics: (A) $n = 1$ and $D = 30\%$, (B) $n = 2$ and $D = 30\%$, (C) $n = 3$ and $D = 30\%$, and (D) $n = 1 \times 10^4$ and $D = 30\%$.

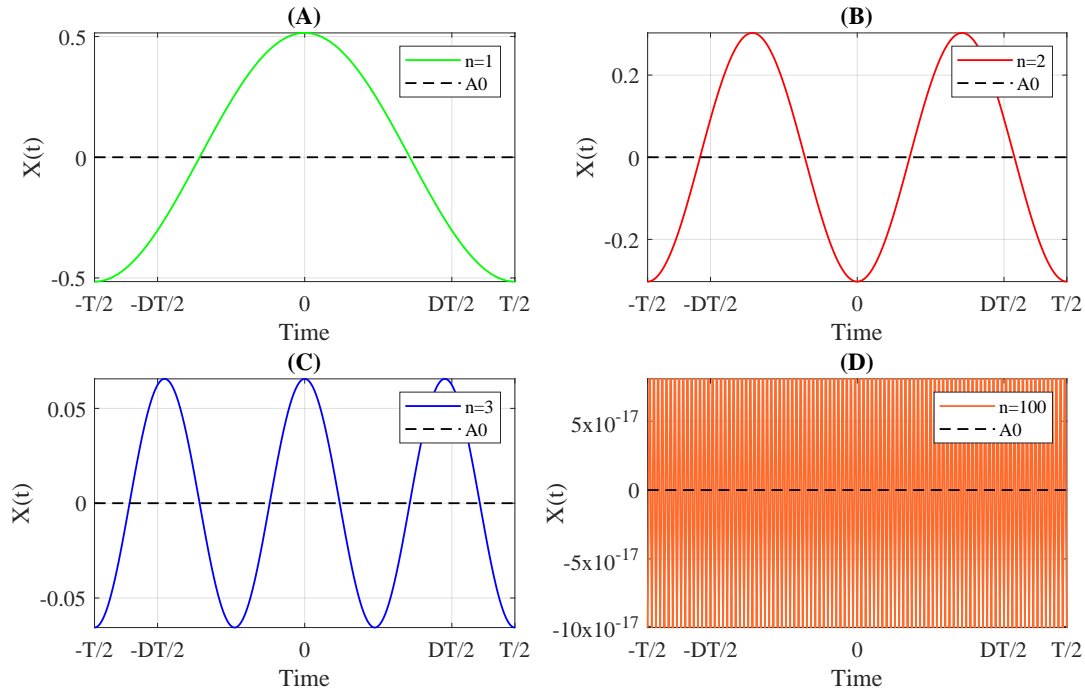


Figure A.6: Rectangular Pulses with Individual Odd and Even Harmonics: (A) $n = 1$ and $D = 70\%$, (B) $n = 2$ and $D = 70\%$, (C) $n = 3$ and $D = 70\%$, and (D) $n = 100$ and $D = 70\%$.

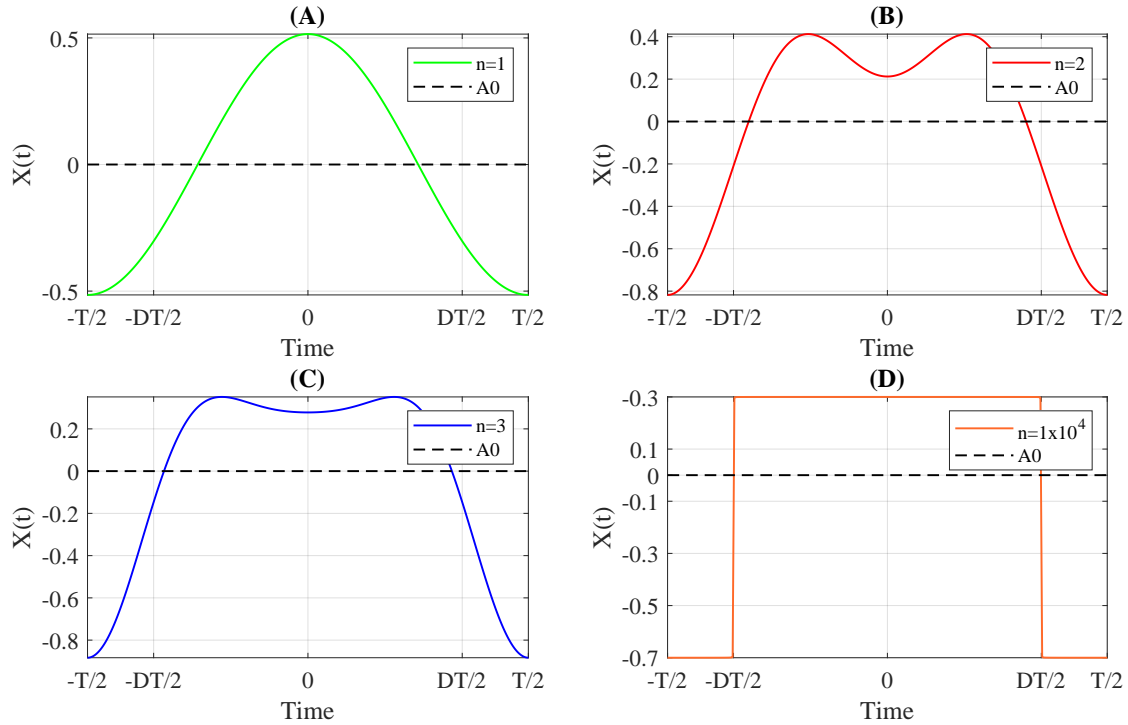


Figure A.7: Rectangular Pulses with Aggregated (Summation) Odd and Even Harmonics: (A) $n = 1$ and $D = 70\%$, (B) $n = 2$ and $D = 70\%$, (C) $n = 3$ and $D = 70\%$, and (D) $n = 1 \times 10^4$ and $D = 70\%$.

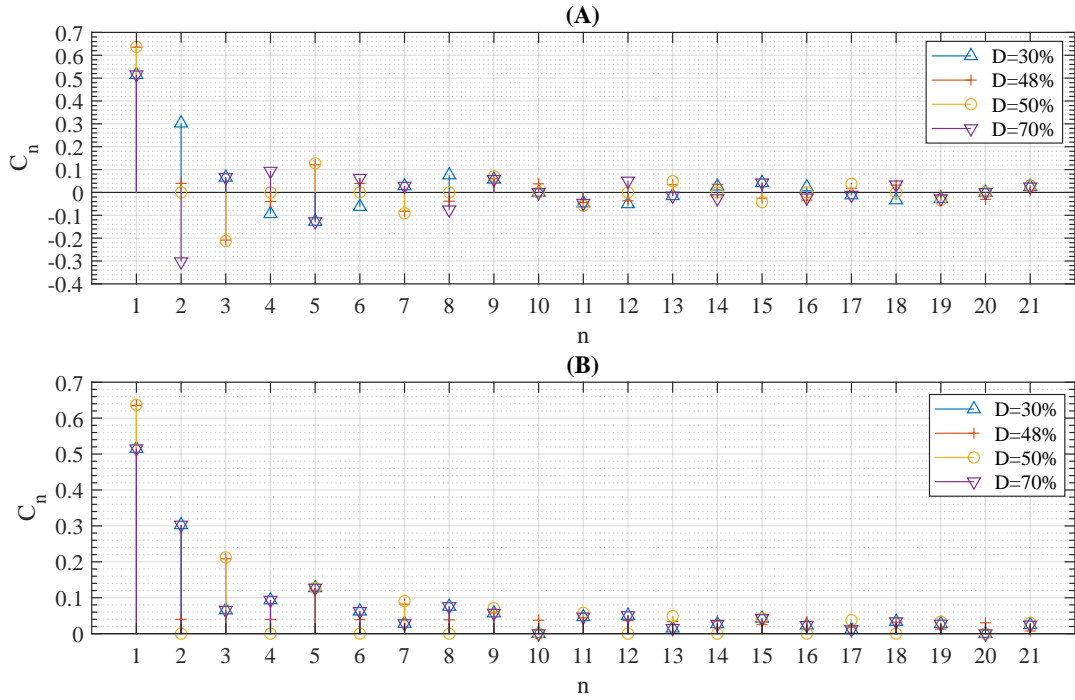


Figure A.8: C_n calculation: (A) normal distribution and (B) absolute values.

that $\omega_0 = 2\pi f_0 = \frac{2\pi}{T}$ (A.23), and the Euler's identity for sine $\sin(\theta) = \frac{(e^{j\theta} - e^{-j\theta})}{2j}$ (A.24), thus:

$$C_n = \int_{-\frac{T}{2}}^{\frac{T}{2}} X(t) \left(\frac{t}{DT} \right) e^{-jn\omega_0 t} dt = \frac{1}{T} \int_{-\frac{DT}{2}}^{\frac{DT}{2}} e^{-jn\omega_0 t} dt, \quad (\text{A.22})$$

$$C_n = \frac{1}{-jn\omega_0 T} \left(e^{-jn\omega_0 \frac{DT}{2}} - e^{jn\omega_0 \frac{DT}{2}} \right) = \frac{1}{-jn2\pi} \left(e^{-j\frac{n\pi DT}{T}} - e^{j\frac{n\pi DT}{T}} \right), \quad (\text{A.23})$$

$$C_n = \frac{1}{-jn2\pi} 2j \sin \left(-\frac{n\pi DT}{T} \right) = \frac{1}{n\pi} \sin \left(\frac{n\pi DT}{T} \right) = \frac{\sin \left(\frac{n\pi DT}{T} \right)}{\left(\frac{n\pi DT}{T} \right)}. \quad (\text{A.24})$$

The equation (A.24) presents the normalized *sinc* function and the C_n can be expressed by (A.25):

$$C_n = \text{sinc} \left(\frac{n\pi DT}{T} \right). \quad (\text{A.25})$$

Figure A.8 shows the C_n calculation up to $n = 21$ with the D equal to 30%, 48%, 50%, and 70%. Also, Figure A.9 shows harmonics up to $n = 10$, based on the interval of integration defined by (A.19), $f_0 = 20$ Hz ($T=0.05$ s), $A = 1$, and with the D equal to 30%, 48%, 50%, and 70%.

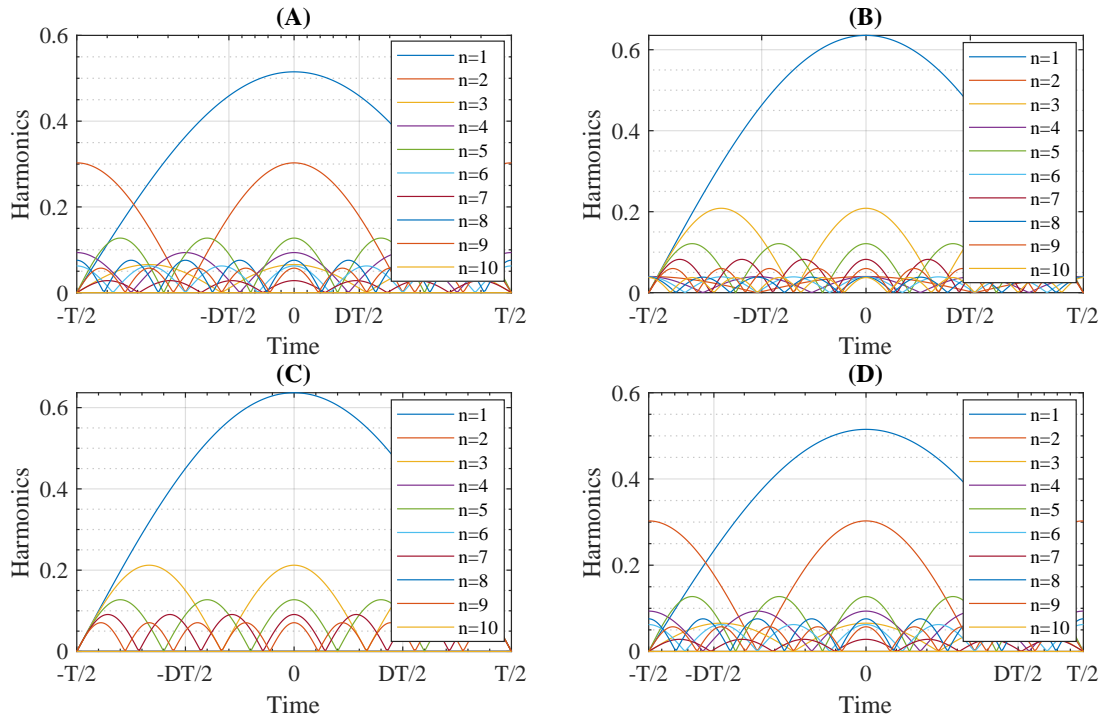


Figure A.9: Harmonics up to $n = 10$: (A) $D = 30\%$, (B) $D = 48\%$, (C) $D = 50\%$, and (D) $D = 70\%$.

In both figures, Figure A.8 and Figure A.9, as $D \neq 50\%$ both odd and even harmonics become present. In the case of Figure A.9-B, a value of D with a variation of 4% from the $D = 50\%$, i.e., $D = 48\%$, is already sufficient for the presence of the even harmonics with constant amplitude. Moreover, it is noteworthy that C_n values (Figure A.8-B) are constant over time period defined in (A.19).

Furthermore, as $D \neq 50\%$, the "width" of the *sinc* function increases (Figure A.8-A and Figure A.8-B). Based on that, we may highlight:

- As the $X(t)$ becomes more localized in time (that is, narrower), it becomes less localized in frequency (wider). In other words, if a $X(t)$ happens very quickly in time, the signal must contain a wider distribution of the coefficients to allow for rapid change;
- The product of width in frequency (i.e., Δ_n) multiplied by the width in time (Δ_t) is constant - if one is doubled, the other is halved. Or, as one gets more localized in time, it is less localized in frequency.

A.3 Aggregation of Rectangular Pulse Trains

In practical applications with DC/DC converters [44], usually, there are no apparent symmetries between the aggregation of two different $X(t)$. Thus, a simple integration over a sine or cosine based function might not be sufficient to represent the sum of the two different $X(t)$.

In the case where two $X(t)$ with both values of $D \neq 50\%$ are adding, considering the interval of integration defined by (A.19). Also, based on (A.18), and in the concept of adding two sinusoidal oscillations $X(t)_\Sigma$, expressed bellow:

$$X(t)_\Sigma = 2A_\Sigma \cos(n\varpi t) \cos\left(n\left(\frac{\Delta\omega}{2}\right)t\right), \quad (\text{A.26})$$

where ϖ and $\Delta\omega$ are the mean and differential values of the two (angular) frequencies, and the term $2A_\Sigma$ represent the adding of two sinusoidal oscillations. Furthermore, considering that $\sin(a) + \sin(b) = 2\sin\left(\frac{a+b}{2}\right)\cos\left(\frac{a-b}{2}\right)$. The behavior of the $X(t)_\Sigma$, from $n = 1$ to ∞ , considering the adding of two $X(t)$ with both values of $D \neq 50\%$ can be expressed by (A.28):

$$A_\Sigma = \left(\frac{A}{n\pi}\right) \left(2\sin\left(\frac{\left(\frac{n\pi DT}{T}\right) + \left(\frac{n\pi DT}{T}\right)}{2}\right) \cos\left(\frac{\left(\frac{n\pi DT}{T}\right) - \left(\frac{n\pi DT}{T}\right)}{2}\right)\right), \quad (\text{A.27})$$

$$X(t)_\Sigma = \sum_{n=1}^{\infty} 2A_\Sigma \cos(n\varpi t) \cos\left(n\left(\frac{\Delta\omega}{2}\right)t\right). \quad (\text{A.28})$$

To exemplify, Figure A.10 shows the performance of (A.28) considering the adding of two $X(t)$, with both values of $D \neq 50\%$ (Figure A.10-A and Figure A.10-B). For further information about the MATLAB script used, please see B.1 and B.2.

The difference between both $X(t)$ presented in Figure A.10-A and Figure A.10-B is related to the frequency. Figure A.10-A considers $f_0 = 20$ Hz, and Figure A.10-B considers $f_0 = 19$ Hz. Thus, (A.28) provides the beat¹ at $\left|-\frac{1}{(f_0-f_1)} < t < \frac{1}{(f_0-f_1)}\right|$, as is possible to observe in Figure A.10-C for a $t = 2$ s.

Futhermore, since both $X(t)$ presented in Figure A.10-A and Figure A.10-B, consider the interval of integration represented by (A.19), originally set to $f_0 = 20$ Hz and centered around the origin, i.e., 0. Clearly, the integration interval becomes improper to $f_0 = 19$ Hz, i.e. Figure A.10-B, once the region of integration includes a point at which the integrand is undefined. Thus, the improper integrals² becomes a problem for C_n calculation of the $X(t)_\Sigma$.

¹It is noteworthy that different integration periods can affect the envelope's group and phase velocity, from the point of view of the frequency beat [145].

²An improper integral is a definite integral that has either or both limits infinite or an integrand that approaches infinity at one or more points in the range of integration. Improper integrals cannot be computed using a normal Riemann integral.

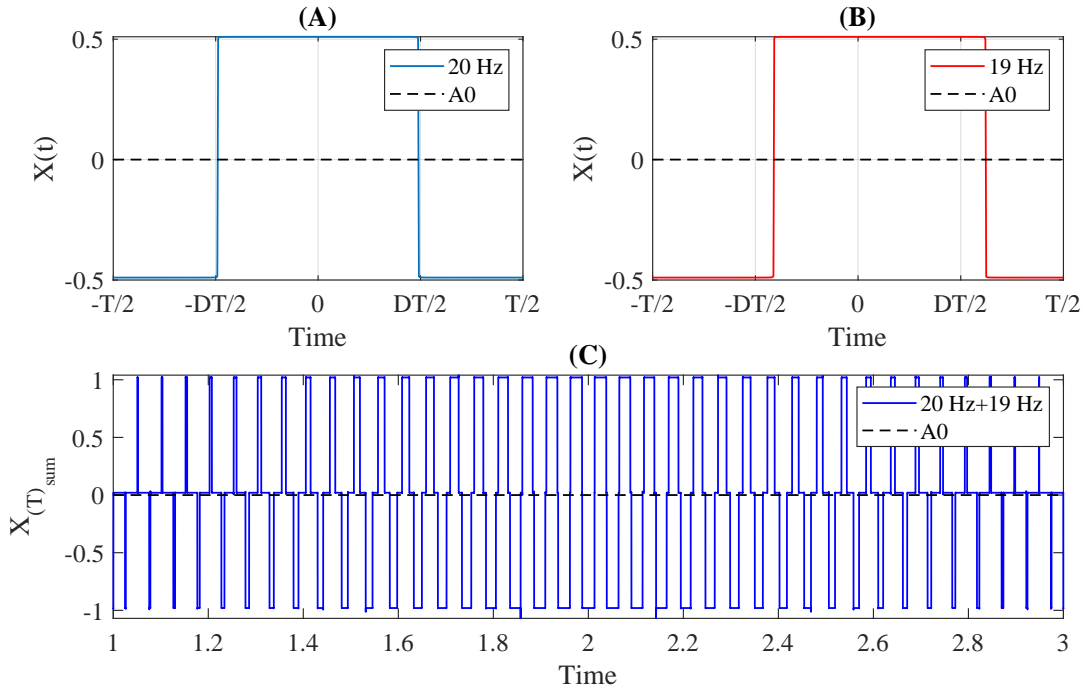


Figure A.10: The adding of two $X(t)$, with both values of $D \neq 50\%$: (A) $f_0 = 20$ Hz, (B) $f_0 = 19$ Hz and (C) $X(t)_\Sigma$.

Initially, assuming that in terms of C_n it's possible to apply the sum considering the non-normalized sinc function, as expressed by (A.29) [146]:

$$C_{n_\Sigma} = \sum_{x=1}^{\infty} \text{sinc}(x) = \sum_{x=1}^{\infty} \text{sinc}^2(x) = \frac{\pi}{2} - \frac{1}{2}, \quad (\text{A.29})$$

$$C_{n_\Sigma} = \frac{1}{\left(\pi - \left(\left(\frac{\sin\left(\frac{n\pi DT}{T}\right)}{\left(\frac{n\pi DT}{T}\right)} \right) + \left(\frac{\sin\left(\frac{n\pi DT}{T}\right)}{\left(\frac{n\pi DT}{T}\right)} \right) \right) \right)}, \quad (\text{A.30})$$

where the term $-\frac{1}{2}$ in the (A.29) represent the even harmonics components, since the $D \neq 50\%$. Thus, Figure A.11 presents the C_{n_Σ} calculation up to $n = 21$ of the $X(t)_\Sigma$ considered in Figure A.10-C and based on the (A.30).

Therefore, based on Figure A.11-C, it is observed that the modelling of C_{n_Σ} needs to handle improper integrals. Thus, based on [146], it's assumed the Lebesgue integral³ to model the C_{n_Σ} .

³Lebesgue integration is an alternative way of defining the integral in terms of measure theory that is used to integrate a much broader class of functions than the Riemann integral or even the Riemann-Stieltjes integral.

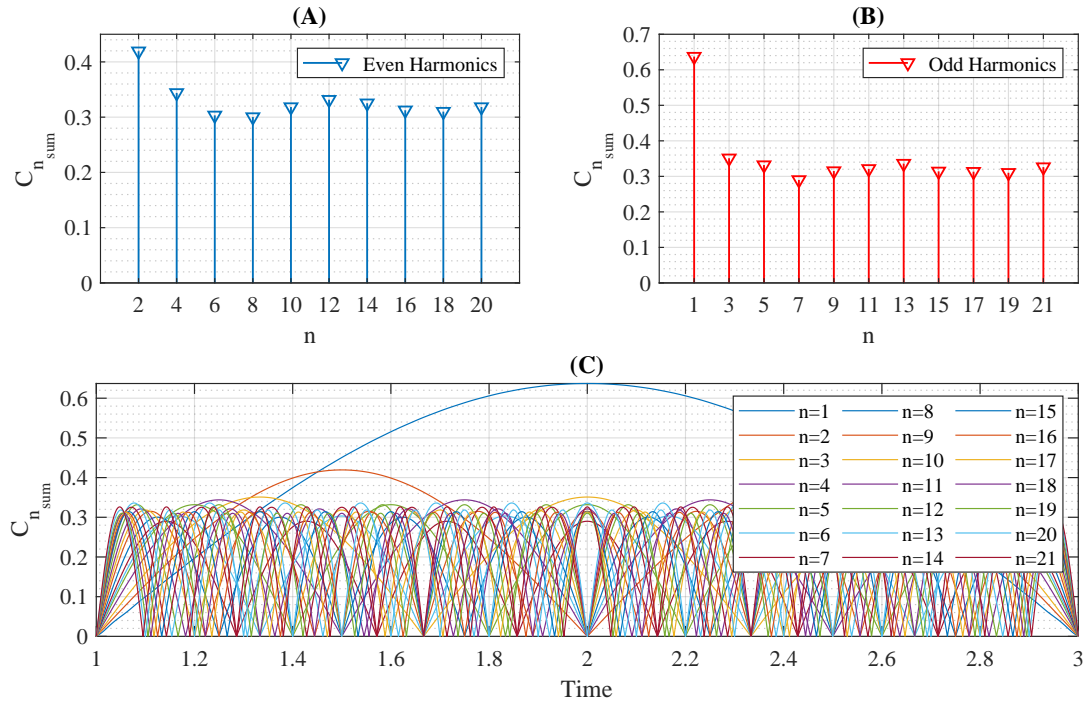


Figure A.11: $C_{n\Sigma}$ calculation based on the (A.30): (A) $C_{n\Sigma}$ of even harmonics, (B) $C_{n\Sigma}$ of odd harmonics and (C) $C_{n\Sigma}$ distribution in time.

A.4 The Lebesgue Integral

The notation and original development in this section A.4 was based on [146]. Therefore, supposing that G is the Lebesgue integrable over $(-\infty, \infty)$ and define its Fourier transform g by (A.31):

$$g(x) := \frac{1}{\sqrt{2\pi}} \int_{-\infty}^{\infty} e^{-iux} G(u) du. \quad (\text{A.31})$$

At any point u such that G is of bounded variation on $[u - \delta, u + \delta]$ for some $\delta > 0$ we have that [146]:

$$\frac{1}{2} \{G(u+) + G(u-)\} = \lim_{T \rightarrow \infty} \frac{1}{\sqrt{2\pi}} \int_{-T}^T e^{iux} g(x) dx, \quad (\text{A.32})$$

where $G(u\pm)$ denotes $\lim_{x \rightarrow u} \pm G(x)$.

Suppose, in addition, that $G(x) = 0$ for $x \notin (-\alpha, \alpha)$ for some $\alpha > 0$, and that G is of bounded variation on $[-\delta, \delta]$ for some $\delta > 0$. Then (A.31) might be expressed as:

$$g(x) = \frac{1}{\sqrt{2\pi}} \int_{-\alpha}^{\alpha} e^{-iux} G(u) du. \quad (\text{A.33})$$

Hence, the exponential summation is represented by $r = 0, 1, 2, \dots$, as **Theorem**

5.12 in [147]:

$$\sum_{n=-r}^r g_{(n)} = \frac{1}{\sqrt{2\pi}} \int_{-\alpha}^{\alpha} G_{(u)} \frac{\sin\left((r + \frac{1}{2})u\right)}{\sin\left(\frac{u}{2}\right)} du. \quad (\text{A.34})$$

Also, considering that $0 < \alpha < 2\pi$, thus:

$$\sum_{n=-r}^r g_{(n)} = \frac{1}{\sqrt{2\pi}} \int_{-\alpha}^{\alpha} G_{(u)}^* \frac{\sin\left((r + \frac{1}{2})u\right)}{u} du, \quad (\text{A.35})$$

where:

$$G_{(u)}^* := G_{(u)} \frac{u}{\sin\left(\frac{u}{2}\right)}. \quad (\text{A.36})$$

Since G^* is of bounded variation on $[-\delta, \delta]$ and Lebesgue integrable over $(-\alpha, \alpha)$ and vanishes outside of $G^*(0+) = 2G(0+)$ and $G^*(0-) = 2G(0-)$, the limit of r is [147], [148]:

$$\lim_{r \rightarrow \infty} \int_{-\alpha}^{\alpha} G_{(u)}^* \frac{\sin\left((r + \frac{1}{2})u\right)}{u} du = \frac{\pi}{2} \{G^*(0+) + G^*(0-)\}. \quad (\text{A.37})$$

However, in the case of *sinc* integrals, as explained by **Theorem 1** in [149], in [150], and more explicitly in [151], it is necessary to define whether the right-hand term in (A.37) is rational or not. Thus, considering that $0 < \alpha < 2\pi$, i.e., distribution of α as a rational multiple of π . The right-hand term in (A.37) can be considered as $\frac{\pi}{2a_0}$, where a_0 is an index of harmonic summation (n), thus $a_0 = n$. Since n , based on (A.28), is the only factor responsible for changing the volume of G , the equation (A.35) might be expressed as:

$$\sum_{n=-r}^r g_{(n)} = \frac{1}{\sqrt{2\pi}} \frac{\pi}{2a_0}, \quad (\text{A.38})$$

where g can be used to the modelling of $C_{n\Sigma}$ based on Figure A.10-C.

Therefore, Figure A.12 presents the $C_{n\Sigma}$ calculation up to $n = 21$ of the $X(t)_{\Sigma}$ considered in Figure A.10-C and based on (A.38). For further information about the MATLAB script used, please see B.1 and B.2.

Since the values of $D \neq 50\%$, the equation (A.38) can be easily applied to calculate $C_{n\Sigma}$, once regardless of the value of n , the change due to the sum occurs only in the amplitude of $C_{n\Sigma}$, i.e., a constant decrease of the density as the n values increase (see Figure A.12-C).

Furthermore, the amplitude $n = 1$ (Figure A.12-B and Figure A.12-C) remains the same as presented in Figure A.8-A, Figure A.9-B, Figure A.11-B and Figure A.11-C for the cases where the $D \neq 50\%$, reinforcing that an ideal $X(t)$ must consider a D

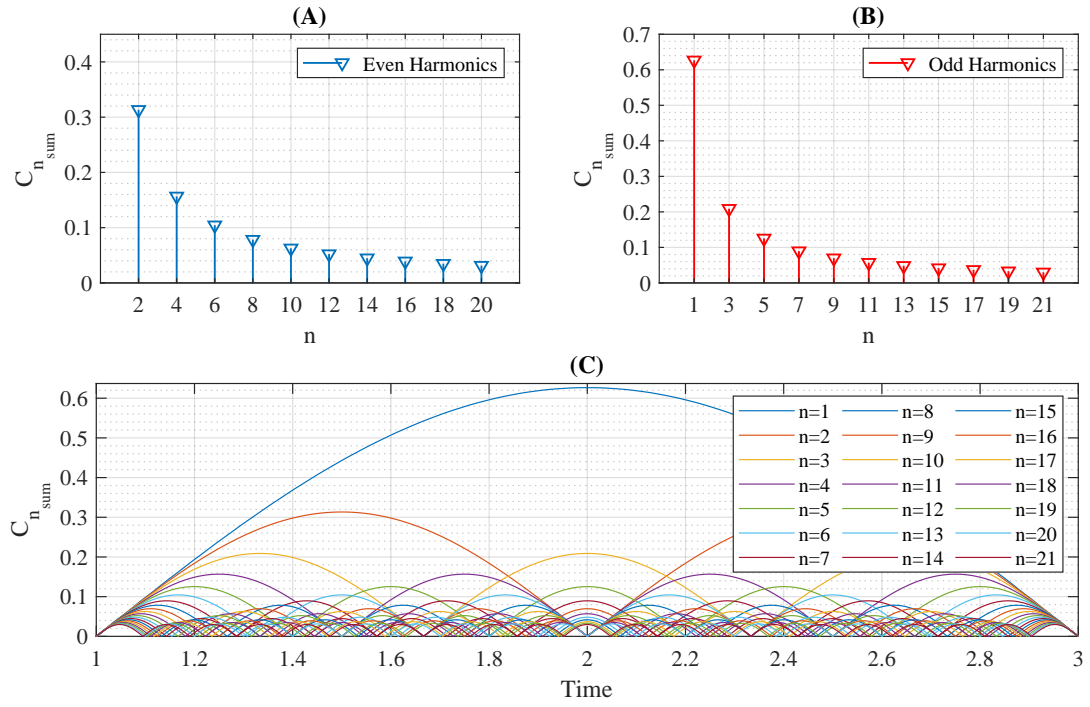


Figure A.12: $C_{n_{\Sigma}}$ calculation based on (A.38): (A) $C_{n_{\Sigma}}$ of even harmonics, (B) $C_{n_{\Sigma}}$ of odd harmonics and (C) $C_{n_{\Sigma}}$ distribution in time.

between 0 and t , in the case of a sinusoidal pulse of the fundamental frequency $n = 1$ if we consider the positive values to be the high state then $D = \frac{T}{2}$.

Appendix B

MATLAB scripts

B.1 MATLAB script used in the appendices A.2 and A.3

```
1 % MATLAB script used in the appendices A.2 and A.3
2 % Hermes Loschi - ESR 2 of the SCENT project
3 % The SCENT project has received funding from the European Union's ...
   Horizon 2020 research and innovation programme under the Marie ...
   Sklodowska-Curie grant agreement No 812391.
4
5 clc; clear all; close all
6
7 fs = 10e+3; %sampled frequency
8
9 t = [0.025:1/fs:0.075]; %sampled time for individual Xt
10 t1 = [1:1/fs:3]; %sampled time for Xtsum
11
12 f_An_1 = 20; % fundamental frequency Hz for An_1
13 f_An_2 = 19; % fundamental frequency Hz for An_2
14
15 A = 1; % Amplitude
16
17 D_An_1 = 0.5; %Duty cycle specification for An_1
18 D_An_2 = 0.5; %Duty cycle specification for An_2
19
20 omega=((2*pi*f_An_1)+(2*pi*f_An_2))/2; %Mean component for Xtsum
21 OMEGA=((2*pi*f_An_1)-(2*pi*f_An_2))/2; %Differential values for ...
   Xtsum
22
23 n = 1; %Index of Harmonics Summation - even and odd harmonics
24
```

```

25 Acc_An_1 = 0; %Acumulador to compute the summation process of Xt_1
26 for n1=n % Index of Harmonics Summation
27 % to compute the An
28 An_n1 = ((2*(A/(n1*pi)))*(sin((n1*pi)*D_An_1))); %Eq.(A.17)
29 % to compute the Xt_1
30 Xt_1 = (An_n1*(cos(n1*2*pi*f_An_1*t))); %Eq.(A.18)
31 Acc_An_1 = Acc_An_1+Xt_1;
32 end
33
34 Acc_An_2 = 0; %Acumulador to compute the summation process of Xt_2
35 for n1=n % Index of Harmonics Summation
36 % to compute the An
37 An_n2 = ((2*(A/(n1*pi)))*(sin((n1*pi)*D_An_2))); %Eq.(A.17)
38 % to compute the Xt_2
39 Xt_2 = (An_n2*(cos(n1*2*pi*f_An_2*t))); %Eq.(A.18)
40 Acc_An_2 = Acc_An_2+Xt_2;
41 end
42
43 Acc_Cn_1 = 0; %Acumulador to compute the Cn_1 calculation
44 for n1=n % Index of Harmonics Summation
45 % to compute the Cn_1
46 Cn_1 = (sin((pi*n1*D_An_1)/1))/((pi*n1*D_An_1)/1); %(A.25)
47 Acc_Cn_1 = Acc_Cn_1+Cn_1;
48 end
49
50 Acc_Cn_2 = 0; %Acumulador to compute the Cn_2 calculation
51 for n1=n % Index of Harmonics Summation
52 % to compute the Cn_2
53 Cn_2 = (sin((pi*n1*D_An_2)/1))/((pi*n1*D_An_2)/1); %(A.25)
54 Acc_Cn_2 = Acc_Cn_2+Cn_2;
55 end
56
57 Xt_An_1_2 = 0; %Acumulador to compute the Xtsum process of An_1 + An_2
58 for n1=n % Index of Harmonics Summation
59 % to compute the Asum
60 An1_An2_n1 = (A/(pi*n1)).*(2*sin(((n1*pi*D_An_1)+(n1*pi*D_An_2))/2))
61 .* (cos(((n1*pi*D_An_1)-(n1*pi*D_An_2))/2)); %Eq.(A.27)
62 % to compute the Xtsum
63 An1f_An2f_n1 = 2.*(An1_An2_n1).*(cos((n1*omega*t1)))
64 .* (cos(n1*(OMEGA/2)*t1)); %Eq.(A.28)
65 Xt_An_1_2=Xt_An_1_2+An1f_An2f_n1;
66 end
67
68 Acc_Cn_1_1_2 = 0; %Acumulador to compute Cnsum calculation - ...
    Normal Integral Approach
69 for n1=n % Index of Harmonics Summation
70 % to compute the Cnsum

```

```

71 Cn_1_1_2 = ((pi-((sin(1*D_An_1*pi)/(1*D_An_1*pi)))+(sin(1*D_An_2*pi)
72 /(1*D_An_2*pi))))^(-1)); %Eq. (A.30)
73 Acc_Cn_1_1_2 = Acc_Cn_1_1_2+Cn_1_1_2;
74 end
75
76 Acc_Cn_2_1_2 = 0; %Acumulador to compute Cnsum calculation - ...
    Lebesgue Integral Approach
77 for n1=n % Index of Harmonics Summation
78 % to compute the Cnsum
79 Cn_2_1_2 = (1/sqrt(2*pi))*((pi)/(2*n1)); %Eq. (A.38)
80 Acc_Cn_2_1_2 = Acc_Cn_2_1_2+Cn_2_1_2;
81 end

```

B.2 Complementary MATLAB script used in appendices A.2 and A.3

```

1 % MATLAB script complementary used in appendices A.2 and A.3
2 % Hermes Loschi - ESR 2 of the SCENT project
3 % The SCENT project has received funding from the European Union's ...
    Horizon 2020 research and innovation programme under the Marie ...
    Sklodowska-Curie grant agreement No 812391.
4
5 clc; clear all; close all
6
7 %% Variation of the Frequency Stability
8
9 %--> Random number steps
10 N=10e3;
11 Fmin=39;
12 Fmax=40;
13 dF=Fmax-Fmin;
14 Frn=1.*rand(N,1);
15 Frn1=(Frn.*dF)+Fmin;
16 F1 = Frn1(1, : ) % Frequency Stability Randomized 1
17
18 Frn2=1.*rand(N,1);
19 Frn3=(Frn2.*dF)+Fmin;
20 F2 = Frn3(1, : ) % Frequency Stability Randomized 2
21
22 figure(1);
23 subplot(2,2,1);
24 plot(Frn1, '.', 'Color', [0 1 0]);
25 xlabel('m'); % \in <1: 10000>');

```

```

26 ylabel('Variation F1 [Hz]');
27 legend(' (a) ');
28 axis([0,10e3,39,40]);
29
30 subplot(2,2,2);
31 hist(Frn1,30);
32 xlabel('Variation F1 [Hz]');
33 ylabel('Frequency of m appearance');
34 legend(' (b) ');
35
36 subplot(2,2,3);
37 plot(Frn3, '.', 'Color',[0 1 0]);
38 xlabel('m'); % \in <1: 10000>');
39 ylabel('Variation F2 [Hz]');
40 legend(' (c) ');
41 axis([0,10e3,39,40]);
42
43 subplot(2,2,4);
44 hist(Frn3,30);
45 xlabel('Variation F2 [Hz]');
46 ylabel('Frequency of m appearance');
47 legend(' (d) ');
48
49 %% Retangular Pulse Generation Summation
50
51 fs = 10e+3; %Sampled Frequency
52 t = [0:1/fs:81]; %Sampled Time
53 A = 1; %Amplitude of square wave
54
55 FPwave1 = 0; %Counter of the Frequency Period Wave 1
56 FPwave2 = 0; %Counter of the Frequency Period Wave 2
57
58 % -> Fourier Series Expansion of Rectangular Pulse Train
59 for nd=1:1:1 % Index of Harmonics Summation
60
61 v1 = (A/nd)*sin(2*pi*nd*F1*t); % Frequency Period Wave 1
62 v2 = (A/nd)*sin(2*pi*nd*F2*t); % Frequency Period Wave 2
63
64 FPwave1 = FPwave1+v1;
65 FPwave2 = FPwave2+v2;
66
67 end
68
69 FPwave_sum=FPwave1+FPwave2; %Summation
70
71 figure (2)
72 subplot(2,2,1)

```

```

73 plot(t,FPwave1)
74 grid on
75 xlabel('Retangular Pulse - F1 ')
76 ylabel('Ampitude')
77 title('Index of Harmonics Summation - n=1000')
78 axis([0,81,-1,1]);
79
80 subplot(2,2,2)
81 plot(t,FPwave2)
82 grid on
83 xlabel('Retangular Pulse - F2 [Sec]')
84 ylabel('Ampitude')
85 title('Index of Harmonics Summation - n=1000')
86 axis([0,81,-1,1]);
87
88 subplot(2,2,3)
89 plot(t,FPwave_sum)
90 grid on
91 xlabel('Retangular Pulse - F1+F2 [Sec]')
92 ylabel('Ampitude')
93 title('Index of Harmonics Summation - n=1000')
94 axis([0,81,-2,2]);
95
96 subplot(2,2,4)
97 FPwave_sum2=abs(FPwave_sum);
98 plot(t,FPwave_sum2)
99 grid on
100 xlabel('Retangular Pulse - F1+F2 [Sec]')
101 ylabel('Ampitude')
102 title('Index of Harmonics Summation - n=1000')
103 axis([0,81,0,2]);
104
105 %% Fourier series + Retangular Pulses Generations
106
107 Tau = 40; % Total range/width in which the square wave is defined
108 T0 = 80; % Period (time of repeation of square wave)
109 C = 10; %Coefficients (Sinusoids) to retain
110 N = 1001; %Number of points to consider
111
112 t1=linspace(-(T0-Tau),(T0-Tau),N); %Time Axis for duty cycle 30%
113
114 X30=zeros(1,N); X30(t1>=-Tau/3.333 & t1<=Tau/3.333) = A; %Original ...
    Signal duty cycle 30%
115 X50=zeros(1,N); X50(t1>=-Tau/2 & t1<=Tau/2) = A; %Original Signal ...
    duty cycle 50%
116 X70=zeros(1,N); X70(t1>=-Tau/1.429 & t1<=Tau/1.429) = A; %Original ...
    Signal duty cycle 70%

```

```

117
118 R = 0; %Initialize the approximated signal - D30 - F1%
119 P = 0; %Initialize the approximated signal - D50 - F1%
120 W = 0; %Initialize the approximated signal - D70 - F1%
121 r = 0; %Initialize the approximated signal - D30 - F2%
122 p = 0; %Initialize the approximated signal - D50 - F2%
123 w = 0; %Initialize the approximated signal - D70 - F2%
124
125 kR = -C:C; %Fourier coefficient values - D30 - F1%
126 kP = -C:C; %Fourier coefficient values - D50 - F1%
127 kW = -C:C; %Fourier coefficient values - D70 - F1%
128 kr = -C:C; %Fourier coefficient values - D30 - F2%
129 kp = -C:C; %Fourier coefficient values - D50 - F2%
130 kw = -C:C; %Fourier coefficient values - D70 - F2%
131
132 fR = zeros(1,2*C+1); %Fourier coefficient values - D30 - F1%
133 fP = zeros(1,2*C+1); %Fourier coefficient values - D50 - F1%
134 fW = zeros(1,2*C+1); %Fourier coefficient values - D70 - F1%
135 fr = zeros(1,2*C+1); %Fourier coefficient values - D30 - F2%
136 fp = zeros(1,2*C+1); %Fourier coefficient values - D50 - F2%
137 fw = zeros(1,2*C+1); %Fourier coefficient values - D70 - F2%
138
139 % Loop for plotting approximated signals for different retained ...
    coeffs.
140
141 for c = 1:C % Number of retained coefficients
142     for n = -c:c % Summation range
143         %Sinc part of the Fourier coefficients calculated separately
144         if n~=0
145             Sinc30 = (sin(pi*n*0.3)/((pi*n*0.3))); %At n NOTEQUAL to 0 - 30%
146         else
147             Sinc30 = 1; %At n EQUAL to 0
148         end
149         Cn30 = (A*0.3)*Sinc30; %Actual Fourier Series coefficients
150         fR(kR==n) = Cn30; %Put the Fourier coefficients at respective places
151         R = R + Cn30*exp(1j*n*F1*2*pi/T0.*t1); %Sum all the coefficients
152     end
153
154 R = real(R); % So as to get rid of 0000000000i (imaginary) factor
155 Max30 = max(R); Min30 = min(R); M30 = max(abs(Max30),abs(Min30)); ...
    %Maximum error
156 Overshoot30 = ((M30-A)/A)*100; %Overshoot calculation
157 %E30 = sum((X30-R).^2); %Error energy calculation
158
159 for n = -c:c % Summation range
160     %Sinc part of the Fourier coefficients calculated separately
161     if n~=0

```

```

162 Sinc50 = (sin(pi*n*0.5)/((pi*n*0.5))); %At n NOTEQUAL to 0 - 50%
163 else
164 Sinc50 = 1; %At n EQUAL to 0
165 end
166 Cn50 = (A*0.5)*Sinc50; %Actual Fourier Series coefficients
167 fP(kP==n) = Cn50; %Put the Fourier coefficients at respective places
168 P = P + Cn50*exp(1j*n*F1*2*pi/T0.*t1); %Sum all the coefficients
169 end
170
171 P = real(P); % So as to get rid of 00000000000i (imaginary) factor
172 Max50 = max(P); Min50 = min(P); M50 = max(abs(Max50),abs(Min50)); ...
    %Maximum error
173 Overshoot50 = ((M50-A)/A)*100; %Overshoot calculation
174 %E50 = sum((X50-P).^2); %Error energy calculation
175
176 for n = -c:c % Summation range
177 %Sinc part of the Fourier coefficients calculated separately
178 if n~=0
179 Sinc70 = (sin(pi*n*0.7)/((pi*n*0.7))); %At n NOTEQUAL to 0 - 50%
180 else
181 Sinc70 = 1; %At n EQUAL to 0
182 end
183 Cn70 = (A*0.7)*Sinc70; %Actual Fourier Series coefficients
184 fW(kW==n) = Cn70; %Put the Fourier coefficients at respective places
185 W = W + Cn70*exp(1j*n*F1*2*pi/T0.*t1); %Sum all the coefficients
186 end
187
188 W = real(W); % So as to get rid of 00000000000i (imaginary) factor
189 Max70 = max(W); Min70 = min(W); M70 = max(abs(Max70),abs(Min70)); ...
    %Maximum error
190 Overshoot70 = ((M70-A)/A)*100; %Overshoot calculation
191 %E70 = sum((X70-W).^2); %Error energy calculation
192
193 figure(4)
194 % Plot the Fourier coefficients
195 subplot(2,2,1); stem(kR,fR,'g','LineWidth',1); axis tight; grid on;
196 xlabel('Fourier coefficient index');ylabel('Magnitude');
197 title('Fourier coefficients');
198
199 subplot(2,2,2); stem(kP,fP,'r','LineWidth',1); axis tight; grid on;
200 xlabel('Fourier coefficient index');ylabel('Magnitude');
201 title('Fourier coefficients');
202
203 subplot(2,2,[3,4]); stem(kW,fW,'b','LineWidth',1); axis tight; ...
    grid on;
204 xlabel('Fourier coefficient index');ylabel('Magnitude');
205 title('Fourier coefficients');

```

```

206
207 figure(5)
208 subplot 221; plot(t1,R,'g','LineWidth',1); axis tight; grid on;
209 xlabel('Time (t) - d30%'); ylabel('Amplitude');
210 title(['Approximation for N = ', num2str(c), ...
211 '. Overshoot = ', num2str(Overshoot30)] )
212
213 subplot 222; plot(t1,P,'r','LineWidth',1); axis tight; grid on;
214 xlabel('Time (t) - d50%'); ylabel('Amplitude');
215 title(['Approximation for N = ', num2str(c), ...
216 '. Overshoot = ', num2str(Overshoot50)] )
217
218 subplot (2,2,[3,4]); plot(t1,W,'b','LineWidth',1); axis tight; ...
    grid on;
219 xlabel('Time (t) - d70%'); ylabel('Amplitude');
220 title(['Approximation for N = ', num2str(c), ...
221 '. Overshoot = ', num2str(Overshoot70)] )
222
223 for n = -c:c % Summation range
224 %Sinc part of the Fourier coefficients calculated separately
225 if n≠0
226 Sinc31 = (sin(pi*n*0.3)/(pi*n*0.3)); %At n NOTEQUAL to 0 - 30%
227 else
228 Sinc31 = 1; %At n EQUAL to 0
229 end
230 Cn31 = (A*0.3)*Sinc31; %Actual Fourier Series coefficients
231 fr(kr==n) = Cn31; %Put the Fourier coefficients at respective places
232 r = r + Cn31*exp(1j*n*F2*2*pi/T0.*t1); %Sum all the coefficients
233 end
234
235 r = real(r); % So as to get rid of 0000000000i (imaginary) factor
236 Max31 = max(r); Min31 = min(r); M31 = max(abs(Max31),abs(Min31)); ...
    %Maximum error
237 Overshoot31 = ((M31-A)/A)*100; %Overshoot calculation
238 %E31 = sum((X30-r).^2); %Error energy calculation
239
240 for n = -c:c % Summation range
241 %Sinc part of the Fourier coefficients calculated separately
242 if n≠0
243 Sinc51 = (sin(pi*n*0.5)/(pi*n*0.5)); %At n NOTEQUAL to 0 - 50%
244 else
245 Sinc51 = 1; %At n EQUAL to 0
246 end
247 Cn51 = (A*0.5)*Sinc51; %Actual Fourier Series coefficients
248 fp(kp==n) = Cn51; %Put the Fourier coefficients at respective places
249 p = p + Cn51*exp(1j*n*F2*2*pi/T0.*t1); %Sum all the coefficients
250 end

```



```

251
252 p = real(p); % So as to get rid of 00000000000i (imaginary) factor
253 Max51 = max(p); Min51 = min(p); M51 = max(abs(Max51),abs(Min51)); ...
    %Maximum error
254 Overshoot51 = ((M51-A)/A)*100; %Overshoot calculation
255 %E51 = sum((X50-p).^2); %Error energy calculation
256
257 for n = -c:c % Summation range
258 %Sinc part of the Fourier coefficients calculated separately
259 if n~=0
260 Sinc71 = (sin(pi*n*0.7)/((pi*n*0.7))); %At n NOTEQUAL to 0 - 50%
261 else
262 Sinc71 = 1; %At n EQUAL to 0
263 end
264 Cn71 = (A*0.7)*Sinc71; %Actual Fourier Series coefficients
265 fw(kw==n) = Cn71; %Put the Fourier coefficients at respective places
266 w = w + Cn71*exp(1j*n*F2*2*pi/T0.*t1); %Sum all the coefficients
267 end
268
269 w = real(w); % So as to get rid of 00000000000i (imaginary) factor
270 Max71 = max(w); Min71 = min(w); M71 = max(abs(Max71),abs(Min71)); ...
    %Maximum error
271 Overshoot71 = ((M71-A)/A)*100; %Overshoot calculation
272 %E71 = sum((X70-w).^2); %Error energy calculation
273
274 figure(6)
275 % Plot the Fourier coefficients
276 subplot(2,2,1); stem(kr,fr,'g','LineWidth',1); axis tight; grid on;
277 xlabel('Fourier coefficient index');ylabel('Magnitude');
278 title('Fourier coefficients');
279
280 subplot(2,2,2); stem(kp,fp,'r','LineWidth',1); axis tight; grid on;
281 xlabel('Fourier coefficient index');ylabel('Magnitude');
282 title('Fourier coefficients');
283
284 subplot(2,2,[3,4]); stem(kw,fw,'b','LineWidth',1); axis tight; ...
    grid on;
285 xlabel('Fourier coefficient index');ylabel('Magnitude');
286 title('Fourier coefficients');
287
288 figure(7)
289 subplot(2,2,1); plot(t1,r,'g','LineWidth',1); axis tight; grid on;
290 xlabel('Time (t) - d30%'); ylabel('Amplitude');
291 title(['Approximation for N = ', num2str(c), ...
292 '. Overshoot = ',num2str(Overshoot31)]);
293
294 subplot(2,2,2); plot(t1,p,'r','LineWidth',1); axis tight; grid on;

```

```

295 xlabel('Time (t) - d50%'); ylabel('Amplitude');
296 title(['Approximation for N = ', num2str(c), ...
297 '. Overshoot = ', num2str(Overshoot51)]);
298
299 subplot (2,2,[3,4]); plot(t1,w,'b','LineWidth',1); axis tight; ...
    grid on;
300 xlabel('Time (t) - d70%'); ylabel('Amplitude');
301 title(['Approximation for N = ', num2str(c), ...
302 '. Overshoot = ', num2str(Overshoot71)]);
303
304 % Rectangular Pulses Generations Summations
305 Rr1=R+r; % - d30 + d30
306 Pp1=P+p; % - d50 + d50
307 Ww1=W+w; % - d70 + d70
308
309 Rr2=R+p; % - d30 + d50
310 Pp2=W+p; % - d70 + d50
311 Ww2=r+W; % - d30 + d70
312
313 figure (8)
314 subplot (2,2,1); plot(t1,Rr1,'g','LineWidth',1);axis tight; grid on;
315 xlabel('Time (t) - d30 + d30 - F1 + F2'); ylabel('Amplitude'); ...
    title('Index of Harmonics Summation - n=1');
316
317 subplot (2,2,2); plot(t1,Ww1,'b','LineWidth',1);axis tight; grid on;
318 xlabel('Time (t) - d70 + d70 - F1 + F2'); ylabel('Amplitude'); ...
    title('Index of Harmonics Summation - n=1');
319
320 subplot (2,2,[3,4]); plot(t1,Pp1,'r','LineWidth',1);axis tight; ...
    grid on;
321 xlabel('Time (t) - d50 + d50 - F1 + F2'); ylabel('Amplitude'); ...
    title('Index of Harmonics Summation - n=1');
322
323 figure (9)
324 subplot (2,2,1); plot(t1,Rr2,'g','LineWidth',1);axis tight; grid on;
325 xlabel('Time (t) - d30 + d50 - F1 + F2'); ylabel('Amplitude'); ...
    title('Index of Harmonics Summation - n=1');
326
327 subplot (2,2,2); plot(t1,Ww2,'b','LineWidth',1);axis tight; grid on;
328 xlabel('Time (t) - d30 + d70 - F1 + F2'); ylabel('Amplitude'); ...
    title('Index of Harmonics Summation - n=1');
329
330 subplot (2,2,[3,4]); plot(t1,Pp2,'r','LineWidth',1);axis tight; ...
    grid on;
331 xlabel('Time (t) - d70 + d50 - F1 + F2'); ylabel('Amplitude'); ...
    title('Index of Harmonics Summation - n=1');
332

```

```

333 pause(0.1); % Pause for a while
334 R = 0; % Reset the approximation to calculate new one
335 P = 0; % Reset the approximation to calculate new one
336 W = 0; % Reset the approximation to calculate new one
337 r = 0; % Reset the approximation to calculate new one
338 p = 0; % Reset the approximation to calculate new one
339 w = 0; % Reset the approximation to calculate new one
340 end

```

B.3 MATLAB script used in the section 2.1 and subsection 4.2.1

```

1 % MATLAB script used in section 2.1 and subsection 4.2.1.
2 % Figures 2.14, 2.15, 2.16, 2.17, 2.18 and 4.10.
3 % Hermes Loschi - ESR 2 of the SCENT project
4 % The SCENT project has received funding from the European Union's ...
   Horizon
5 % 2020 research and innovation programme under the Marie ...
   Sklodowska-Curie
6 % grant agreement No 812391.
7
8 clc; clear all; close all;
9
10 % Randomization of 25% around 20kHz
11 N = 10E3; % Size of the random numbers
12 Nmin = 175; % + \Delta N = 12.5% from 20kHz/N=200=40E6/(20E3*10) - ...
   Nmin 175/22.8kHz
13 Nmax = 225; % - \Delta N = 12.5% from 20kHz/N=200=40E6/(20E3*10) - ...
   Nmax 225/17.8kHz
14 dN0=Nmax-Nmin; % Total stream of numbers associated with \Delta N
15 rn0 = round(((dN0.*rand(N,1))+1)+Nmin); % Total stream of random ...
   numbers used by N
16 figure(1)
17 histogram(rn0) %Uniform distribution
18 xlabel('\Delta N');
19 ylabel('Frequency of variable appearance');
20 legend('Histogram of N');
21
22 % Randomization of the RSCTL - Concept RanM2 with RSCTL presented ...
   in the paper FPGA-based ...
23 SCTL=1/40; % value in [us]
24 f = 8; % Assumed minimum value
25 h = 12; % Assumed maximum value

```

```

26 RSCTL = SCTL.*round(((h-f).*rand(N,1)+f)); % Total stream of ...
    random numbers used by RSCTL
27 figure(2)
28 histogram(RSCTL) %Uniform distribution
29 xlabel('RSCTL');
30 ylabel('Frequency of variable appearance');
31 legend('Histogram of RSCTL');
32
33 % Randomized TPWM and FPWM - Both close of Gaussian Distribution
34 TPWM = RSCTL.*rn0; %TPWM
35 FPWM=1e3./TPWM; %FPWM
36 figure(3)
37 subplot(1,2,1);
38 hist (TPWM,40);
39 xlabel('Values of T_{PWM} [\mus]');
40 ylabel('Frequency of variable apperance - \Delta N 25%');
41 %axis([0,100,0,1300]);
42 legend('a');
43 subplot(1,2,2);
44 hist(FPWM,40);
45 xlabel('Values of f_{PWM} [kHz]');
46 ylabel('Frequency of variable apperance - \Delta N 25%');
47 %axis([0,200,0,1300]);
48 legend('b');
49
50 % PWM Modulator Algorith presented in the paper FPGA-based ...
51
52 % Set of ten random times, from x1 to ... - Increase the while ...
    loops as the desired Xt.
53 Fa = 0; % Fault signal
54 St = 0; % Stop signal
55 CS = Fa + St; % Iteration with the hardware signals
56 f1 = 1/1e3; % Sampled frequency
57 x1 = (TPWM(1,:)); % 1st random TPWM in [us]
58 t2 = x1; % Completed sampled time, divide per 2, due to the ...
    condition xk = [-1,1].
59 t0 = t2-t2; % S - sampled time initial condition used by YoutT
60 t1 = (t2-(t2/2)); % S - sampled time intermediate condition used ...
    by YoutT and YoutF
61
62 ix1 = 0; % Counter ramp iFPGA
63
64 while ix1 ≤ x1 % Loop1 of the PWM Modulator Algorithm
65 if CS ≤ 0 % Iteration with the hardware signals
66 for ix1 = 1:x1 % Loop2 of the PWM Modulator Algorithm
67 if ix1 ≤ t1 % Establishing the D
68 YoutF = [t0:f1:t1]; % Neutral level counter, i.e. 0 and negative time

```

```

69 YF = (square(2*pi*((1/(t2)).*1e6)*YoutF,0))+1; % Square wave d = 0
70 else
71 YoutT = [t1:f1:t2]; % Positive level counter, i.e. 1 and positive time
72 YT = ...
    (square(2*pi*((1/(t2)).*1e6)*YoutT,100)).*(((1/(x1)).*1e6)/1000); ...
    % Square wave d = 1 in kHz
73 end
74 ix1 = ix1 +1; % Accumulator of the counter ramp iFPGA
75 end
76 else
77 break % Iteration with the hardware signals
78 end
79 Yout = [YoutF YoutT]; % Accumulator of the positive and neutral levels
80 Y = [YF YT]; % Accumulator of the square waves for positive and ...
    neutral levels
81 end

```

B.4 MATLAB script used in the section 3.1

```

1 % MATLAB script used in the section 3.1
2 % Hermes Loschi - ESR 2 of the SCENT project
3 % The SCENT project has received funding from the European Union's ...
    Horizon
4 % 2020 research and innovation programme under the Marie ...
    Skłodowska-Curie
5 % grant agreement No 812391.
6
7 clc; clear all; close all
8
9 % Spectrum of the Hanning Window
10
11 N= 32; % number of time samples
12 win= hanning(N); % hanning window
13 win= win/sum(win); % scale window for |h(0)| = 1
14
15 % NFFT-point FFT of N-point window function
16 fs= 16; % Hz sample frequency
17 L= 32; % Length of the window
18 NFFT= L*N;
19 k= 0:NFFT/2-1; % freq index for NFFT-point FFT
20 f= k*fs/NFFT; % Hz frequency vector
21 h = fft(win,NFFT); % FFT of length NFFT (zero padded)
22 h= h(1:NFFT/2); % retain points from 0 to fs/2

```

```

23  HdB= 20*log10(abs(h));           % dB magnitude of fft
24
25  % N-point FFT of N-point window function
26  m= 0:N/2-1;                     % freq index for N-point FFT
27  f2= m*fs/N;                     % Hz frequency vector
28  h= fft(win,N);                  % FFT of length N (without zero-pad)
29  h= h(1:N/2);                    % retain points from 0 to fs/2
30  HdB_N= 20*log10(abs(h));        % dB magnitude of fft
31
32  figure(1)
33  subplot(2,1,1);
34  stem(win);
35  xlabel('n');
36  ylabel('Amplitude');
37  title('Hanning window for N= 32')
38  subplot(2,1,2);
39  plot(HdB)
40  xlabel('f');
41  ylabel('dB');
42  title('Spectrum of Hanning window for FFT length = N*L')
43
44  figure(2)
45  plot(HdB_N)
46  xlabel('f');
47  ylabel('dB');
48  title('The spectrum of Hanning window for FFT length = N')
49
50  % Windowing a Sinewave
51
52  % Set the fs, create the hanning window, and obtain the
53  % discrete Fourier transform of the hanning window.
54
55  fs= 16;                          % Hz sample frequency
56  N= 32;                           % number of time samples
57  L= 32;                           % Length of the window
58  NFFT= L*N;
59
60  win= hanning(N);                 % hanning window
61  win= win.*sqrt(N/sum(win.^2)); % normalize window for P = 1 W
62
63  A= sqrt(2);                     % sine amplitude for P= 1 W
64  Ts= 1/fs;
65  n= 0:N-1;                       % s time index
66  f0 = 4*fs/N;                    % Hz f0= 2 Hz
67  x= A*sin(2*pi*f0*n*Ts);          % sine at bin center, P= 1 watt
68
69  xw= x.*win';                    % apply window to sinewave

```

```

70 X= fft(xw,NFFT); % FFT of length NFFT (zero padded)
71 X= X(1:NFFT/2); % retain points from 0 to fs/2
72 P= 2/N.^2 * abs(X).^2; % power spectrum into 1 ohm
73 PdB= 10*log10(P); % dB magnitude of zero-padded FFT
74
75 bw = enbw(P,fs) % Obtain the ENBW of the hanning window
76
77 maxgain = abs(X(length(P)/2+1)); % Maximum gain
78
79 figure(3)
80 subplot(2,2,1) % sine at bin center, P= 1 watt
81 plot(x)
82 xlabel('n');
83 ylabel('Amplitude');
84 title('(A)')
85 subplot(2,2,2) % apply window to sinewave
86 plot(xw)
87 xlabel('n');
88 ylabel('Amplitude');
89 title('(B)')
90 subplot(2,2,3) % power spectrum into 1 ohm
91 plot(P)
92 axis([0 (NFFT/2) 0 .7]);
93 xlabel('Hz');
94 ylabel('Watts');
95 title('(C)')
96 subplot(2,2,4) % dB magnitude of zero-padded FFT
97 plot(PdB)
98 hold on
99 plot(bw/2*[720 720 1360 1360],[-100 maxgain maxgain -100],'--')
100 hold off
101 xlabel('Hz')
102 ylabel('Magnitude (dB)')
103 axis([0 512 -100 0.2])
104 title('(D)')

```

B.5 MATLAB script and function used in the section 3.3

```

1 % MATLAB script used in the section 3.3
2 % Hermes Loschi - ESR 2 of the SCENT project
3 % The SCENT project has received funding from the European Union's ...
   Horizon

```

```

4 % 2020 research and innovation programme under the Marie ...
   Skłodowska-Curie
5 % grant agreement No 812391.
6 clc; clear all; close all;
7
8 fc=400; %sampling frequency
9 T=20; %duration of the signal
10 my_zero=10; %zero padding factor
11
12 %generate the signal
13 t=linspace(0,T,fc*T);
14 x=zeros(1,length(t));
15 %thresholds
16 th1=0.25*T*fc;
17 th2=0.5*T*fc;
18 th3=0.75*T*fc;
19 th4=T*fc;
20 x(1:th1)=cos(2*pi*10*t(1:th1));
21 x(th1:th2)=cos(2*pi*25*t(th1:th2));
22 x(th2:th3)=cos(2*pi*50*t(th2:th3));
23 x(th3:th4)=cos(2*pi*100*t(th3:th4));
24
25 %calculate and show the spectrograms
26 [spectrogram, axisf, axist]=stft(x,10,1,fc,'blackman',my_zero);
27 spectrogram=spectrogram/max(spectrogram(:));
28 subplot(2,2,1),imagesc(axist,axisf,spectrogram),
29 title('(A) - Spectrogram with T_m = 25 ms'),
30 ylabel('Frequency [Hz]'), xlabel('Time [s]'), colorbar;
31
32 [spectrogram, axisf, axist]=stft(x,50,1,fc,'blackman',my_zero);
33 spectrogram=spectrogram/max(spectrogram(:));
34 subplot(2,2,2),imagesc(axist,axisf,spectrogram),
35 title('(B) - Spectrogram with T_m = 125 ms'),
36 ylabel('Frequency [Hz]'), xlabel('Time [s]'), colorbar;
37
38 [spectrogram, axisf, axist]=stft(x,80,1,fc,'blackman',my_zero);
39 spectrogram=spectrogram/max(spectrogram(:));
40 subplot(2,2,3),imagesc(axist,axisf,spectrogram),
41 title('(C) - Spectrogram with T_m = 200 ms'),
42 ylabel('Frequency [Hz]'), xlabel('Time [s]'), colorbar;
43
44 [spectrogram, axisf, axist]=stft(x,400,1,fc,'blackman',my_zero);
45 spectrogram=spectrogram/max(spectrogram(:));
46 subplot(2,2,4),imagesc(axist,axisf,spectrogram),
47 title('(D) - Spectrogram with T_m = 1000 ms'),
48 ylabel('Frequency [Hz]'), xlabel('Time [s]'), colorbar;
49

```



```
50 % MATLAB funtion used in the setion 3.3 Measurement Standards
51 function [spectrogram, axisf, axist] = ...
    stft(s,win_size,my_step,fc,win,zeropad)
52 if nargin<6
53 zeropad=1;
54 end
55 if nargin<5
56 win='boxcar';
57 end
58
59 N=length(s);
60 i_tot=floor((N-win_size)/my_step); %number of iterations
61 spectrogram=zeros(floor(win_size*zeropad/2),i_tot); ...
    %initialization of the output matrix
62
63 %create the right window
64 if isequal(win,'boxcar')
65 my_window=ones(win_size,1);
66 elseif isequal(win,'hamming')
67 my_window=hamming(win_size);
68 elseif isequal(win,'blackman')
69 my_window=blackman(win_size);
70 end
71
72 my_window=my_window';
73
74 for ii=1:i_tot
75 %starting index
76 a=1+(ii-1)*my_step;
77 %ending index
78 b=win_size+(ii-1)*my_step;
79 %part of the signal to be processed
80 temp=s(a:b);
81 %scale with the chosen window
82 temp=temp.*my_window;
83 %initialize the zero-padded version
84 zeropadded=zeros(1,win_size*zeropad);
85 %create the zero-padded vector
86 zeropadded(1:win_size)=temp;
87 %FFT
88 zeropadded=abs(fft(zeropadded));
89 %get frequencies only once
90 zeropadded=zeropadded(1:floor(win_size*zeropad/2));
91 %store in the final matrix
92 spectrogram(:,ii)=zeropadded';
93 end
94
```

```

95 %create axis to be used to plot the output
96 axisf=linspace(0,fc/2,floor(win.size*zeropad/2));
97 axist=linspace(win.size/fc,N/fc,ii);

```

B.6 MATLAB script used in the subsection 4.2.7

```

1      % MATLAB script used in the subsection 4.2.7.
2      % Figures 4.21 to 4.25.
3      % Hermes Loschi - ESR 2 of the SCENT project
4      % The SCENT project has received funding from the European ...
      Union's Horizon
5      % 2020 research and innovation programme under the Marie ...
      Skłodowska-Curie
6      % grant agreement No 812391.
7
8      clear all; close all; clc;
9
10     N=10e3; % Total size of the random stream
11     SCTL=1/40; % To convert the values in [us]
12     f = 7;
13     g = 10;
14     h = 13;
15     RSCTL = SCTL.*round(((h-f).*rand(N,1)+f)); %Random Single ...
      Cycle of the Time Loop
16
17     %35 kHz-ΔN=10%: 33.25 kHz/36.75 kHz = 120.3 Ticks/108.8 Ticks ...
      - p/ SCTL=10
18     Nmin1 = 109;
19     Nmax1 = 120;
20     dN1=Nmax1-Nmin1;
21     r1 = round(((dN1.*rand(N/2,1))+1)+Nmin1); % random stream for ...
      35 kHz-ΔN=10%
22
23     %95 kHz-ΔN=10%: 90.25 kHz/99.75 kHz = 44.3 Ticks/40.1 Ticks - ...
      p/ SCTL=10
24     Nmin2 = 40;
25     Nmax2 = 44;
26     dN2=Nmax2-Nmin2;
27     r2 = round(((dN2.*rand(N/2,1))+1)+Nmin2); % random stream for ...
      95 kHz-ΔN=10%
28
29     %35 kHz-ΔN=20%: 31.5 kHz/38.5 kHz = 126.9 Ticks/103.9 Ticks - ...
      p/ SCTL=10

```

```

30     Nmin3 = 103.9;
31     Nmax3 = 126.9;
32     dN3=Nmax3-Nmin3;
33     r3 = round(( (dN3.*rand(N/2,1))+1)+Nmin3); % random stream for ...
        35 kHz-\Delta N=20%
34
35     %95 kHz-\Delta N=20%: 85.5 kHz/104.5 kHz = 46.7 Ticks/38.3 Ticks - ...
        p/ SCTL=10
36     Nmin4 = 38.3;
37     Nmax4 = 46.7;
38     dN4=Nmax4-Nmin4;
39     r4 = round(( (dN4.*rand(N/2,1))+1)+Nmin4); % random stream for ...
        95 kHz-\Delta N=20%
40
41     %35 kHz-\Delta N=30%: 29.75 kHz/40.25 kHz = 134.45 Ticks/99.4 Ticks ...
        - p/ SCTL=10
42     Nmin5 = 99.4;
43     Nmax5 = 134.4;
44     dN5=Nmax5-Nmin5;
45     r5 = round(( (dN5.*rand(N/2,1))+1)+Nmin5); % random stream for ...
        35 kHz-\Delta N=30%
46
47     %95 kHz-\Delta N=30%: 80.75 kHz/109.25 kHz = 49.5 Ticks/36.61 Ticks ...
        - p/ SCTL=10
48     Nmin6 = 36.6;
49     Nmax6 = 49.5;
50     dN6=Nmax6-Nmin6;
51     r6 = round(( (dN6.*rand(N/2,1))+1)+Nmin6); % random stream for ...
        95 kHz-\Delta N=30%
52
53     %35 kHz-\Delta N=40%: 28 kHz/42 kHz = 142.8 Ticks/95.3 Ticks - p/ ...
        SCTL=10
54     Nmin7 = 95.3;
55     Nmax7 = 142.8;
56     dN7=Nmax7-Nmin7;
57     r7 = round(( (dN7.*rand(N/2,1))+1)+Nmin7); % random stream for ...
        35 kHz-\Delta N=40%
58
59     %95 kHz-\Delta N=40%: 76 kHz/114 kHz = 52 Ticks/35 Ticks - p/ SCTL=10
60     Nmin8 = 35;
61     Nmax8 = 52;
62     dN8=Nmax8-Nmin8;
63     r8 = round(( (dN8.*rand(N/2,1))+1)+Nmin8); % random stream for ...
        95 kHz-\Delta N=40%
64
65     %35 kHz-\Delta N=50%: 26.25 kHz/43.75 kHz = 152.3 Ticks/91.4 Ticks ...
        - p/ SCTL=10

```

```

66     Nmin9 = 91.4;
67     Nmax9 = 152.3;
68     dN9=Nmax9-Nmin9;
69     r9 = round(((dN9.*rand(N/2,1))+1)+Nmin9); % random stream for ...
        35 kHz-\Delta N=50%
70
71     %95 kHz-\Delta N=50%: 74.25 kHz/118.75 kHz = 53.9 Ticks/33.7 Ticks ...
        - p/ SCTL=10
72     Nmin10 = 33.7;
73     Nmax10 = 53.9;
74     dN10=Nmax10-Nmin10;
75     r10 = round(((dN10.*rand(N/2,1))+1)+Nmin10); % random stream ...
        for 95 kHz-\Delta N=50%
76
77     Nm1 = [r1;r2]; % - final random stream with \Delta N=10%
78     TPWM1 = RSCTL.*Nm1; % - TPWM with \Delta N=10%
79     Y1=1e3./TPWM1; % - F0 with \Delta N=10%
80
81     Nm2 = [r3;r4]; % - final random stream with \Delta N=20%
82     TPWM2 = RSCTL.*Nm2; % - TPWM with \Delta N=20%
83     Y2=1e3./TPWM2; % - F0 with \Delta N=20%
84
85     Nm3 = [r5;r6]; % - final random stream with \Delta N=30%
86     TPWM3 = RSCTL.*Nm3; % - TPWM with \Delta N=30%
87     Y3=1e3./TPWM3; % - F0 with \Delta N=30%
88
89     Nm4 = [r7;r8]; % - final random stream with \Delta N=40%
90     TPWM4 = RSCTL.*Nm4; % - TPWM with \Delta N=40%
91     Y4=1e3./TPWM4; % - F0 with \Delta N=40%
92
93     Nm5 = [r9;r10]; % - final random stream with \Delta N=50%
94     TPWM5 = RSCTL.*Nm5; % - TPWM with \Delta N=50%
95     Y5=1e3./TPWM5; % - F0 with \Delta N=50%
96
97     figure (1) %J just the first case
98     subplot(1,2,1);
99     h5 = histogram(TPWM1,40);
100    xlabel('values of T_{PWM} [\mu s]');
101    ylabel('frequency of variable appearance');
102    title(['(A)']);
103    subplot(1,2,2);
104    h10 = histogram(Y1,40);
105    xlabel('values of f_{0} [kHz]');
106    ylabel('frequency of variable appearance');
107    title(['(B)']);

```

Differences in the Control Hardware Features

In this appendix C, it is shown that the 2D conventional EMC test standard based on frequency scanning might not be sufficient to appropriately provided an EMI assessment¹. The EMI measurements were carried out with two DC/DC converters into the concept of parallel electrical installations' topologies. Besides, to investigate the possible associated phenomena further, the EMI measurements were carried out in the outputs voltage and current. Once these waveforms have different time-domain shapes (rectangular wave and triangular wave), different behaviour in the spectrum of frequency might be expected.

C.1 Experimental Setup Description

The EMC-test bench system was built utilizing two similar Buck converters controlled by two separate controllers. The main parameters of those two Buck converters are presented in [152]. Also, both Buck converters are connected to the same load as shown in Fig. C.1. Hence, the setup provides controlling the switching signal based on DetM.

Two types of commercial controllers were used. The FPGA 7854R from NI, and Atmega328p from Atmel used in Arduino UNO board. The FPGA 7854R controllers use a crystal of 40 MHz with maximum variation of ± 100 ppm, while the Atmega328p controllers use one of 16 MHz with maximum variation of ± 50 ppm. The frequency stability variation in the case of FPGA 7854R might be between 54 kHz to 66 kHz with 60 ± 6 kHz variation around the f_0 , while in case of Atmega328p, might be between 57 kHz to 63 kHz with 60 ± 3 kHz variation around the f_0 .

¹Parts of this appendix C are published in [152].

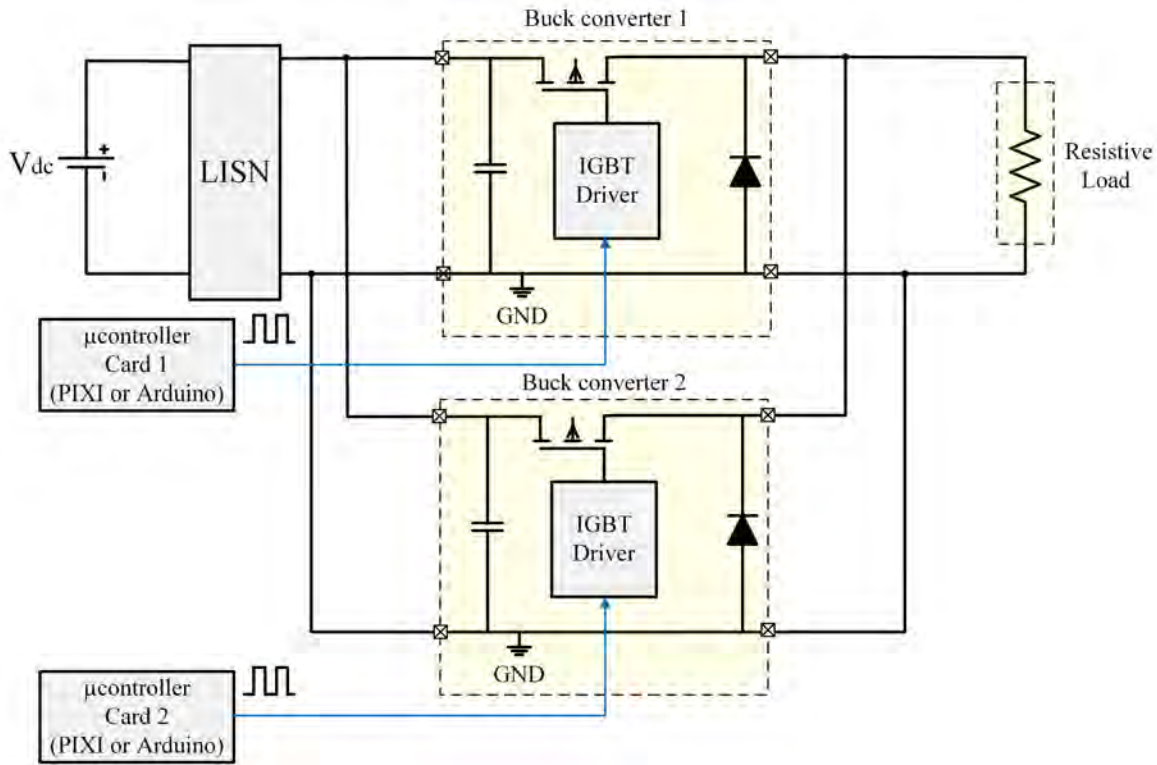


Figure C.1: Experimental setup connection diagram.

C.2 Results and Discussions

The AV detector with the IFBW = 200 Hz was used in all conducted EMI measurements carried out, following CISPR A standard [78]. The beat appears faster in case of using two Atmega328p as controller than in case of using two FPGA 7854R. The beat variation of amplitude appears in case of two Atmega328p every 0.6 seconds as shown in Fig. C.2. Thus, the frequency stability variation is in range of 60000 ± 1.6 Hz.

In the case of two FPGA 7854R, the beat variation of amplitude is repeated every 150 seconds as shown in Fig. C.3. Thus, the frequency stability variation is 60000 ± 0.0066 Hz.

The frequency spectrum amplitude of the output voltage (Fig. C.2 and Fig. C.3) presents different behaviour from the case of output current (Fig. C.4 and Fig. C.5). In the case of the voltage, the measured signal is a rectangular pulse train. The spectrum amplitude of the harmonics decreases with the increase of the harmonic order (Fig. C.2 and Fig. C.3).

The highest amplitude of EMI appears in the harmonics related with the f_0 , i.e., $115 \text{ dB}\mu\text{V}$. The amplitude of the 2^{nd} and 3^{rd} harmonics are $108 \text{ dB}\mu\text{V}$ and $105 \text{ dB}\mu\text{V}$, respectively, as shown in Fig. C.2 and Fig. C.3. It's noteworthy that the amplitude of the even and odd harmonics decreased gradually by a definite pattern.

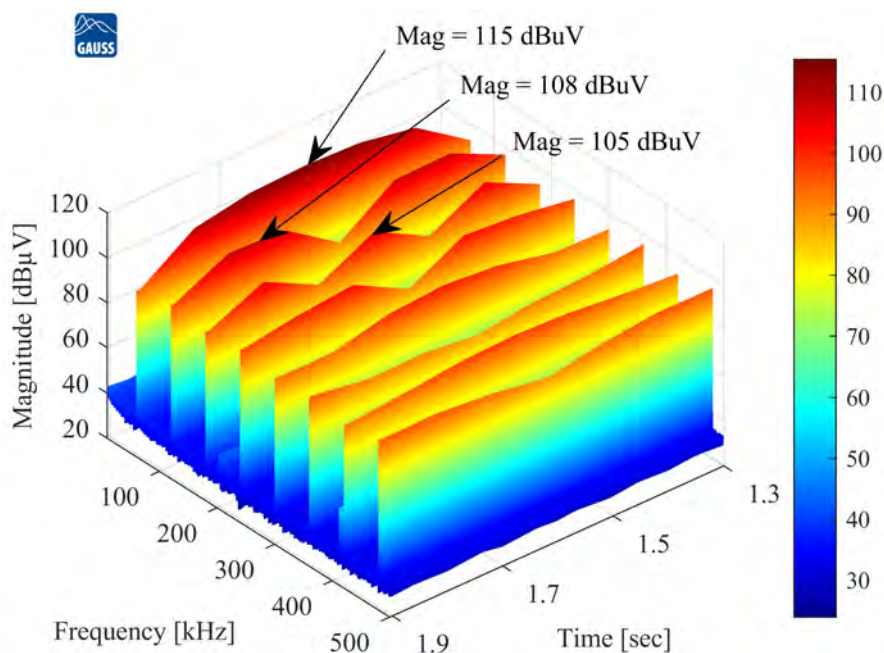


Figure C.2: 3D spectrogram of the output voltage in case of using two Atmega328p controllers.

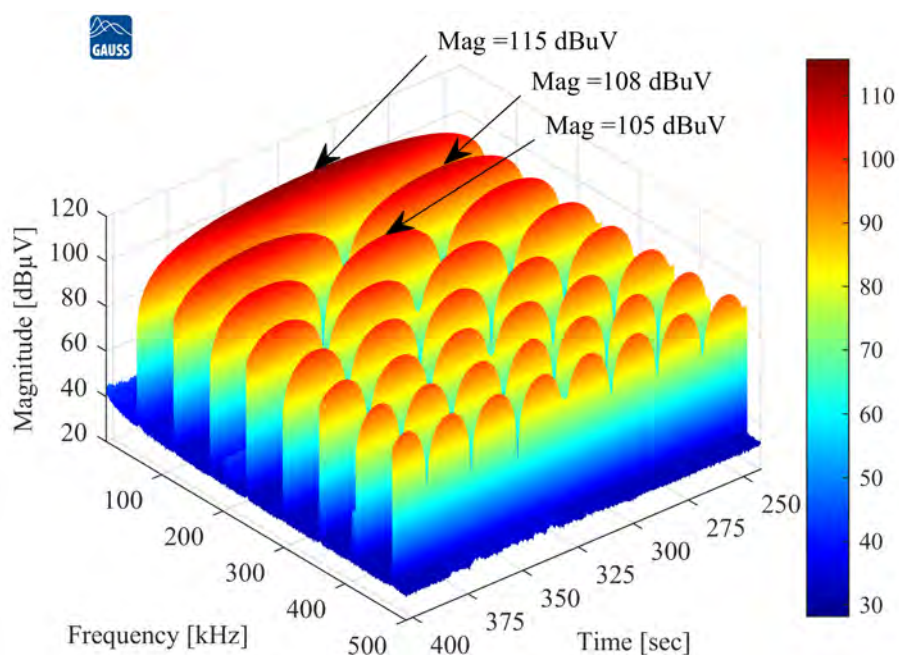


Figure C.3: 3D spectrogram of the output voltage in case of using two FPGA 7854R controllers.

On the other hand, in the case of output current, the even harmonics spectrum amplitude is lower than that in odd harmonics. Fig. C.4 and Fig. C.5 show the amplitude of the 3rd harmonic higher than the 2nd harmonic by 10 dB.

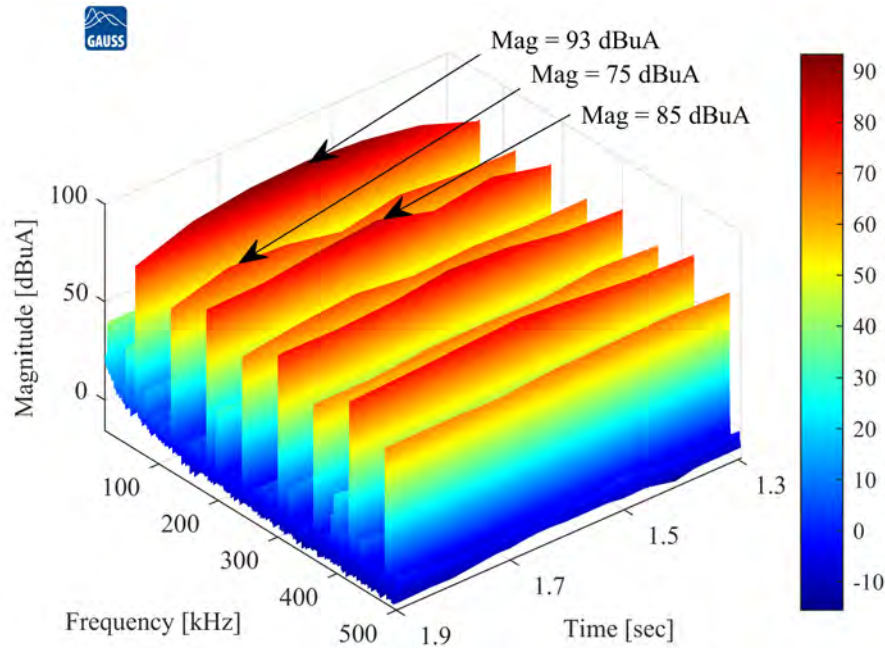


Figure C.4: 3D Spectrogram of the output current in case of using two Atmega328p controllers.

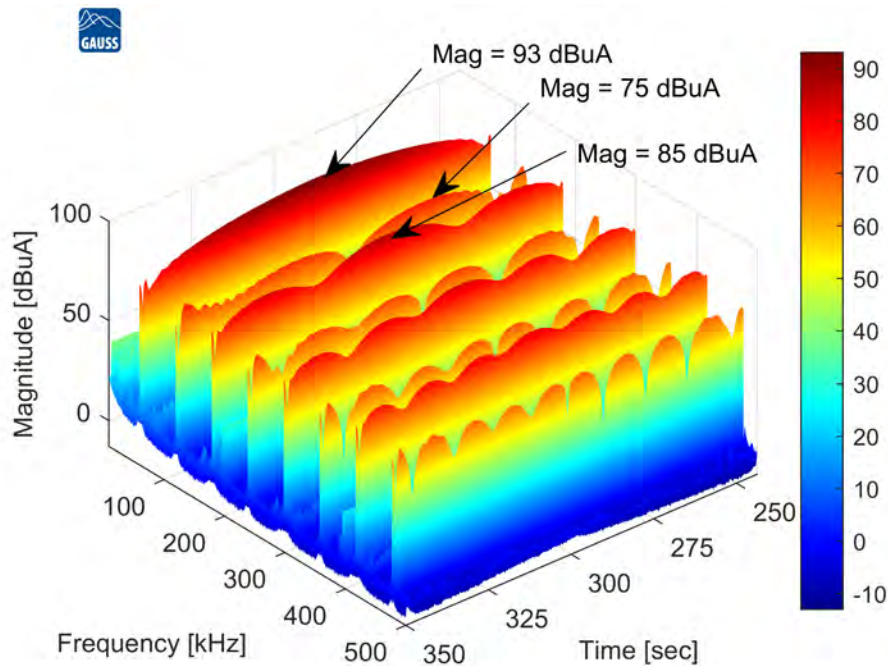


Figure C.5: 3D Spectrogram of the output current in case of using two FPGA 7854R controllers.

Once these waveforms have different time-domain shapes (rectangular wave and triangular wave), different behaviour in the frequency spectrum was presented in all the cases, i.e., Fig. C.2, Fig. C.3, Fig. C.4 and Fig. C.5. Moreover, the frequency sta-

bility variation related to the power conversion equipment clock signals, i.e., control hardware, was within the expected range. Since the frequency stability variation behavior depends on the variation of the controller's onboard crystal frequency, which may be affected by other parameters such as the temperature, circuit impedance and ground, or the quality of the manufactured crystal.

The control signal from FPGA 7854R, at the hardware level, is provided by the NI SCB-68A shielded connector block. Combined with the shielded cables, it provides rugged, very low-noise signal termination to the transistor gate drive. Thus, as verified through the EMI measurements carried out and presented in Fig. C.3, the FPGA 7854R provides better performance in terms of frequency variation stability, i.e., 60000 ± 0.0066 Hz.